Aus dem
Department für Frauengesundheit Tübingen
Forschungsinstitut für Frauengesundheit

WAT-Liver-Chip with Integrated Sensors to Study Human White Adipose and Hepatic Tissue Crosstalk

Thesis submitted as requirement to fulfill the degree 'Doctor of Philosophy' in *Experimental Medicine* (Ph.D.)

at the
Faculty of Medicine
Eberhard Karls Universität
Tübingen

By

Tanvi Shroff

2023

Dean: Professor Dr. B. Pichler

First reviewer: Professor Dr. P. M. Loskill

Second reviewer: Professor Dr. A. Birkenfeld

Date of oral examination: 08.12.2023

To my family

Table of Contents

List of Abbreviations

2D	Two-Dimensional
3D	Three-Dimensional
apoB	Apolipoprotein B
APTES	(3-Aminopropyl) triethoxysilane
ASGPR1	Asialoglycoprotein receptor 1
ASS1	Argininosuccinate synthetase 1
ATP	Adenosine triphosphate
bFGF	Basic fibroblast growth factor
BMI	Body mass index
BSA	Bovine serum albumin
CAD	Computer-aided design
CD106	Cluster of differentiation 106 [also: vascular cell adhesion molecule 1 (VCAM-1)
CD31	Cluster of differentiation 31 [also: platelet endothelial cell adhesion molecule 1 (PECAM-1)]
CYP3A4	Cytochrome P450 3A4
CFD	Computational Fluid Dynamic
DAPI	4', 6-diamidino-2-phenylindole
DMEM/F-12	Dulbecco's Modified Eagle Medium/Nutrient Mixture F-12
DMSO	Dimethyl sulfoxide
E-Cadherin	Epithelial cadherin, Cadherin-1
ECM	Extracellular matrix
ECGM	Endothelial cell growth media
ECGS	Endothelial cell growth supplement
EDTA	Ethylenediaminetetraacetic acid
EUROoCS	European Organ-on-Chip Society
FA	Fatty acid
FCS	Fetal calf serum
FDA	Fluorescein diacetate
FEM	Finite element method
FFA	Free fatty acid
FGF21	Fibroblast growth factor 21
FITC-dextran	Fluorescein isothiocyanate-dextran
GLUT4	Glucose transporter type 4
GST-α	Glutathione S-transferase-α
HepaRG™	Hepatocyte-like cell line
HEPES	(4-(2-hydroxyethyl)-1-piperazineethanesulfonic acid)
HUVEC	Human umbilical vein endothelial cell
HyA	Hyaluronic acid
iPSC	Induced pluripotent stem cell
LDH	Lactate dehydrogenase
LogP	N-octanol/water partition coefficient
LPL	Lipoprotein lipase
LPS	Lipopolysaccharide
MACS	Magnetic activated cell sorting
MOC	Multi-organ-chip
MRP2	Multidrug resistance-associated protein 2
mVEC	Microvascular endothelial cell
NADH/NAD+	Reduced/oxidized form of nicotinamide adenine dinucleotide (NAD)

NAFLD	Non-alcoholic fatty liver disease
NASH	Non-alcoholic steatohepatitis
OoC	Organ-on-Chip
OUR	Oxygen uptake rate
PAS	Periodic acid-Schiff
PBS	Dulbecco's phosphate-buffered saline without calcium chloride and without magnesium chloride
PBS+	Dulbecco′s Phosphate Buffered Saline with magnesium chloride and calcium chloride
PC	Polycarbonate
PCR	Polymerase chain reaction
PDMS	Polydimethylsiloxane
Pen/Strep	Penicillin/Streptomycin
PET	Polyethylene terephthalate
PI	Propidium iodide
PMMA	Poly(methyl methacrylate)
PPARγ	Peroxisome proliferator activated receptor γ
RNA	Ribonucleic acid
ROI	Region of interest
SCFA	Short chain fatty acid
SVF	Stromovascular fraction
TEER	Transepithelial/endothelial electrical resistance
TNF-α	Tumor necrosis factor α
TPE	Thermoplastic elastomer
VE-Cadherin	Vascular endothelial cadherin
WAT	White adipose tissue
WEM	William's Media E

List of Figures

List of Tables

1. Introduction

1.1. Organ-on-chip technology and multi-organ interactions

Advances in microfabrication, tissue engineering and stem cell biology led to the emergence of organ-on-chip (OoC) technology, a new generation of *in vitro* models to combat the original challenges faced by traditional non-clinical models (Bhatia & Ingber, 2014). These systems enable the cultivation of human-specific cells with physiological shear and perfusion via a vascular channel, with a tailored microenvironment for the cells. A group of experts from the ORCHID (*Organ-on-Chip In Development)* Consortium defined OoC as a '*fit-for-purpose microfluidic device, containing living engineered organ substructures in a controlled microenvironment, that recapitulates one or more aspects of the organ's dynamics, functionality and (patho)physiological response in vivo under real-time monitoring*' (Mastrangeli et al., 2019). This highly interdisciplinary technology promises translatability and the potential of 3Rs (reduction, replacement, and refinement) in animal testing (Russell & Burch, 1959).

With average drug development times extending over a decade, costs incurred for a new drug to reach the market could add up to billions of US dollars (Kaitin, 2010; Paul et al., 2010; Aghila Rani et al., 2021). High research and development costs are cited as a reason for high drug prices, with the requirement for better predictive models in the non-clinical phases. While traditional *in vitro* models and animal models have provided valuable data, certain shortcomings make them less favorable for drug screening or disease modeling. In spite of their high throughput and ease of establishment, static well plate systems have a lack of medium renewal over extended periods of time and are unable to recapitulate the complex spatial arrangement of cells (Bale et al., 2016). On the other hand, animal models provide a complete response due to an interconnected organ-system (Reitman, 2018; Staiger et al., 2017). However, the challenges faced there relate to interspecies differences and the inability to recapitulate human-specific responses (*e.g.* different immune systems) in addition to ethical issues. OoC models can combat these challenges and have the potential to reduce pharmaceutical R&D costs by 10-26%, according to an expert survey analysis on this topic (Franzen et al., 2019).

The main structure of organ-chips comprises a tissue compartment separated from media perfusion by a diffusion barrier for the exchange of nutrients without direct exposure of tissues to shear forces. In addition to the biological complexity of various cell types in each tissue, the OoC field comprises various aspects to reliably recapitulate organ function and study the effect of therapeutics. These aspects include perfusion methodologies, sensors to track tissue-function in real time, the effect of material of construction on the dose of therapeutics, etc. Another aspect of complexity building on the OoC system includes connecting organ-chips together to form a multi-organ-chip (MOC) system. This adds considerations of vascularization, immune cell interactions, and connection strategies. The next subsection highlights these considerations and presents the state of the art in the MOC field.

1.2. Multi-organ chips and connections – practical design considerations

Complex pathophysiological processes in the body progress through the interaction of different organs. Drugs act on combined mechanisms affecting multiple organ systems. Single organ-chips enable the integration of complexity to some extent, with the inclusion of non-parenchymal cells, resident immune cells, and stromal cells for organ-specific mechanistic research (Booth & Kim, 2012; Huh et al., 2010; Jang et al., 2019; Kim et al., 2012). While single organ-chips provide detailed insights into targeted mechanisms within a functional unit of an organ, multi-organ-chips (MOCs) build on the complexity related to organ-interactions, enabling the investigation of response on a systemic level with potentially higher accuracy and throughput compared to animal models. Pioneering work in this topic was done by Shuler and colleagues (Viravaidya, Sin, et al., 2008), and since then, various other publications have investigated organ-chip linking (Abaci & Shuler, 2015; Rogal et al., 2017; Wikswo, Block, et al., 2013; Zhang et al., 2009). This section highlights the state-of-the-art of engineering MOC systems, with a focus on minimizing dead volume, scaling organ-chips relative to each other, mechanisms of connecting the OoCs, perfusion regimes, materials of construction of the MOCs and sensor integration (Shroff et al., 2022).

1.2.1. Minimization of dead volume: Fixation mechanisms to connect MOCs

Dead volume is the volume of liquid that remains between the connected organ-chips as the media circulates across the MOC. It is the volume of liquid to be traversed before the next organ-chip sees the cytokines and cues secreted by the one before. Dead volume also influences the time taken by an external stimulus to traverse across the OoCs, and the collection time of sample effluents for downstream analysis. The MOC's goal is to minimize this dead volume to allow for physiological fluid circulation between the organ chips. Sampling possibilities should be assessed depending on the intended study. Dead volume can be minimized on-chip at the following stages of the perfusion setup:

i. Dead volume at the connections between OoCs: Minimizing tubing diameter and length of the connection between the OoCs such that the chips interface directly with each other and connections between them are as small as possible.
ii. Dead volume at the system inlet: Incorporation of switches to minimize the time between the switch of applied media containing a drug or stimulus and the regular cell culture media, although this could lead to an increase in the complexity and cost of the setup.
iii. Dead volume at the system outlet: A collection reservoir at the outlet of the chip with a certain volume for mid-experiment sampling.

The connection methodology of OoCs to the perfusion mechanisms or to each other is called a sealing strategy. (Temiz et al., 2015). There are two broad categories of sealing strategies: Chip-to-chip sealing connects OoCs to each other, and world-to-chip sealing connects OoCs to the perfusion regime at the inlet and outlet. Two rigid chips connected to each other require a uniform distribution of sealing pressure, which is achieved by a flexible material called a gasket placed between the two chips. Sealing pressure has been created in **chip-to-chip connection** systems with the help of magnets or screws to ensure tight connections and flow of media from one OoC, across the gasket to the other. A 'stick and play' modular connection approach used a 3D printed chip and magnetic ends which could be stacked onto each other reversibly (Yuen, 2016). Magnetic pressure was used to create the 'TILE' connectors which snap-sealed onto

each other (Ong et al., 2019). In a separate report on 'Lego connectors', capillaries were incorporated into the connectors, which when inserted into the ports of the PDMS chips, creating a tight but reversible seal (Loskill et al., 2015). Tight chip-to-chip connections were also created by adding screws, as in the case of the TOP fluidic interface platform (Vollertsen et al., 2020). The **world-to-chip connectors** provide a mechanism of interfacing the tubing with the chip. For chips with flexible tops such as PDMS, a metal cannula or rigid material fitted at the end of the tubing provided a simple and tight press-fit connection (Chen & Pan, 2011). If the surface of the chip is rigid, the tubing can be directly fitted into a port on the chip. Connectors have also been incorporated into the rigid plastic material, hence reducing the amount of elastomeric material and hence reduce the potential for small-molecule absorption. Embedded flexible connectors were developed for reversible insertion of tubing in and out of the chip (Snakenborg et al., 2007). A PDMS O-ring embedded into a PMMA chip allowed for simple interfacing with a capillary or cannula with tubing (Evander & Tenje, 2014). Soldering metal connectors onto chips with silicon surfaces, such that the cannulas could connect directly to the tubing, avoided the need for additional connection mechanism (Murphy et al., 2007). Similarly, permanently attaching a metal needle onto the plastic chip enabled future interfacing with tubing (Chen et al., 2009). Force-fit connectors with multiple tubes attached into a metal-based compression element and reversibly screwed onto the surface of the chip allowed for a series of fluidic connections onto the chip (Wilhelm et al., 2013). Magnets allowed for a reversible sealing mechanism, such as for sealing a PDMS top onto a glass surface with cells in culture, or a ring magnet that held the tubing attracted a disk magnet at the base of the chip, creating a strong force to hold the tubing to the chip (Tkachenko et al., 2009, Atencia et al., 2009). Reports of vacuum sealing a manifold containing the tubing onto the fluidic chip showed another flexible connection mechanism, which would additionally need bulky vacuum apparatus (Cooksey et al., 2009). Springs provided a pressure-force, again requiring additional construction apparatus as in the 'Reusable Standardized Universal Interface Module' (Sun et al., 2019). While this introduces the possibility of adhesives leaching into the media perfused across the chips, gluing connectors via adhesive tape onto the chips has also been reported (Glavan et al., 2013)

1.2.2. Relative organ scaling

The relative size of tissues in an MOC becomes important from the perspective of creating a physiologically relevant correlation, with a reasonable concentration of metabolites going from one tissue to another. A review of the relative organ scaling approaches resulted in the broad categories, allometric, residence time-based and functional scaling (Wikswo, Curtis, et al., 2013). **Allometric scaling** applies the quarter power law to scale down organ weight or volume to a micro-scale correlated to the body weight (Ahluwalia, 2017). However, this could lead to disproportionately sized OoCs compared to each other and does not account for relative organ function (Wikswo, Block, et al., 2013). Another type of physiological downscaling was applied in scaling down the cell numbers in a pancreas-liver MOC by 1 to 100,000 as seen *in vivo* (Casas et al., 2022). While this led to a total circulating volume comparable to that *in vivo*, the insulin secretion of the pancreatic islets and liver function values were reportedly off from *in vivo* by an order of 10. **Residence time-based scaling** relates to sizing the organs based on the flowrate of blood across the organs. This concept has been applied to body-on-chip models that

split the media such that 25% flowed into the liver chamber, 9% to the adipose chamber and 66% to the 'other tissues' (Viravaidya & Shuler, 2008). **Functional scaling** emerged out of the realization that the organ-chips scaled by the other methods might function completely differently from the *in vivo* case, depending on the cell types used and spatial orientation of the cells. A study of insulin-dependent glucose uptake in adipose tissue suggested that scaling should be performed based on volume for organs that are functionally 3D (secretory or storage functions) and based on surface area for organs that are functionally 2D (filtration, absorption, or molecular transport functions) (Moraes et al., 2013).

Integrating data from MOCs with *in silico* models could create a powerful platform for the prediction of clinical response in the study of a particular mechanism. Physiologically based pharmacokinetic (PBPK) models structure the MOC into compartments, taking the mechanism being studied into consideration (Maass et al., 2017). Since signaling mechanisms between cells and effluent readouts are concentration dependent, it is crucial to establish a realistic ratio of liquid to cell volume. For quantification of metabolism readouts, the metabolic burden of the chip (for example, liquid per hepatocyte) becomes important. A model was developed connecting the liver and heart OoC to study the administration of terfenadine causing QT-prolongation, a toxic effect on the heart. The study showed that when the CYP3A4 enzyme metabolized terfenadine to fexofenadine, the QT prolongation of the heart was reduced (McAleer et al., 2019). Cryopreserved hepatocyte functionality was assessed through albumin secretion and gene expression upon exposure to six drugs (Tsamandouras et al., 2017). The data from the OoC was coupled with simulations to predict *in vivo* clearance of drugs. Scaling and characterization of the organ-chips in an MOC is an iterative process and the ideas presented above provide for a starting point to setup the model, but further rigorous optimization is required depending on the cell types, assays, and study design.

1.2.3. Organ connection methodology

A comprehensive review of the different methodologies to connect OoCs led to three distinct categories namely inbuilt, modular, or systemic connections:

Inbuilt connection systems comprise of two or more organ tissue chambers built into the same chip, with a fixed cell ratio and a common cell medium flowing across the tissues, either in direct contact or separated by a porous semi permeable membrane. A 14-organ microscale cell culture analog with fluidics channels connecting the tissue chambers, considered physiological, organ-specific fluid residence times (Miller & Shuler, 2016). A 4-organ micro-scale cell culture analog comprising of lung, liver, fat and 'other tissue' chambers, was scaled based on the PBPK model of a rat (Viravaidya & Shuler, 2008). This model demonstrated accumulation, distribution, and toxicity of compounds with hydrophobic compounds partitioning to a higher extent in the fat chamber. While inbuilt connection systems have the lowest dead volumes between the tissue compartments, each tissue might have different maturation times as in the case above, where the pre-adipocytes had a longer differentiation protocol and were plated on the MOC first before the other cell types. This can reduce the flexibility of the on-chip culture protocol. Additionally, each tissue compartment is unique to the requirements of the cells of a specific organ, with every new experiment requiring new design criteria depending on the organs being connected.

In the case of **modular connection** systems, it is more convenient to culture tissues separately and then link the systems via tubing or fluidic inserts. This enables separate tissue culture until a mature tissue is established. Lego-inspired modular connectors connected several organ-chips in series, in a flexible manner with low dead volumes (Loskill et al., 2015). These connectors were attached to the organ-chips via capillaries and could allow for the possibility of sensor integration to track parameters like glucose or pH in real-time as the media flowed from one organ to another. A report of a 3-bioreactor model connected hepatocytes, adipose tissue, and endothelial cells via tubing to study glucose and fatty acid metabolism (Iori et al., 2012). While convenient, the high dead volume increased response times of the downstream organ-chips and diluted the effluents. Another report presented a snap-fit connection system where magnets provided a tight seal between the two connected OoCs (Ong et al., 2019). A stick and play modular connector was created by stacking PDMS-chips such that the outlet of one chip led to the inlet of the next, with magnets to seal the chips (Yuen, 2008; Yuen, 2016). Modular connection systems have several detachable parts directly at the chip ports, and hence require more complex engineering approaches to ensure a leak free connection.

Systemic connection involves plugging the organ-chips into a fluidic interface, with inbuilt fluidic connections. This concept takes the externally applied connection methods one step further where multiple chips can be inserted into an interface to allow for streamlined interactions and the possibility of integrating in-line sensing. The communication between lung and liver tissue investigated the potentially toxic effects of inhaled substances in the HUMIMIC platform (Schimek et al., 2020). This platform involved the culture of the individual organ tissues on inserts and a subsequent perfusion with an optimized media across both organs. They were able to demonstrate that the liver metabolized the aflatoxin B1 and had a protective effect on the lung-OoC. The multi-organ platform comprised a transwell-based system connecting various organ-models via the vasculature (Ronaldson-Bouchard et al., 2022). A liver spheroid was cultured with a skin biopsy punch over a period of 28 days with endothelial cells lining the vascular channels. The organ-tissues were cultured on inserts before being placed into the platform (Materne et al., 2015). The organ models could be placed in any order, reversibly into the system. A breadboard setup showed a connected liver-cancer-heart system connected via a fluidic breadboard with integrated valves for flow control, a reservoir, bubble trap and sensors (Zhang et al., 2017). However, this platform still used tubing as the main connection mechanism, increasing the dead volume at the connection sites, and introducing an additional site of small-molecule absorption by the flexible tubing. In the case of the systemic connection method, the organ-chips are designed with ports at specific locations to enable being clicked into the same place, irrespective of the organ-chip being connected. Once standardized, the system can interface with automated liquid handling capabilities, as shown with the interrogator platform. (Novak et al., 2020). Another example of a fluidic circuit board with modular inserts for sensors and chips called the TOP fluidic platform was developed (Vivas et al., 2022).

The interactions of organs are complex, but one essential feature in most interactions mentioned above is the vasculature, for the exchange of nutrients, metabolic waste, immune cell trafficking and endocrine signaling. While some models have been presented with a direct

connection of the organs across a perfused media channel, a majority of the MOCs seek to mimic this interaction via an endothelial cell-lined vascular connection channel.

1.2.4. Perfusion regimes

One of the key defining features of OoC technology is the incorporation of physiological vascular-like perfusion across the organ-tissue, promoting the exchange of oxygen, nutrients, and byproducts across the tissues, simulating the case of arterioles, venules, and capillaries. With dimensions ranging from 10 μm to 500 μm in diameter, the perfusion is unidirectional, and dampened or less pulsatile compared to aortic flow (Pollet & den Toonder, 2020). In the OoC setting, a pumping methodology is used to drive the perfusion and systems exhibit one of the following perfusion regimes – linear (push or pull), recirculating (unidirectional or vacillating).

In the case of linear perfusion regimes, a unidirectional flow is directed from an inlet source to an outlet reservoir, across the OoC. Positive or negative pressure is applied to perfuse the media. In the **linear push regime**, the inlet medium reservoir at the chip inlet is connected via tubing to the chip and a sampling reservoir at the outlet. The inlet medium reservoir could be a syringe in the case of syringe pump-driven push perfusion, or a beaker in case of a pressure pump-driven push regime. This regime allows for time-resolved sampling at the outlet reservoir (Rogal et al., 2020), and the inlet media could be changed by the integration of switches as in the case of a pancreas-on-chip system, exposing the chip to high and low glucose media conditions and effluents sampled at regular time intervals (Zbinden et al., 2020). The **linear pull regimes** comprise of a reservoir connected via tubing or directly located on a chip, connected to a pump (syringe or peristaltic) located downstream of the chip. The media perfused across the chip is pre-equilibrated with a reduced chance of bubble formation. Refilling of the reservoirs is simpler, making this a convenient method for long-term perfusion and testing drug dosing regimens with the ability to change media conveniently at the site of the upstream reservoir, in addition to perfusing delicate cell types like immune cells (Cipriano et al., 2022) and whole blood through the OoCs (Barrile et al., 2018). The challenge with these systems comes in the presence of even a small leak, which could lead to a stream of bubbles infiltrating into the system, and time-resolved sampling being more challenging at the outlet. The linear perfusion regimes could also be used to create gradients, as with the case of a gradient of oxygen and free fatty acids to observe a gradient of metabolizing functions in hepatocytes in a liver-sinusoid mode (Kang et al., 2020) .

The recirculating perfusion regime involves a closed-loop perfusion of media across the OoC, leading into a reservoir. The **unidirectional recirculating perfusion regime** employs a peristaltic pump enabling sampling, dosing, and media replenishment at the single reservoir in the closed loop system. This system was applied for perfusion across a four-organ system, allowing for periodic sampling of effluents and ‘intravenous dosing’ of a drug candidate to test the drug pharmacodynamics (Ronaldson-Bouchard et al., 2022). In another instance, immune cells were injected into a gut-liver-cerebral MPS to observe interaction of the immune system with the organs over a four-day period (Trapecar et al., 2021). A 3D-tilting platform for gravity-driven pumpless unidirectional perfusion enabled the culture vascular endothelial cells along the channels and liver organoids within the tissue chambers. (Busek et al., 2023). Additionally,

immune cells were perfused across the platform without activation or entrapment. The **vacillating recirculating perfusion regime** involves media flowing back and forth across the organ-chips on a rocker, flanked by reservoirs at both ends driven mostly by gravity (Kim et al., 2021; Sung et al., 2010). Vacillating flow can also be generated in pressure pumps by switching between pull and push mode. One feature of the recirculating perfusion regime is that the metabolites and cellular components in the media are pooled in the reservoirs, where cumulative effects on the organ-chip are seen as opposed to being able to study the specific time-resolved effects of one organ-chip on another.

1.2.5. MOC Materials

The choice of material of construction of the MOC depends on the scale of operation and the study design. In the academic prototyping phase (50 chips per month), common techniques to fabricate MOCs include soft lithography, laser cutting, CNC milling and for larger-scale production (pilot scale ranges from 120 to 160 chips per month), processes lean more towards injection molding, thermal fusion bonding, hot embossing. In case of soft lithography, PDMS and OSTE are the most reported in literature. In the case of laser cutting and hot embossing, rigid plastics like PMMA, COC, PC or thermosets like TPE are used (Paoli et al., 2021; Rogers & Nuzzo, 2005). Optical transparency is important for live imaging of tissues through the chip material. Fluorescent imaging requires that the material of the MOC is also non-auto fluorescing. Some materials allow for oxygen tunability of media within the chip while others mirror the oxygen concentrations of the environment of the chip. OSTE-mer tends to be oxygen scavenging if not completely cured, and thus, a baseline readout should be conducted before running experiments. PDMS is gas permeable and ensures that the media is saturated with gases from the environment of the chip. Rigid plastics like PMMA or COC allow for gas-concentrations to be locally tuned around the tissue, allowing for fine-tuning the oxygen concentration in media (Oomen et al., 2016). Adjusting the flowrate of the media or the material of the chip will ensure sufficient oxygen delivery, and it can be validated with the help of simulations, taking care not to dilute the cell metabolites in the chip effluent. A final feature of the material of the MOC to be characterized is the capacity of drug absorption as a baseline, before running a study to quantify PKPD in a multi-organ MPS. PDMS has been shown to absorb small molecules and some fluorescent molecules to varying extents (Wang et al., 2012). There is a loose correlation between the logP, number of hydrogen bond donors, molecular weight and chemical structure of small molecules which could enable them to penetrate tissue better and hence partition into materials like PDMS to a large extent (Wang et al., 2012). This amounts to absorptive compound losses, in addition to adsorptive compound losses which involve random non-specific binding of the compound to the material of the MOC. Before characterizing the effects of the drug on the MOC, a baseline characterization of drug concentration in the system should be performed to quantify the extent of adsorption and absorption of the drug by the system in the absence of cells (Grant et al., 2021; Wang et al., 2012).

1.2.6. Method of fabrication of MOCs

Manufacturing techniques can be broadly classified into formative, subtractive and additive. With formative manufacturing (FM) methods, the final geometry is cast into a mold where the fluid form of the material conforms to the shape of the mold. Upon solidifying, the material

can be removed from the mold. Examples of these methods include injection molding, hot embossing, PDMS casting. Another class of FM methods rely on changing the bulk properties of soft materials in their solid state. Examples of these methods include extrusion or rolling. With subtractive manufacturing (SM) methods, the material is removed from the bulk to reveal the desired shape (Braian et al., 2018). Examples of this include lasercutting, etching and CNC milling. The final method is additive manufacturing (AM), where the part is created by depositing material layer by layer (Tian et al., 2022). AM can be used to produce complex geometries without the use of dies and molds (Pereira et al., 2019). Examples include the various types of 3D printing. Taking select examples from literature, one or the other of these methods of fabrication have been employed in the OoC field. PDMS casting is a method of FM, where the material is cast off a wafer (produced by SM or AM) or 3D printed mold (produced by AM) (Cameron et al., 2022; Jang et al., 2019). Larger scales of chips are produced by injection molding (FM), which allows for a level of automation of production (Raasch et al., 2015). TPE can be embossed by molds or extruded (Schneider, Brás, et al., 2021). Thermoplastics could also be lasercut or embossed to create channel features (Jeon et al., 2011).

The final assembly steps involve methods of fusing the parts produced by FM, SM or AM in a controlled fashion. Surface modifications are used to bond PDMS layers to each other via plasma treatment, or PDMS to plastic layers via silanization of the surfaces (Borók et al., 2021; Novak et al., 2018). Thermal fusion bonding is employed in the case of thermoplastics, where the layers are heated to glass transition temperature of the plastics and bonded together under pressure (Chuchuy et al., 2021). Laser welding involves bonding a transparent thermoplastic layer to a compatible opaque absorbing layer, without heating the entire bulk material (Schneider, Gruner, et al., 2021). Other bonding processes include solvent bonding, ultrasonic welding and direct gluing of parts together (Wen et al., 2021).

The application of each of these methods depends on the scale of intended chip fabrication, required surface finish of parts, the target feature dimensions, complexity of design of the part and intended method of final chip assembly (Ko et al., 2022; Nahak et al., 2022). No one method fits all, so design criteria must be established at the start of the MOC development phase in order to narrow down the best fit for use method.

1.2.7. Sensor integration

Markers indicating tissue function can be analyzed from the effluent of the MOCs. Integrating sensors in-line between the MOCs will enable monitoring the change of certain cell culture parameters in real-time. For metabolizing systems, parameters like glucose, oxygen, pH and reactive oxygen species are essential for understanding the organ interactions and for tracking the function of the MOC. A detailed review of in-line sensors has been presented in literature, where sensors can be classified as electrical, electrochemical or optical (Fuchs et al., 2021). Typically, the sensors for media properties are either of the latter two since electrical sensors mostly monitor cell growth or mechanical responses. Several approaches can be used to integrate the sensors into MOCs. Electrochemical sensors could be immobilized onto the surface of beads or covalently bonded to electrode materials, and optical sensing material could be either integrated into a thin film, spot or on beads. Considerations should also be made given the sensing mechanism and the material of construction of the MOC. Modular sensors were

developed, presenting a breadboard system with sensors tracking pH, temperature, oxygen and certain proteins like albumin, GST-a and CK-MB (Zhang et al., 2017). Another report had small glass capillary plug-ins for the sensors for continuous measure of glucose and lactate (Misun et al., 2016). A report about in-line sensing measured glucose-stimulated insulin secretion in a pancreas-chip model (Glieberman et al., 2019).

1.3. White adipose tissue-chip models

The body comprises of many types of adipose tissue, serving endocrine, storage and metabolic functions. White adipocytes, the parenchymal cells of white adipose tissue (WAT), are important for the maintenance of energy and lipid homeostasis (Corrêa et al., 2019). Non-parenchymal cells include stromal vascular fraction components such as the resident immune cells, adipose-derived mesenchymal stem cells, fibroblasts etc. (Corvera, 2021). The rise in global obesity, has led to an increase in the onset of cardiovascular diseases, type II diabetes, and a compromised immune system due to the body's inflammatory state (Alarcon et al., 2021; Hornung et al., 2021). In the event of overnutrition and neurometabolic dysregulation, adipose tissue expands in size (hypertrophy) and in number (hyperplasia), leading to higher circulating free fatty acids and a cascade of inflammatory pathways.

Data to understand adipose tissue signaling comes mostly from clinical studies, genome-wide association studies, animal models and immortalized cell lines. *In vitro* models based on mature white adipocytes are limited, given their buoyancy and fragility (Li & Easley, 2018). The cells line models are typically based on 3T3-L1, 3T3-F442A, or human Simpson-Golabi-Behmel syndrome (SGBS) cells (Fischer-Posovszky et al., 2008; Green & Kehinde, 1975; Kuri-Harcuch & Green, 1978). The adipocytes differentiated from the cell lines have similarities to mature primary adipocytes in terms of lipid storage, insulin sensitivity, but lack the unilocular lipid droplet and adipokine secretome (Bahmad et al., 2020; Fain et al., 2010; Mandrup et al., 1997). Animal models do not exhibit the same functional adipocytes as primary human (Bart van der Worp et al., 2010; Greek & Menache, 2013a; Mestas & Hughes, 2004; Van Der Worp et al., 2018). Other *in vitro* models utilized explants, with a 3D printed fixture to trap adipose tissue explants in a chamber, to study the effect of glucose stimulated insulin secretion from pancreatic islets on the adipocytes (Brooks et al., 2016). Another report developed a construct of sandwiched white adipose tissue (SWAT), where primary white adipocytes were sandwiched between tissue-engineered sheets of adipose-derived stromal cells (Lau et al., 2018). This 3D construct could trap the adipose tissue and maintained viability up to eight weeks in static culture. However, the gene expression over the long-term did not capture native adipocyte profiles and required further optimization of culture conditions.

OoC models of adipose tissue provide a framework catering to all the requirements of the fragile buoyant tissue, including trapping the adipocytes, extracellular matrix incorporation, perfusion and sampling, and live-imaging capabilities. One such example is of a reversibly sealable dual-chip platform which allowed for the perfused culture of the 3T3-L1 adipocyte cell line, along with a fluorescence-based enzyme assay to monitor glycerol secretion (Clark et al., 2009). Upon stimulation with a β-adrenergic agonist (isoproterenol), a 3-fold increase in glycerol from the baseline was observed. This was read on a glycerol-detection chip, connected to the adipose-tissue chip via a capillary channel. Another *ex vivo* model was developed to

study insulin sensitivity of human adipocytes, by measuring insulin dependent glucose uptake (Zambon et al., 2015). The model dynamics were coupled with a mathematical model to add a layer of predictability, and glucose in effluent was measured with commercially available glucometer strips. The explants survived in culture for several days, before the tissue began to deteriorate, to study glucose uptake in response to insulin spikes in healthy patients compared to diabetic patient samples. One of the first known WAT-chip models to trap primary murine adipocytes in a moat situated above a perfused channel, exhibited the possibility of stimulation with insulin and observing the adiponectin release (Godwin et al., 2015). A high-throughput pancreas-WAT platform with live sensing capabilities assessed the insulin and fatty acid response of murine primary adipocytes and pancreatic islets. The system had 9 inlets for 9 different media conditions, which could be sequentially tested on the murine adipose tissue explants (Li et al., 2017). Another model comprised a large-scale pneumatically driven, automated PDMS-based platform for the formation, long-term culture, and study of 3D adipose microtissues (Compera et al., 2022). The microtissues were differentiated from human adipose stem cells and cultured for up to two weeks and were exposed to varying glucose concentrations in media.

1.4. Liver-chip models

The liver, as the prime metabolizing organ in the body, is composed of millions of roughly hexagonally shaped lobules which branch into sinusoids, comprising of a specialized fenestrated endothelium for the close exchange of metabolites, nutrients, and dissolved gases (Krishna, 2013). The liver is supplied with blood from the portal vein (from the digestive system) and the hepatic artery (from the systemic circulation). The portal vein brings nutrients and xenobiotics from the GI tract, while the hepatic artery brings oxygenated blood into the liver sinusoid. The blood from the liver flows into the central vein, which connects to systemic circulation (Irwin M. Arias et al., 2009; Eipel C, et al., 2010; Malarkey et al., 2016). A liver model mainly comprises of hepatocytes, with the potential of adding complexity by including one or more of the other liver-specific cells – liver sinusoidal endothelial cells (LSECs), hepatic stellate cells (HSCs) and Kupffer cells (KCs).

In vitro liver models have seen a shift from the traditional 2D primary human hepatocyte (PHH) in sandwich cultures to 3D spheroid models. This is due to mounting evidence indicating that 3D models exhibit more physiological cell morphology and expression of drug metabolizing enzymes and markers (Bell et al., 2018; Gaskell et al., 2016; Serras et al., 2021). Hepatocytes lose their polarity and functionality over time in 2D static culture (Zeigerer et al., 2017). Precision cut slices offer the advantage of primary tissue with intact vascular and spatial arrangement of cells along the middle of the slice, along with donor heterogeneity but there is a dearth of healthy tissue for research (Lerche-Langrand & Toutain, 2000). While rodent models can alleviate issues of donor scarcity, they introduce complications of species variations and ethical concerns (Kuzbari et al., 2013). Immortalized cell lines exhibit a genetic proximity to PHHs, with some variations in function. Two prominent cell lines are the HepG2 and HepaRG™ cell lines. While phenotypically stable and widely characterized, HepG2 exhibits lower CYP enzyme expression compared to PHHs (Gómez-Lechón et al., 2014). HepaRG™ cells retain many liver-specific functions and the expression of many cytochrome P450s on a similar level to PHHs, with the possibility of differentiation into both hepatocyte and biliary

lineages (Mueller et al., 2014). With the advancement of stem cell biology and -omics analysis methodologies, well characterized stem cell lines have been consistently differentiated into the various liver cell types (Gage et al., 2020; Koui et al., 2017).

OoC offers the capability of nutrient replenishment, shear stress and the possibility for a tunable 3D environment to prolong the culture of hepatocytes *in vitro* (Dickson, 2019; Rashidi et al., 2016; Vinci et al., 2011). Liver-on-chip models were among the first OoCs to be developed, mostly due to the liver being the prime metabolizer of drugs and late-stage drug attrition being often caused by unexpected hepatotoxic effects (Ewart et al., 2022, Ehrlich et al., 2019; Moradi, Messelmani et al., 2022). Complexity of liver tissue culture was captured on chip, in a coculture model of HepaRG™ cells, a Kupffer cell line, an HSC cell line and primary HUVECs in a rigid plastic chip (Rennert, et al., 2015). The chip has a tissue and media channel, separated from each other via an isoporous membrane. The model was evaluated under static and perfused conditions, assessing the oxygen consumption rate and demonstrating increased hepatic function in the perfused coculture compared to static, with increased MRP-2 and CYP enzyme expression. Another model was a 3D-printed liver-on-chip where cell layers were deposited in a 3D arrangement in a chip with an endothelial and biliary system (Lee et al., 2019). The coculture of the hepatocytes with endothelial cells showed an increased hepatocyte function, with higher CK19 and MRP2 expression in the presence of an apical and basal channel. The effect of flow on HepaRG™ cells was investigated, comparing expression of genes encoding CYP enzymes and transporter proteins for 8 weeks in culture (Duivenvoorde et al., 2021). The expression of selected CYPs were like that of primary human hepatocytes, with a relatively high CYP1 activity.

1.4.1. Models studying zonation

The hepatocytes in the sinusoid make up the parenchyma, and exhibit the unique property wherein the same cells, given different cues, perform different functions. The oxygen and nutrient rich region of the sinusoid surrounding the hepatic artery and portal vein is the periportal zone 1. The oxygen-depleted region surrounding the central vein is the pericentral zone 3. The functional properties of the hepatocytes vary along the gradient down the sinusoid, created from zone 1 to zone 3 such as gluconeogenesis and ß-oxidation dominating zone 1, and glycolysis, lipogenesis and Wnt signaling dominating zone 3 (Malarkey et al., 2016; Cunningham and Porat-Shliom, 2021).

OoC technology allows for the control of fluidics leading to the creation of gradients within liver-on-chip models, of not just dissolved media components, but also control of dissolved gas concentrations in the media. A zonation model with spatially controlled zonation of primary rat and human hepatocytes was exposed to gradients of insulin, glucagon and the chemical 3-methylcholanthrene (McCarty, et al., 2016). By introducing two parallel flow streams where the media mixed sequentially, the hepatocytes were exposed to an opposing gradient of insulin and glucagon. Gradients were reported in lipid droplet storage and drug conjugation via PAS staining, immunofluorescent staining of carbamoyl phosphate synthetase 1 and CYP enzyme activity. Another demonstration of zonation was through the induction of a gradient of oxygen in the model of primary rat hepatocytes (Kang et al., 2020). The gradient was created with sodium sulphite as an oxygen scavenging solution, to enable an oxygen gradient from 15% in

Zone I to 0% in Zone III. In addition to the increased expression of hypoxia markers, ROS accumulation and H1F expression was also established with the descending oxygen gradient. An oxygen gradient was also created in a model with a nitrogen gas channel parallel to the cell channel, separated by a membrane (Tonon et al., 2019). The gradient along the width of the cell channel enabled hepatic metabolic zonation during the differentiation of hESCs towards hepatocytes. High throughput drug testing with a gradient model exposed it to different culture areas on the hepatocyte culture to different drug concentrations (Toh et al., 2009). This 3D HepaTox Chip was able to determine the IC50 values of five known drugs and was able to predict *in vivo* toxicity. Another liver-sinusoid model with a vertical arrangement of primary rat liver cells mimics the bionic liver hypoxia conditions and flow-guided angiogenesis leading to the spontaneous formation of a radiating sinusoid network (Ya et al., 2021).

1.5. WAT-Liver interaction models

Liver and adipose tissue are the primary organs involved in the storage of energy. In addition to being a powerful endocrine organ, adipose tissue, making up 20-50% of the body, serves as a fatty acid storage organ and influences metabolism via the secretion of adipokines and free fatty acids (FFAs) (Young, et al., 2013). In the fed state, circulating insulin inhibits lipolysis, while during fasting lipolysis is increased by catecholamine (Frayn, 2002). The endocrine function of the adipose tissue is regulated by adipokines (Rosen & Spiegelman, 2006). Adiponectin is primarily involved in the maintenance of insulin sensitivity. Leptin is another adipokine, involved in the suppression of appetite and promotion of energy expenditure. As a consequence of obesity, adipocyte hypertrophy leads to hypoxic regions within the tissue, leading to local inflammation and adipocyte dysfunction (Weisberg et al., 2003). Lipotoxicity is one of the main events in the pathogenesis of NAFLD where circulating FFAs are observed in the serum and liver, and they are esterified into triacyl glycerides in the liver. Increased FFAs impair the insulin sensitivity of the liver, promoting *de novo* hepatic lipogenesis and FFAs are proinflammatory, activating the Kupffer cells in the liver via the (NF)-κB pathway (Tang et al., 2013). In this section, the application of models connecting WAT- and/or liver-chips has been discussed, spanning the disease model development and modeling pharmacokinetics and pharmacodynamics (PK/PD).

1.5.1. Disease models

This era of processed foods, rising obesity, and metabolic syndrome has also seen another increased prevalence, that of the chronic hepatic disorder, NAFLD (non-alcoholic fatty liver disease). NAFLD is characterized by increased accumulation of fat in the hepatocytes (Younossi et al., 2019). A state of metabolic injury leads to the development of non-alcoholic steatohepatitis (NASH), followed by fibrosis and cirrhosis. Multi-organ platforms could provide insights into understanding the signaling mechanisms leading to these conditions. A report of a model connecting adipose, liver and endothelial cells monitored glucose and fatty acid homeostasis over a period of 72 hours (Iori et al., 2012). To model the effects of hyperglycemia, the system was challenged with insulin and high glucose levels. The effect of WAT-liver signalling and the development of NAFLD was explored with a two-organ model of PHH and adipocytes differentiated from human cardiac preadipocytes, with gravity-driven recirculating flow (Slaughter et al., 2021). The system was perfused with a basal serum-free medium with two conditions (healthy: 5 mM glucose, 1 nM insulin and diabetic: 25 mM

glucose, 69 μM insulin). TNF-α and FFAs were added to create proinflammatory and obese plasma conditions respectively, with the hepatocytes accumulating a higher fat percentage when exposed to a diabetic and lipid-rich medium. The adipose-liver system showed an increase in hepatic steatosis in the obese and proinflammatory medium, compared to liver-chips exposed to these media, given the *in vivo* case of TNF-α secreted by macrophages that infiltrate into adipose tissue driving adipose tissue lipolysis and insulin resistance. While these were the prime examples of WAT-Liver interactions, metabolic diseases were also studied with other MOCs. A gut-liver-chip platform demonstrated via mRNA sequencing that FFAs accumulating in the gut and liver led to elevated levels of gene expression for glucuronidation and endoplasmic reticulum stress respectively (Yang et al., 2020). Another gut-liver connected model investigated the onset of hepatic steatosis in the liver by FFA accumulation upon absorption by the gut chip (Lee & Sung, 2018). TNF-α increased the steatosis events while α-lipoic acid and butyrate alleviated the steatosis tendencies.

Another disease progression model is towards type II diabetes, where an insulin-secreting pancreatic islet-chip was coupled with a liver model in the study of glucose uptake and metabolism of the liver in the presence of insulin secreted by the islet cells, with the subsequent breakdown of the mechanism in the presence of diabetic conditions in culture (Bauer et al., 2017). The effect of insulin-producing rat pancreatic islets on rat hepatocytes was explored in another model, where insulin from the pancreas improved liver metabolic function with regards to the expression of genes related to glucose metabolic pathways (Essaouiba et al., 2020).

In general, very few models discuss WAT-Liver connection and hence, there exists a great need for novel approaches to study the effect of adipose tissue lipolysis on fat accumulation in the liver.

1.5.2. Pharmacological and toxicological studies

An *in vitro* platform comprising of a WAT- and liver-chip component could enable the investigation of drugs influencing the metabolism of glucose and FFAs. A model connecting liver-adipose-lung-other tissues assessed the distribution and toxicity of drugs on the microscale cell culture analog (μCCA) platform (Viravaidya & Shuler, 2002). According to this study, the hydrophobic drug fluoranthene was taken up by the adipocytes, reducing its availability for the liver and lung chambers, resulting in reduced naphthalene metabolism and naphthoquinone-induced glutathione depletion.

Pharmacological treatments for NAFLD and NASH exist to target the symptoms of the disease itself, but an opportunity for MOCs is clearly visible in the field of target identification and gaining mechanistic understanding. *In vitro* models for NAFLD currently being used in drug development pipelines are for therapeutics in Phase III clinical trials, including the farsenoid X receptor obeticholic acid, the staroyl coenzyme A desaturase inhibitor Aramchol, the GLP-1 receptor agonist Semaglutide, etc. (Ramos et al., 2022, Anstee et al., 2019; Rinella et al., 2022). Of note, are the recently failed therapies of phase III clinical trials because they did not meet efficacy targets. These include the chemokine 2 and 5 receptor agonist Cenicriviroc, the antioxidant Pioglitazone or vit. E, the angiotensin II receptor type I agonist Losartan etc. (NCT03028740, ClinicalTrials.gov, 2021; Newton et al., 2008; Hoofnagle et al., 2013). Immune system intervention plays a role in the progression of NAFLD, with cues from resident

immune cells in the liver and adipose tissue as well as the circulating immune cells (Moayedfard et al., 2022; Ramadori et al., 2022). To the best of our knowledge, no existing multi-organ models investigate the PK/PD of drugs involved in the NAFLD pathways which include the immune cell pathways on the platform.

1.6. Immune cell integration into OoCs

Immune cells have been integrated into and perfused across OoC platforms over short time periods. Peripheral blood mononuclear cells (PBMCs) with immunomodulators were perfused across the choroid-chip platform to evaluate immune cell recruitment towards a stromal tissue (Cipriano et al., 2022). The freshly isolated and pre-labeled PBMCs were perfused across the chip with a pipette tip reservoir at the chip media inlet and a linear pull perfusion regime via a syringe pump pulling the cells across the system. $CD4^+$ T cells were perfused across an MOC model of gut-liver-brain-chips to demonstrate the influence of short chain fatty acids on the pathophysiological development of Parkinson's disease (Trapecar et al., 2021). Fresh immune cells were infused into the platform every two days over a short period and then allowed the unidirectional recirculating pump to perfuse the cells across the MOC. There is scope for a mechanism for long term perfusion of immune cells to mimic chronic inflammatory conditions. Inspiration for immune cell suspension could be drawn from stirred tank reactor principles to maintain cells in suspension. For example, cultivation of cells in bioreactors, which include theoretical calculations of shear, mixing speed, and the liquid level or reports of perfusion culture for mammalian cells, with a focus on filtration, gravitational settling and centrifugation (Doran, 1999, Tokashiki & Takamatsu, 1993). The design criteria for immune cell handling includes precautions to avoid activation of the immune cells, including minimal shear, sharp edges or direct contact of the cells with a mixing apparatus, as with commercially available ball mixers and magnetic impeller culture flasks (volumes above 150 mL). The rotating-wall vessel provided an appropriate mixing platform except for the rotating components which could be bulky and prone to leakage if applied to an MOC platform (Hammond & Hammond, 2001). A stirred tank pump comprising a magnetic stirrer was mounted on a computer fan to drive Jurkat cells across an organ chip for two hours (Cook et al., 2022). While the cells were in direct contact with the mixer, the viability was maintained over the culture period. A twisted microfluidic mixer with the fluidic channel alternating across two different levels was proposed such that the components were constantly moved and more likely to stay suspended (Sivashankar et al., 2016). Acoustic or electrophoretic trapping are some other strategies which could be applied to suspend the immune cells (Busche et al., 2020; Ding et al., 2012).

1.7. Aim of the thesis

The aim of this thesis is to build a robust and physiologically relevant MOC platform that allows for sensor integration and immune cell circulation, using microfabrication approaches. To achieve this aim, the work was split across multiple objectives:

1. Designing, fabricating, and developing a **robust, flexible, and reversible connection strategy** to connect two organ-chips.
2. Designing and developing organ-chips with minimally absorbing materials that would interface with the MOC platform, taking the case of metabolic interaction between **human white adipose tissue and hepatic tissue** as an example.
3. **Integrating sensors** into the WAT-Liver MOC.
4. Designing, fabricating, and characterizing a model to study **zonation** within a liver-chip
5. Designing and fabricating an **immune cell reservoir** for the long-term suspension and circulation of immune cells, and simple integration with an MOC platform

Establishing the two-organ connection will allow for the investigation of organ interactions, taking the case of WAT-liver interactions. Design considerations such as choice of material of the chips, low dead volume and connection strategies make this concept applicable to a variety of studies covering drug metabolism, PKPD and time-resolved effluent analysis in efficacy or toxicity studies. Incorporating the sensors will allow for additional in-line monitoring of cell culture parameters and hence offer insights into the metabolic status of the organ-chips in real-time. The integration of the immune cell reservoir serves to enable long-term suspension culture and perfusion of immune cells across a connected organ platform. Finally, the design and fabrication of the zonation model-on-chip allows for the study of the physiological complexity of a liver-chip model. Overall, this thesis aims to explore the design criteria and requirements of building MOCs and incorporating features into the platform.

2. Materials and methods

2.1. List of materials and devices

2.1.1. Cell culture reagents

Table 1: List of reagents used in cell culture of adipocytes, hepatocytes and endothelial cells.

Name	Manufacturer (Product no.)
Bovine serum albumin	Merck KGaA (A9647-50g)
Collagen I, bovine	Advanced Biomatrix (5133)
Collagenase	Serva Electrophoresis GmbH (DS17454.01)
Dispase	Merck KGaA (D4693)
DMEM/F-12, no phenol red	Thermo Fisher Scientific (21041025)
DMSO	Merck KGaA (C6164)
Dulbecco′s Phosphate Buffered Saline with magnesium chloride and calcium chloride (PBS+)	Merck KGaA (D8662)
Dulbecco´s Phosphate Buffered Saline: without Magnesium, without Calcium (PBS)	Biowest (MS00SG1001)
EBM™-2 basal medium	Lonza (CC-3156)
Endothelial Cell Growth Medium	Promocell GmbH (C22010)
EGM™-2 SingleQuots™	Lonza (CC-4176)
Endotoxin-free water	Thermo Fisher Scientific (J65589-K2)
Fibronectin	Merck KGaA (F1141)
FCS (Cytiva HyClone™ FetalClone™ II Serum)	Thermo Fisher Scientific (10326762)
Freezing medium classic	Ibidi GmbH (80022)
Gentamycin (10mg/mL)	Thermo Fisher Scientific (15710049)
Gibco™ TrypLE™ Select Enzyme (1X), no phenol red	Thermo Fisher Scientific (50-591-419)
Glucose solution	Gibco (A24940-01, 1M stock)
Glutamax ™	Thermo Fisher Scientific (35050061, 100x)
HEPES Buffer (1M)	Thermo Fisher Scientific (15630056)
Hxdrocortisone 21-hemisuccinate sodium salt	Merck KGaA (H2270-100MG)
HyStem®-C	CellSystems® GmbH (GS313)
Insulin solution human	Merck KGaA, Darmstadt, Germany (I9278)
PBS-	Biowest (L0615)
Penicillin-Streptomycin (10,000 U/mL)	Thermo Fisher Scientific (15140122)
Rosiglitazone	Merck KGaA (R2408)
Trypsin	Merck KGaA (59418C)
Versene	Thermo Fisher Scientific (15040033)
William's media E with glucose	PAN Biotech (P04-29510) [2000 mg/L glucose (11.1 mM), 2.24 g/L $NaHCO_3$]
William's media E without glucose	PAN Biotech (P04-29050S4) [2.24 g/L $NaHCO_3$]

2.1.2. List of chemicals, assays, and staining reagents

Table 2: List of chemicals, assay reagents and staining materials used for chip-characterization.

Name	Manufacturer (Product no.)
3- Aminopropyltriethoxysilane	Merck KGaA (440140)
Albumin antibody, goat host	RnD Systems (AF3329)
Alexa Fluor™ 488 (goat anti-mouse)	Thermo Fisher Scientific (A-28175)

Alexa Fluor™ 488 (goat anti-rabbit)	Thermo Fisher Scientific (A-11008)
Alexa Fluor™ 546 (goat anti-goat)	Thermo Fisher Scientific (A-11003)
Alexa Fluor™ 647 (goat anti-mouse)	Thermo Fisher Scientific (A-21235)
Alexa Fluor™ 546 Phalloidin	Thermo Fisher Scientific (A-22283)
Amylase solution	Merck KGaA (A3176)
Antibody diluent	DAKO (S3022)
Anti-Cytochrome P450 Enzyme CYP3A4 Antibody	Merck KGaA (AB1254)
Anti-human GST A1-1 Goat polyclonal antibody	Oxford Biomedical Research (GS68)
apoB antibody	Santa Cruz Biotechnology (sc-13538)
BODIPY™ 493/503 dye	Thermo Fisher Scientific (D3922)
BODIPYTM 500/510 C1, C12	Thermo Fisher Scientific (D3823)
Calcium chloride dihydrate	Fluka (21097)
CD31 (monoclonal (Clone JC70A) mouse anti-human)	DAKO (M0823)
CellTiter 96® AQ_{ueous} One Solution Cell Proliferation (MTS) Assay	Promega (G3582)
CellTox™ Green Cytotoxicity Assay	Promega (G8741)
CellTracker™ Deep Red Dye	Thermo Fisher Scientific (C34565)
DAPI solution	Merck KGaA (MBD0015)
Fluorescein diacetate	Thermo Fisher Scientific (F1303)
FITC-Dextran (3kDa)	Merck KGaA (FD4)
Glutamine synthetase, goat host	Abcam, 176562
Hoechst 33342 Solution (20mM)	Thermo Fisher Scientific (62249)
Human/Mouse E-Cadherin Antibody	R&D Systems (AF748)
LDH-Glo™ Cytotoxicity Assay	Promega (J2380)
MRP2/ABCC2 (R260) Antibody	Cell Signaling Technology (#4446)
Normal Donkey Serum	Jackson ImmunoResearch (017-000-121)
PDMS Silicone Elastomer Base and Curing Agent	Biesterfeld Spezialchemie GmbH, Hamburg, Germany (SYLGARD™ 184; 5498840000)
pH indicator strips	Merck KGaA (109557)
Periodic acid, Schiff reagent kit	Merck KGaA (395B)
Pierce™ Chromogenic Endotoxin Quant Kit	Thermo Fisher Scientific (A39552)
Phalloidin (6.6 uM)	Thermo Fisher Scientific (A34055)
Propidium iodide	Thermo Fisher Scientific (P3566)
Purified Mouse Anti-ASGPR 1	BD Biosciences (563654)
QuantiChrom™ Glucose Assay Kit	Bioassay Systems (DIGL-100)
Recombinant anti-ASS1 antibody	Abcam (170952)
Recombinant Anti-Glutamine Synthetase antibody	Abcam (176562)
Roti ® - Histofix 4%	Carl Roth GmbH + Co. KG (P087.4)
Saponin	Merck KGaA (SAE0073)
Sodium sulfite	Merck KGaA (S0505)
Triglyceride-Glo™ Assay	Promega (J3160)
Triton™ X-100	Merck KGaA (X100)

2.1.3. List of Consumables

Table 3: List of consumables used in the production of chips and the connection platform

Name (specification)	**Manufacturer**
21, 23 GA stainless steel plastic hub dispensing needles	RS Components GmbH (400-3895, 400-8272)

384 well plate – white opaque walls	Greiner Bio-One (781074)
3M Scotchpak™ (Coated foil)	3M, Saint Paul (1022 Release Liner Fluoropolymer Coated)
96-, 48-, 6-well plate for cell culture, Cellstar®	Greiner Bio-One (655182, 677180, 657160)
96-well plate, black wall, transparent bottom for cell culture	Greiner Bio-One (655090)
Biopsy punch (0.75 mm diameter)	World Precision Instruments (504529)
Block magnet, 25 x 6 x 2 mm	Supermagnete (Q-25-06-02-SN)
Breathe-Easy® sealing membrane	Merck KGaA (Z380059-1PAK)
Cell culture dish (90 x 17 mm,	Avantor, VWR (10062-878)
Cell culture flask (T25, T75, T175)	Greiner Bio-One (690175, 658175, 660175)
Conical centrifuge tube (50 mL, 15 mL)	Corning (CLS430829, CLS430791)
DIN 934 hex nuts	Reidl Fastener (SKU: 21886)
Disposable syringe Injekt® With Luer-Lock fitting, 2 mL (B. Braun)	Carl Roth GmbH + Co. KG (EP95.1)
Dosing needle; ¼'' (ID 0.09 mm)	IP732025, GONANO Dosiertechnik GmbH
ARcare® Double sided tape	Adhesives Research (90106NB)
Foldback clips	Jakob Maul GmbH (2141999)
ipCellCulture™ PET membrane, 5 µm pore size	It4ip (2000M12/510M503)
Luer Adapter with top cap	MoBiTec (M3003)
Luer connectors	Nordson Medical, USA (BDMFTLL-9)
Luer stopper ROTILABO® (female)	Carl Roth (CT69.1)
DIN 912, A4, M3 screws	Minischrauben.com (10 mm long, 912-4-310)
Male Mini Luer Plugs	Darwin Microfluidics (CS-10000030)
Male Luer Plugs	Darwin Microfluidics (CS-10000230)
Male Mini Luer Fluid Connectors	Darwin Microfluidics (CS-10000095)
Mobicol "Classic" with 2 different screw caps without filters	MoBiTec (M1002)
Omnifix®-F Luer Solo syringe (1 mL)	Braun Melsungen (9162909V)
Stand-Alone Female Mini Luer Ports	Darwin Microfluidics (CS-10000701)
Inkjet® Solo 2-part disposable Luer Lock syringe (2 mL, 5 mL, 10 mL)	Braun Melsungen (4606027V, 4606051V, 4606108V)
Track etched membrane (5 µm pore size ipPore™, 3 µm pore size ipCellCulture™)	It4ip (1000M25/541M500/XY, 1000M25/610M303/XY)
Tygon® ND-100-80 Non-DEHP Medical Tubing	VWR (89404-302) [ID x OD: 0.020 x 0.060"]
PCR tape (sterile)	Carol Roth (ThermaSeal, 100-THER-PLT)
Peristaltic Pump tubing (PharMed® BPT)	VWR (228-1684) [Tubing internal diameter: 0,50 mm (0,020")]
Stainless steel springs	Federtechnik Knoerzer GmbH (50/3/1)
Tactile Pressure Indicating Sensor Film	Sensor Products Inc. (SPF-D)
UHU superglue plastic 3ml + 2g	Selva (358221)
UHU Superglue Pipette	UHU GmbH & Co. KG (35732)
UV glue - Norland Optical Adhesive 81	Norland Products (NOA81)
VWR® non-frosted Microscope Slide	Avantor, VWR (631-0701)

2.1.4. List of Devices

Table 4: List of machines and devices utilized in fabrication and experiments.

Device (specification)	Manufacturer
Cutting Plotter	Graphtec Corporation (CE7000)
Phasefluorometer	Pyroscience GmbH, Germany
Hydraulic Laboratory Press	Fontijne Presses (LabEcon)
Incubator Flow box	Automated Lab Solutions GmbH
Inverted fluorescence microscope	Leica Microsystems CMS GmbH (DMi8)
Inverted fluorescence microscope with apotome	Carl Zeiss Microscopy GmbH (ZeissAxio Observer 7 ApoTom)
Incubator	Binder (BD Series)
Laminar flow bench	Spetec GmbH (Cleanboy)
Laser cutter with 10 W CO_2 laser	Universal Laser Systems Inc. (VLS2.30)
Laser scanning microscope	Carl Zeiss Microscopy GmbH (LSM 710)
Laser welder	LPFK GmbH (PowerWeld 3D 8000)
Multimode microplate reader	Tecan (Spark®)
Plasma generator	Diener electronic GmbH & Co KG (Zepto One, Rotary Switch)
Reglo Digital Pump with MasterflexLive™, 4-Channel, 12-Roller	Avantor, VWR (MFLX78018-24-CH)
SLA 3D-printer	Formlabs (Form 3, V2.0)
Spinning disc confocal microscope	Carl Zeiss Microscopy GmbH (Cell Observer® System with spinning disk head)
Syringe pump	Landgraf Laborsysteme HLL GmbH (LA-190, 12-channel)
Syringe pump with mixer	Cetoni GmbH (Nemix)
Peristaltic pump	Cetoni GmbH (Persys-S)
UV lamp	UWAVE (UV Chamber™)

2.2. Fabrication of the WAT-chip

The general structure of the WAT-chip has been described previously (Rogal et al., 2020) (Figure 1.a). White adipocytes are injected into a tissue chamber below an isoporous membrane, with media perfused across a media channel above the membrane. The exchange of nutrients, waste and metabolites takes place across the membrane, with endothelial cells lining the media channel (Figure 1.b).

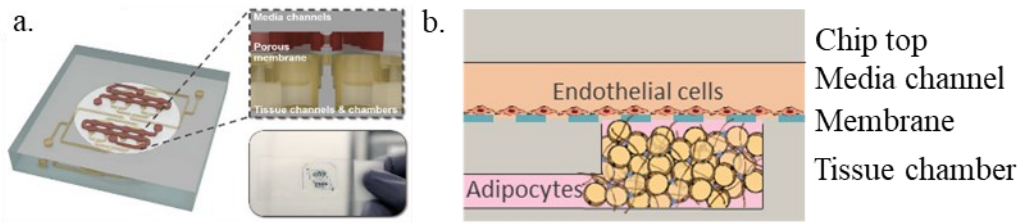

Figure 1: Design of the WAT-chip. (a.) The PDMS-based WAT-chip described previously (Rogal et al., 2020), (b.) Cross-sectional schematic of the cell organization within the WAT-chip.

While the initial version of the WAT-chip was fabricated from PDMS via soft lithography and exclusion molding, the chips used in this thesis were fabricated out of rigid plastics and

thermoset elastomers. Throughout the thesis, multiple versions of the thermoplastic WAT-chip were developed each comprising various layers of different polymers (Figure 2 & Appendix section 8.2). Two versions were most widely used in experiments, where the first version was built out of PMMA with a PDMS chip top, while the second version had embedded connectors for connection to tubing, and a material combination of TPE and PC. The WAT-chip also underwent a variation in the overall chip shape, port alignment, membrane dimensions and fabrication protocols in Version 2, to fit the MOC connection setup. This allowed for a scale-up in production of Version 2 WAT-chips, as explained in the upcoming sections which include an overview of the materials and elaborate on each step of fabrication (Table 5), with process details, schematics, and pictures.

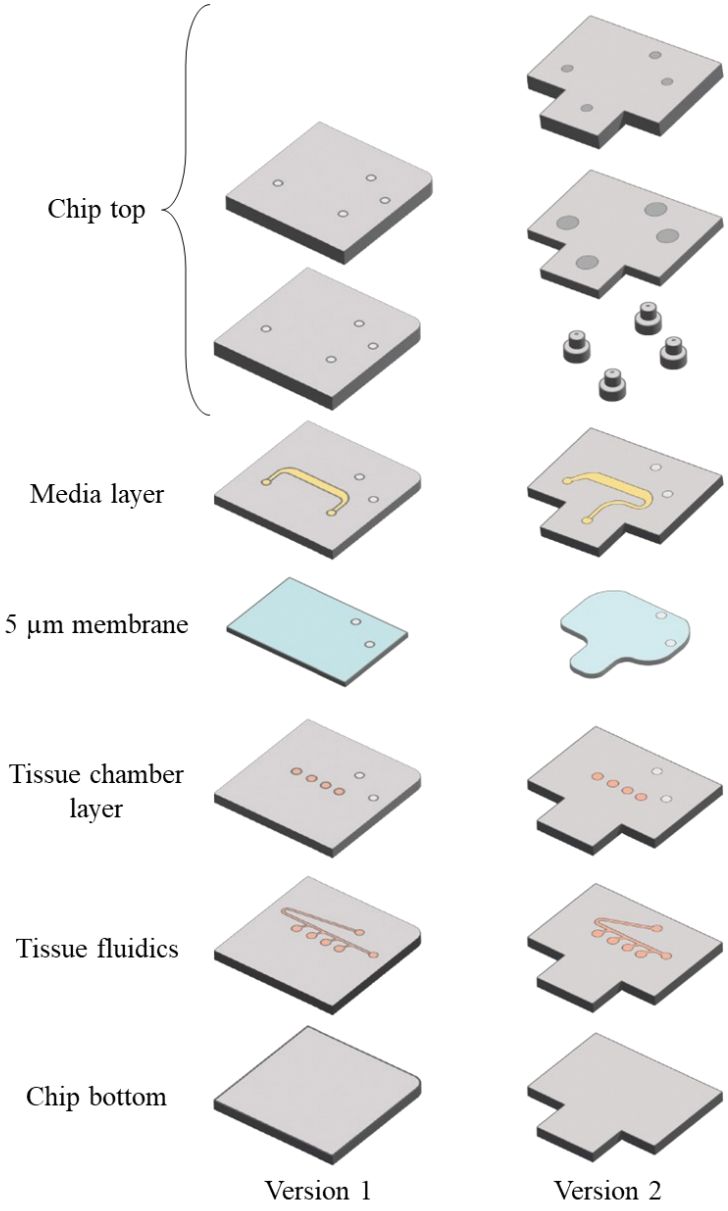

Figure 2: Schematic and annotations of chip layers for the WAT-chips versions 1 and 2.

Table 5: Fabrication steps and process parameters for versions 1 and 2 of the WAT-chip.

	Material, Layer	Height	Structure	Process Step 1	Step 2	Step 3	Step 4	Step 5
Version 1	PDMS, chip top	2 mm	Molded, punched	APTES treat PMMA, plasma treat PDMS and bond at 60°C for 30 min	Assemble between glass slides and clamps and bond in the oven at 130°C for 10 min, 60°C for 30 min and allow to cool completely to RT before disassembling			
	PMMA, chip top	250 µm	Lasercut					
	PMMA, media layer	250 µm	Lasercut					
	5 µm pore, PC membrane	22 µm	Lasercut	Bond with PDMS stamp method in the oven at 130°C for 10 min. Cool completely before disassembling glass slides and clamps				
	PMMA, Tissue chamber layer	75 µm	Lasercut					
	PMMA, Tissue fluidics layer	175 µm	Lasercut					
	PMMA, chip bottom	250 µm	Lasercut					
Version 2	PMMA, Chip top, small ports	1 mm	Lasercut	Mix and degas PDMS. Bond in hotpress with metal frame at 105°C, 20 minutes, 8 kN.	Add PCR tape and pour PDMS into the step connector.	Cure PDMS for 2h at 80 °C. Cut off excess cured PDMS, punch ports.	UV treatment for 30 sec, 99% intensity (16.4 mW/cm^2), bond and roll to remove air bubbles	Apply pressure at RT in hotpress with 8 kN force for 25 min. Place overnight in oven with 1.5 kg weight/chip and ramp at 1.5˚C/min to 60°C, hold for 6h then ramp down at 1.5°C/min
	PMMA, Chip top, big ports	1.5 mm	Lasercut					
	TPE, Media layer	250 µm	Lasercut					
	5µm pore, PC membrane	22 µm	Lasercut	PDMS stamp (110 µm high) method in hot press at 100°C, 20 min, 8 kN	UV treatment for 30 secs, 99% light 16.4 mW/cm^2	Apply 8 kN force for 25 min at RT in the hot press. To avoid membrane sagging, membrane is unsupported.	UV treatment for 30 sec, 99% intensity (16.4 mW/cm^2), bond and roll to remove air bubbles	
	PMMA, Tissue chamber layer	2x 50 µm (100 µm)	Lasercut					
	TPE, Tissue fluidics layer	100 µm	Hot-embossed	Emboss the TPE with epoxy stamp and bond against the PC in hot press at 130 °C, 16 kN for 20 min. Cut out chip shapes with a scissor.	UV treatment for 30 secs, 99% light 16.4 mW/cm^2			
	PC, Chip bottom	175 µm	Lasercut					

2.2.1. WAT-chip version 1: PMMA chip with PDMS top interface layer

Version 1 of the WAT-chip involved individually fabricated chips out of PMMA layers (Figure 2, Figure 3.a). The layers for each chip were clamped together with steel foldback clamps between glass slides cut to dimensions of 26 by 26 mm. Individual chips were bonded in the oven in a 'prototyping-scale' amount, comprising of about 50 chips per month.

2.2.1.1. 2D laser-structuring and cleaning of chip materials

The materials of construction of the chips comprised varying thicknesses of PMMA (polymethylmethacrylate), PC (polycarbonate), 5 µm pore size PC or PET (polyethylene terephthalate) membranes, and TPE (thermoplastic elastomer) (Table 6). The designs of the features to be patterned in the materials were created using the CorelCAD and AutoCAD software.

Table 6: List of materials of construction of chips and connection apparatus.

Material	Processing involved	Manufacturer
50 µm PMMA	Lasercutting	Schlösser GmbH & Co. KG (5509-0005-36)
75 µm PMMA	Lasercutting	Röhm (PLEXIGLAS® Film 0F072)
175 µm PMMA	Lasercutting	Röhm (PLEXIGLAS®, FF99524GT-0-175)
250 µm PMMA	Lasercutting	Röhm (PLEXIGLAS® FF99524GT-0-250)
500 µm PMMA	Lasercutting	Röhm (PLEXIGLAS® 0F301)
1 mm PMMA	Lasercutting	Röhm (PLEXIGLAS® FF99524GT-0-1000)
1.5 mm, 2 mm, 3 mm PMMA	Lasercutting	Modulor GmbH (0279836, 0133420, 0342098)
5 µm pore ipPORE™ PET membrane	Lasercutting	It4ip (2000M23/541M500)
5 µm pore ipPORE™ PC membrane	Lasercutting	It4ip (1000M25/541M500)
175 µm PC	Lasercutting	König Kunstoffe, (Makrofol DE 1-1, 500 x 915 x 0,175mm)
250 µm, 750 µm TPE	Lasercutting, hot embossing	HEXPOL (Mediprene OF 400M), extruded by Fraunhofer IVV, Germany
PDMS Silicone Elastomer Base and Curing Agent	Mixing, degassing and curing	Biesterfeld Spezialchemie GmbH (SYLGARD™ 184; 5498840000), mixed in the ratio 10:1 of base to curing agent

Channel features were created in PMMA, membranes and PC layers by laser-assisted structuring with a carbon dioxide laser cutter (Figure 3.b). The backing foils of materials were kept on while cutting to keep the materials free of debris. Under a laminar flow bench, the backing was removed from each part with tweezers, the part was wiped with a cleanroom wipe (Hans Michael GmbH, RTPRT1091L) damp with isopropanol and allowed to dry under the bench. A nitrogen gun was used to remove any dust and debris prior to chip-assembly.

2.2.1.2. Stamp method of bonding PC membranes to PMMA parts

The WAT-chip comprised tissue chambers of diameter 1.5 mm, enclosed by a PC membrane. This membrane was embedded into the PMMA tissue layer with the stamp method, where it retained its flatness over its large freely suspended area. A PDMS stamp was molded from a 3D printed mold (clear resin, Formlabs), designed to ensure a fixed height of the stamp every

time (Figure 3.c). The cleaned PMMA parts (tissue fluidics, tissue chambers and membrane layers) were placed such that the open tissue chamber region exactly fit around the protruding portion of the PDMS stamp. The layers were aligned with each other around the stamp with the help of a stereomicroscope (Zeiss) and this hybrid material combination was enclosed between glass slides and clamped with foldback clamps. The hybrid was placed in the oven at 130°C for 10 min and then allowed to cool to ambient temperature before disassembly (Figure 3.d).

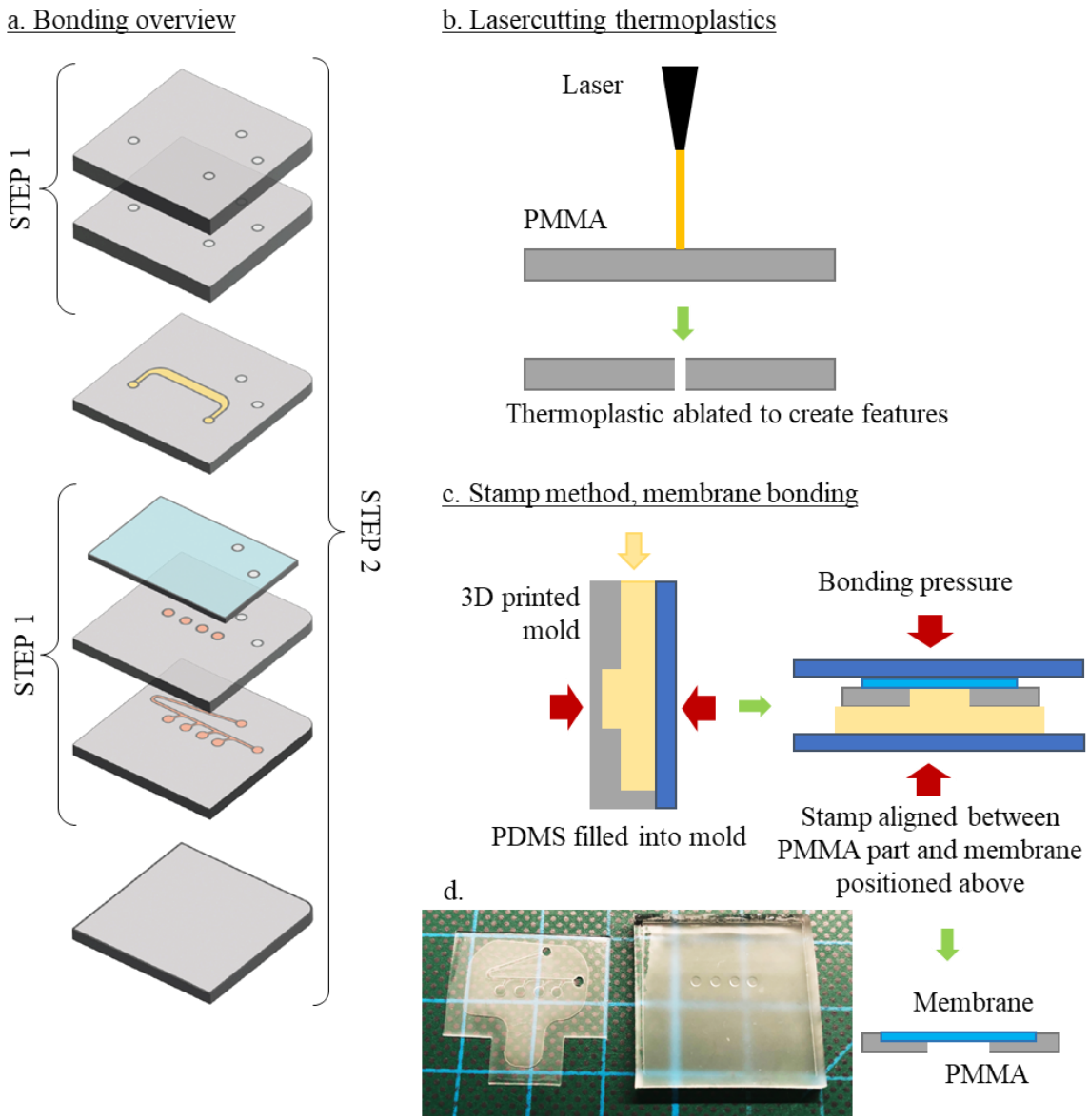

Figure 3: Fabrication of version 1 of the WAT-chip. (a.) Overview of the steps and layers involved in the bonding process, (b.) Schematic of the laser-structuring of thermoplastic layers, (c.) Schematic of the stamp method of bonding, starting with a 3D printed mold to create a PDMS stamp, then aligning the membrame and PMMA pieces with the stamp such that the membrane was embedded into the PMMA layer and retained its flatness, (d.) Pictures of the WAT tissue chambers bonded to the membranes, and the PDMS stamp.

2.2.1.3. PDMS top part fabrication and bonding to thermoplastic layers

Version 1 of the WAT-chip consisted of a layer of PDMS bonded to the PMMA top layer to facilitate connection with cannulas to the perfusion setup. To this end, PDMS was covalently bonded to PMMA using a silane-bonding method. A mixture of PDMS was created using the PDMS precursor and curing agent (SYLGARD 184®), stirring vigorously then degassing for 30 min under vacuum to remove air bubbles. 30 gm of the PDMS mixture was poured into a Petri dish and cured on a flat surface at 60°C overnight. Once cured, features were rastered (etched) on the top of the piece with the lasercutter to facilitate cutting the top parts with a blade. A biopsy punch with a diameter of 0.75mm was used to punch out the ports. The PDMS parts were cleaned with a wipe soaked in isopropanol and sprayed with an air gun to dry completely. Ports of diameter 1.4 mm were lasercut into PMMA parts of thickness 250 µm and 175 µm thick PC parts (larger than PDMS ports to allow for manual alignment), then backing foil removed and wiped with isopropanol-soaked wipes and left to airdry in the laminar flow bench. The thermoplastics parts were first plasma-treated at 75 W, 10 sccm O_2 for 30 sec (Zepto One, Diener Electronics) and then placed plasma-treated-side down onto a droplet of 1% (3-aminopropyl) triethoxysilane (APTES, 440140**,** Merck, KGaA, Germany) solution in deionized (DI) water (Figure 4.a.). The surface treatment proceeded for 45 min, after which the parts were washed with DI water and sprayed dry with an air gun. They were immediately aligned by ports and bonded to the PDMS parts that were plasma-treated bottom side-up at 75 W, 10 sccm O_2 for 30 sec. The bond was strengthened by placement into a 60°C oven for 30 min (Figure 4.b).

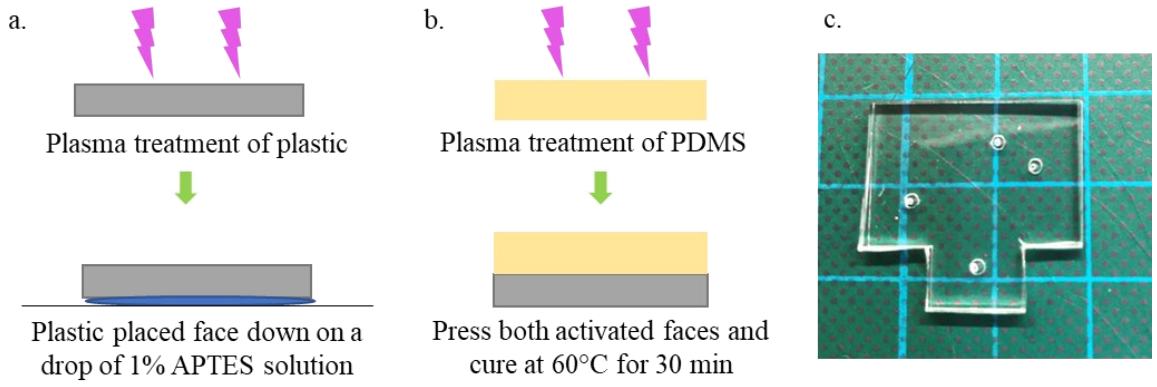

Figure 4: Schematic of PDMS-PMMA bonding for the fabrication of WAT-chip version 1. (a.) Silanization of the plastic layer with a 1% APTES solution, (b.) Bonding the APTES-treated plastic with plasma-activated PDMS layer, (c.) A picture of the top part of the WAT-chip

2.2.1.4. Final chip assembly

After the preparation of the membrane and tissue channel hybrid and the PDMS-PMMA top, the WAT-chip was bonded via thermal-fusion bonding in the oven in one final step. This was a quick and effective strategy to bond PMMA parts using easily available equipment. The cleaned PMMA parts were stacked, aligned, and placed between glass slides (631-0701, VWR) that were either whole or cut to a size of 26 by 26 mm. This assembly was then clamped with steel foldback clamps (2141999, Jakob Maul GmbH, Germany) to uniformly apply pressure across the shape of the parts being bonded and then placed in a convection oven set to 130°C for 10 minutes (Figure 5.a.). The parts were then placed in a 60°C oven for 30 minutes followed

by removal from the oven and allowed to cool to room temperature before disassembly, in a two-step cooling process to prevent a sudden shrinkage of the different materials in the chip, and hence maintaining the flatness of the membrane (Figure 5.b).

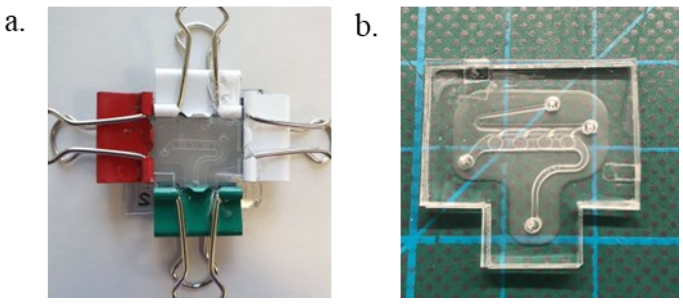

Figure 5: Thermal-fusion bonding of the WAT-chip version 1. (a.) Preparation of the individual chips with steel foldback clamps and glass slides, (b.) End result of the bonding process in the oven.

2.2.2. WAT-chip version 2: PMMA-TPE hybrid chip with embedded PDMS connectors

In Version 2 of the WAT-chip, TPE was introduced to facilitate low temperature bonding processes and to scale up production. The scale of operation could be increased depending on the parts fabricated, to even fit a 'pilot scale production' of about 150-200 chips per month. Additionally, new fabrication methods were employed for the top of the chip and tissue fluidics layers.

2.2.2.1. 2D laser-structuring and cleaning of chip materials

Version 2 of the WAT-chip was composed of a PMMA top with embedded PDMS connectors, a TPE-based media channel and tissue fluidic channel, a PMMA tissue chamber layer with a PET membrane (Figure 6. a.). The plastic parts were lasercut and cleaned as mentioned in previously (sub-section 2.2.1.1). The TPE foils were custom-extruded from commercial SEBS pellets into films of approx. thickness 750 µm and 250 µm externally by Fraunhofer Institute for Process Engineering and Packaging IVV. TPE layers were first sandwiched between two sheets of 250 µm PMMA, and then lasercut. The cutting process for TPE led to the production of sticky debris which remained on the PMMA backing foil, thus leaving the TPE underneath clean and dust-free. Under the laminar flow bench, the backing PMMA sheets were removed with tweezers to avoid touching the TPE. The TPE parts were aligned on Teflon-lined paper in petri dishes to protect the sticky TPE surface until ready for chip-assembly.

2.2.2.2. TPE hot-embossing, preparation of TPE-thermoplastic hybrid

The tissue fluidics channel of the WAT-chip was embossed into TPE with the help of an epoxy mold. This allowed for smooth channels within the TPE, maintaining its transparency and allowed for up to 9 embossed chips per epoxy mold in one go in the hotpress. The TPE films were hot-embossed in accordance to protocols established earlier (Schneider, Bras, et al., 2021). First, a wafer was fabricated using **photolithography** with features to be embossed into the TPE. For this, a mask with the features was designed using the AutoCAD software and printed on a transparent sheet (Schrift + Bild GmbH, Germany) (Figure 6.b.I). Wafers were produced in the cleanroom at the Natural and Medical Sciences Institute, Reutlingen, Germany, by Dr. Eduardo Brás. Wafers with features of thickness of 100 µm were created by spincoating

SU-8 50 negative photoresist (micro resist technology GmbH) at 1000 rpm (Convac, APEX Semiconductor GmbH) and pre-exposure baking at 65°C for 10 minutes and 95°C for 30 minutes. The wafers were then exposed through a transparent mask with energy of 500 mJ/cm^2 (Karl Suss MA6 mask aligner, SUSS MicroTec SE, Germany), followed by a post-exposure bake at 65°C for 1 min and 95°C for 10 min. Features of thickness 250 µm were fabricated in a two-step process to achieve an accurate, uniform feature height. This was achieved by first spincoating and preparing the wafer with SU-8 50 for a film thickness of 100 µm. Then, a second layer of SU-8 100 was spincoated at 2000 rpm, based at 65°C for 20 minutes and 95°C for 50 minutes, exposed with energy of 550 mJ/cm^2 and post exposure baked at 65°C for 1 min and 95°C for 15 min. After all post-exposure baking steps, the resist was developed in a glass tin with MRDev 600 (micro resist technology GmbH) to remove the unexposed resist and washed thoroughly with acetone and IPA. Finally, the wafers were hard baked at 180°C for 45 min, followed by a natural cooling down of the oven. The last step of the wafer preparation involved silanization with trichlorosilane (175552, Merck KGaA, Germany). Upon exposure to oxygen plasma for 5 minutes, the wafer was placed in a desiccator pot connected to a vacuum pump. 200 µL of the silane was placed in a beaker in the desiccator and vacuum applied to create silane vapors, which were allowed to coat the wafer over 1 hour.

This fabricated wafer was used as a template for soft lithography of PDMS, to prepare a negative replica mold. Multiple PDMS molds could be cast off the wafer, increasing the scale of the operation. The wafers with features to be molded were sprayed with isopropanol and dried with a nitrogen gun prior to use. They were then placed into a 15-inch round petri dish (Greiner BioOne). A mixture of 0.07 kg of PDMS base and 10% of curing agent was prepared, degassed to remove bubbles and was carefully poured in a wafer. The petri dish was then left overnight on a horizontal level surface (confirmed with a bubble-level indicator), followed by curing at 60°C for four hours in the oven. The PDMS was carefully peeled off the SU-8 wafer, and edges trimmed to reveal a flat PDMS mold with a negative impression of the features for the stamp (Figure 6.b.II).

PDMS, being a soft material, was not employed directly as an embossing mold. However, it was used as a template off which hard-curing epoxy resin was cast, to prepare this embossing mold. A custom molding tool was fabricated in aluminum by an external manufacturer (CNCTeile24). The assembly consisted of an aluminum vacuum base with the PDMS mold on top, followed by an O-ring lined aluminum top ring and PMMA top sprayed with WD40 mold release agent (Conrad Electronics). Screws held the assembly in place, while 50 mL syringes were connected to the PMMA top plate for a controlled filling with a degassed epoxy resin mixture. The mixture was prepared as a two component (100:16 parts A:B components by mass) epoxy resin (EpoxAcast 670 HT, Smooth-On), with an addition of 10% supplement of part A with an epoxy thinner (Epic Epoxy Thinner, Smooth-On). After weighing and mixing the components with a spatula, the mixture was degassed for 10 minutes under vacuum and filled into the mold. This setup was allowed to partially cure overnight at room temperature with the baseplate of the assembly connected to a vacuum pump (KNF 035, membrane vacuum pump, Carl Roth GmbH). The pump and syringes were then disconnected, and the mold placed into the oven at 60°C for 24 hours for complete curing of the resin. Upon demolding, the stamp

was tempered for 2 hours at 80°C and 3 hours at 150°C before being allowed to cool to room temperature with the oven switched off (Figure 6.b.III).

Finally, the TPE foils were embossed against the epoxy stamps on one side and simultaneously press-bonded to 175 µm PC films on the other side. This was achieved with the help of a programmable hotpress (Fontijne Presses). A layered assembly was created with the epoxy stamp on the bottom, the 250 µm TPE foil and the PC/ PMMA foil on top, a roller being used to remove as many air bubbles as possible from the assembly. This setup was placed onto a steel plate, sprayed with mold releasing agent (11450400, Weicon). With the hotpress preheated to 130°C, the assembly was placed inside and pressed with 16 kN force (2.17 MPa pressure) for 20 minutes, followed by a cooling to 40°C with cooling water running through the plates of the press (Figure 6.b.IV). At this stage, the TPE-plastic hybrid was demolded from the stamp, individual chip shapes cut out with a scissor and the parts stored in a square petri dish lined with Teflon paper.

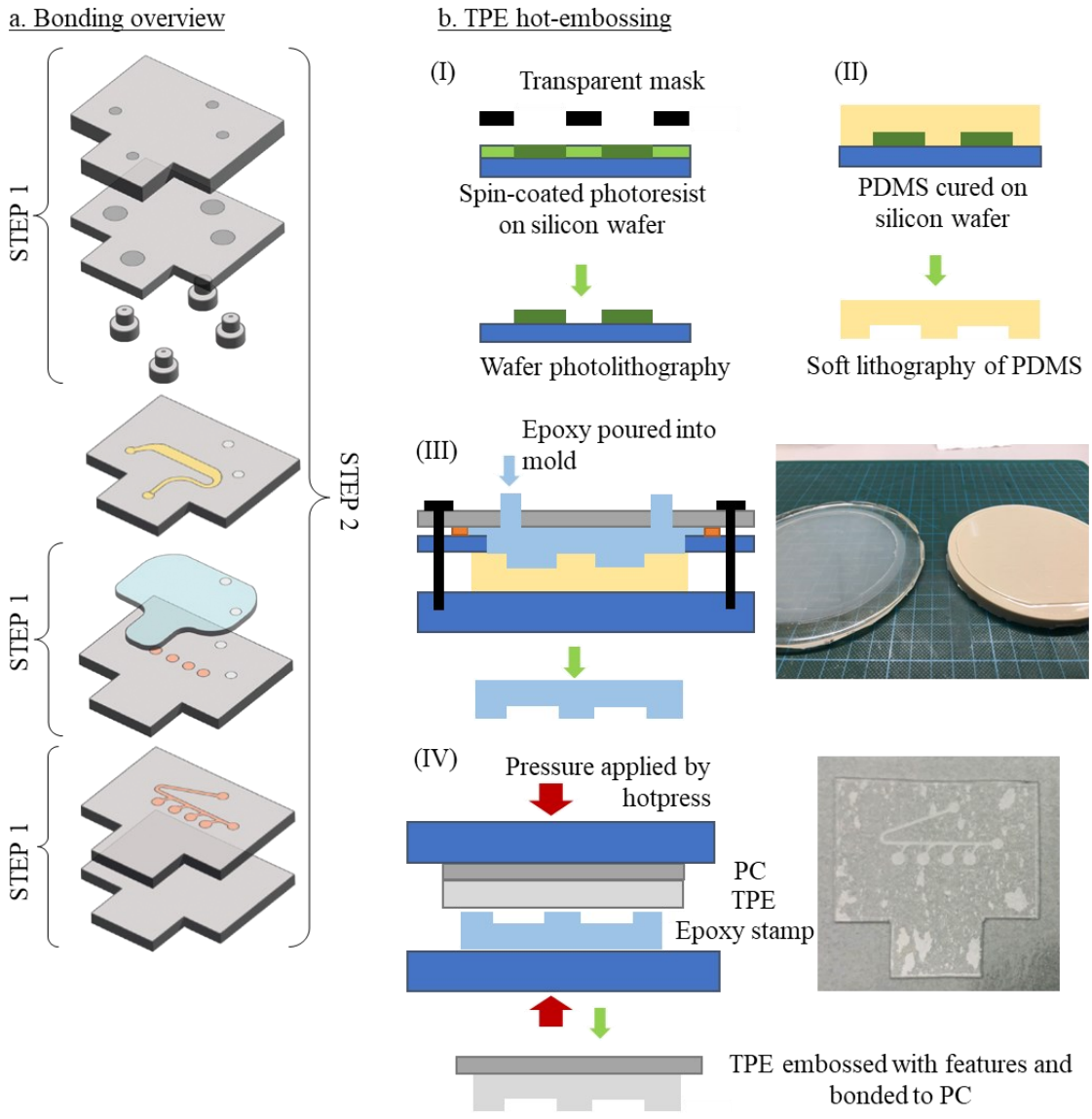

Figure 6: Fabrication of version 2 of the WAT-chip. (a.) Schematic of the various layers and steps of chip fabrication, (b.) TPE hot embossing process to produce the tissue fluidics layer with schematics

of (I) The wafer fabrication (II) PDMS soft lithography (III) epoxy molding and (IV) Hot-embossing of TPE against the epoxy mold with a picture of the result.

2.2.2.3. Embedded PDMS connector fabrication

A new type of world-to-chip connector was developed to include a small piece of PDMS embedded into the PMMA chip-top, together with Johanna Chuchuy. Briefly, thick PMMA layers were lasercut to include large holes at the ports; e.g. ports of diameter 3 mm were lasercut into 1.5 mm thick PMMA pieces and ports of diameter 1.5 mm lasercut into the 1 mm thick PMMA pieces. These layers were aligned and bonded with two strategies – on a smaller scale, each of the pair of PMMA were sandwiched between glass slides and steel foldback clamps and bonded in the oven at 130°C for 10 min. On a larger scale, the pairs of PMMA were bonded in the hotpress at 105˚C with 2.1 MPa pressure for 20 minutes. A metal frame was custom built to accommodate the PMMA layers by CNC milling aluminum (FlatCom M30, Isel, Germany) with a 1.5 mm diameter drill bit (668.500-0150, SPPW GmbH) in the workshop of the Natural and Medical Sciences Institute by Dr. Eduardo Brás (Figure 7). A piece of propylene sealing film (ThermalSeal) was attached below all ports and PDMS filled with a syringe from above. After curing at 60°C overnight, the tops cleaned, excess PDMS shaved off and ports punched with a 0.75 mm biopsy punch.

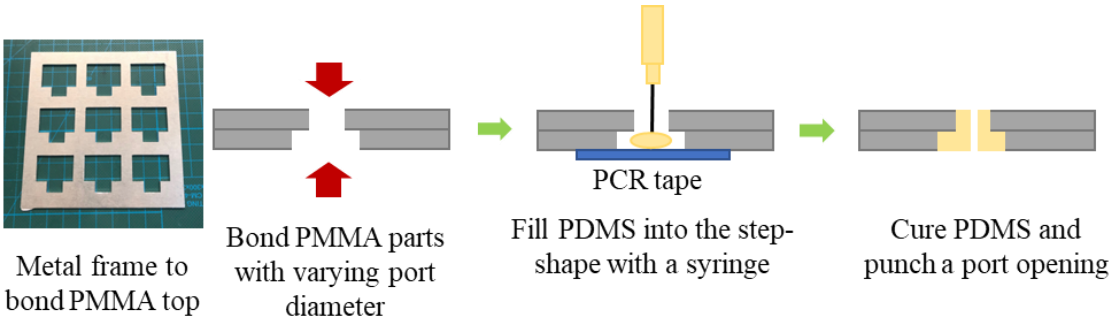

Figure 7: Fabrication of the PMMA top parts with embedded PDMS connectors. For the hotpress, a metal frame (pictured left) was used to bond 9 PMMA tops simultaneously.

2.2.2.4. Stamp method in hotpress

The membrane was bonded to the PMMA tissue channel with the stamp method as highlighted previously (sub-section 2.2.1.2). However, a larger scale methodology was applied in that the PDMS stamps for 9 chips were placed in the hotpress with the PMMA tissue chamber layer (two layers of 50 µm thickness each) and 5 µm pore size PC membrane aligned around the chamber pillars of the stamp. This setup was bonded at 100°C for 20 minutes with 8 kN force (2.22 MPa pressure) and cooled to RT before disassembly.

2.2.2.5. Final chip assembly

With the individual components created, the entire chip was bonded in a simultaneous operation in the hotpress. TPE films of thickness 250 µm were lasercut to create the media channel. The first step of the chip assembly involved bonding of the embossed tissue fluidic bottom to the tissue chamber with membrane. The two faces to be bonded to each other were exposed to a UV lamp (UWAVE) for 30 sec, followed by fine contact by rolling with a handheld rolling tool (VWR). The next step involved UV treating the media channel top and PMMA top and rolling (Busek et al., 2021). The entire chip was aligned and assembled and

bonded in the hotpress at RT for 10 minutes with 8 kN force, then placed in the oven at 60°C for 6 hours, with a ramp up and down at 1.5°C/min (Figure 8).

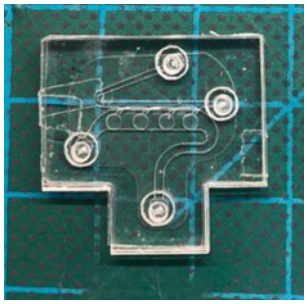

Figure 8: Final chip assembly of version 2 of the WAT-chip.

2.3. Fabrication of the liver-chip

The liver-chip in this thesis inspired by the liver Biochip model, comprising a tissue channel lined with a hepatocyte cell line (HepaRG™) and the media channel lined with endothelial cells (Rennert et al., 2015). The tissue channel was positioned above the media channel, with an exchange of nutrients via the endothelial cell monolayer. The model in this thesis utilized HepaRG™ cells and primary microvascular endothelial cells (mVECs) (Figure 9).

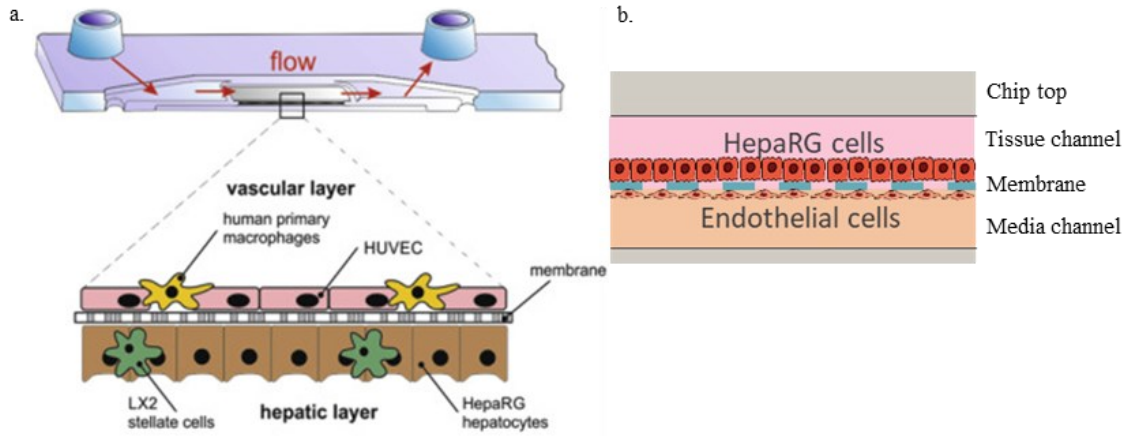

Figure 9: Design of the liver-chip. (a.) Schematic of a cross-section of the liver-chip concept (Rennert et al., 2015)(b.) The cross-sectional schematic overview of the cell organization within the Liver-chip

The previously published liver Biochip was fabricated by an injection molding process, with the membrane laser-welded onto the chip body and had a size footprint of a 75 by 25 mm glass slide. The liver-chip in this thesis underwent a significant size-reduction to 25 by 25 cm, maintaining the hexagonal chamber shape to create a low-shear region above the hepatocyte-endothelial coculture area, and to facilitate cell alignment in the tissue chamber. The liver-chips were fabricated by thermal fusion bonding of various layers of laser-structured plastics (Figure 10). Like the WAT-chip, the liver-chip underwent a variation in the overall chip shape, port alignment and membrane dimensions in Version 2 and 3, to fit the connection setup (other versions of the liver-chip design have been summarized in Appendix section 8.3). Three versions of the chips were most widely used in the experiments. Fabrication methods of the three chip versions varied depending on the material of construction of the chips.

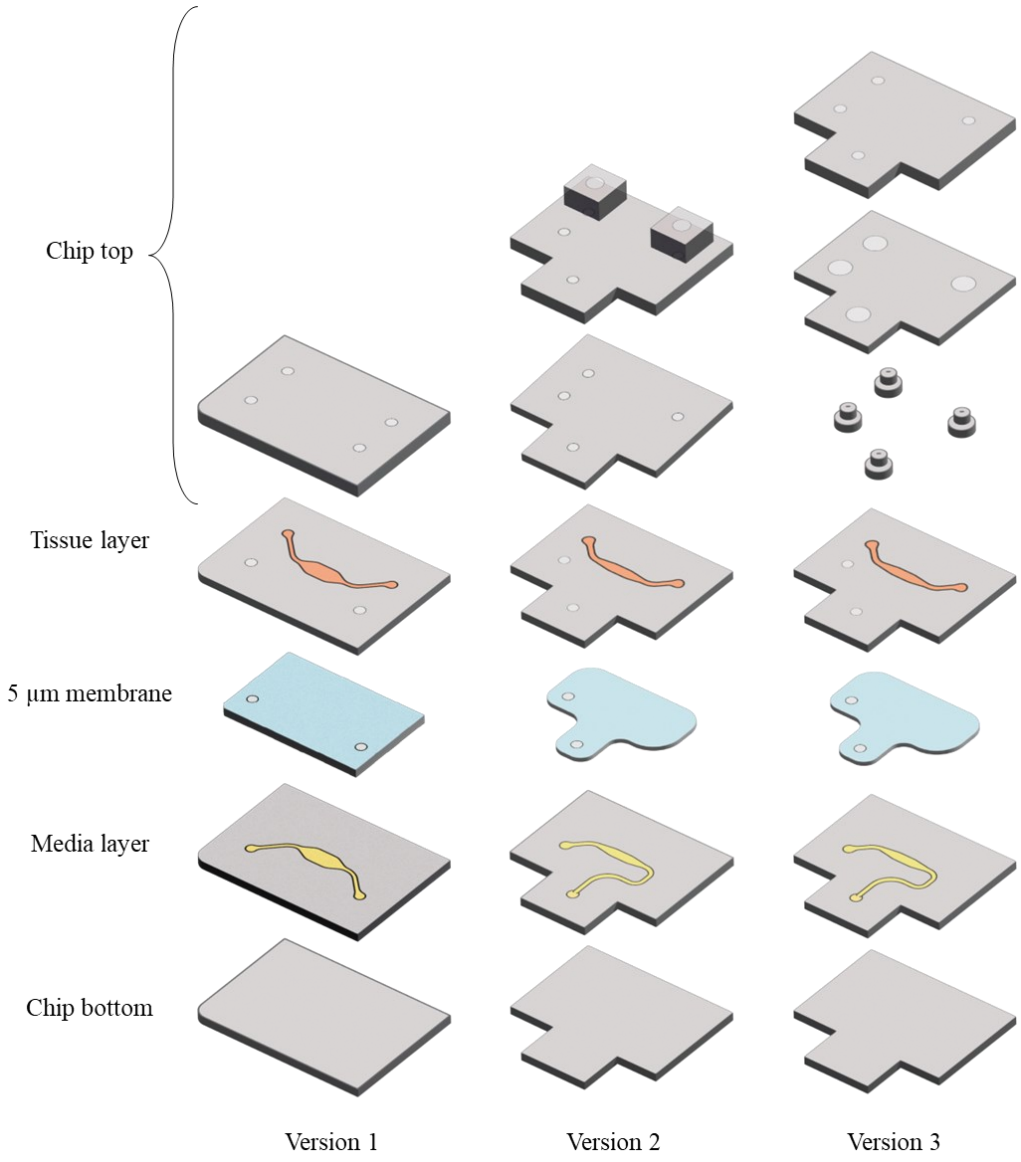

Figure 10: Schematic and annotations of chip layers for the liver-chips version 1-3.

2.3.1. Liver-Chip version 1: PMMA chip

The first version of the liver-chip was fabricated entirely out of PMMA, in a similar manner to the Version 1 of WAT-chip (Figure 11. a). The rigid plastic top directly interfaced with the perfusion setup. The fabrication procedure for this chip started with a stamp method to bond a 5 µm pore size PC membrane with a cleaned 175 µm PMMA tissue layer, (Methods sub-section 2.2.1.2), to maintain the flatness of the large free-standing membrane region. The bonding was performed in the oven (sub-section 2.2.1.4) (Figure 11.b.). In the next step, the remaining cleaned plastic layers were assembled. These included the 2 mm PMMA top, the tissue channel-membrane hybrid, the 175 µm media channel and 250 µm chip bottom (Figure 11.c). Bonding was performed in the oven at 130°C for 10 min, followed by a two step cooldown first at 60°C for 30 min, after which the chips were allowed to cool to RT before disassembling the glass slides and clamps (sub-section 2.2.1.4). The large free-standing membrane still sagged in step 2, which led to a reduction in membrane area for versions 2 and 3. Additionally, in this

version, the cannulas were inserted into the ports with a small piece of tubing to provide a soft interface to the rigid connection, but this was prone to leakage and slippage if wetted by media.

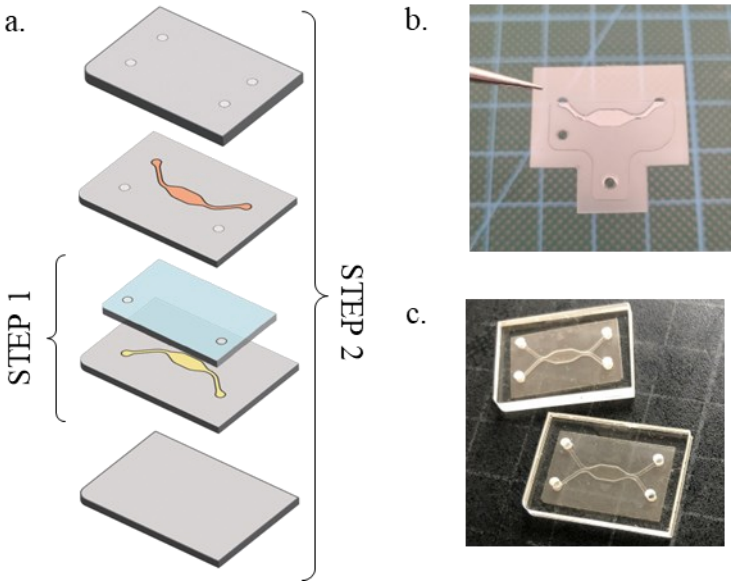

Figure 11: Fabrication strategy of liver-chip version 1. (a.) Schematic of the chip layers and fabrication steps, with Step 1 being the stamp method, followed by assembly of the entire chip in Step 2. (b.) Picture of the flat membrane bonded to the PMMA tissue layer with the stamp method, (c.) Picture of the whole chip assembly

2.3.2. Liver-chip version 2: TPE-PC chip with PDMS reservoirs

In this version of the liver-chip, material improvements were made which facilitated a simplified manufacturing methodology to ensure membrane flatness with low-temperature bonding (Figure 12.a). The chip bottom and top layers were lasercut 175 µm PC, while tissue and media channels were 750 µm high lasercut TPE. A 5 µm pore size PET membrane was sandwiched between the tissue and media channels. PET has better optical properties than PC, enabling better imaging and is also simpler to lasercut leaving clean edges. However, PET does not bond to PMMA and thus, the WAT-chip and version 1 of liver-chip were restricted to the use of a PC membrane.

2.3.2.1. Fabrication of the PDMS reservoir top part

The tissue channel of the liver-chips consisted of a monolayer of HepaRG™ cells in static culture, nourished by a reservoir situated above the ports of the tissue channel. This reservoir layer was fabricated out of PDMS, capable of holding 150 µL of media. The mold for the reservoirs was 3D printed, and once poured and cured, the PDMS was cut into squares and bonded to a 2 mm 2 mm thick slab of PDMS cut to the size of the chip, and ports punched with a 0.75 mm biopsy punch. The bottom of the reservoir squares and the top of the PDMS slab were plasma-activated at 75 W, 10 sccm O_2 for 30 sec, pressed together and the bond allowed to cure at 60°C for 2 h.

2.3.2.2. Final chip assembly

To fabricate this chip, the first step involved layering the 175 µm PC chip bottom, 750 µm lasercut TPE media channel and 5 µm pore sized PET membrane, sandwiching between glass slides and securing with steel foldback clamps (Figure 12.b). The setup was placed in the oven

to ramp overnight with the following protocol: ramping up over 4 hours to 60°C (~1.5°C/min), maintaining for 6 hours at 60°C and ramp down over 4 hours to room temperature. Care was taken to place the membrane flat and evenly on the TPE media channel, because this alignment was permanent and had to be achieved in one step. In the next step, the 750 µm lasercut TPE tissue channel and 175 µm PC top were layered onto the bonded parts, the assembly once again clamped and placed in the oven to follow the ramping protocol. In the final step, the PDMS top part was bonded to the chip by silanization with APTES (as per sub-section 2.2.1.3) (Figure 12.c). Plugs were 3D printed (clear resin, Formlabs, USA) for this version of the liver-chip, to be inserted into the reservoir cavities to maintain static media conditions at the site of the liver tissue channel (Figure 12.d).

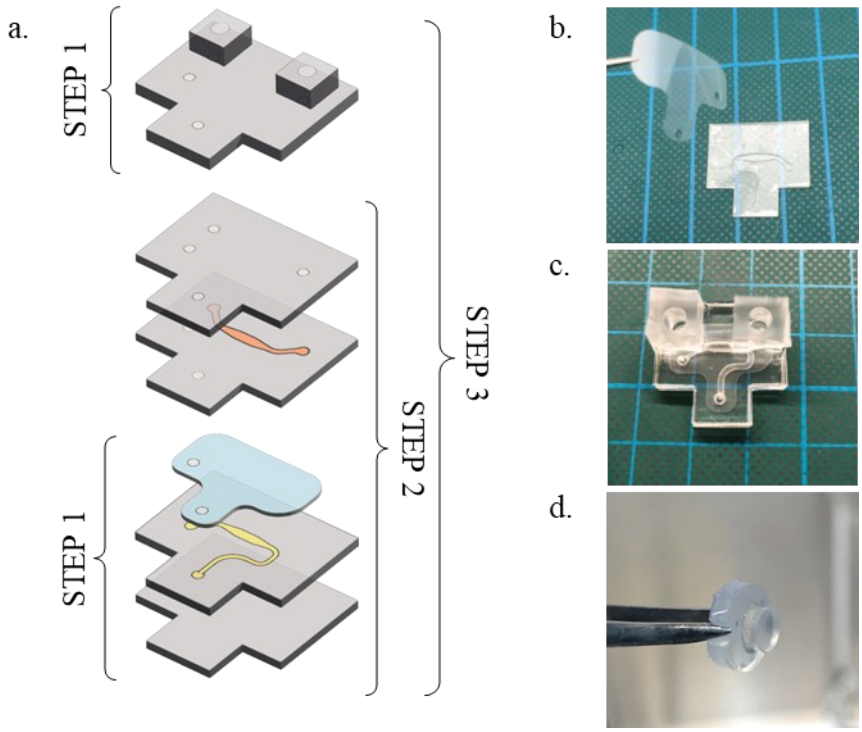

Figure 12: Fabrication steps involved for liver-chip version 2. (a.) Schematic of chip layers and fabrication steps, (b.) Picture of bonding the PC bottom layer, TPE media channel and 5 µm pore PET membrane, (c.) Picture of the final chip assembly (d.) Picture of the 3D printed plug for the tissue channel reservoir.

2.3.3. Liver-chip version 3: TPE-PC chip with embedded PDMS connectors

The final version of the liver-chip matched the outer shape of the final version of the WAT-chip with a 250 µm high TPE media channel and top part with embedded PDMS connectors (Figure 13.a). This chip was to be used with organ-chip connection platform and connected to the WAT-chip in future experiments. It also bore similarities to liver-chip Version 2 in that the PC bottom layer, 250 µm TPE media channel and membrane were bonded in an identical manner to the WAT-chip, as well as the top part with embedded connectors (Methods sub-section 2.3.2.2) (Figure 13.b).

Upon fabrication of the chip top, the top of the 750 µm lasercut TPE tissue channel and the base of the chip top were exposed to UV at 16.4 mW/cm^2 for 30 sec and bonded together. A roller was used to push out any trapped air bubbles to ensure good contact between the TPE and PMMA (Figure 13.c). Then, the top part of the chip was stacked onto the bottom part, clamped between glass slides with steel foldback clamps and returned to the oven for the ramp protocol (Figure 13.d).

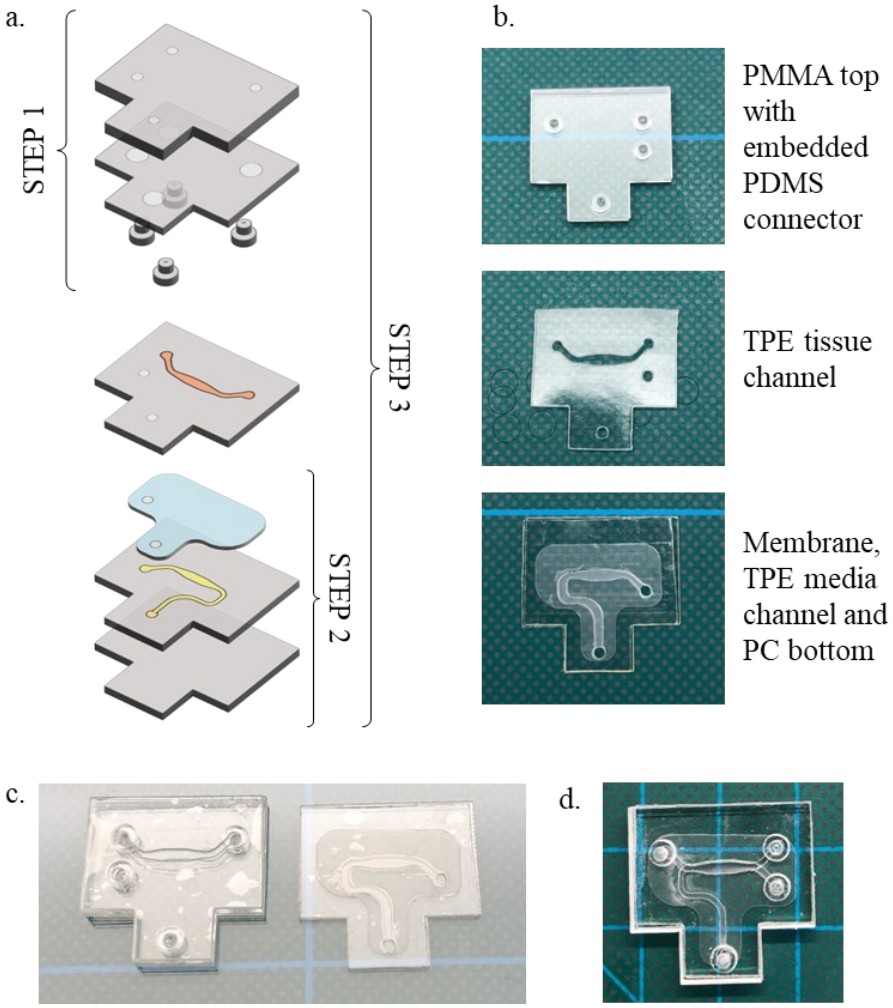

Figure 13: Fabrication steps involved for liver-chip version 3. (a.) Schematic of the various chip layers, with fabrication steps, (b.) Pictures of the parts corresponding to steps 1 and 2, before bonding (c.) Pictures of the chip components for the final step of chip assembly, (d.) Picture of the final chip assembly.

Table 7: Fabrication process steps for the liver-chip: Version 1 and 2

	Material, Layer	Height	Structuring	Process step 1	Step 2	Step 3
Version 1	PMMA, chip top	2 mm	Laser cut		Assemble between glass slides and clamps and bond in the oven at 130°C for 10 min, 60°C for 30 min and allow to cool completely to RT before disassembly	
	PMMA, tissue layer	250 µm	Laser cut	Bond with PDMS stamp method in the oven at 130°C for 10 min		
	5 µm pore, PC membrane	22 µm	Laser cut			
	PMMA, media layer	250 µm	Laser cut			
	PMMA, chip bottom	250 µm	Laser cut			
Version 2	PDMS reservoir	4 mm	Molded	Mold PDMS into 3D printed mold, cure and clean	Plasma treat and bond at 60°C for 1 hour	APTES treat the PC top of the chip, plasma treat PDMS and bond at 60°C for 30 min.
	PDMS, chip top	2 mm	Molded, punched	Mix and degas PDMS, cure		
	PC, chip top	175 µm	Laser cut		Align and bond together between glass slides and clamps with a ramp protocol: Ramp up to 60°C over 4 hours, hold at 60°C for 6 hours, ramp down to RT over 4 hrs.	
	TPE, tissue layer	750 µm	Laser cut			
	5 µm pore, PET membrane	22 µm	Laser cut	Align and bond together between glass slides and clamps with a ramp protocol: Ramp up to 60°C over 4 hours, hold at 60°C for 6 hours, ramp down to RT over 4 hrs.		
	TPE, media layer	750 µm	Laser cut			
	PC, chip bottom	175 µm	Laser cut			

Table 8: Fabrication process steps for the liver-chip: Version 3

	Material, Layer	Height	Structure	Process step 1	Step 2	Step 3
Version 3	PMMA, Chip top, small ports	1 mm	Laser cut	Mix and degas PDMS. Bond PMMA in hotpress with metal frame at 105°C, 25 min. Add PCR tape and pour PDMS into the connector mold. Cure PDMS for 2h at 80 °C. Cut off excess cured PDMS from chip top.	UV treatment for 30 sec, 99% intensity ($16.4\ mW/cm^2$), bond and roll to remove air bubbles	Align and bond together between glass slides and clamps with a ramp protocol: Ramp up to 60°C over 4 hours, hold at 60°C for 6 hours, ramp down to RT over 4 hours.
	PMMA, Chip top, big ports	1.5 mm	Laser cut			
	TPE, tissue layer	750 µm	Laser cut			
	5µm pore, PET membrane	22 µm	Laser cut	Align and bond together between glass slides and clamps with a ramp protocol: Ramp up to 60°C over 4 hours, hold at 60°C for 6 hours, ramp down to RT over 4 hours.		
	TPE, media layer	250 µm	Laser cut			
	PC, Chip bottom	175 µm	None			

2.4. Fabrication of the chip connection setups

This section describes the fabrication involved in the various connection approaches (inbuilt, modular and systemic), and fabrication of the two types of modular cassette connection mechanisms. A detailed description of the design criteria, layout and application of the connection setups has been provided in the Results section 3.1.

2.4.1. Fabrication of inbuilt, modular and systemic connection approaches

The inbuilt connection chips included both organs on the same chip, the media channels connected by a fluidic channel built into the chip (Figure 14.a). The chips were created by thermal fusion bonding PMMA layers of varying thickness using the oven-based bonding process (Section 2.2.1.4). The layers were as follows – 250 µm chip bottom, 5 µm pore PC membrane, 250 µm media channel, 250 µm chip top and an APTES-bonded 2 mm thick PDMS top with 0.75 mm punched ports.

The modular connection chips were stacked over one another at the site of connection (Figure 14.b). The upper chip had similar chip layers as the inbuilt connection chip – a 250 µm chip bottom with a port at the site of connection, a 250 µm media channel, 250 µm chip top and an APTES-bonded 2 mm PDMS port top. In the case of the lower chip, the layers were as follows – 250 µm chip bottom, 250 µm media layer, 250 µm media interface layer, 0.5 mm gasket (cushioning material) holder layer and a 2 mm APTES-bonded PDMS top port layer (Figure 14.c). The gasket holder layer enabled the stabilization of the gasket, created by punching a concentric ring (3mm inner diameter, 6 mm outer diameter) from a 0.5 mm thin sheet of flexible PDMS which was created by pouring 8 g of the 10:1 PDMS:curing agent mixture into a petri dish and curing in the oven.

The systemic connection consisted of two parts – the organ-chips and the fluidic interface which is systemic connection platform that they would be plugged into. These chips were built with the following PMMA layers – a 250 µm chip bottom with ports to interface with the connection platform, 5 µm pore size PC membrane, 250 µm media channel, 250 µm chip top layer, 2 mm APTES-bonded PDMS port layer. The gaskets were punched out of 0.5 mm thick PDMS with an inner diameter of 2 mm and outer diameter of 6 mm. The first version of the connection platform (the inverted port setup) for the media channel flow through studies was built by lasercutting and gluing the following PMMA layers – 500 µm bottom, 175 µm fluidic connection layer, 175 mm port layer with 2 mm high connection layer to connect to the perfusion setups (Figure 15).

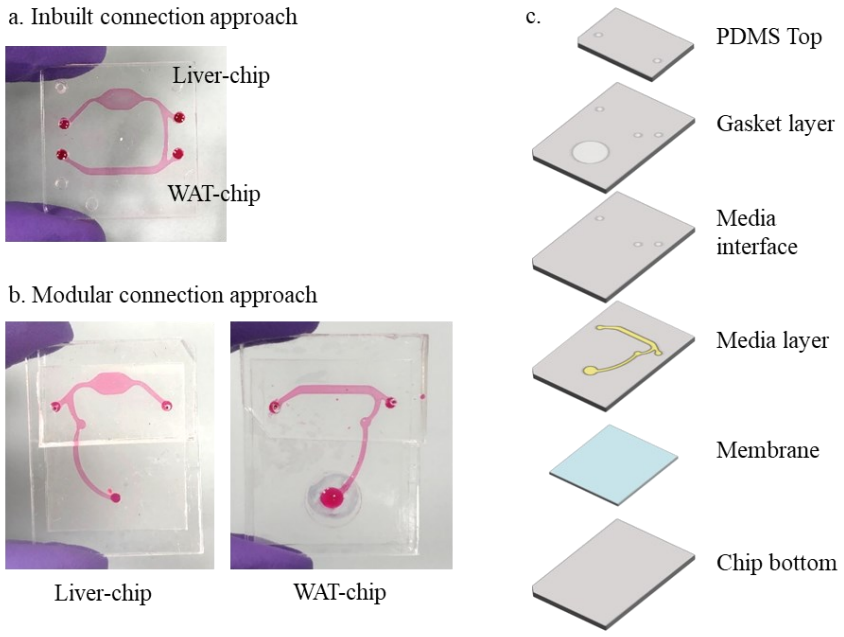

Figure 14: Inbuilt and modular approaches for vascular chip connection (via the media channels) (a.) Inbuilt connection where the WAT and liver-tissue channels are built into the same chip, (b.) Modular connections with the liver-chip as the top chip and WAT-chip as the bottom chip, (c.) Schematic of the WAT-chip layers as the lower chip in the modular connection approach.

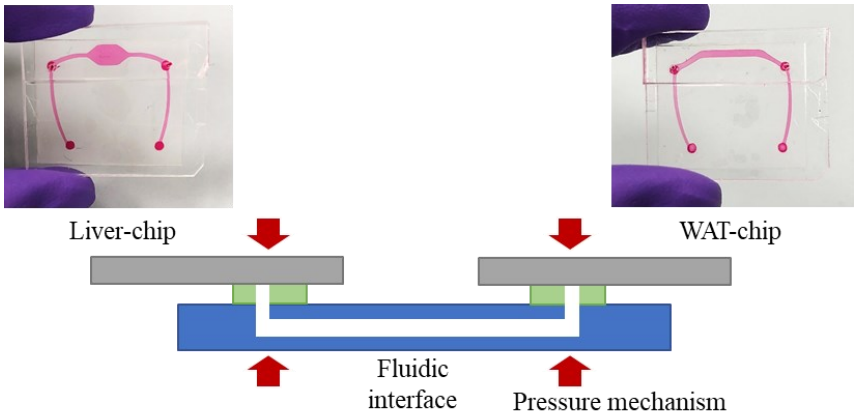

Figure 15: Systemic approach for vascular chip connection (via the media channels) with the WAT- and liver-chips (gray) placed onto the fluidic interface (blue). The gaskets (green) enabled uniform pressure distribution from the pressure mechanism (red) at the point of connection of the chips.

Holders were constructed out of PMMA to simplify the handling of the chips with cells during seeding and connection of the modular and systemic connection platforms. In the case of the magnetic holders, the base magnet holder was created by immobilizing disc or bar magnets into a PMMA block directly under the ports of the chips for the modular and systemic connection systems respectively (Figure 16.a,c). In the case of systemic connection, the fluidic interface was attached onto the holder. The top magnets were also glued into a PMMA enclosure, to prevent rusting and degradation during the experiment. For the screw-based connection, holders were fabricated as a 3 mm base piece with 2.5 mm diameter holes, threaded

with an M3 screw. A piece of 2 mm thick PMMA called a bracket was placed across the screws that it applied pressure at the site of connection of the two chips (Figure 16.b,d).

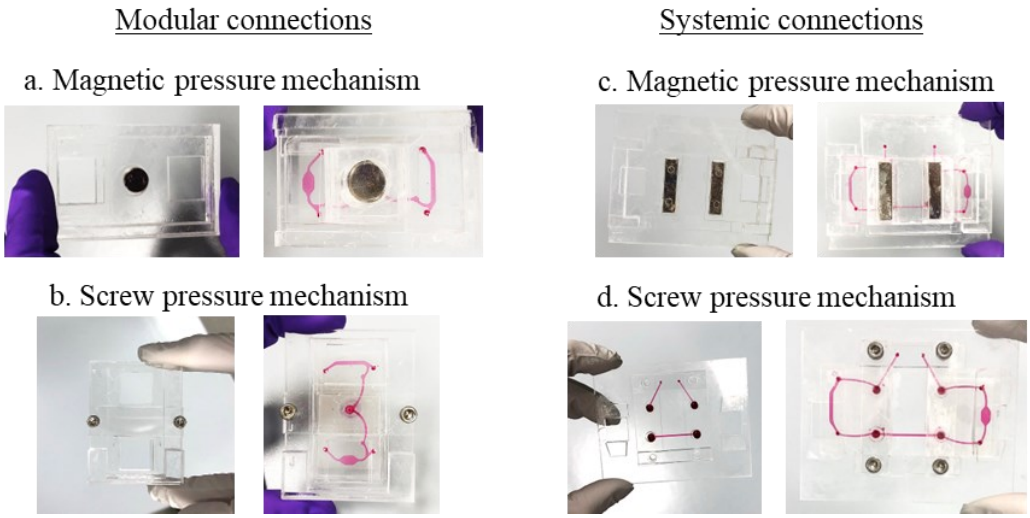

Figure 16: Holders for the modular and systemic connections (a.) For the modular system with magnets, disc magnets applied pressure at the site of connection, (b.) A pair of screws with one bracket across the site of connection provided the required pressure to maintain the connection, (c.) For the systemic connections, a pair of bar magnets provided adequate pressure at the site of connection for two ports per chip and the fluidics of the fluidic interface, (d.) For the screw connections, two brackets and two pairs of screws provided pressure across the points of connection.

Given the challenges of seeding and connection in the inverted chip systemic connection, the next versions of the connection platform were called the modular cassettes. The chips were also modified in shape to fit into the cassette which had a provision for reversibly connecting a fluidic channel across the chips. The modular cassettes were of two iterations – the first was the modular slot and the second was the 3D printed modular insert cassette. For both these approaches, pressure was applied by three ways – magnets, springs or screws. The next sub-section describes the three pressure mechanisms taking the case of the PMMA modular slot cassette.

2.4.2. Fabrication of the modular cassette connection setup

The modular cassette provided a platform into which chips were secured in the x,y, and z directions due to cassette design. The chips were connected to each other by a connection channel and pressure was applied at the site of connection by a pressure mechanism (Figure 17). Gaskets provided an even pressure distribution around the site of connection at the media outlet of each chip and brackets were used in some cases to secure the site of connection. Two types of modular cassettes were developed in this thesis – the PMMA modular slot cassette (which explored 3 pressure mechanisms) and the 3D printed modular insert cassette, which used the optimal pressure mechanism.

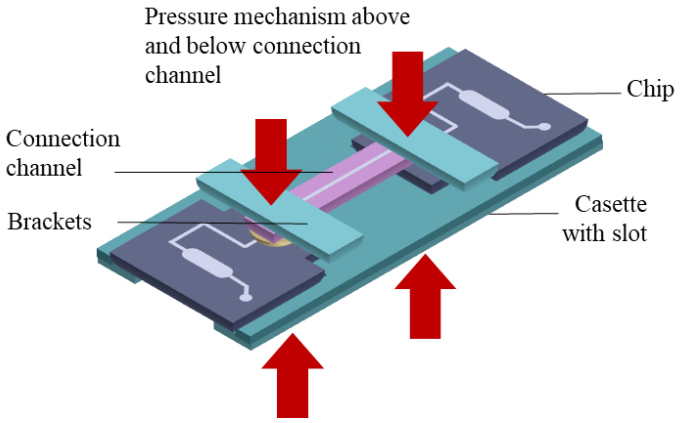

Figure 17: Layout of the modular cassette.

The PMMA modular slot cassette was created by gluing together varying thickness of cleaned lasercut PMMA sheets, with designs differing depending on three mechanism of pressure application, magnets, threaded screws or spring-laden screws (Figure 18). In general, the cassettes consisted of a cassette base (usually 250 µm thick PMMA), the chip slot for the WAT or liver-chips which were built in a specific outer T shape matching the thickness of the chips. The design of the slots secured the chips in the x and y directions. Finally, a 250 µm thick PMMA chip top flap secured the chips in the z direction. In the case of the magnetic pressure mechanism, the cassette base was thicker to accommodate the base magnets, and the connection channel was thicker to house the corresponding magnetic brackets. The threaded screw cassette had a manually threaded PMMA chip slot, to hold M3 screws. Brackets were created as pieces of 1.5 mm thick PMMA to press down on the site of connection as the screws were tightened manually.

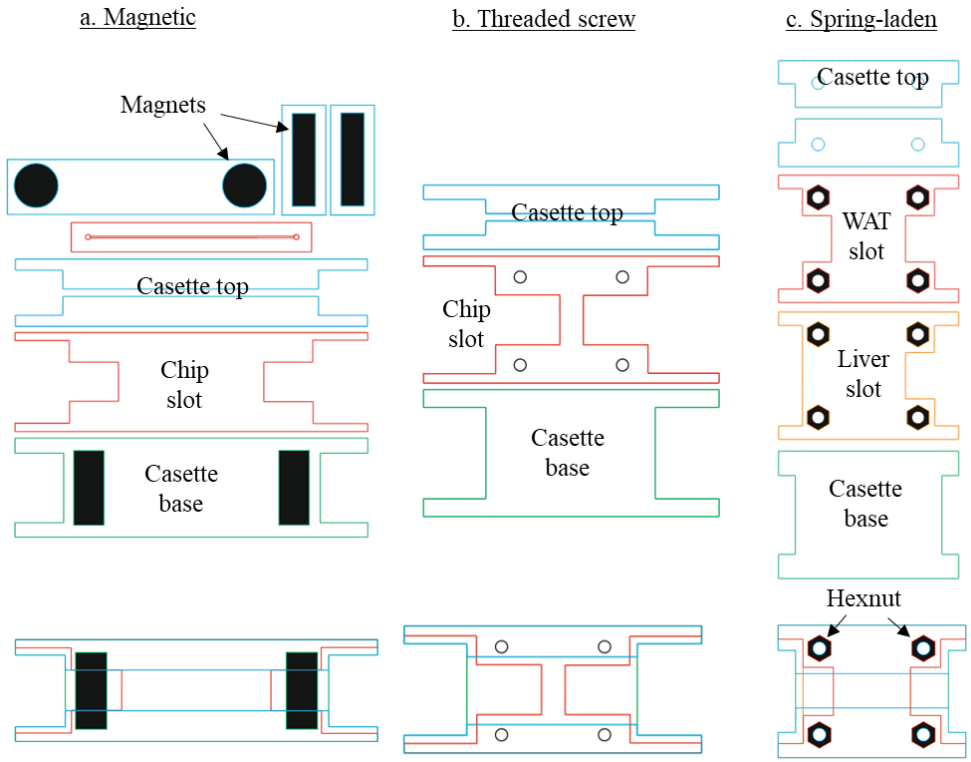

Figure 18: Mechanisms of pressure application in the modular cassettes (a.) Magnetic pressure mechanism comprised a cassette base (green) housing two magnets (black), a chip slot (red) and cassette top flaps (blue). The connection channel (red) across the length of the chips was covered with a channel top (blue) housing the corresponding magnets. (b.) Screw pressure mechanism with a cassette base (green), chip slot (red) with M3 screw holes and threads fabricated into the part directly, and the cassette top flaps (blue). (c.) Spring-laden pressure mechanism with a cassette base (green), liver-chip slot (orange), WAT-chip slot (red) and cassette top(blue). Hex nuts (black) were embedded into the chip slot parts directly and held in place by the cassette top flaps.

For the spring-laden pressure mechanism, M3 hex nuts were added to the chip slot layer during cassette fabrication (Figure 19.c). Above the brackets, springs were added to screws which enabled application of force without much manual screwing as was the case of the threaded screw pressure mechanism (Figure 19.a, d). Gaskets for the PMMA modular slot cassette were punched out of a 250 µm thick TPE layer with inner diameter 2 mm and outer diameter 6 mm. The connection channel consisted of three layers of 250 µm thick PMMA, thermal fusion bonded together in the oven with glass slides and steel foldback clamps. The gaskets were then bonded to the connection channels via low temperature bonding at 60°C in the oven at the ports (Figure 19.b).

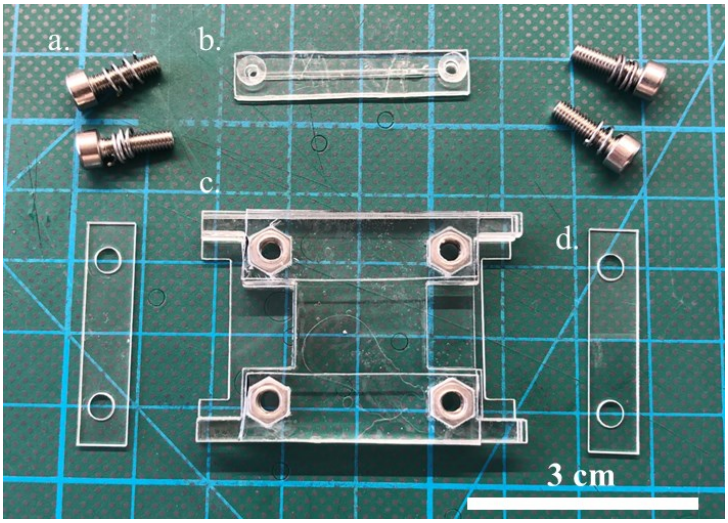

Figure 19: Summary of components in the PMMA modular slot cassette system with spring-laden pressure mechanism, (a.) M3 screws with springs, (b.) PMMA connection channel with TPE gaskets, (c.) The PMMA slot cassette with integrated hex nuts, (d.) Bracket to add pressure at the site of connection. Scale bar: 3 cm.

The 3D printed modular insert cassette improved on the design of the spring-laden modular slot cassette, in that the cassette was now 3D printed and had additional features to simplify handling during cell culture. The cassette was designed with the Solidworks software and 3D printed with clear resin (Formlabs) (Figure 20.a). Chips could be inserted into the cassette from the top while hex nuts mounted onto a hex nut holder could be inserted from the bottom (Figure 20.b). This chip was designed for an assay to read glucose uptake of a single chip connected to recirculation perfusion. For this, the cassette had one chip insertion spot, and a region to secure the connection channel which connected to the chip via a gasket on one side and had an outlet port to connect to the peristaltic pump on the other side (Figure 20.a.VIII). 250 µm thick TPE with 250 µm PMMA backing was lasercut to create gaskets in bulk, with an inner diameter of

1.5 mm to allow a tolerance during chip alignment (Figure 20.c). Once the backing was removed, the outer hole of diameter 3 mm was punched to reveal the gasket ring.

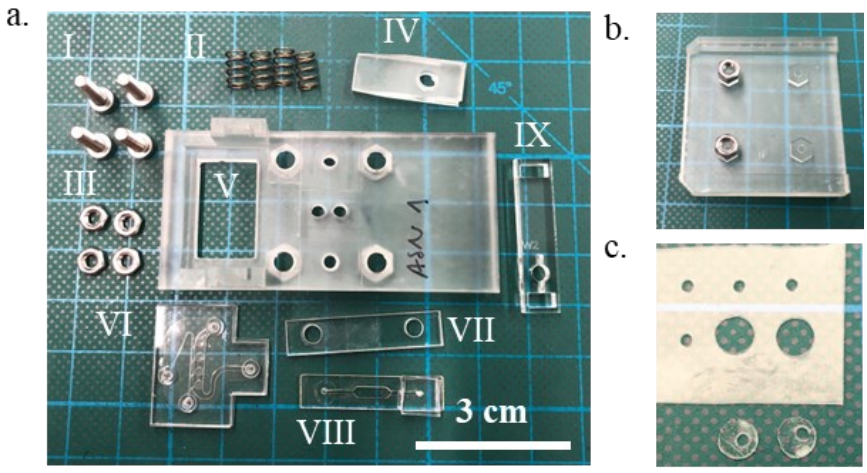

Figure 20: Components of the 3D printed modular insert cassette, (a.) An overview of all components involved in the connections of the 3D printed modular insert cassette with (I) M3 screws, (II) springs, (III) hex nuts being added under the cassette, (IV) connection channel securing stylus, (V) cassette with viewing window for the chip tissue channel and holes for the insertion of sensor cables to measure the sensor readout, (VI) the WAT-chip in this case, (VII) bracket to add pressure at the site of connection of channel and chip, (VIII) sensor chip, (IX) reservoir holder for the recirculation setup, (b.) Picture of the hex nut holder, (c.) Picture of the sensor chip, (d.) Schematic of the various chip layers of the sensor chip, (e.) TPE gaskets for this connection setup

2.5. Burst pressure characterization test

The pressure that the compression-mechanisms of the connections in the PMMA modular slot cassette could withstand was measured with a burst test (Schneider, Brás, et al., 2021). The three pressure mechanisms (screw, magnets and spring-laden connectors) were assembled with connection channels, chip, cassette and gaskets, and outlet ports of the connection channels sealed with superglue (UHU). A Luer connector was attached to the chip inlet, which connected it to a regulated compressed air pressure source via a pressure regulator (Figure 21.a.) This connected system was submerged under water and the compressed air pressure was incrementally increased in steps of 200 mbar going up to a maximum possible pressure of 6 bar or until bubbles formed at any point in the assembly to indicate material failure (Figure 21.b). The ramping of air pressure was used to maintain experimental consistency across the samples.

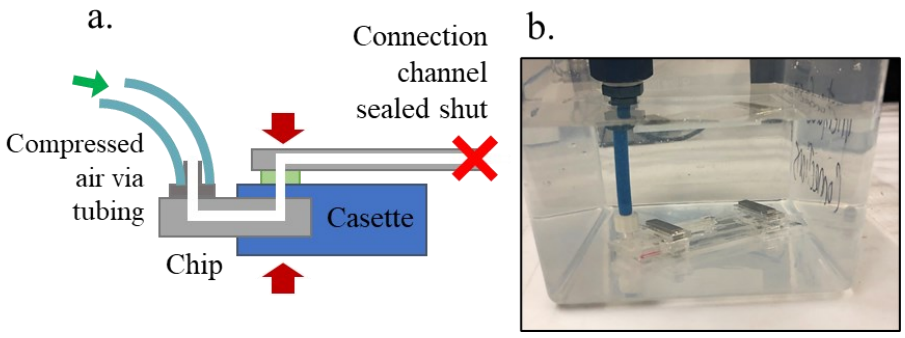

Figure 21: Burst pressure characterization test setup (a.) Schematic of the burst pressure characterization test, with the cassette setup attached to a compressed air inlet at the chip and the connection channel sealed (b.) Picture of the setup submerged under water

2.6. Cell culture

2.6.1. Isolation of primary human adipocytes

Primary human adipocytes were freshly isolated from biopsies of subcutaneous adipose tissue obtained from plastic surgeries performed by Dr. Wiebke Eisler (BG Klinik Tübingen, Tübingen, Germany) and Dr. Ulrich E. Ziegler (Klinik Charlottenhaus, Stuttgart, Germany), approved by the local medical ethics committee. The protocol for isolation of adipocytes from the biopsies was published previously (Rogal, et al., 2020). Briefly, the adipocyte-laden fat tissue layer was separated from the dermis, washed twice with PBS+, and the connective tissue and blood vessels cut away. The adipose tissue was then minced into small pieces and digested in a collagenase solution (0.13 U/mL collagenase type NB4 in Dulbecco's Modified Eagle Medium with 1% bovine serum albumin (BSA)) for 1 hour at 37°C on a rocking shaker (50 cycles/min). The digested tissue was stirred with a glass pipette and strained through a 500 µm mesh sieve. The isolated adipocytes were collected in a 50 mL conical tube, washed twice with DMEM/Ham's F-12 medium and placed in a T75 cell culture flask in WAT-culture medium overnight.

2.6.2. Cell culture and differentiation of HepaRG™ cells

The HepaRG™ cell line, originally derived from a patient suffering from hepatitis C and hepatocarcinoma was obtained in the cryopreserved, undifferentiated form and cultured in collaboration with the group of PD Dr. Alexander Mosig at the Jena University Hospital according to their established protocols. A vial of the HepaRG™ cells was thawed into 9 mL of maintenance media (MM) and centrifuged at 200 *g* for 3 min (Table 9). Upon resuspension in maintenance media, the cells were seeded at a density of 20000 cells per cm^2 in a T25 flask and cultured in an incubator at 37°C, 5% CO_2 and 95% relative humidity. Media change was performed two times per week and the cells were passaged every two weeks in a ratio 1:6. During passaging, the flask with cells was washed with warm PBS. The cells were then incubated for 3 min with 0.05% trypsin in 0.48 mM EDTA solution at 37°C to facilitate their detachment. The trypsinization step was stopped with inactivation medium, the cells were collected into a 50 mL conical tube and centrifuged at 200 *g* for 3 min. The pellet was then resuspended in MM and seeded at a density of 20000 cells per cm^2 in a T25 flask. After two weeks of culture in MM, transition medium (MM with 1% DMSO) was added and four days later changed to differentiation medium (DM: MM with 2% DMSO) to differentiate the culture

into a 50% hepatocyte-50% biliary cell phenotype. After two weeks of culture in DM, the cells were differentiated and ready for injection into the chips. The cells could be then used for up to two more weeks. One week after the completion of differentiation, the cells were also frozen and banked to be thawed or used directly. To freeze the cells, they were resuspended in freezing medium (80022, Ibidi GmbH) and 1 million cells were frozen per mL in a cryovial. The vials were frozen in an IPA bath in the -80°C for 12 hours and transferred to a liquid nitrogen storage, and the cells used between passages 15 to 20.

Experiments were also performed with thawed differentiated HepaRG™ cells. To prepare the cells for direct use in experiments, a 6 well plate was coated with a 0.1 mg/mL collagen I solution in PBS for 30 min at 37°C. After coating, the collagen solution was aspirated, and MM was added per well to be seeded. A vial containing 1 million frozen differentiated HepaRG™ cells was thawed with MM and plated into 2 wells resulting in a cell number of 0.5 million cells per well. The cells were cultured for approximately 1 week in MM until confluent with media change every two days, after which, they were cultured in transition medium until ready to use.

Table 9: Media components of maintenance media, and inactivation media for HepaRG™ culture

Medium component	Maintenance Media (MM)	Inactivation Media (IM)
Medium	William's medium E (WEM)	PBS
FCS	10%	10%
GlutaMAX™	2 mM	
Human insulin	5 µg/mL	
Hydrocortisone	24.7 µg/mL	
Penicillin/ Streptavidin	1%	

2.6.3. Cell culture of primary microvascular endothelial cells (mVECs)

The isolation and culture of primary mVECs has been described previously (Rogal, Roosz, Teufel, et al., 2022). Briefly, the cells were isolated from the same biopsies which yielded the adipocytes, where the skin layer was cut away from the rest of tissue and blood vessels, into strips of approximately 4 cm by 1 mm. After washing the strips of skin in PBS, they were incubated in 10 mL of skin digestion solution (2.0 U/mL dispase D4693, Merck KGaA, in PBS) at 4°C overnight. The next day, the epidermis was peeled away with tweezers and the dermis washed with PBS twice, before incubation in versene solution followed by 40 min in 0.05% Trypsin in EDTA Solution (59418C; SAFC) at 37°C to initiate cell separation from tissue, shaking every 5 min. The trypsinization was stopped with inactivation medium and the strips transferred to a dish with PBS, where each strip was scraped with a scalpel to gently scrape away the cells from the tissue. The resulting cell suspension was strained in a 70 µm mesh, centrifuged at 200 *g* for 5 min and resuspended in 10 mL of pre-warmed ECGM medium (C-22010, PromoCell GmbH) with 10 mg/mL Gentamicin (mVEC expansion medium) The cells were seeded into two T25 cell culture flasks and incubated at 37 °C, 5% CO_2 and 95% relative humidity (rH) overnight. The next day, the culture was rinsed with PBS and mVEC expansion medium to remove dead cells and debris. Versene treatment was performed as needed on the culture to remove fibroblasts during the first days of culture as needed. Here, the cells were washed with PBS and incubated with versene solution at 37°C for 5 min until

the fibroblasts detached. Pre-warmed mVEC expansion media was added once more after washing with PBS to remove the versene solution. Media was changed every three days until the cells reached 80% confluency after which they were either passaged, frozen to be banked or injected into the chips. The isolated mVECs were used up to P6 in chip.

2.7. Chip culture and perfusion

2.7.1. Priming of chips, cassettes and consumables

In preparation for an experiment, the chips were plasma treated for 5 min at 75 W and 15 sccm O_2 with ports-side up. For the chips with ports on opposite faces, each face was plasma-treated sequentially. Holders were sterilized with 70% ethanol and dried in the biosafety cabinet. Springs, screws, tweezers and collection tubes for sampling (with holes drilled into the top) were autoclaved. Sterile PCR tape was cut with autoclaved scissors in a biosafety cabinet and maintained sterile in a petri dish sealed with parafilm. Cassettes were washed with 70% ethanol and wiped with wipes soaked in ethanol, placed into the biosafety cabinet where they were allowed to air-dry and exposed to UV for 30 minutes.

After plasma treatment, the chips were placed in a biosafety cabinet and flushed with room temperature PBS (priming) and then placed with sterile tweezers into the degassing holder in a 50 mL collection cup (Medi Shop) with an additional 25 mL of PBS (Figure 22). The lid for the cup was partially screwed on (to leave an air gap) and taped in place (so as not to fall off during degassing), then placed into a desiccation pot. Attached to a vacuum pump, degassing was carried out for 45 min. After degassing, the chips were placed into a petri dish, 2 chips per dish, and inspected for bubbles in the channels. If bubbles were present, the chips were placed channel side pointed upwards into a 50 mL conical tube with 25 mL PBS and centrifuged at 200 *g* for 10 min to remove any residual bubbles. At this stage, both channels of the liver-chip and media channel of the WAT-chip were coated with 0.1 mg/mL of ice-cold collagen I in PBS. The collagen solution was injected into the channels, with droplets placed at ports to prevent the channels drying out. 15 mL conical tube caps filled with PBS were then placed next to the chips inside each petri dish and the system was placed in the incubator for coating at 37°C for 30 min. After coating, the channels were flushed with the respective pre-warmed media corresponding to each channel, with extra droplets placed on each port, and the chips were returned to the incubator until ready for seeding over the next hour. Over the rest of the experiment, care was taken to only add pre-equilibrated media to the chips and that the chips were outside the incubator for a maximum of 2 min at a time, to ensure a constant temperature of chips during handling. Connection channels for the cassette were prepared by plasma activation port side up in the same manner as chips. After flushing the channels with 200 µL drop of PBS, the chips were dropped into a 50 mL conical tube containing 25 mL of PBS. These were centrifuged at 200 *g* for 10 min to remove any bubbles and stored at 37°C on the day of connection of chips, to equilibrate. Prior to use with the connection platform, the conical tube was centrifuged again to remove any residual bubbles and returned to the incubator during connection.

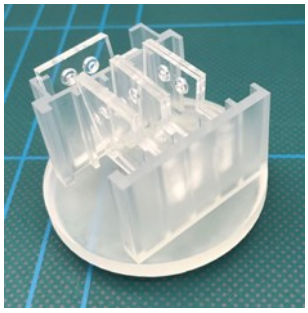

Figure 22:Degassing holder for chips, to fit in a collection cup

2.7.2. Cell injection into the WAT-chip

The adipocytes were injected into the chips within 12-24 hours of isolation. From the culture flask, the cells were transferred to a 50 mL conical tube where they were left static for 1 min to allow the adipocytes to float to the top. Upon aspirating the media below the adipocytes, they were washed twice with adipocyte seeding medium (Table 10) and split into two 15 mL conical tubes which alternated in remaining in the incubator to equilibrate while the other was in use.

For the preparation of the Hystem®-C gel (Advanced Biomatrix, USA), the components of the kit were thawed to room temperature in a dry environment and prepared according to the manufacturer's instructions. 1 mL of degassed water was added to each of the vials containing glycosil and gelin, and 0.5 mL of degassed water added to the Extralink vial. The vials were placed on a rotary mixer for 30 min and then aliquoted with syringes for the calculated amount of each component into separate Eppendorf tubes. The gel mixture was prepared as Gelin:Glycosil:Extralink in the ratio 2:2:1 as per the manufacturer's recommendations. 75 µL of cells was added to 25 µL of the gel mixture and gently pipetted up and down to mix without introducing bubbles into the gel mixture. 25 µL of this mixture was then pipetted into the tissue fluidics channel of the WAT-chip so that each chamber filled via sequential loading. Once all four chambers were filled, 25 µL of pure gel mixture was injected into the channel, causing the adipocytes in the fluidics part to be flushed out, ensuring that only the tissue chamber region directly below the media channel was filled with adipocytes. The tissue channel ports were then dried by wiping gently with a Kimtech wipe damp with 70% ethanol and plugged with a piece of PCR tape. Warm equilibrated adipocyte seeding medium (Table 10) was pipetted into the media channel and extra droplets were left at the ports, and the chip was placed in the incubator in a petri dish to allow the hydrogel to crosslink for 1 hour. At that point for the recirculation setup, the chips were directly connected to flow. For the experiments with push perfusion regime or for endothelial cell coculture experiments, P100 filter pipette tips with 100 µL of media each were placed into the media inlet and outlet and the chips were placed overnight into the incubator.

2.7.3. Cell injection into the liver-chip

Upon differentiation, the HepaRG™ cells in flasks were trypsinized, detached and centrifuged (Methods section 2.6.2). The pellet was resuspended in HepaRG™ seeding medium (Table 10) to obtain a cell density of 4 million cells/mL. 20 µL of the cell suspension was injected into the tissue channel of the prepared liver-chip, with an empty pipette tip placed at the outlet of the

tissue channel. Once more than 70% of the mixture was injected into the channel, the pipette tips were removed simultaneously to ensure that the cells were not disturbed due to backflow of media. The cells were allowed to attach in the chip over four hours in the incubator, after which a droplet of media was placed at the tissue channel inlet and gravitational flow gently flushed out the unattached cells. At this stage, the tissue channel reservoirs for version 2 of the liver-chip were plugged with the 3D printed plug, while the ports in versions 1 and 3 were plugged with PCR tape. P200 filter pipette tips with 100 µL of corresponding media were placed at the media tissue inlets and outlets.

Table 10: Media components of adipocyte seeding medium, HepaRG™ seeding medium, mVEC culture medium and FullW connection culture medium

Adipocyte seeding medium	HepaRG™ seeding medium
DMEM/F12-Ham's medium (w/o Phenol red) 1% Pen/strep 10% FCS 10 mM HEPES buffer 0.1 µM Rosiglitazone 60 nM human insulin	WEM Media (w/o phenol red) 1% Pen/strep 10% FCS 100 mM Glutamax 5 µg/mL Insulin 5 µg/mL Hydrocortisone
mVEC culture medium	FullW medium
ECGM Medium 1% Pen/strep SingleQuot kit comprising 2% FCS 12 µg/mL ECGS 1 ng/mL bFGF 0.1 mg/mL EGF 1 µg/mL Hydrocortisone	DMEM/F12-Ham's medium (w/o Phenol red) 1% Pen/strep 10% FCS 10 mM HEPES buffer 0.1 µM Rosiglitazone 60 nM human insulin 12 µg/mL ECGS 1 ng/mL bFGF 0.1 mg/mL EGF 1 µg/mL Hydrocortisone

2.7.4. Cell injection of endothelial cells into the inbuilt, modular and systemic connection chips.

In the case of the inbuilt connection chip, the ports beyond the connection channel were dried and plugged with PCR tape. The endothelial cells in the flask were trypsinized, detached and centrifuged as mentioned previously (Methods section 2.6.3). The pellet was resuspended in mVEC culture medium (Table 10) to obtain a cell density of 6 million cells/mL and 15 µL of this mixture was injected into the systems, running from the WAT-chip to the liver-chip. The cells were allowed to attach for a period of two hours after which a droplet of media was placed at the media channel inlet to flush unattached cells via gravity. For the modular connection system, the WAT-chip was placed into the holder and a PDMS gasket added to the connection port. 50 µL was flushed into the chip to fill the channel and a 20 µL droplet of media was added to the gasket to ensure liquid-liquid contact during the connection of the liver-chip which was subsequently aligned at the site of the port. Magnets were added carefully, and screws were

fastened simultaneously one turn at a time, to ensure an even distribution of pressure across the site of connection. The chip-seeding then followed in a similar manner to the inbuilt system. For systemic connection, the downward facing connection ports leading to the cassettes of each chip were dried and plugged with PCR tape. The media channels of the chips were injected with cells and allowed to attach for a period of two hours after which a droplet of media was placed at the media channel inlet to flush unattached cells via gravity.

2.7.5. Chip connection to push perfusion regime

Syringe pumps were employed for the positive pressure-driven perfusion of chips in push regime. Tygon tubing of inner diameter 0.51 mm connected the syringes of volume 1,3, or 5 mL to the chips. To connect tubing to chips, cannulas were prepared by soaking the blunt needle tips in acetone overnight and detaching the metal cannula from plastic with a tweezer. The metal cannulas were washed with ethanol, dried, and set aside until connected. The inlet tubing was prepared by connection of a 30 cm long piece of tubing to a 23-gauge blunt cannula on one end which would be connected to the syringe, and the metal cannula for connection to the chip. In the case of version 1 liver-chips, the part of the metal cannula that connected with the chip also contained an additional cladding of tygon tubing. For experiments that needed extended inlet tubing, an additional 10 cm long tygon tubing was attached onto the end of the metal cannula, to enable tubing change at the point of extension. The outlet tubing was prepared by connecting 10 cm long tygon tubing to a metal cannula. The tubing was then placed into autoclave bags and autoclaved before the start of the expt.

During connection, the media to be perfused through the chip was prepared and pre-warmed to 37°C. It was then poured into a collection cup for ease of handling. Syringes were loaded with the media and each inlet tubing was carefully removed from the autoclave bags and connected at the plastic Luer part to the syringes. The tubing was filled with media from the syringe until a droplet of media appeared at the metal cannula. A chip (individual or connected system) was placed into a chip perfusion holder and the metal cannula from the inlet tubing was connected into the chip and tubing fixed at the holder. This holder was constructed out of 2 mm thick PMMA to hold 3 chips at a time and had the outer dimensions of a well plate to enable interfacing with microscope stages.The outlet tubing was pre-filled with media to again have a droplet at the metal cannula, which was inserted into the chip. The free end of the outlet tubing was placed into the hole in the 1.5 mL collection tube placed into the chip perfusion holder.

After the establishment of a confluent monolayer of endothelial cells, in the case of inbuilt and modular connection systems, the WAT-chip inlet was connected to the syringe pump, while liver-chip outlet was connected to the short outlet tubing, leading to flow from WAT to Liver. The flowrate was ramped from 5, 10, 20 to 40 μL/h every 2 hours. Culture perfusion was maintained at 40 μL/h. The channels in the systemic fluidic interface were plasma-treated and pre-flushed with warm PBS and warm media and stored in the incubator until it was time to connect the chips. Gaskets were also added with 20 μL each of media just before the chips were placed on top. The downward-facing connection ports on the chips were unplugged, and chips were aligned onto the cassette. Magnets or screws were added in a similar manner to the modular connection system and push perfusion was ramped as mentioned before.

In the case of the modular cassettes (PMMA slot and 3D printed insert cassettes), a seeding schedule was followed depending on the availability of fresh adipocytes from surgery (Figure 23.a.). The workflow began with the adipocytes injected into chips (sub-section 2.7.2) and placed static in the incubator overnight with pipette tips filled with WAT maintenance media and humidity reservoirs (15 mL conical tube cap with 1 mL of PBS). A day before connection to perfusion, the mVECs were seeded in the WAT- and precoated liver-chips (sub-section 2.7.4). In the case of the WAT-chip, the chips remained upright and after the 2 hours of attachment, the pipette tips with ECGM medium were added to the chips, maintained static for yet another day in the incubator. The liver-chips were flipped onto the flipping box (Figure 23.b) and allowed to attach to the bottom of the membrane for four hours after which they were returned to the upright position and pipette tips with ECGM medium added to ports and left static overnight in the incubator. On the day of connection, the HepaRG™ cells were injected into the liver-chips (sub-section 2.7.3), and after the two hours of attachment and removal of unattached cells, the tissue channels plugged, and pipette tips with FullW media inserted into the media channels until ready for connection (Table 10).

Working with one system at a time, one WAT- and one liver-chip were added to the sterilized cassette (sub-section 2.7.5). In the case of the PMMA slot cassette, the PDMS gaskets were added to the chip tops and FullW media pipetted onto the connection ports to allow liquid-liquid contact. A connection channel was removed form the conical tube storage and aligned onto the gasket with tweezers. At this stage, the brackets containing either the spring-laden screws for spring connectors or screws for the screw connectors were placed onto each connection port and fastened with a screwdriver, alternating the tightening a little at a time to ensure a similar amount of pressure. Then, with an empty pipette tip placed at the Liver-media inlet and a pipette tip with 200 µL Full W media placed at the WAT-media inlet, the connected setup was placed in a petri dish and returned to the incubator until time for connection to perfusion. Once all connection setups were established, the chips were connected to perfusion with a syringe pump. Perfusion proceeded at 40 µL/h.

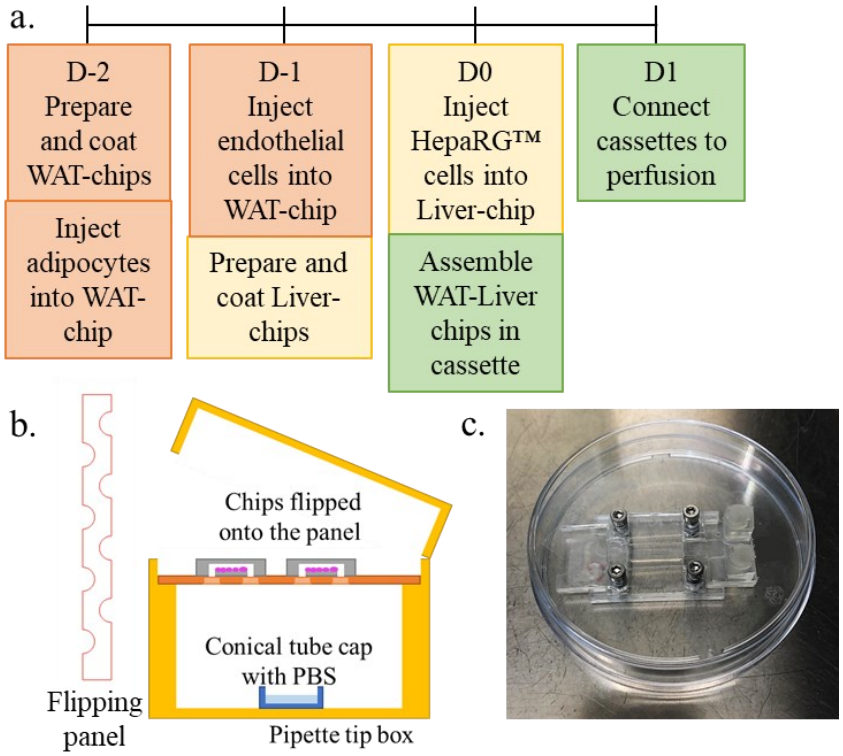

Figure 23: Experimental timeline and apparatus during connection of WAT- and liver-chips in the modular cassettes. (a.) Experimental timeline of cell seeding and connection, (b.) Schematic of the flipping panel and box while seeding endothelial cells in the liver-chip, (c.) Picture of the connected WAT- and liver-chips before connection to perfusion

2.7.6. Sensor integration into the 3D printed modular insert cassette and recirculating perfusion regime

2.7.6.1. Design, fabrication, and preparation of the sensor chips

The sensor cocktail for the glucose and oxygen sensors was developed and prepared by Stefani Fuchs at TU Graz in Graz, Austria (Fuchs et al., 2022). The cocktail was a homogenized mixture of a polyurethane-based hydrogel, ethanol, water, glucose oxidase crosslinked enzyme aggregates, and polystyrene beads stained with the oxygen sensitive dye Pt-TPTBPF (platinum(II) meso-tetra(4-fluorophenyl) tetrabenzoporphyrin), tuthenium(IV) oxide hydrate and catalase or ruthenium(IV) oxide for hydrogen peroxide degeneration. The cocktail was dispensed as 500-800 µm spots onto a pressure sensitive adhesive (ThermalSeal RTS, Excel Scientific) with a microdispenser (MDS3200+, VERMES Microdispensing GmbH). Given the enzymatic nature of the cocktail and a temperature stability of less than 40°C, the pressure sensitive adhesive offered a convenient method of sensor integration onto the base of fluidic channels. Once dried, a diffusion barrier (1 µm pore size PET membrane, ipCellCulture, it4ip) was placed directly onto the sensor spot. A piece of this pressure sensitive adhesive containing the glucose and oxygen sensors was cut and stuck onto the base of the connection channel, with the oxygen sensor oriented before the glucose sensor in the direction of flow (Figure 24.a). The connection channel comprised a 250 µm TPE fluidic channel layer sandwiched between two layers of 175 µm thick PC (Figure 24.b). The bottom PC layer had

the channel inlet port and the sensor window, while the top PC layer had the channel outlet port, onto which a PDMS interface layer was APTES-bonded (sub-section 2.2.1.3). A day before the connection and perfusion experiment, the connection channel was plasma treated and centrifuged in a 50 mL tube of PBS+. The falcon was then placed into the incubator to swell the sensor spots and to equilibrate the connection channel to the incubator temperature.

2.7.6.2. Setup of the 3D printed cassette for recirculation perfusion regime and sensor integration experiments

The 3D printed modular insert cassette was employed for these experiments, to assess the individual glucose and oxygen consumption of adipocytes or hepatocytes with the glucose and oxygen sensors in the connection channel. First, the primed chip was inserted into the cassette and a piece of BreatheEasy membrane placed onto the surface of the chip to fluidically seal the embedded PDMS-connectors and to prevent leakade (Figure 24.c). A small hole was punched with a sharp serological 23 G needle at the media outlet, allowing fluid flow across the chip and connection channel. The sensor connection channel was placed at the site of connection and pressure at the brackets was created with M3 screws or the spring laden screws with the hex nut holder slid below the cassette. The stylus was connected to secure the connection channel (Figure 24.d) and reservoir holder added on top of the pillars of the cassette (Figure 24.e). The cassettes were mounted onto the cassette holder in the ALS box (Automated Laboratory Solutions) and the setup maintained at 37°C and 60% rH. The cassette holder setup consisted of a PMMA frame with metal legs to raise the cassettes and allow for the insertion of sensor cables attached to a phasefluorometer from below the holder (Busche et al., 2022), (Figure 24.f). The fibers were passed through holes in the holder, 4.3 mm apart and corresponded to the cassettes which could be positioned directly on the fibers (Figure 24.g). Autoclaved reservoirs and tubing were prefilled with 700 µL media and placed onto the media channel inlet of each chip with the reservoir holder. The outlet tubing was plugged into the sensor chip outlet to close the loop.

The system was set to a flowrate of 100 µL/h and the glucose calibration proceeded by filling the reservoirs sequentially with a calibration solution I through III (Table 11). After calibration, 6 chips were injected with cells while the other 6 were maintained as blanks. During the experiment, perfusion proceeded at the rate of 100 µL/h and the chips were exposed to two types of media, fed and fasted (Table 11). At the end of the experiment, calibration was once again performed.

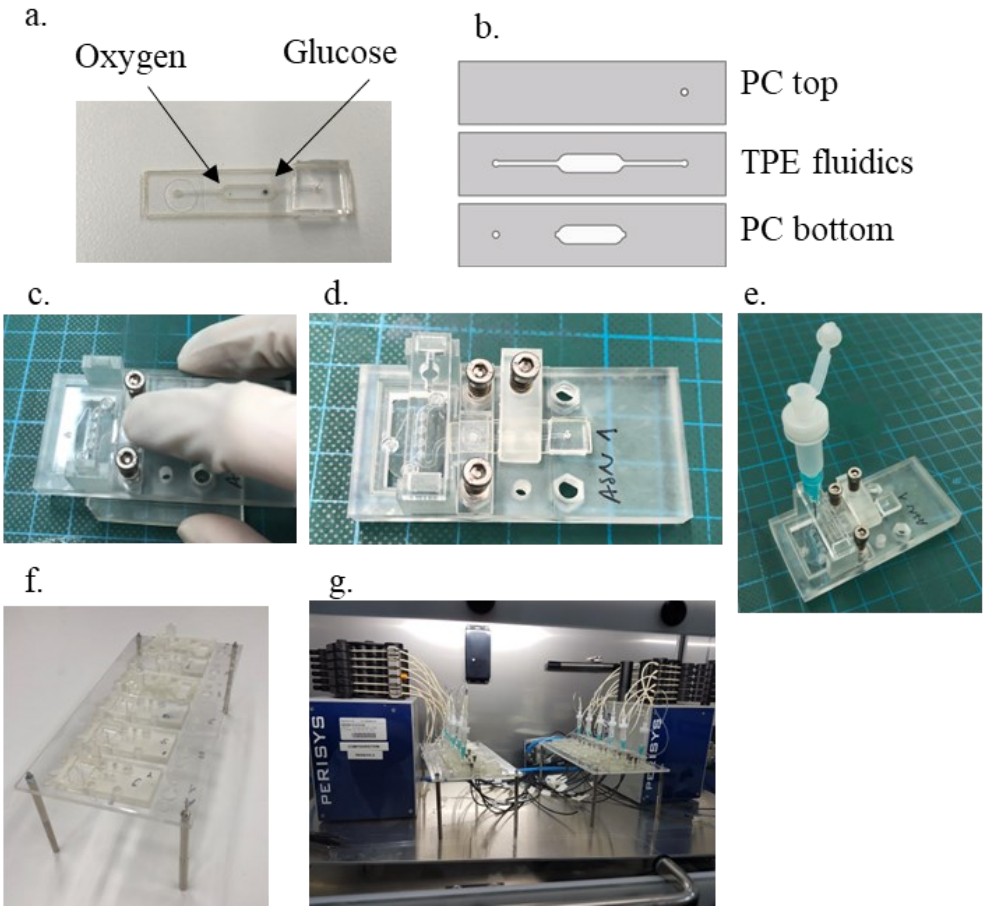

Figure 24: Setup of the 3D printed cassette for recirculation perfusion (a.) Picture of the assembled connection channel showing the oxygen sensor located before the glucose sensor as perfusion proceeds from left to right, (b.) Schematic of the layers and features of the connection channel, (c.) Insertion of the chip into the 3D printed cassette, mounted on the hex nut holder, (d.) Assembled cassette with the chip, connection channel, stylus and reservoir holder, (e.) Assembled cassette with mounted reservoir, (f.) Cassettes mounted onto the cassette holder, (g.) Pictures of the setup in the ALS box with 2 peristaltic pumps, 12 chips and sensor cables connected to the Phasefluorometer

Table 11: Compositions of the calibration solutions, Liver and WAT media (fed and fasted)

Calibration solutions	Liver media	WAT media
I – zero glucose, respective supplemented media	WEM (w/o phenol red, w/o glucose) 0.2% BSA 100 mM Glutamax 5 µg/mL Hydrocortisone 0.1% DMSO <u>Fed:</u> 60 nM insulin 11 mM glucose <u>Fasted:</u> 60 pM insulin 7 mM glucose	DMEM/F12-Ham's (w/o Phenol red, w/o glucose) 0.2% BSA <u>Fed:</u> 60 nM insulin 11 mM glucose <u>Fasted:</u> 60 pM insulin 7 mM glucose
II – 10 mM glucose, respective supplemented media		
III – 20 mM glucose, respective supplemented media		

To compare the sensors with a commercially available glucose detection assay, the sensor resolution, limit of detection and limit of quantification were calculated as –

$$Resolution = \frac{Standard\ deviation\ of\ response}{Slope\ of\ calibration\ curve}$$

$$Limit\ of\ detection\ (LOD) = 3.3 * Resolution$$

$$Limit\ of\ Quantification\ (LOQ) = 10 * Resolution$$

2.8. Chip characterization

2.8.1. Live-staining of cells on-chip

2.8.1.1. Live-dead staining

The viability of cells on chip was assessed by a live/dead-assay with fluorescein diacetate (FDA) and propidium iodide (PI). The chips were flushed with warm PBS+ with gravity-driven flow by placing an empty pipette tip at the media outlet and a pipette tip with 100 µL solution at the media inlet. A solution of 1 µg/mL Hoechst in PBS+ was added to the chip (100 µL) via gravity flow for 20 min in the incubator to allow the live staining of nuclei with Hoechst. Next, a staining solution was prepared comprising of 27 µg/mL FDA and 50 µg/mL PI in PBS+ and flushed into the media channel by gravitational flow. The chips with cells in direct contact with the staining solution (liver, mVECs) were incubated for 5 minutes with the solution, while the WAT-chips were incubated for 25 minutes with the solution to allow staining molecules to diffuse across the membrane and hydrogel to the cells. The media channels were then flushed with PBS+ via gravitational flow and imaged immediately with an inverted fluorescence microscope (Leica DMi8, LEICA Microsystems GmbH, Germany).

2.8.1.2. Cell tracker staining

Cells were stained with Cell Tracker™ Deep Red Dye for live-imaging and tracking during culture on chips. The dye solution was prepared according to the manufacturer's instructions by first preparing a 1 mM stock solution in DMSO, followed by further dilution to 2.5 µM in FCS-free cell culture medium. The endothelial cells were labelled on-chip with the solution by incubating for 45 min in the incubator with the solution via gravity-flow across two pipette tips inserted into the media inlet and outlet. The chips were then connected to push perfusion regime and mounted onto an inverted microscope (Leica DMI8) with an incubation chamber and imaged overnight at 10 min time intervals.

2.8.1.3. CellTox™ Green Cytotoxicity Assay

The CellTox™ Green Cytotoxicity Assay was performed to assess any adverse effect of various media compositions on the adipocyte viability on-chip. The kit was used as recommended, where a 1:1000 dilution of the CellTox™ Green reagent was prepared with the media and perfused across the chip in the push perfusion regime over a period of three days. The chips were imaged in brightfield and fluorescent fields with the Leica DM microscope. To quantify the fluorescence, a region of interest spanning the chamber area was selected and mean grey value quantified for each chamber.

2.8.2. MTS assay on- and off-chip

The CellTiter 96® AQ_{ueous} One Solution Cell Proliferation (MTS) Assay assessed the viability of adipocytes in the WAT-chips or mVECs in 96 well plates exposed to various media

combinations (summarized in the Table 12), and the assay was used as per the manufacturer's protocols.

Table 12: Media compositions of the ECGM, W, 1to1, FullE and FullW medium

	WAT Medium	ECGM Medium	1 to 1 Medium	FullW Medium	FullE Medium
Media components	DMEM/F12-Ham's medium (w/o Phenol red) 1% Pen/strep 10% FCS 10 mM HEPES buffer 0.1 µM Rosiglitazone 60 nM human insulin	ECGM Medium 1% Pen/strep SingleQuot kit comprising - 2% FCS 12 µg/mL ECGS 1 ng/mL bFGF 0.1 mg/mL EGF 1 µg/mL Hydrocortisone	DMEM/F12-Ham's medium (w/o Phenol red) ECGM Medium 1% Pen/strep 6% FCS 5 mM HEPES buffer 0.5 µM Rosiglitazone 30 nM human insulin 6 µg/ mL ECGS 0.5 ng/ mL bFGF 0.05 mg/ mL EGF 0.5 µg/ mL Hydrocortisone	DMEM/F12-Ham's medium (w/o Phenol red) 1% Pen/strep 10% FCS 10 mM HEPES buffer 0.1 µM Rosiglitazone 60 nM human insulin 12 µg/ mL ECGS 1 ng/ mL bFGF 0.1 mg/ mL EGF 1 µg/ mL Hydrocortisone	ECGM Medium 1% Pen/strep 10% FCS 10 mM HEPES buffer 0.1 µM Rosiglitazone 60 nM human insulin 12 µg/ mL ECGS 1 ng/ mL bFGF 0.1 mg/ mL EGF 1 µg/ mL Hydrocortisone
Glucose conc. (mM)	17.48	5.5	11.5	17.48	5.5
FCS %	10%	2%	6%	10%	10%

The MTS reagent was mixed with the media in the ratio 1:6 and the mVECs in well plates were exposed to this media for 2.5 hours. Cell viability was quantified by measuring the absorbance in the plate reader at 490 nm, subtracting the background absorbance value measured in a well with reagent but without cells. The cell viability was quantified every three days over a 15-day period of the experiment. The assay was modified for the perfused WAT-chips, which had been exposed to different media compositions as part of the media optimization experiment for two weeks, with extension tubing connected to the syringe pump. At the end of the experiment, the extension tubing was clamped, and the long inlet tubing and syringe switched with the corresponding media containing the MTS reagent (mixed in the ratio 1:6). Perfusion was started once again at 20 µL/h and 1 hour later, the effluent tubes were changed to sample further effluents (this was taken as t0). After 4 hours, the collected effluent volume was pipetted in triplicates of 25 µL into 3 wells of a 384 well plate (dark wall, clear bottom) and absorbance was measured at 540 nm. For background, the effluent of reagent with media flowing through blank chips without cells was subtracted from the corresponding chip effluent. The values of absorbance from background and from the inlet of the chips were subtracted from the absorbance values of effluents to give the net viability of the adipocytes in the chip.

2.8.3. LDH-Glo™ Cytotoxicity Assay

With the LDH-Glo™ Cytotoxicity Assay, the lactate dehydrogenase in the effluent of the WAT-chip was analysed and compared for the different media compositions perfused across

the WAT-chips. The effluent samples were collected every day and centrifuged at 500 *g* for 10 minutes, and 5 µL of effluent was diluted in 95 µL of LDH storage buffer (10% glycerol, 1% BSA in 200 mM Tris HCl solution at pH 7.3). These solutions were stored at -80°C until assayed. The assay was performed in accordance with manufacturer's protocols, where 12.5 µL of samples were pipetted into an opaque white wall 384 well plate. 12.5 µL LDH solution was added, and the reaction proceeded at RT for 30 minutes, after which luminescence was quantified with a plate reader (Tecan Spark).

2.8.4. Bodipy uptake and release

The functionality of adipocytes in the WAT-chip was assessed by their ability to take up and release fatty acid in real-time. This assay was performed in accordance with previously published reports (Rogal et al., 2020), where the chips were perfused with a 4 µM solution of BODIPY (a fluorescent fatty acid analog) in a push flow regime for 60 min at 80 µL/h. Each chamber of the chips was imaged with a temperature and humidity-controlled spinning disc confocal microscope every 2 min to capture the increase in fluorescence within the lipid droplet as the cells took up the fluorophore. The pump was then switched to pull flow regime and a pipette tip with only plain culture medium (WAT or FullW) was added to the media outlet and pulled across the chip. A reference image was captured for each chamber at t=0 min. ImageJ 1.50i software (National Institute of Health, USA) was used to quantify the fluorescent intensity variations during the uptake and release of the BODIPY dye. The mean gray value of the fluorescence of the individual tissue chambers and the background was measured at each time point, the background levels subtracted from the fluorescent intensities measured per chamber and the offset calculated, setting the fluorescence of t0 to a value of zero A.U. The intensities of each chamber were reported as a percent of the highest recorded intensity within that chamber during the experiment and averaged for the four chambers to report an uptake rate per chip.

2.8.5. Triglyceride and glycerol quantification in effluent

Triglyceride and glycerol content in chip effluents were assessed using the Triglyceride-Glo™ Assay as per manufacturer's instructions. Originally, effluent coming from the chips were centirfuged at 500 *g* for 10 min, pipetted to appropriately labelled 1.5 mL tubes and frozen at -80°C. At the time of the assay, the effluents were thawed and sampled in duplicates of 20 µL into a 384 well plate (opaque white wall). Glycerol lysis solution with (GLS+) and without lipase (GLS-) and glycerol detection reagent (GDR) were prepared and added to the samples and incubated at 37°C for 30 min. Reductase was then added, and an hour later, kinetic enhancer was added to the samples. Lastly, GDR was added to the wells, incubated at RT for 60 min and the luminescence recorded. The samples incubated with GLS+ yielded total glycerol content while the samples with GLS- yielded the free glycerol content. Triglyceride secretion was quantified by subtracting the values of free glycerol from total glycerol content and after a final background subtraction.

2.8.6. Cell fixation, blocking and permeabilization

The adipocytes were fixed on-chip by first flushing with PBS+, followed by 4% phosphate-buffered formaldehyde solution (Roti®- Histofix 4%) for 30 minutes at room temperature by gravity-flow (100 µL). Endothelial cells cocultured in the chip were fixed simultaneously. The

HepaRG™ cells were fixed on chip by first flushing with PBS+, followed by 4% phosphate-buffered formaldehyde solution (Roti®- Histofix 4%) for 10 minutes at room temperature by gravity-flow (100 µL/s). The fixative solutions were washed out three times with PBS+ by gravity flow and the chips could be stored at 4°C until processed further.

In the WAT-chip, the adipocytes were first permeabilized with 0.1% Triton in PBS+ for 20 minutes at RT, followed by blocking with 0.1% Triton in PBS with 10% normal donkey serum for 45 minutes in the media channel. In the liver-chip, the hepatocytes were blocked and permeabilized with 0.1% saponin and 3% normal donkey serum in PBS for 30 min at room temperature in the media channel.

2.8.7. Immunofluorescence staining

Primary antibody solutions were prepared by diluting the appropriate amount of antibody in antibody diluent (0.1% saponin and 3% NDS in PBS) (Table 13). 50 µL of the antibody solution was added to the chips via gravity flow and incubated for 16 hours at 4°C.

Table 13: List of primary antibodies used during experiments with the three cell types

Adipocytes	HepaRG™ cells	mVECs
GLUT-4, Ms (9001, Cell Signaling Technology)	Albumin, Gt (AF3329, R&D System Biotech) GST-α, Gt (GS68, Biomedical Research) E-Cadherin, Gt (AF748, R&D Systems Biotech) CYP3A, Rb (AB1254, Millipore) Glutamine Synethetase, Rb (ab73593, abcam) MRP-2, Rb (4446, Cell Signaling Technology)	VE-Cadherin, Rb (555289, BD Biosciences) CD31, Ms (3528, Cell Signalling Technology)

The cells were then washed with wash solution (0.1% Saponin in PBS for liver, 0.1%Triton in PBS for WAT) three times. Secondary antibodies and DAPI solutions were prepared by diluting the antibodies 1:100 in antibody diluent. Bodipy was also diluted in the secondary Ab solution in a ratio 1:1000, and the 488 secondary Ab was withheld. DAPI or Hoechst were mixed into this solution in the ratio 1:500. This was then added to the chips and incubated for 1 hour in the dark at room temperature. The chips were washed again three times with PBS via gravity flow, and then imaged with the Zeiss widefield, LSM microscope and spinning disc confocal microscope (Table 14).

Table 14: List of filter sets used for the fluorophores on the fluorescence microscope

Fluorophore	Filter set	Excitation	Emission
Alexafluor 488 (A-21202, Invitrogen), Bodipy (D3922; Thermo Fisher Scientific Inc.)	38 (HE)	BP 470/40	BP 525/50
Alexafluor 546 (705-165-147, Jackson ImmunoResearch Labs)	43 (HE)	BP 550/25	BP 605/70
Alexafluor 647 (A10036, Invitrogen)	50	BP 640/30	BP 690/50
DAPI/Hoechst (D1306, Invitrogen)	96 (HE)	BP 390/40	BP 450/40

2.8.8. Periodic Acid and Schiff Reagent (PAS) staining

PAS staining was performed to detect glycogen in fixed HepaRG™ cells in well plates as per the manufacturer's instructions. After rinsing the plates with running tap water for 1 minute, the negative control was prepared by adding 5 mg/mL of amylase solution in 30 mM $CaCl_2$ solution to the cells in one well and incubating for 15 minutes at 37°C. This digested the

glycogen for the negative control, while the other wells were incubated with DI water. Periodic acid solution was then added to each well and incubated for 5 minutes at RT. After rinsing the wells three times over one minute with distilled water, Schiff's reagent was added to each well and incubated for 15 minutes at RT. The wells were then washed over 5 minutes in running tap water. The nuclei were then stained with Hoechst (1 µg/mL in tap water) for 20 minutes at RT, after which fluorescence was measured in a plate reader and imaged with a fluorescence microscope (Zeiss). Measuring the fluorescent intensity of the immunofluorescent and PAS staining was found to be the most quantitatively rigorous and time efficient method of assessing marker expression, as opposed to imaging individual wells (Chawla et al., 2017) (Table 15).

Table 15: Excitation and emission on the fluorescent plate reader to measure PAS staining

	PAS	**Hoechst**
Excitation wavelength	535	360
Emission wavelength	680	465
gain	100	60

2.9. Liver-Sinusoid-on-Chip (LSOC)

2.9.1. Formula derivation of fluidic resistance across the pores in the branched shower concept

The radii of the pores were calculated using resistance equations, ensuring that the corresponding resistance of each pore along the branch was the same, and an equal flow of fluid existed across all pores (Figure 25). The fluidic channel had a rectangular cross section, and the pore was treated as a cylinder for the resistance calculations. The resistance of a channel of rectangular cross section of height h, length l and width w where l >> w and w >> h and µ as dynamic viscosity of the fluid is

$$R_{rectangular} = \frac{1}{1 - 0.63(\frac{h}{w})} \frac{12\mu l}{h^3 w}$$

The resistance of a cylindrical channel with diameter d and length l here l >> d is

$$R_{cylindrical} = \frac{128\mu l}{\pi d^4}$$

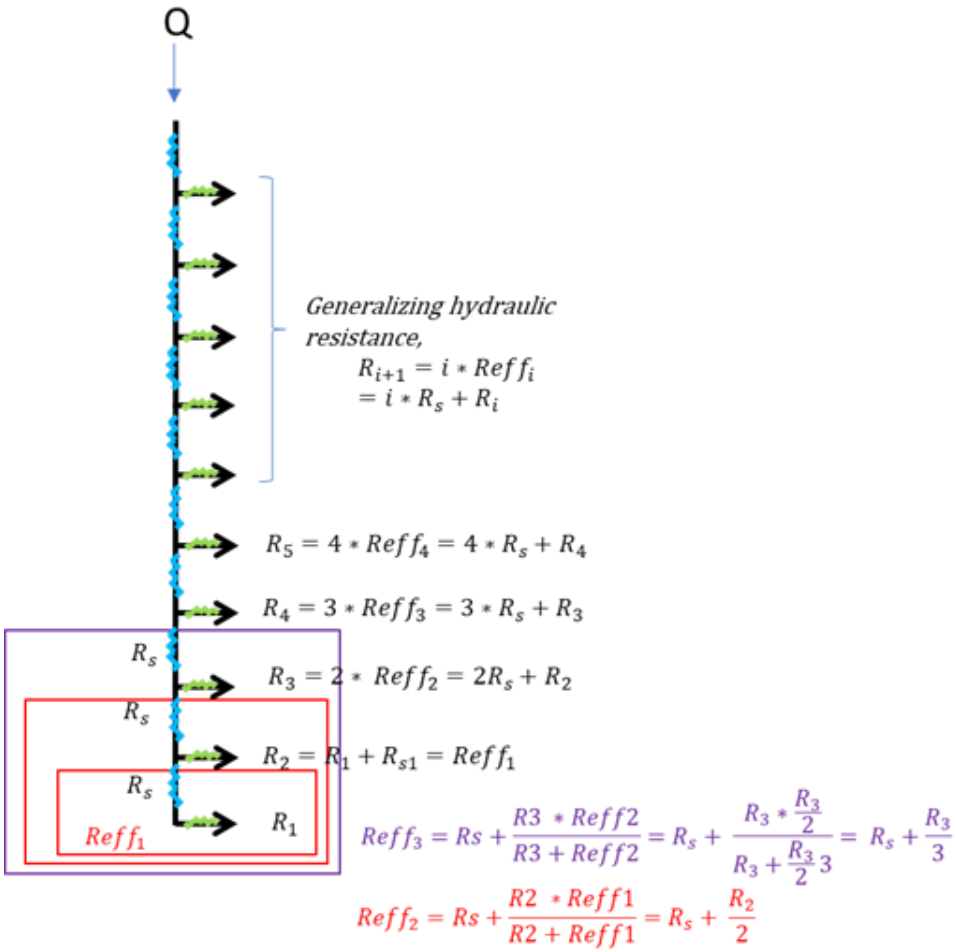

Figure 25: Derivation of pore resistance across a shower branch

2.9.2. Fabrication of the LSOC

The fabrication of the liver Biochip (LB) was performed by Dynamic42 GmbH in Jena, Germany where the chip body was made of injection molded polybutyl terephthalate (PBT) with a 50 µm PC foil laser welded on the bottom of the chip (LPKF). An 8 µm pore PET membrane was laser welded into the membrane cavity and the ShowerTop laser welded onto the top of the chip. The idea was to provide a gradient of dissolved species in the media as it flowed from the shower top, mixing with the flow from the media channel and exposing the hepatocytes in the Biochip to a gradient of species.

Experiments were performed on two versions of the LB and the ShowerTop integrated onto the chips. Version BC002 of the LB had a hexagonal tissue chamber with culture volume of 100 µL while BC005 had a straight channel architecture for the tissue channel and a culture volume of 55 µL, requiring fewer cells in the tissue chamber and hence a smaller perfusion volume. The ShowerTop comprised three lasercut layers – the 50 µm PC pore layer, 250 µm TPE shower channel and 175 µm PC top (Figure 26.a). Pores of approximate diameter 200 µm were lasercut is the PC pore layer, and the other layers were lasercut and cleaned (sub-section 2.2.1.1). The three layers were arranged on top of eachother with the lowest being the pore layer, placed between glass slides with a 2 mm thick cured PDMS spacer to evenly distribute pressure, clamped with steel foldback clamps and bonded in the oven with the same ramp

protocol as for the liver-chips (sub-section 2.3.2.2). The assembled ShowerTops were then laser welded onto the liver Biochip by Dynamic42 GmbH. The ShowerTops were lined with UV glue (NOA 81, Norland Adhesives) by application of a thin line of glue outside the ShowerTop with a 1 mL syringe and cured under a UV lamp (UWAVE) at 99% intensity for 10 minutes. Finally, a PET female mini Luer connector (Darwin Microfluidics, France) was glued onto the top port to enable simple connections. To achieve this, the 2-part UHU glue (UHU, Germany) was used where in the first step, the solvent marker was applied onto both faces to be bonded. Next, the connector was positioned onto the top port and the UHU glue was dropped at the boundary with the help of a fine-dispenser (Ultimus I, Nordson EFD) and a ¼'' (ID 0.09 mm) dosing needle (GONANO Dosiertechnik GmbH) (Figure 26.c).

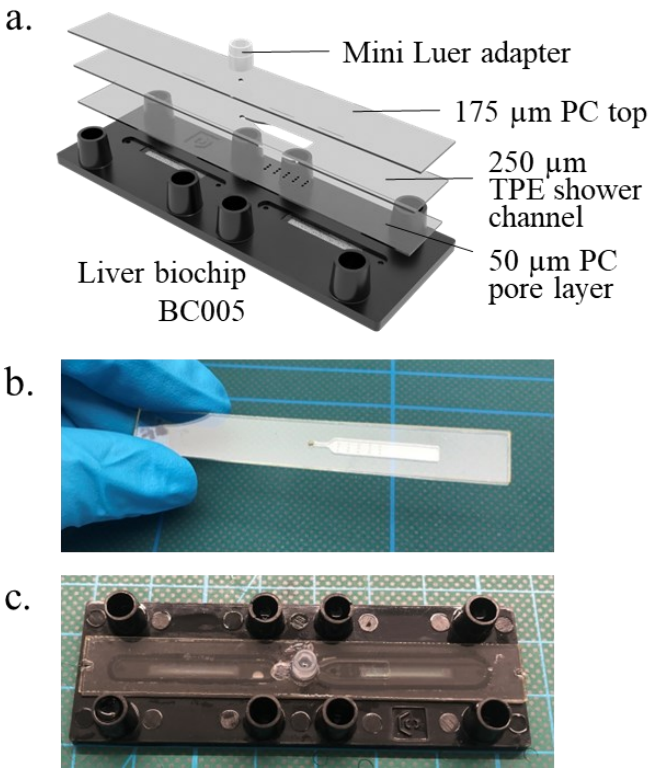

Figure 26: Design and fabrication of the LSOC. (a.) Schematic of the layers of the Shower Top and alignment onto the LB, (b.) Picture of the assembled shower top, (c.) Picture of the assembled chip, with luer connector and the shower top.

2.9.3. Preparation of the LSOC for perfusion

Connections with the LSOC were made with Luer adapters (M3003, MoBiTec). Tubing with inner diameter 0.51 mm (SC0731, PharmMed BPT, Ismatec) connected a 21G blunt needle tip with the luer adapter. The shower channel tubing consisted of a similar setup with the 21 G blunt needle tip, 0.51 mm ID tubing and a male mini luer connector to interface with the female mini luer connector on the LSOC. Two sets of the shower tubing were prepared, to enable a time-controlled introduction of the solution to create the gradient on-chip. The outlet tubing was built by connecting the 0.51 mm ID tubing with a luer adapter.

These tubings were autoclaved before use in the experiment. At the start of an experiment, the chips were plasma treated and first primed with 70% ethanol with a P1000 pipette starting with

the shower channel then the media channel inlet (subsection 2.7.1). This was immediately followed by flushing with PBS and the chip was then placed into a conical tube filled with 25 mL PBS with the shower channel facing towards the cap. The tube was centrifuged at 200 *g* for 10 minutes to remove any bubbles from within the system.

2.9.4. Zonation of FITC-Dextran across the LSOC

To demonstrate the principle of zonation, a solution of FITC-dextran was perfused across the shower channel such that it mixed with the media channel and the zonation of fluorescent signal could be analyzed by fluorescent microscopy (Figure 27.a). At the start of connection, the tissue channel of the primed LSOC was blocked with male luer plugs (CS-10000230, Darwin Microfluidics). A solution of 1 mg/mL of FITC Dextran (FD4, Merck KGaA) was prepared in PBS. One set of tubing was loaded with the FITC solution for perfusing into the shower channel, while another set of tubing was loaded with PBS for perfusing across the media channel. The primed chip was first connected to the media channel inlet, after which the media outlet tubing connected the chip to a 15 mL centrifuge tube as a reservoir outlet. The media channel syringe was mounted onto a syringe pump. The two syringes for the shower channel were loaded onto a separate syringe pump, and the tubing filled with PBS connected to the shower channel at first. The perfusion setup was mounted onto a spinning disc microscope (Zeiss), programmed to obtain tile scan images of 4 columns with 10 tiles each, running across four regions perpendicular to the direction of flow (Figure 27.b). The pumps were programmed to perfuse PBS at 50 µL/min across the media channel and FITC solution at 5 µL/min across the shower channel. At a specific time (t0), the shower inlet tubing was switched to enable the perfusion of FITC-dextran solution across the shower channel. Images were obtained in the brightfield and FITC channels at t0 and when the experiment was terminated, after 160 minutes. The tiles per column were stitched together and mean gray values obtained for each column.

2.9.5. Zonation of oxygen across the LSOC

Another demonstration of zonation was by flushing an oxygen scavenging solution of sodium sulfite across the shower channel, which scavenged oxygen from the PBS perfused across the media channel. This zonation of oxygen could be observed by an oxygen sensor embedded into the tissue channel. For this, the primed chips were placed in a petri dish with a PBS-filled 15 mL conical tube cap and equilibrated to 37°C in the incubator. OXNANO beads (Pyroscience GmbH) were resuspended in sterile miliQ water as per the manufacturer's instructions, to obtain a stock of 10 mg/mL. An oxygen sensing gel solution in MiliQ water was prepared on ice with the following components – 10% OXNANO bead stock, 10% of 10x PBS, 6% 0.1M NaOH solution, 30% of bovine Collagen I solution (10 mg/mL stock Fibricol™, Advanced Biomatrix, 3 mg/mL final concentration). The pH was checked with pH indicator strips to ensure a qualitative value between 7 and 7.5. 150 µL of the gel was injected into the tissue channel below the membrane and immediately plugged with male luer plugs (CS-10000230, Darwin Microfluidics) (Figure 27.c). Care was taken not to introduce bubbles into the gel mixture during preparation and injection, and the gel was allowed to crosslink in the incubator for 1 hour. The crosslinked gel was then inspected for bubbles and discarded if there were any present, due to future interference with the sensor experiment. For the experiment, one set of tubing was prepared for the media inlet and two for the shower inlet (section 2.7.1). A solution

of 40 mg/mL of sodium sulfite solution was prepared 20 min before the start of the experiment and the media inlet tubing was loaded with PBS and syringe loaded onto a syringe pump. The shower inlet tubing was loaded with the Na_2SO_3 solution, and the shower inlet was initially plugged with a male mini-luer plug (CS-1000003, Darwin Microfluidics) (Figure 27.d).

A sensor cable holder was fabricated with a rectangular PDMS piece cut in the size of the chip of height 5 mm with three holes punched with a 4 mm biopsy punch. The sensor cables were fed into the holes and secured onto a conical tube rack. The chip was mounted onto the sensor fiber holder first away from the sensors to perform a background calibration. Then, the chip was positioned such that the tissue channel containing the sensor gel aligned exactly on top of the three sensor cables, to enable capturing oxygen concentrations at three different points along the length of the tissue channel. The sensor cables were connected to the Phasefluorometer (Pyroscience GmbH), set to capture readouts every 5 minutes over a six-hour duration of the experiment.

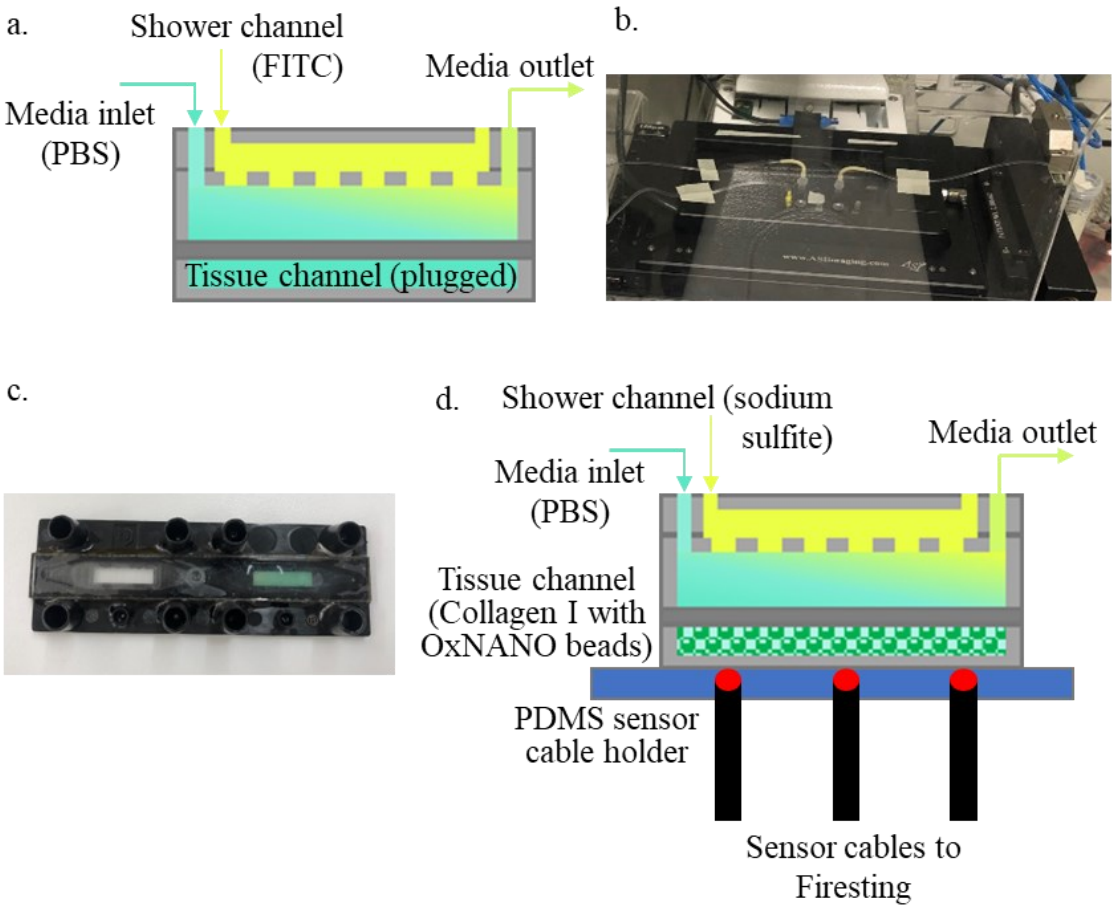

Figure 27: Testing zonation of media components with the LSOC. (a.) Schematic of the zonation setup for FITC-dextran zonation across the LB, (b.) Picture of the acquisition setup on the spinning disc microscope, (c.) Picture of LSOC with oxygen sensor-laden hydrogel injected into the tissue channel, (d.) Schematic of the zonation setup for oxygen zonation across the LB.

2.9.6. Effect of zonation parameters on HepaRG™ cells in well-plates

The effect of concentrations of media components such as glucose, insulin and glucagon was tested on the HepaRG™ cells in well plates. The conditions were chosen based on a publication

by Greco *et al.* (Greco et al., 1979) and cell culture and experimental protocols were developed to reprogram the sensitivity of the HepaRG™ cells. Differentiated HepaRG™ cells were seeded at a density of 2500 cells/cm^2 (0.1 million cells/ well) into dark-walled clear bottom 96 well plates in seeding medium (MM with 0.1% DMSO), without antibiotics. The medium was changed every 2 days and cells were maintained until confluent (approx. 5 days). On day 5, starvation was induced with starvation medium (WEM medium without phenol red, 4.55 mM glucose and 0.2% BSA) for three days. At the start of the experiment, the cells were exposed to varying concentrations of glucose, insulin, glucagon, and ammonium chloride (Table 16).

Table 16: Description of media component concentrations for the zonation experiments in well plates

Description of condition	ID#	Zone	Insulin [nM]	Glucagon [nM]	Glucose [mM]	NH_4Cl [mM]
in vivo conc.	1	Zone 1	60	0.070	5.550	-
	2	Zone 2	39	0.049	5.345	-
	3	Zone 3	18	0.028	5.139	-
Effect of glucose variation	7	Zone 1	100	0.000	7.000	-
	8	Zone 2	100	0.000	11.000	-
	9	Zone 3	100	0.000	17.000	-
Control for HepaRG™	20	Control FED	860	-	11	-
	21	Control FASTED	-	100	4.55	-
in vivo conc., ammonia cycle activated	1*	Zone 1-3	60	0.07	5.55	3
	7*	Zone 1-3	100	0.000	7.000	3
Control for HepaRG™, ammonia cycle activated	20*	Control FED-3	860	-	11	3
	21*	Control FASTED-3	-	100	4.55	3

A 1 mg/mL stock solution of glucagon was prepared in 0.05 M acetic acid and diluted for the experiment. At the end of the experiment, effluent was sampled, and the cells fixed and stained. PAS staining or immunofluorescence staining was performed on the HepaRG™ cells (sub-sections 2.8.7 and 2.8.7 respectively). The staining was characterized on the plate reader (Tecan Spark) (Table 17) –

Table 17: Excitation wavelengths for the immunofluorescence quantified on the plate reader

Fluorophore	Excitation [nm]	Emission [nm]
Bodipy	485	535
Alexa Fluor 546	535	590
Alexa Fluor 647	620	680
Hoechst	360	465

The data was normalized by dividing the fluorescence value per channel by the nuclei fluorescence. Then, comparisons were made of the fold change of expression of markers for zone 3 compared to zone 1 for each media condition.

2.10. Computational modeling

Finite element models were used to simulate fluid flow in the WAT, liver-chips, chip connections and in the Liver-Sinusoid-on-Chip by finite element method (FEM; COMSOL Multiphysics® v5.5, COMSOL). The modules used were laminar fluid flow, free and porous media flow and transport of diluted species.

For the WAT- and liver-chips, a time dependent study of 'Transport of Diluted Species in Porous Media' was used to study the diffusive transport of a dissolved media component perfused into the media channel and diffusing across the membrane. The membrane was assumed to be a porous region and hydraulic permeability (κ) and porosity (ε) calculated as 5.27×10^{-14} m^2 and 0.0785 respectively (Loskill et al., 2017). These values were calculated for a 5 µm pore size membrane of pore density 400,000 pores/cm^2. The Navier–Stokes equation governed the flow in the free region, and the Brinkman equation in the porous region, with the assumption of a water-like medium and a fully developed flow at the inlet face of the media channel. No-slip boundary conditions were defined, and a constant zero Pa relative pressure at the outlet face of the media channel. A fluid flow rate was chosen as 20 µL/h across the media channel. A steady inflow concentration of 1 M was chosen, and a diffusion coefficient (D) of 10^{-9} m^2/s was chosen to model biological molecules in water.

Oxygen consumption differences were quantified comparing two different heights of the tissue channel in the liver-chip. The top surface of the membrane was chosen as a reacting surface with a rate of oxygen consumption of -4.3×10^{-3} nmol s^{-1} for the cell number in chip. With a diffusion coefficient of 3.15×10^{-5} cm^2s^{-1} (Brischwein et al., 2009), an inflow oxygen concentration of 0.2 mM was selected at the chip ports and as an initial value for the system. For a tissue channel of height 250 µm with an inflow of 20 µL/h, the variation of oxygen concentration along the channel length was compared to a tissue height of 750 µm, where additional inflows of 60 and 100 µL/h were also evaluated.

For the LSOC, the shower inlet concentrations and diffusion coefficients corresponding to a physiological range of the dissolved species at the base of the channel have been summarized in Table 18.

Table 18: Simulated concentrations of dissolved species in the shower inlet and media outlet

Species	Shower inlet [mM]	Diffusion coefficient [m^2/s]	Reference
Glucagon	1.44×10^{-3}	1.5×10^{-10}	(Buladi et al., 1996)
Glucose	55	9.1×10^{-10}	
Insulin	11.1×10^{-3}	1.5×10^{-10}	
Oxygen	0.2	3.15×10^{-9}	(Brischwein et al., 2009)

A computational model was set up to study the flow profiles of various designs of the immune cell holder. A stationary porous media flow model was set up, in a 2D model with radial symmetry. The angular velocity in radian/s was calculated as

$$\Omega = \frac{2\pi}{60}\omega$$

Where ω is the revolutions per minute (rpm). A disc impeller model was created by designing the outline of a bar magnet and projecting it via the axial symmetry option about the central axis of the mixer. A pressure point constraint was selected at the interface of the liquid level and the wall of the immune cell mixer. A moving wall boundary condition was provided at the outline of the bar magnet, to rotate with the angular velocity **Ω**.

2.11. Development of the immune cell reservoir

2.11.1. Fabrication of the holder and components

The immune cell holder was designed to interface with a fluidic platform and to support the long-term culture and perfusion of immune cells across MOCs. Components for the holder were fabricated in collaboration with Mr. Martin Gaier at the Natural and Medical Sciences Institute, Reutlingen, Germany. Two mixing mechanisms were fabricated (Table 19), the parts for which were either 3D printed or lasercut by me (Form3+, Formlabs) or turned on the turning machine in the workshop of the NMI by Mr. Martin Gaier (Weiler Condor) (Table 20).

Table 19: Components of the mixing mechanisms of the immune cell reservoir

Common components	
Outer cylinder - Main mixing chamber, enclosing the components	
Inner cylinder - Cell chamber, holding the cell suspension	
Cannula legs - Support the inner cylinder, connect to the MOC platform	
Membrane - Confined the cells within the inner cylinder	
Silicone base - Interfaced with the MOC	
Bayonet fastening mechanism - To support the immune cell holder	
Voltmeter – to modulate the motor power	
Motorized impeller holder components	**Magnetic impeller holder components**
Top membrane fastening ring – had high walls to guide the flow to the impeller	Bottom membrane fastening ring and base wall mount – high walls below the inner cylinder for flow focusing
Impeller head attached to a motor via a shaft	Impeller attached to a disc magnet – to generate upward flow
Motor and motor holder – to support and drive the impeller to generate an upward flow	Magnetic stirrer mounted on a computer fan – to drive the inner magnet
Shaft seal – to maintain a water-tight system	Silicone top lid – to seal the system shut

Table 20: Summary of parts of the immune cell holder and manufacturer details

Part	**Material**	**Fabrication method**	**Manufacturer**
Outer cylinder	PMMA	Turning	KTK GmbH, PMMA extruded hollow tube, 502424
Inner cylinder	PMMA	Turning	Reiff GmbH, PMMA extruded cylinder, 9735448
Membrane	8 um pore PET	Lasercutting	It4ip, ipCellCulture
Cell chamber rings	Polyethylene	Turning	Reiff GmbH, PE1000
Silicone base	Silicone rubber	Molded out of a PTFE form	SiliTech AG, Bluesil RTV 3428
Bayonet fastener and ring	Clear resin	3D printed	Formlabs
Impeller	Clear resin	3D printed	Formlabs

Motor holder	High polymerization polyvinyl chloride	Turning	Hildi GmbH, HPVCR070GR
Base wall mount	Clear resin	3D printed	Formlabs

2.11.2. Flow test setup for endotoxin tests

The setup for the magnetic impeller holder was used to run this experiment, quantifying the endotoxins in the system and the effect of sodium hydroxide treatment on these endotoxin levels. The components of the holder and fluidic interface were wiped with a Kimtech wipe soaked in 70% ethanol and placed in a sterile workbench. They were then exposed to UV within the bench for 30 min before assembly and connected to push perfusion of PBS. Effluent was collected over 24 hours for a flowrate of 100 µL/h. The reservoir setup was then disconnected from the pump, and pipette tips containing a 1 M solution of NaOH filled into the cell chamber. The mixing chamber was washed by filling with NaOH. The setup was left static for one hour as a general recommended treatment to purge a system of endotoxins, after which the setup was washed three times with endotoxin-free water. The setup was perfused overnight, and effluent collected. The collected effluents were stored at 4°C until the endotoxin assay (A39552, Thermo Fisher) was performed, according to the manufacturer's instructions, immediately upon termination of the experiment. Briefly, the samples and endotoxin standard curve solutions were pipetted into a 96 well plate maintained at 37°C on a heating block. Amebocyte lysate reagent was added to the wells and incubated for 10 minutes, after which the chromogenic substrate was added to the well plate. After 6 min, the reaction was stopped with 25% acetic acid and absorbance read at 405 nm.

2.12. Image processing and statistical analysis

Fiji [Image J version 1.53c] was utilized to adjust brightness and contrast of images, to create maximum intensity projections of z-stacks and to insert scale bars. Fluorescent intensity was measured by calculated mean gray values, also performed using Fiji. GraphPad Prism version 9.5.1 for Windows was used to analyze effluent-based assays, generate standard curves and graphs, and perform statistical significance testing. Bar graphs are represented as average values ± SEM (standard error of means) unless stated otherwise and the sample size (n) representing technical and biological replicates is detailed in each figure caption. To test statistically significant differences between two groups of samples, one-way or two-way ANOVAs were performed. The p values are denoted in every figure caption where specified. To generate standard curves of glucose, lactate, and glycerol/triglyceride concentrations linear regression was used.

3. Results

3.1. Developing connection strategies for OoCs

An ideal MOC platform allows for a robust, flexible, and reversible connection of the OoCs via their vascularized media channel. The chips are either integrated directly onto or easily plugged into the platform, with minimal dead volume to enable quick response times to stimuli. The platform should be constructed out of minimally absorbing materials and allow for the integration of sensors, for the study of cell culture parameters in real-time. To this end, the connection approaches for two organ-chips were compared, to select the ideal approach given certain design criteria. Mechanisms of pressure application to secure the organ-chip connection and mechanisms of leak-free and robust world-to-chip connection strategies were explored, and characterized, taking the case of connecting two metabolising organ-chips, the white adipose and liver-chips.

3.1.1. Approaches for the connection of two organ-chips

Design criteria were studied after observing the requirements of the state of the art in literature (Introduction section). An optimal connection strategy accounts for criteria such as the ease of platform design and fabrication, seeding timing and flexibility, dead volumes, ease of sensor integration, total system size and most importantly, the possibility of a vascularized interface. The three following approaches to multi-organ connection were explored (Figure 28):

i. The ***inbuilt connection approach*** involves tissue channels integrated onto the same chip with a common media being perfused across the two tissues. Here, the tissue layers, membranes and media channels for both OoCs are integrated into the same chip with a fluidic connection between the two tissues.

ii. The ***modular contact approach*** allows two independently fabricated chips, which can be injected with cells and cultured separately and connected flexibly in time, by directly stacking the chips on top of each other. One chip is stacked on 'top' while the other remains at the 'bottom', with a gasket inserted in the middle, a ring of cushioning material to provide uniformly distributed pressure at the site of connection. This pressure can be applied either by magnets or screws. Flow would proceed from the media channel of one chip, across the gasket to the other chip.

iii. The ***systemic connection approach*** involves the two organ-chips inserted into a fluidic interface containing the connection fluidics to interconnect the inserted organ-chips. The two chips have the same spatial alignment of ports, are cultured with cell separately, and then plugged into the fluidic interface via gaskets. Media is perfused into the fluidic interface, across Chip 1, through the fluidic interface to Chip 2 and out back through the fluidic interface.

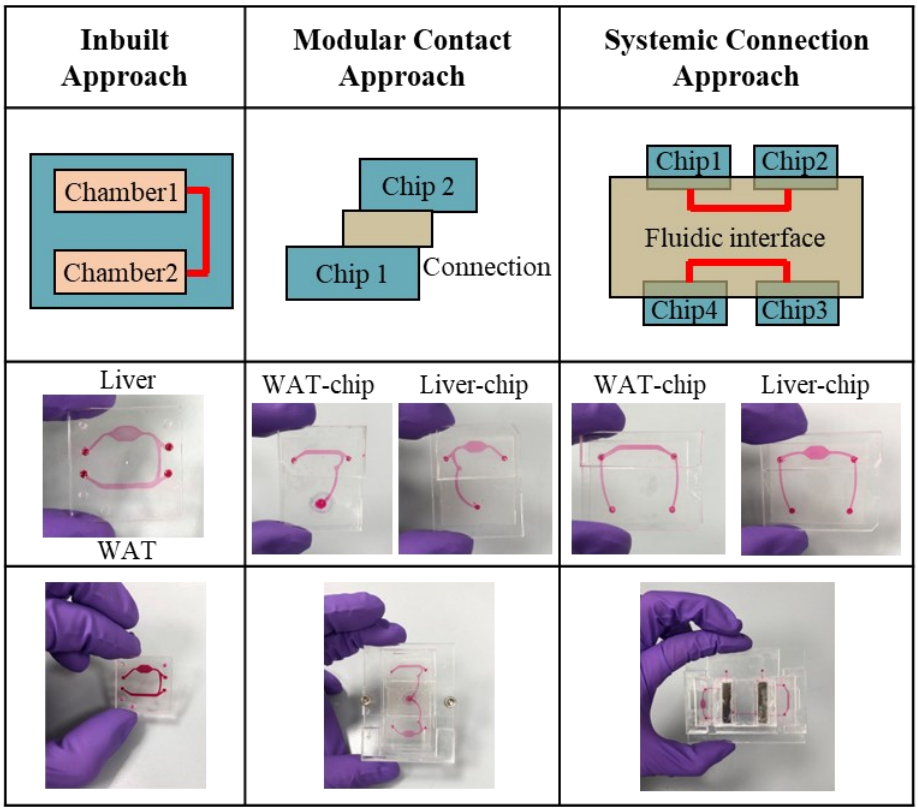

Figure 28: Approaches for vascular connection of organ-chips (representative pictures of chips with colored water in the media channel connections). As an example, for the modular contact approach, the liver-chip was the upper chip, stacked onto the WAT-chip as the lower chip.

3.1.1.1. Design and fabrication of the three connection approaches

The chips were designed in CorelCAD (Corel™) and the proof-of-concept testing was performed with chips containing only the media channel and membrane, with the culture of endothelial cells. The inbuilt connection approach connected two tissue chips, designed based on previously established designs of the WAT-chip (Rogal et al., 2020) and the liver-chip (Rennert et al., 2015). The relative tissue-volume ratio for visceral fat to liver as per physiological values was calculated as 3.12:1 (Chan et al., 2006; S. Jang et al., 2011; Mubbunu et al., 2018). The modular and systemic connection approaches were designed during supervision of the master's thesis of Jillian Gamboa where the media channel structures for the WAT- and liver-chips matched that of the inbuilt connection approach (Figure 29).

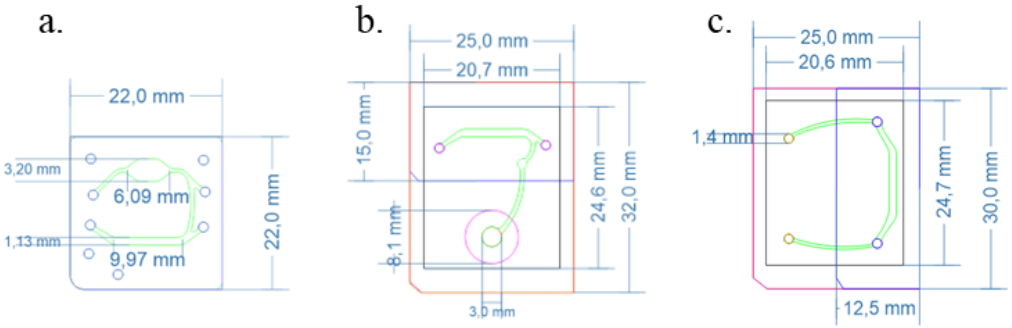

Figure 29:Design and dimensions of chips in the three connection approaches (a.) The Inbuilt connection approach had WAT and liver media channels (green) on the same chip, (b.) The media

channel for the WAT-chip (green) for the modular contact connection approach, with a gasket holder layer (magenta at channel outlet), (c.) The media channel for the WAT-chip (green) for the systemic connection approach.

The modular contact WAT-chip was the bottom chip, with the liver-chip stacked on top. The liver-chip had a connection port facing downwards, and flow proceeded from the WAT chip, up to the liver via the gasket inserted in between. The WAT- and liver-chips in the systemic connection approach both had ports facing downwards, so that they could be placed on top of a fluidic interface which contained the fluidics to connect the two chips.

3.1.1.2. mVEC injection and culture in the connection approach chips

Experiments of cell seeding densities and initial perfusion tests were performed with mVECs in the inbuilt connection approach setup (Table 21). These tests involved iterations in cell injection strategies (single or double injections), cell densities and cell volumes during injection, and ramping strategies during perfusion. Experiments with the mVECs established a seeding density of 6 million cells/mL and a volume of 15 µL per chip to achieve a confluent monolayer after 24 hr of attachment time. A volume of 10 µL led to inconsistencies in seeding densities, with gradients of coverage across the length of the media channel of the second organ-chip. Thus, this volume was increased to 15 µL to ensure the minimal number of cells per chip needed to ensure a fully confluent monolayer across the media channel. An additional observation was that the cells were washed away upon connection to perfusion if they did not form a confluent monolayer before connection. This resulted in the reduced coverage in the lower seeding density cases after connection to perfusion.

Table 21:Cell injection study of endothelial cells into the connection chips

Cell seeding density	Injection volume (µL)	Results after 24 hours	Reduced cell coverage upon perfusion?
2 million cells/ mL	20 µL	40% confluency	Yes
4 million cells/ mL	10 µL	80% confluency	Yes
6 million cells/ mL	10 µL	80% confluency	Yes
6 million cells/ mL	15 µL	100% confluency	Cell coverage maintained
8 million cells/ mL	15 µL	>100% confluency	Cell coverage maintained

After coating the chips with Collagen I, a series of steps were followed to facilitate chip connection and mVEC seeding. In the inbuilt chip case, the seeding strategy involved plugging one set of ports, namely the WAT media outlet and liver media inlet, and then injecting the mVECS across the chip (Figure 30.a). The cells were seeding and maintained static with daily media replenishment via pipette tips at the inlets and outlets until the cells formed a confluent monolayer. In the first instance, the cells were stained with cell tracker (Thermo Fisher) and images obtained before connection (Figure 30.b). In the case of the modular connection approach, the cell injection strategy involved first connecting the chips and then injecting the cells to yield a uniform endothelial cell coverage before connection to perfusion (Figure 30.c). In the case of the systemic connection approach, the endothelial cells were first injected into the chips, after which the chips were connected to the fluidic interface upon the achievement of a confluent monolayer of endothelial cells (Figure 30.d). Cells were allowed to proliferate over a period of two days before connection and initiation of perfusion (Figure 30.e).

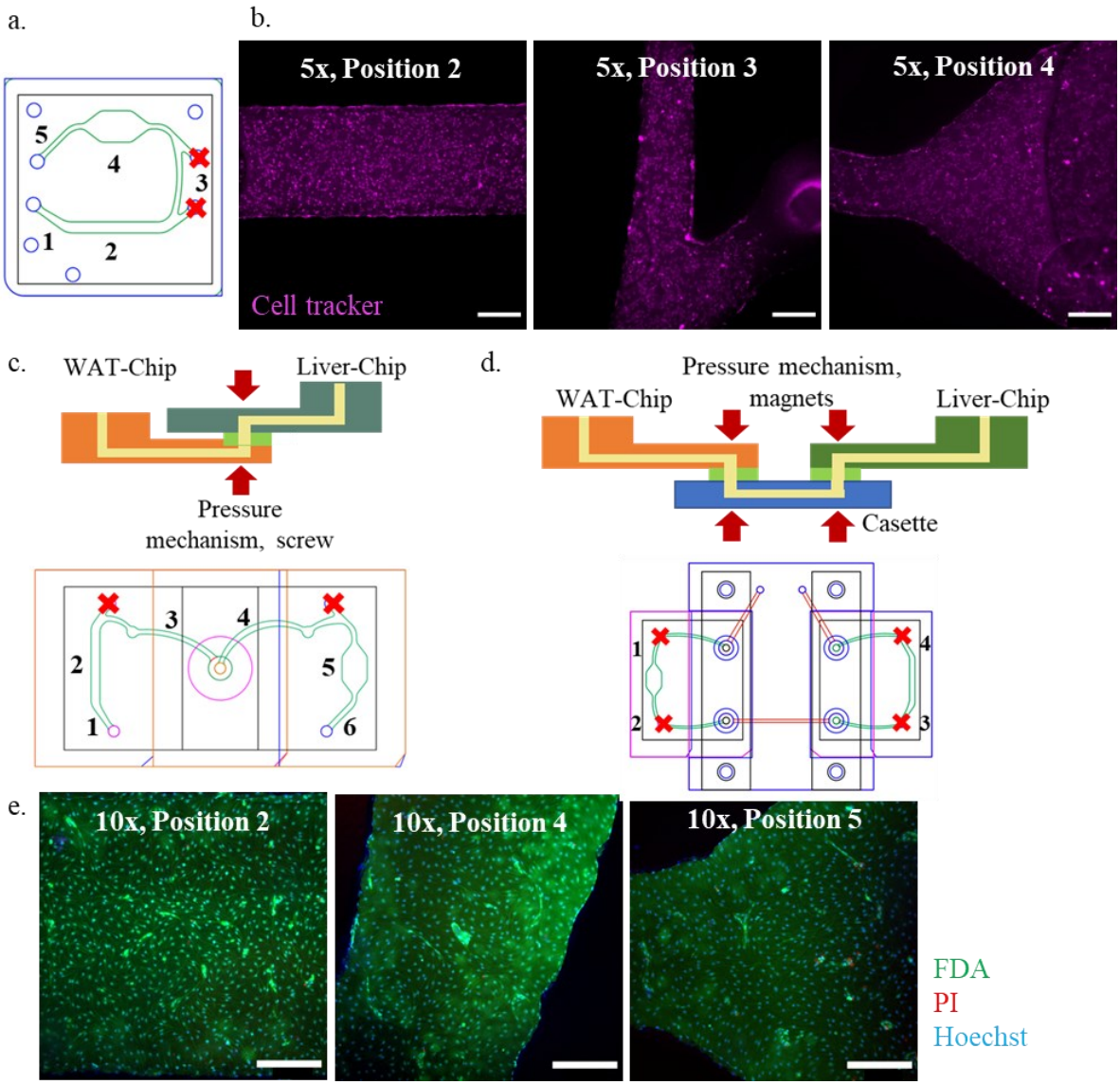

Figure 30: Endothelial cell injection strategies for the connection approaches. (a.) Schematic of inbuilt chip with plugs (red) at the media outlets and cell injection from position number 1 to 5, (b.) Fluorescent images on day 2 of the confluent monolayer of endothelial cells in the channels at position 2,3,4 (cells stained in Celltracker® deep red, scalebar: 500 µm) (c.) Schematic of modular connection, with the liver-chip stacked on top of the WAT-chip, and cell injection proceeded from position 1 to 6, (d.) Schematic of systemic connection, with cell injection taking place in each chip separately, but once connected, perfused from position 1 to 4, (e.) Representative fluorescent images of live-dead staining (FDA in green, PI in red, Nuclei in blue) of the positions 2,4,5 in the modular connection system (Scalebar: 300 µm).

A push perfusion regime was established by ramping the flowrate from 5 to 40 µL/h by doubling every two hours. Upon three days of perfusion of the system, the coverage of cells in the first chip seemed to have diminished compared to the second downstream chip in all cases of the connection. Representative live/dead images obtained at various points along the chips in the modular connection (Figure 31.a) approach showed that from the WAT to liver perfusion, the WAT-chips had lower cell coverage compared to the maintenance of the monolayer at the liver-chips (Figure 31.b), and vice versa when the direction perfusion was reversed (Figure 31.c).

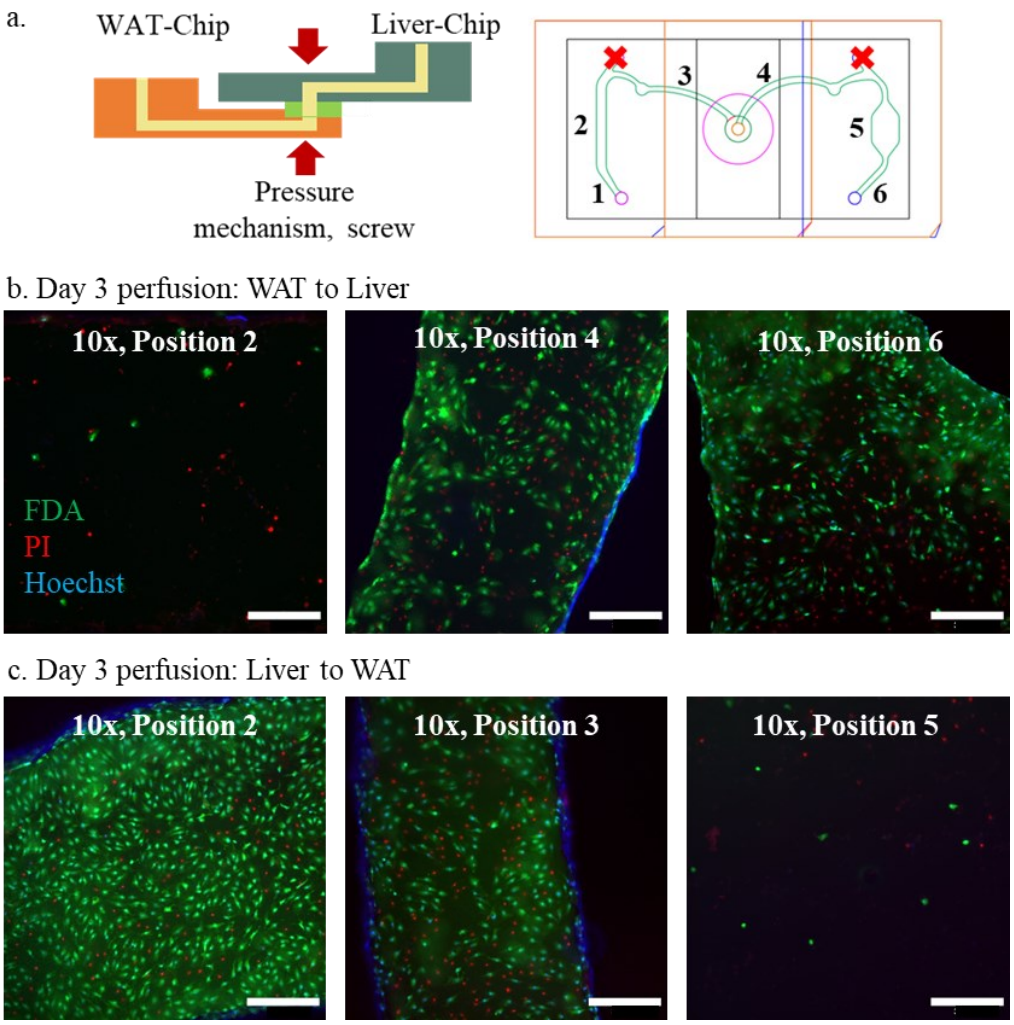

Figure 31: Effect of media flow direction on cell coverage. (a.) Schematic and definition of positions at WAT- and liver-chips in the modular connection approach, (b.) Live-dead images of positions 2,4,6 on day 3 indicating endothelial cell coverage with perfusion from WAT to liver-chip, (c.) Live-dead images of positions 2,3,5 on day 3 indicating endothelial cell coverage with perfusion from liver to WAT-chip. (Scalebars: 300 µm).

3.1.1.3. Feature comparison of the three connection approaches

In an attempt to find the optimal connection approach for the application of connecting the WAT- and liver-chips, the three connection approaches were compared given the design criteria for the construction of a robust, compact, and flexible system with minimal dead volume, quick turnaround for any organ-chip connection, sensor integration capability and ease of handling (Table 22). Scoring proceeded based on two aspects: The priority of the criteria or the influence of that criteria on the success of the experiment, where priority 1 was the most important and 3 is the least important. The second aspect was the ease of integration of a feature (Ease), where a score of 1 for the easiest to integrate and 3 for the most difficult. The two scores were multiplied to obtain a weighted score for various phases of chip handling during an experiment.

The MOC design and fabrication phase considered the ease of construction of individual chips, overall size of the setup, requirements for additional accessory components. The chip culture phase considered the ease of degassing each of the fluidics and components of the MOC system, in addition to cell injection. Here, for the systemic approach, both chips had the same overall layout whereas in the inbuilt approach, the chip shape varied with the tissues being connected. While a base accessory is not required for the inbuilt or modular system, a fluidic interface is required for the systemic approach. Cell injection and culture times could vary depending on the cell type and this could be different for the inbuilt approach, requiring a specific culture schedule based on the study being performed. For the systemic and modular approaches, it is possible to inject cells and culture the chips separately before connection. The chip connection and perfusion phase consider the possibility of leakage between the chips during perfusion, dead volume, sensor integration possibilities for real-time tissue monitoring and the possibility of tissue retrieval after the experiment. Since the inbuilt approach involves a direct connection between the tissue media channels, the chance of leakage between the chips is minimal compared to the modular and systemic approaches where the chips are placed in physical contact with each other or the fluidic interface. This also makes dead volume for the inbuilt system minimal. Finally, the functional assays phase interrogated the live imaging and sampling possibilities between the chips during culture. Sampling reservoirs would need to be designed into the inbuilt system, whereas sampling switches could be integrated into the modular or system approaches in a relatively flexible fashion.

Overall, the systemic approach received the lowest score of 39, while the inbuilt system received the highest score of 49. The modular system was scored 45, indicating that for an experiment to connect two different organ chips in a robust and flexible manner with many integrated capabilities for real-time analysis and sample acquisition, the systemic and modular approaches are preferred to the inbuilt approach.

Table 22: Weighted assessment and comparison of the three connection approaches

				Inbuilt approach			Modular approach			Systemic approach		
Chip phase	**No.**	**Design feature**	**Priority**	**Details**	**Ease**	**Weighted score**	**Details**	**Ease**	**Weighted score**	**Details**	**Ease**	**Weighted score**
Design and fabrication	1	Individual chip construction	1	Varies with tissue structure of each organ-chip	3	3	Different chip construction for the top and bottom chips	2	2	Both chips same layout, only tissue channel is diff.	1	1
	2	Base accessory	1	Not needed	1	1	Not needed	1	1	Fluidic interface	2	2
	3	Additional accessory	3	Not needed	1	3	Needed to stabilize chips during cell injection and chip connection	2	6	Needed to stabilize chips during connection	2	6
	4	Overall system size	3	Changes based on each tissue, not a standard size	2	6	Two sets of standardized chips but support needed to stabilize top chip	2	6	Standard chip size but additional fluidic interface adds to bulk	2	6
	5	Additional OoC integration capabilities (valves, reservoir)	2	Difficult if not planned, entire chip is to be changed	3	6	Chip design adaptation between first chip and last chip, and top and bottom chips	2	4	Can proceed when the fluidic interface is modified	2	4
Chip culture	6	Degassing of fluidics	2	Tissue channels can be degassed	1	2	Both chips can be degassed	1	2	Might not be possible for fluidic interface	2	4
	7	Individual cell injection	1	Could vary for each tissue depending on cell culture and differentiation protocol	2	2	Possible	1	1	Possible	1	1

				Inbuilt approach			Modular approach			Systemic approach		
Chip phase	**No.**	**Design feature**	**Priority**	**Details**	**Ease**	**Weighted score**	**Details**	**Ease**	**Weighted score**	**Details**	**Ease**	**Weighted score**
Chip connection and perfusion	8	Chance of leakage between chips	1	Minimal	1	1	At chip to chip connections	2	2	At the chip to fluidic interface	2	2
	9	Dead volume	1	Minimal	1	1	Only from one gasket volume per connection	2	2	Gaskets and connection channels in the fluidic interface	2	2
	10	Sensor integration between chips	2	Difficult, should be fabricated in from the beginning	3	6	Between 2 chips, will increase the connection chain	2	4	Can proceed when the fluidic interface is modified	1	2
	11	sensor integration before after chip	2	Needs to be fabricated in, new chip every time sensor expires	2	4	Not so easy, can change the orientation of chips with respect to eachotehr	2	4	Can proceed when the fluidic interface is modified	1	2
	12	Flow stabilization before first chip	1	No, tubing directly interfaces with first chip inlet	3	3	No, tubing directly interfaces with first chip inlet	3	3	Yes. Connections to tubing are via fluidic interface	1	1
	13	Tissue retrieval after expt.	2	Impossible to separate the tissues without destroying the chip	3	6	Possible	1	2	Possible	1	2
Functional assays	14	Live intact imaging	2	All tissues are in same plane	1	2	Stacked chips, different focal planes, but compact for microscopy	2	4	Both chips are on the same plane but raised due to fluidic interface	1	2
	15	Sampling between chips	1	Difficult if not planned	3	3	Possible with a modular connection of a switch or sampling connector	2	2	Yes, with switches installed in the fluidic interface	2	2
Total						49			45			39

3.1.2. Modular cassette connection mechanism

Based on the findings from the assessment table, a combination of features from the systemic and modular connection approaches were combined to yield the Modular Cassette. This cassette platform was developed for the following design and use criteria:

- A base platform into which the chip could be flexibly and reversibly plugged
- Minimal dead volumes
- Flexible connection channel between the organ-chips, with the possibility of sensor integration between the chips
- Chips with a standardized outer shape with ease of modification of tissue channel designs, and minimally absorbing materials of construction
- Ease of imaging upon connection
- Possibility to reuse most parts of the connection system upon cleaning with appropriate and validated cleaning methods

The workflow of connection allowed for the separate co-culture of two organ-chips, with the integration of each tissue and an endothelial cell monolayer into the media channel of each tissue. The two tissues are then connected to each other with the help of a cassette, a platform designed for the insertion of the organ-chips, connected with a fluidic channel. Pressure is applied at the point of connection of each chip to the fluidic channel to enable leak-proof reversible connections. After the experiment, the setup can be disconnected, and individual organ-chips studied. The final two cassette designs have been specified below – The *PMMA modular slot* cassette, and the *3D printed modular insert* cassette insert (Figure 32).

The next sections discusses the iterations of the modular cassette. The first iteration is built in PMMA and called the PMMA modular slot cassette. Significant improvements were made to this, and the next iteration is the 3D printed modular insert cassette.

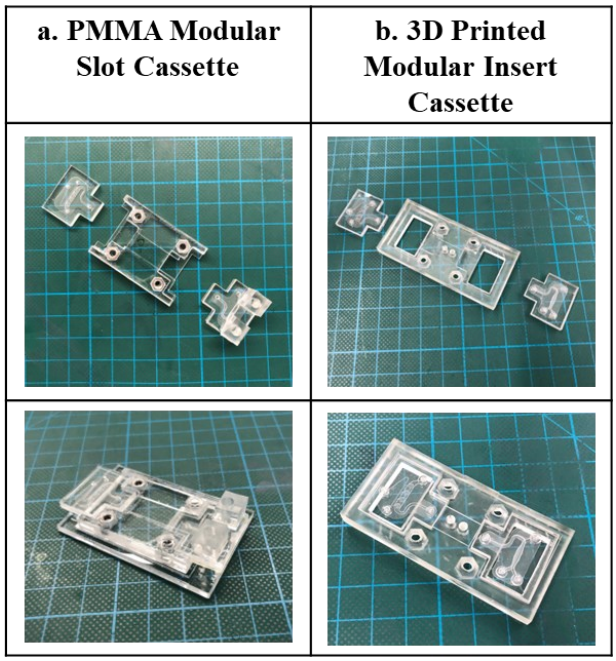

Figure 32: Modular cassette setups (a.) The PMMA Modular slot cassette, (b.) The 3D printed modular insert cassette

3.1.3 PMMA modular slot cassette – design and fabrication

This cassette design involved laser-structured PMMA layers glued together to create a slot to slide in the organ-chips along the sides. A straight connection channel bridged the two chip media channels with gaskets to interface with the chips and pressure applied at the points of contact (Figure 33.a). This fully transparent slot cassette enabled easy viewing of the inserted chips, the possibility to prototype the dimensions and layers of the cassettes for different chips and to allow for the integration of sensors to the middle of the cassette. The design of the cassette was such that chips with varying thickness could be integrated into the cassette in a way that ensured the top ports of the chips and thus the chip connections remained in the same plane (Figure 33.b). The modular slot cassette consisted of layers of varying thickness of lasercut PMMA, glued on top of each other (UHU). Thermal fusion bonding of thick PMMA parts led to warping and uneven heat distribution along the height of the parts. The low height of the cassette due to the 250 µm thin PMMA layer allowed for lower microscope working distances.

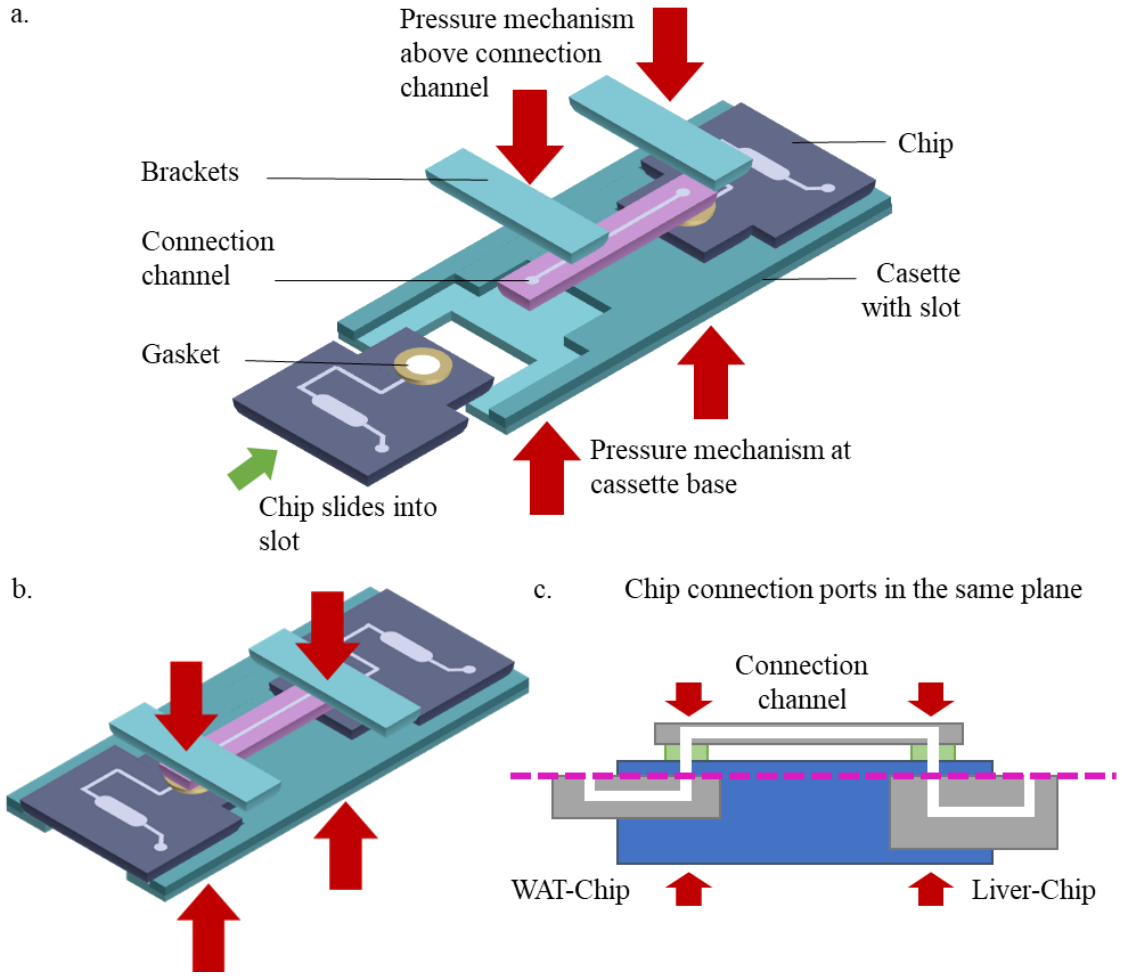

Figure 33: Design schematic of the PMMA modular slot cassette (a.) Labelled schematic of the cassette setup with the slot base and pressure application mechanism (red arrows), (b.) Schematic of the assembled setup, (c.) Side-view cross section schematic of the orientation of ports and connection channel in the same plane in spite of varying chip heights.

3.1.3.1. Mechanisms of pressure application

Pressure at the site of connection is an essential design requirement to ensure leak-free reversible perfusion across both organ-chips. The literature was reviewed for all the methods of connection (section 1.2) and ultimately, the top-down orientation of pressure application was chosen, directly on the sides at the site of connection on the chips. Thus, the connection of the two organ-chips was designed to allow for the application of an appropriate amount of pressure onto the site of connection (Figure 33). The chips were modified to have a specific outer 'T' shape to fit the fastening mechanisms on either side of the media ports, via a bracket (PMMA piece positioned perpendicular to the connection channel at the site of connection) while maintaining a compact cassette footprint close to that of a glass slide.

Upon insertion of the chips into the cassette, the connection channel with gaskets was secured onto the cassette by the pressure mechanisms. Three such strategies were explored for the application of pressure at the points of contact for the chips in the cassettes, namely magnets, springs or screws. The design of the PMMA modular slot cassette varied slightly to accommodate these pressure mechanisms, which provided leak-free flow for 14 days at a flowrate of 60 µL/h (Figure 34.a).

The magnetic cassette holder was designed with a 3 mm high lasercut PMMA base holding two commercially available 45SH bar magnets that measured 25 mm long, 6 mm wide and 2 mm high (Q-25-06-02-SN, Supermagnete) and with a strength of 1.7 kg. The magnets were secured by lasercut slots in the cassette, just above the cassette base. Above the magnet base stood a 3 mm high lasercut PMMA chip slot in the cassette to secure the chips. The top flaps fabricated out of 250 µm lasercut PMMA created the slot that secured the chips in the z direction while connected. Once the connection channel and gaskets were installed at the ports of the two chips, a matching pair of magnets on top of the chips created a tight seal at the point of contact between the chip, gasket, and connection channel. These magnets were encased in a PMMA housing to prevent rusting during use in the incubator. The magnets could be either round magnets or bar magnets, depending on the pressure requirements (Figure 18). The K&J online calculator for magnetic strength showed that the pull force between these magnets was 0.85 kg at 4 mm corresponding to the thickness of chip, gaskets and connection channels (K&J online calculator). Apart from the design considerations of incorporating the bottom magnet into the cassette, the connection points were spaced far enough apart that the magnets did not attract each other from across the ends of the connection channels, adding to the dead volume between the chips. Additionally, a pair of connected chips in one cassette were placed far enough away from the next cassette, so that the magnetic-pressure connections from one set of chips did not interact with another set, or microscopy setups.

The screw slot cassette comprised a 250 µm lasercut PMMA base and 3 mm PMMA chip slot, with 250 µm PMMA slot flaps to secure the chips and prevent vertical movement during connection (Figure 18). 2.5 mm diameter through holes were lasercut into the PMMA cassette and threads were made with M3 threading equipment. Pressure was applied at the site of connection via two brackets of 3 mm thick PMMA through which the screws were screwed into the cassette via a screwdriver. The screws were large enough to allow for sterile handling during the connection with cell-laden chips.

In the case of the spring-laden spring slot cassette, hexagonal features were lasercut in the cassette chip slot at the side of connection ports and housed hex nuts, thus eliminating the need for a threaded screw hole. M3 screws with custom compression springs (50/3/1, Federtechnik Knoerzer GmbH) were inserted into brackets and screwed into the hex nuts to provide uniform pressure at site of connection. During connection of whole chips including tissue chambers, chip heights had to be taken into consideration. The WAT-chips had a height of approximately 3 mm and the liver-chips had a height of approximately 3.5 mm. Thus, the chip cavities of the cassettes had two parts, the liver slot of height 1 mm and the WAT slot of height 3 mm (Figure 34.b). The height difference between the two sides ensured that the ports of both chips are lined up near the top of the cassette so as not to bend the connection channel (Figure 33.c).

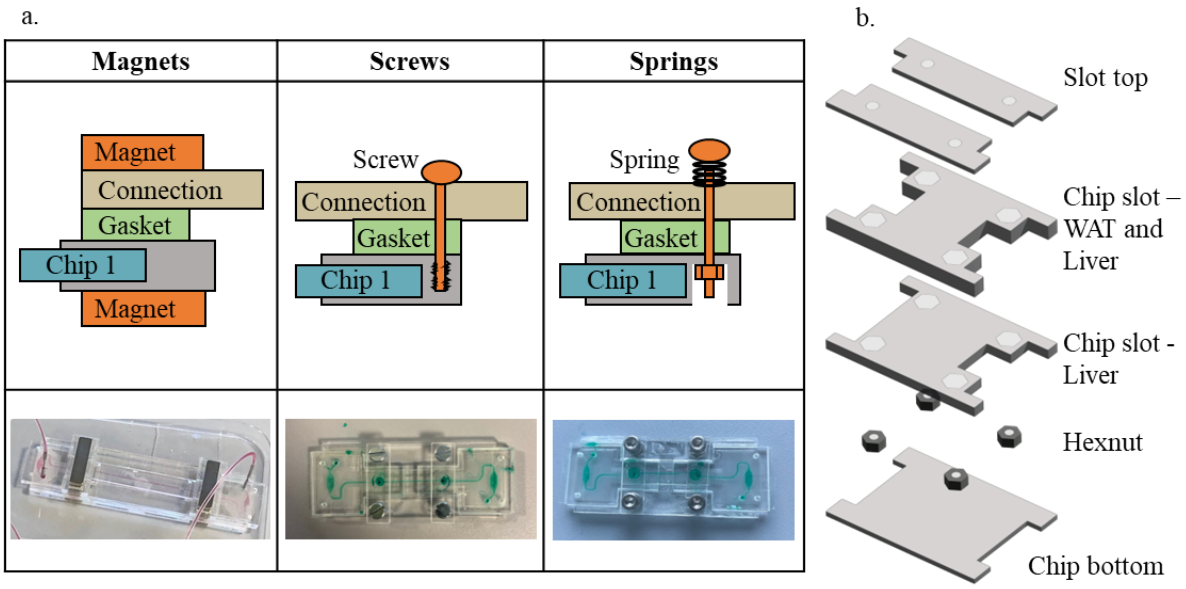

Figure 34: Mechanisms of top-down pressure application in the PMMA modular slot cassette, (a.) Schematic of the cross section of the pressure mechanism at the site of connection for the mangets, screws and spring-laden screws, and pictures of the flow tests conducted with each of the pressure mechanisms (b.) Schematic of the layers of the PMMA modular slot cassette for WAT-liver connection, with the hex nuts embedded into the PMMA for the spring-laden screw pressure mechanism

3.1.3.2. Characterization of sealing strength – burst test

The sealing strength of each pressure mechanism was tested by creating a connection of one chip in a cassette with the connection channel and sealing all ports except the inlet (Methods sub-section 2.5). The pressure measured with a pressure gauge revealed that all pressure mechanisms could withstand a high-pressure range of 4 bar or over, which is comparable to or higher than the bond strength for microfluidic device materials (Eddings, et al., 2008; Yu, et al., 2015). The screw connections could withstand the highest pressure, consistently failing at the chip bonding at an operating pressure of 6 bar, instead of failing at the connection itself. The magnetic pressure mechanism withstood the lowest pressure at around 4 bar. Overall, the connections operated at a higher strength than conventional bond strength of thermoplastics, making all three pressure mechanisms appropriate sealing mechanisms for multi-organ connections (Figure 35).

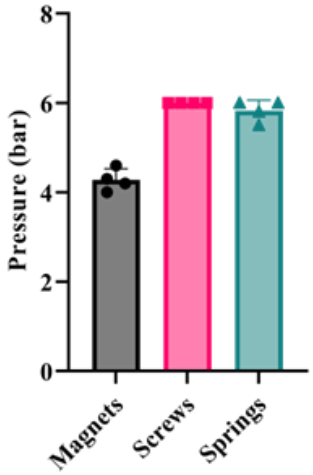

Figure 35: Characterization of the sealing strength of pressure mechanisms using burst tests. In the case of each pressure mechanism, four separate chip-connections were tested.

3.1.4. 3D printed modular insert cassette – design and fabrication

The PMMA modular slot cassette ensured a flexible, reversible connection of two organ-chips. However, the aspect of robustness could be improved given that over time with repeated use, the glued layers detached or warped. The labour-intensive fabrication of the slot cassette was mitigated by 3D printing the cassette in a new format. The 3D printed modular insert cassette allowed for the chips to be placed into the cassette, on top of a viewing window to allow for convenient microscopy of organ-chips while connected to one another. The spring-laden screw connection mechanism was chosen for further testing, and the cassette had hex-nut shaped holes from the bottom for the simple incorporation of hex-nuts into the body of the cassette. The material of this cassette was more robust than the PMMA slot version, enabling reuse and some 3D printing resins even allowed for autoclaving capabilities.

This version of the cassette was designed in Solidworks and 3D printed in clear resin (Formlabs) to have an overall footprint of 65 cm by 31 cm and a height of 7 cm (Figure 36.a). The cassette had two locations for the insertion of chips, with a viewing window under the tissue chamber region of the chips for microscopy due to the semi-transparent resin material. The base of the cassette had hex-nut-shaped holes to insert M3 hex nuts. The connection channel was secured in the y direction by raised walls, and only secured in the x direction while being connected to the chips via the pressure mechanisms. The cassette was also equipped with holes between the chips for the insertion of sensor cables for real-time measurement of glucose or oxygen in the connection channel between both chips. Reservoir pillar holders were provided on the cassette in the case of connection to recirculation perfusion regime (Figure 36.b). The hex holder was an accessory that could be slid under the cassette, loaded with hex nuts to allow for the proper positioning and simple incorporation of hex nuts to the spring-laden screws (Figure 36.c,d). Half-cassettes accommodated one chip to assess the glucose or oxygen uptake from one chip during recirculation perfusion, and the other side was maintained flat to support the sensor channel, which was directly connected to the peristaltic pump via a PDMS top (Figure 36.e). A reservoir-holder was introduced directly on top of the chip media inlet to allow for a reservoir with the 23G blunt cannula to fit directly onto the chip media port. Tolerances were provided to accommodate minor deviations in dimensions The inserts for the

chips in the cassette had a tolerance of 500 µm on all sides, hex nut inserts had a 100 µm tolerance, and reservoir holder had a 500 µm tolerance to allow for the simple insertion of reservoir with a 23G needle.

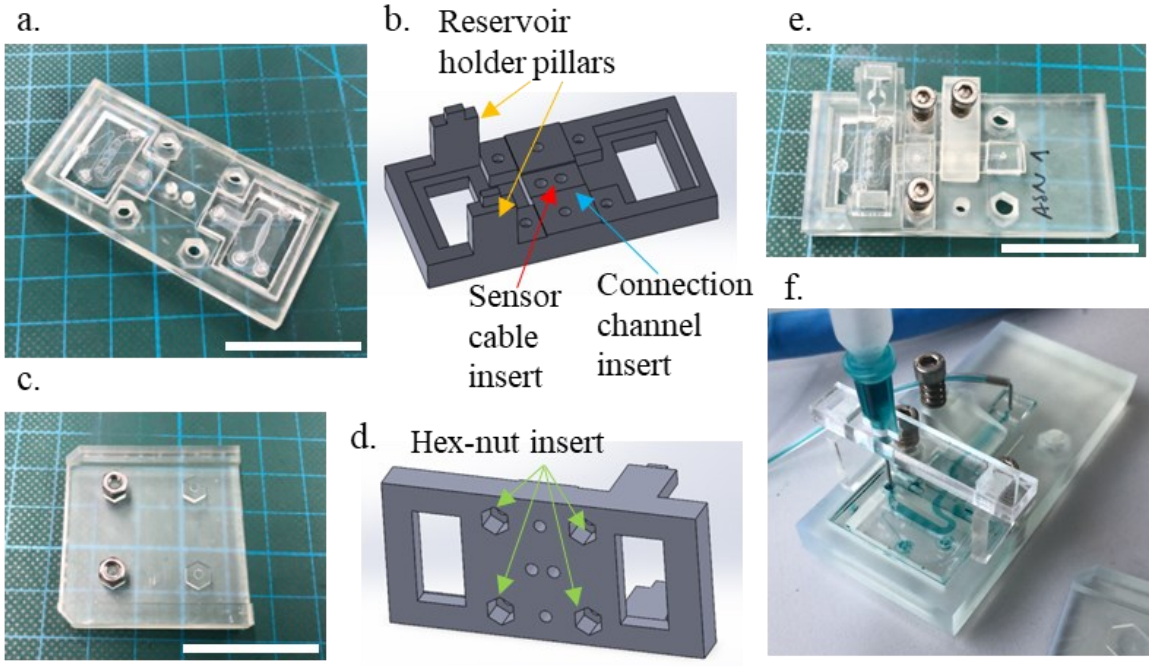

Figure 36: Design and features of the 3D Printed Modular Insert Cassette, (a.) Picture of the WAT- and liver-chips placed into the cassette, (b.) Schematic of the cassette designed for connecting two organ-chips and for recirculating perfusion regime, with the reservoir holder pillars (yellow), sensor cable insert holes (red), and the walls for securing the connection channel (blue), (c.) Picture of the hex-holder with stacked hex nuts, to be slid under the cassette for simple loading of the hex nuts below cassette, (d.) Schematic of the base of the cassette holder showing the hex nut inserts (green), (e.) Picture of the WAT-chip inserted into the cassette, along with the sensor channel secured via the bracket and the pressure-stylus, and reservoir holder in place, (f.) Color water flow test picture with reservoir inserted at the media inlet of the WAT-chip and cannula with tubing connected to the sensor chip outlet, towards the peristaltic pump. (Scalebar: 3 cm)

The high-resolution 3D printing capabilities enable the inclusion of threads into the material of the cassette directly, thus simplifying manufacturing and reducing manufacturing times. However, the 3D printed cassette was prone to bending during fabrication despite being 7 mm thick. This could be attributed to a non-uniform level of curing of the resin and part dimensions (Amera Labs Blog, 2018). Addition of ribs below the cassette body could increase the bending tendency and a reduction in the sharp corners since sharp edges concentrate stresses during shrinkage of resin during the curing steps. The orientation of the print of the model could also be modified to print at an angle, since the horizontal orientation is most prone to warping.

3.2. Design criteria and connectors for the two organ-chips

To test the connection mechanisms developed in the section above, the example of interaction between white adipose tissue (WAT) and hepatocytes was selected, given the motivations highlighted in the Introduction. The design for the WAT-chip was influenced by a previously developed model, where the fragile primary subcutaneous adipocytes were suspended in a

hydrogel and injected into a chamber situated below an isoporous membrane (Rogal et al., 2020). Media was perfused in the channel running across the tissue chambers and the adipocytes were nourished by diffusion of nutrients through the membrane. The design for the liver-chip was inspired by a previously reported chip, consisting of two channels separated by an isoporous membrane (Rennert, et al., 2015). Hepatocytes were seeded on one side of the membrane and nourished by media perfused along the other channel across the isoporous membrane. Since the interaction was to be studied between the WAT-Liver systems, endothelial cells were incorporated into the media channels to facilitate the vascular connection (Figure 1.b, Figure 9.b).

This sub-chapter dives into the criteria for chip design and fabrication, followed by exploration of the concepts of world-to-chip connectors which would enable connection of both chip types to perfusion. Additionally, the chip layouts and dimensions have been summarized for the WAT- and liver-chips.

3.2.1. Chip design summary

Given the diverse designs, dimensions and fabrication methods of the chips above, an effort was put towards harmonizing the two chips being connected in this thesis. The design and fabrication criteria for the chips interacting with the cassette system, are listed below –

i. Design criteria

- 2D or 3D cell injection, depending on the cell type in question
- Integration possibilities for endothelial cells
- Physiologically scaled organ-chips relative to one another
- Outer chip shape, suitable for tight connection and uniform pressure at the site of connection
- Tissue exposed to physiological shear, with the consideration of perfusion regime (linear or recirculating)
- Ease of sensor integration
- Possibility of effluent sampling

ii. Fabrication criteria

- Minimally absorbing materials of construction, in the form of rigid plastics where possible
- Convenient interface with pumping mechanisms (world-to-chip connection)
- A flat membrane to facilitate a flat monolayer of cells for imaging
- Optically transparent materials of construction
- Gas control of dissolved gases in the media
- Possibility of scaling up chip-production to pilot level production

Based on these criteria, geometries and dimensions for tissue and media compartments of the WAT- and liver-chips were defined (Table 23).

Table 23: Summary of dimensions of the WAT- and liver-chips

	WAT-chip	**Liver-chip**
Tissue compartment		
Chamber dimensions	Radius per chamber: 1.5 mm	Length: 2.56 mm Width: 1.36 mm

	Height of tissue chamber region: 200 µm	Height: 750 µm
Volume	Per chamber: 0.35 µL Entire chip: 1.41 µL	13.44 µL
Co-culture area	Chip: 7.06 mm^2	17.93 mm^2
Media compartment		
Area	38 mm^2	23.53 mm^2
Height	0.25 mm	0.25 mm
Volume	9.5 µL	5.88 µL

3.2.2. World-to-chip connectors

In additions to interfacing chips with one another, approaches were investigated to connect the chips to perfusion mechanisms in a robust and leak-free fashion. Typically, the perfusion mechanisms involved syringe or peristaltic pumps, connected to the chips via tubing with a rigid metal cannula being inserted into the port of the chips. The chips underwent several iterations to accommodate this canula in a convenient manner, without the addition of commercially available ports to maintain system simplicity (Figure 37). These iterations have been listed below –

Cannula with tubing cladding

In this version of world-to-chip connections, the rigid 23G metal cannula was provided with a cladding of tubing at its end. The chip top was constructed from rigid plastic, with a port of diameter 1.4 mm, to accommodate the outer diameter of the tubing cladding, to ensure a snug-fit of the cannula inside the port. In addition to being labor-intensive to fabricate, this connection was prone to leakage if the gap between the cannula and the tubing cladding was wetted, and the cannula slid into the port without the tubing fitting into the port.

PDMS-top interface

Here, a flexible PDMS layer with ports was covalently bonded onto the top of the rigid PMMA chip. The ports in the PDMS layer had a diameter of 0.75 mm which ensured a tight fit around the 23G cannula, and the bond between the PDMS and plastic was created by a silane treatment (methods sub-section 2.2.1.3). In some cases of PMMA-PDMS bonding, the loss of bonding between the PDMS and PMMA layers led to a detachment of the PDMS layer and hence, leakage at the sides of the chip.

Tubing interface

In this version, a 5 mm long piece of tubing with inner diameter 0.5 mm was bonded onto the surface of the chip into the port of diameter 2.2 mm to accommodate the outer diameter of the tubing in a tight fit. The bonding was performed with a drop of UV glue at the site where the tubing met the chip surface (methods sub-section 2.9.2). The inner diameter of the tubing was large enough to enable pipetting cells and media, and the cannula diameter was also fixed to ensure a snug-fit during perfusion. While chip injection and connection to perfusion proceeded smoothly, the bonding of the tubing connector was not durable over the course of 14-day experiments. Additionally, when left unconnected, gravity-driven backflow from the connector into the chip led to the formation of an air bubble at the end of the connector, and care had to be taken not to push it into the chip during connection.

Embedded PDMS connector

In this version, the top of the chip was assembled with a step at the ports, which was then filled with PDMS and punched with a 0.75mm diameter biopsy punch to ensure a snug-fit of the cannula. This minimized the small-molecule absorbing regions and ensured tight, leak-proof world-to-chip connections. A BreatheEasy membrane placed on top of the connector and a port punctured to allow perfusion into the chip and ensure durable and leak-free connections.

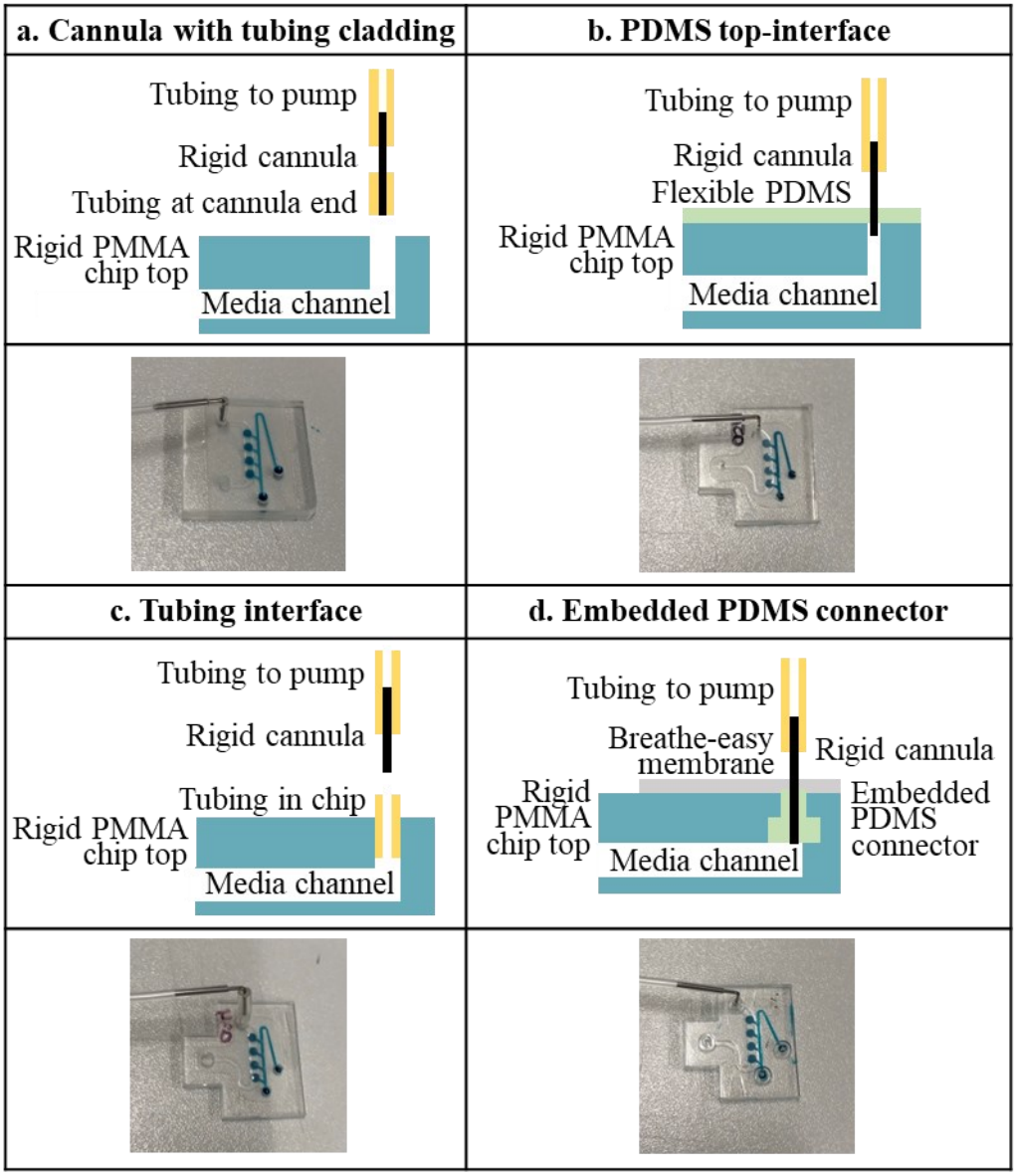

Figure 37: Schematics and design of world-to-chip connector strategies (a.) Cannula with tubing cladding, (b.) APTES-treated PDMS top interface, (c.) Tubing interface, (d.) Embedded PDMS connector built into the PMMA top

3.3. WAT-chip: fabrication, injection and characterization

This sub-chapter discusses the fabrication iterations, computational models, cell injection strategies and on-chip characterization

3.3.1. Design iterations of the WAT-chip

The main construction features of the WAT-chip included a tissue chamber separated from the media channel via an isoporous PC membrane, with connection ports leading into and out of a media channel (Figure 38.a). The tissue-section had a tissue fluidic channel for the injection of the fragile adipocytes suspended in the hyaluronic acid-based hydrogel, leading to four tissue chambers which trapped the adipocytes. The tissue chamber region was taller than the tissue fluidic region, and the adipocytes were trapped within the chamber under the membrane given their buoyancy. The WAT-chip underwent iterations to improve the fabrication, production scale, and world-to-chip connections, with major versions of the WAT-chip emerging in the design process -

Version 1: PMMA chip with PDMS top interface layer

This version of the WAT-chip was constructed entirely out of lasercut PMMA, with a PDMS layer on top of the chip to enable world-to-chip connections. The various layers of the chips were constructed in a sequence of steps and bonded using thermal fusion bonding with the application of heat and pressure in a convection oven (Methods sub-section 2.2.1). This was a small-scale production process where each chip was fabricated individually and in addition to being labor-intensive, the challenges in fabrication included membrane wrinkling and channel deformation due to heat and uneven pressure.

Version 2: PMMA-TPE hybrid chip with embedded PDMS connectors

This version of the WAT-chip alleviated the heat exposure-based wrinkling of the full PMMA chip by introducing a thermoplastic elastomer for a lower temperature bonding process (Figure 38.b). The operational temperature for this version of the WAT-chip was 60°C instead of 130°C for version 1 and was desirable to maintain a uniformly flat membrane across the large unsupported membrane region across the tissue chambers. A hotpress was employed for the sequential steps of the production of the various components and only the final step included bonding each chip at a time in an oven (Methods sub-section 2.2.2). The chip connection method was changed from a PDMS layer in the earlier version to embedded PDMS connectors embedded in a PMMA top, to significantly reduce the volume of PDMS being used in chip construction but to maintain ease of world-to-chip connection. While this version involved more fabrication steps, it was more time efficient and resulted in a high yield due to the simple bonding of TPE to thermoplastics (Table 24).

3.3.2. Simulations of flow and transport of species

COMSOL models were established to simulate the perfusion of media across the WAT-chip, demonstrating the diffusive transport of species through the membrane towards the tissue chambers, perpendicular to media flow direction. This was evident with the evaluation of velocity in the tissue chambers being zero, compared to 2×10^{-5} m/s in the media channel above them (Figure 38.c). The pressure drop across the media channel is about 0.18 Pa, which is lower than the 10 mmHg (1.333 kPa) pressure drop across venules (House & Johnson, 1986) (Figure 38.d) A time-series simulation demonstrated the convective and diffusive transport of an arbitrary small molecule of concentration 1 mM across the media channel into the tissue chambers, where the molecule required 30 minutes to diffuse into the final chamber of the chip at a flowrate of 20 µL/h (Figure 38.e).

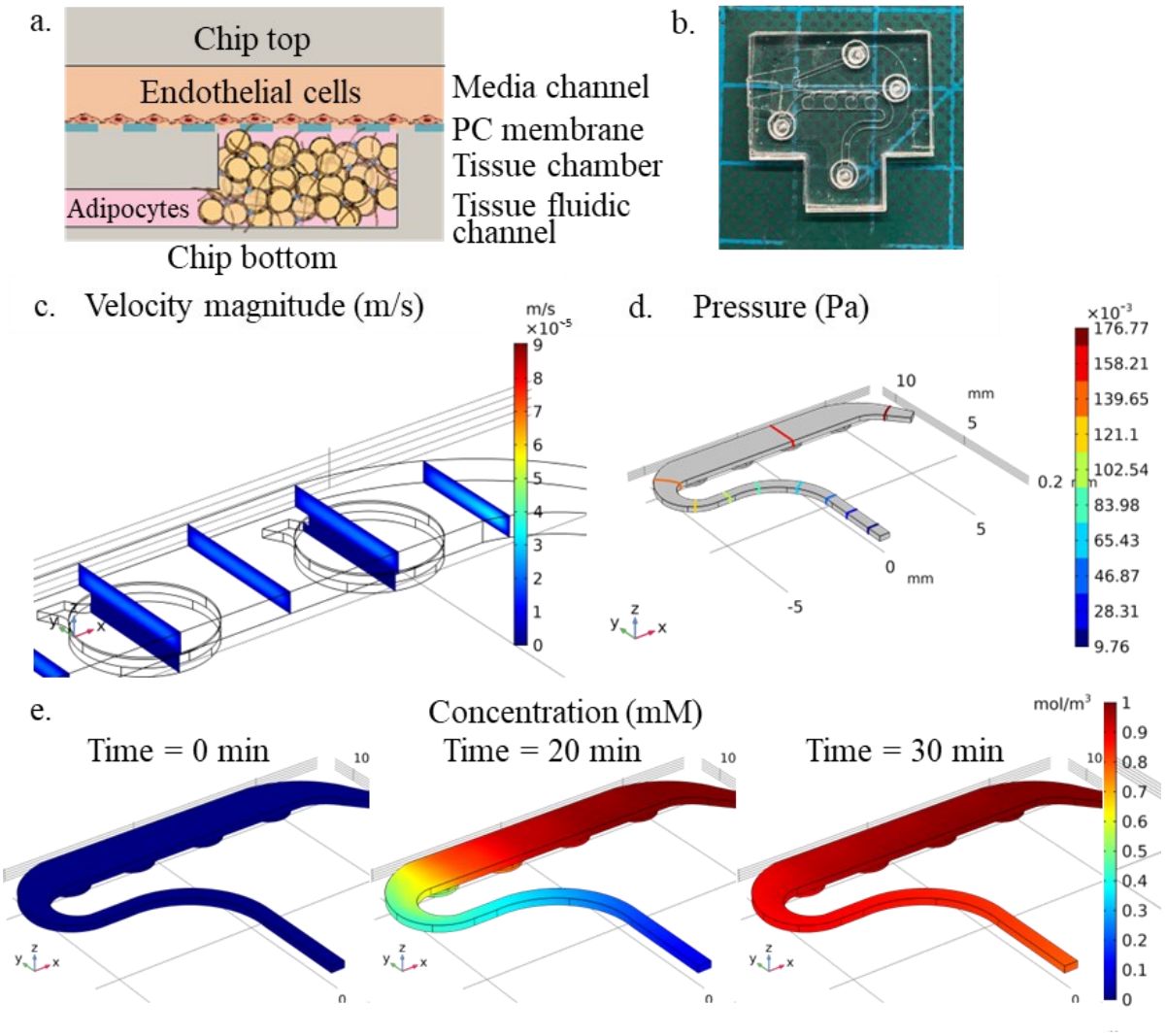

Figure 38: WAT-chip design and simulation of perfusion. (a.) Schematic of the cross-section of the WAT-chip with adipocytes trapped below the membrane in the tissue chambers, and endothelial cells lining the media channel across which perfusion occurs. (b.) Picture of Version 2 of the WAT-chip with embedded PDMS connectors, (c.) Simulations of the velocity of media perfused across the WAT-chip at a flowrate of 20 µL/h, (d.) Pressure drop across the WAT-chip, (e.) Time-series simulation of the transport of species across WAT-chip

Version 2 of the WAT-chip can be fabricated in the hotpress up to 36 parts at a time, assuming 9 parts are embossed by one epoxy mold and 4 such molds can simultaneously be used in the hotpress (Table 24). In version 1, the calculations were made to produce a batch of 16 chips at a time, with the assumption that the PDMS stamp was already prepared. The total time to produce 16 chips was 546 minutes (34.125 min/chip). On the other hand, for version 2, the area of the hotpress could hold 4 epoxy molds at a time, each with 9 chips. Once again, the assumption was that the stamp and epoxy molds were pre-made. The total time to produce 36 chips was 505 minutes (14.03 min/chip).

Table 24: Time improvement of production of version 2 of WAT-chip compared to version 1.

Version 1	Tasks	Total time for 16 chips (min)
PDMS chip top	PDMS weighing, mixing, degassing	30

	PDMS curing	240
APTES bonding PMMA to PDMS	Plasma treatment- PMMA	15
	Silanization	60
	Plasma treatment- PDMS	15
	Bonding in the oven	30
Tissue chamber and membrane	Assembly of the stamp setup	48 (3 min per chip)
	Bonding in the oven	10
	Cooldown before disassembly	20
Full chip assembly	Assembly of parts	48 (3 min per chip)
	Bonding in the oven	10
	Cooldown before disassembly	20
Version 2	**Tasks**	**Total time for 36 chips (min)**
PMMA chip top	Assembling the parts	5
	Preheating the hotpress	20
	Bonding time	10
	Cooldown before disassembly	10
embedded PDMS connector fabrication	PCR tape beneath PMMA top	10
	PDMS weighing, mixing, degassing	30
	PDMS filling	20
	PDMS curing	240
Tissue chamber and membrane	Assembly of the stamp	10
	Preheating the hotpress	20
	Bonding time	10
	Cooldown before disassembly	10
Tissue fluidics and bottom	Assembling the setup	10
	Preheating the hotpress	20
	Bonding time	10
	Cooldown before disassembly	5
Bonding top to media layer	UV, bond and roll to create contact	10
Tissue chamber to bottom	UV, bond and roll to create contact	10
Full chip assembly	Assembling the setup	10
	Preheating the hotpress	20
	Bonding time	10
	Cooldown before disassembly	10

3.3.3. Calculations of sequential loading in Version 2 of WAT-chip

The injection of adipocytes followed the sequential loading principle, where the first chamber filled with adipocytes, followed by the next and so on. With changing dimensions of the chip to create version 2, resistance calculations were performed to confirm the tendency of adipocytes to enter the tissue chambers sequentially as opposed to being flushed out of the tissue fluidic channel directly. For this, the dimensions of the WAT-chip were measured, and regions were demarcated on the chip for which the resistance was calculated. The resistance was calculated for each segment of the tissue fluidic channel (1-5), for the branches and tissue chambers along with membranes (6-9) and for segments of the media channels (10-15). These

values were then compared depending on whether the first, second, third or fourth chambers were being injected, and at every chamber, the resistance for the fluid exiting the media inlet was the lowest. This implied that the fluid tended to perfuse into the tissue chambers, carrying the adipocytes in and filling up each chamber sequentially (Figure 39.a).

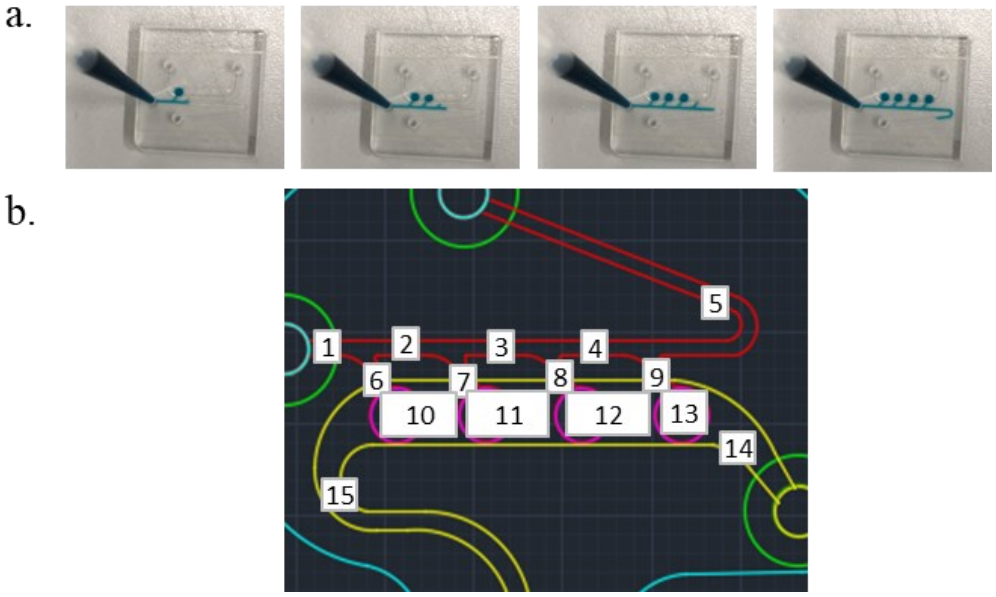

Figure 39: Demonstration of the sequential loading principle in WAT-chip version 2, (a.) Demonstration of sequential loading in WAT-chip version 1, (b.) Allocation of regions for the calculation of resistance to confirm the principle of sequential loading

Table 25: Calculations of resistance per region of Figure 39.b. and the confirmation of sequential loading by comparing resistance

Position	Resistance [Pa.s/mm³]	Position	Resistance [Pa.s/mm³]
1	46.76	7	216.07
2	79.70	8	216.07
3	88.74	9	216.07
4	91.27	10	1.08
5	315.6	11	1.18
6_{total}	216.1	12	1.21
6_{branch}	35.49	13	0.67
$6_{chamber}$	0.0014	14	2.56
$6_{membrane}$	180.58	15	22.23
Chamber	**$R_{fluidics}$ [Pa.s/mm³]**	**$R_{MediaOut}$ [Pa.s/mm³]**	**$R_{MediaIn}$ [Pa.s/mm³]**
1	575.36	238.31	6.71
2	495.66	23.32	5.63
3	406.92	4.45	4.45
4	315.65	3.24	3.24

3.3.4. Cell injection and biological characterization

3.3.4.1. Injection of the adipocytes

The thermoplastic WAT-chips were more prone to bubble formation than the original PDMS chips. A protocol was established to prime the chips before injection, to minimize the presence of nucleation sites (sub-section 2.7.1). This protocol included plasma sterilization followed by degassing and centrifugation, after which the chips were handled one at a time and always equilibrated to 37°C. Cell viability was checked after two weeks in culture with push perfusion at a flowrate of 30 µL/h (Figure 40.b).

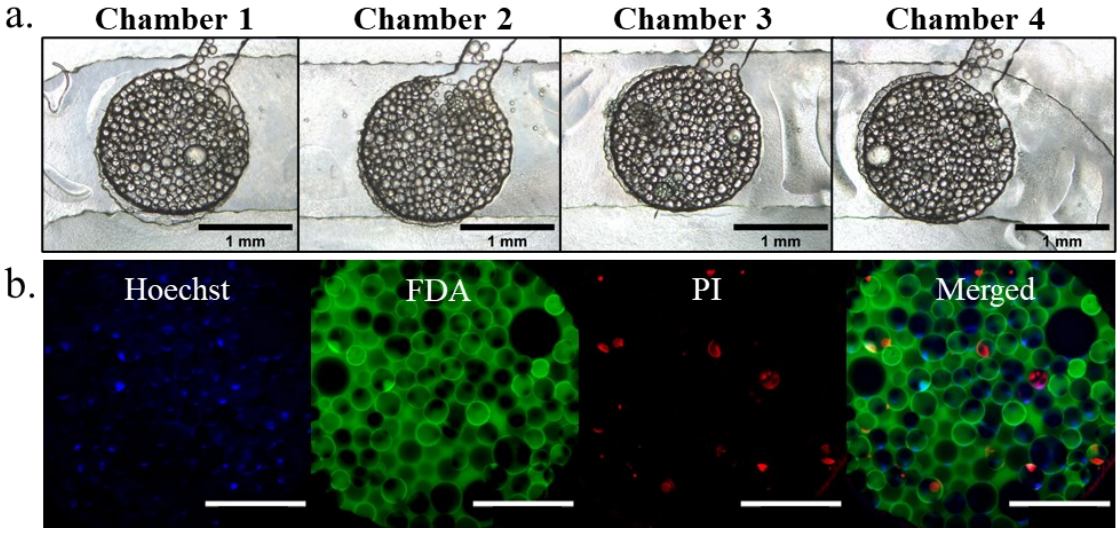

Figure 40: Injection of adipocytes into the WAT-chip, (a.) Adipocytes filling the tissue chambers for all four chambers of the WAT-chip, (b.) Live-dead images of one chamber of the WAT-chip showing live cells in green, dead cells in red and nuclei in blue (Scalebar: 500 µm)

3.3.4.2. Adipocyte-endothelial cell coculture

The adipocytes experienced an exchange of nutrients via the media channel through the membrane. To coculture endothelial cells with the adipocytes, a media optimization was performed to assess the optimal media that would ensure viability of both cell types. The final aim to set up the coculture involved injecting mVECs in the chip the day after the injection of adipocytes, with a high cell density to ensure a confluent monolayer within two days of seeding. The mVECs were to be injected with ECGM medium and the media was changed to the newly determined optimal medium the next day after seeding. The goal of the first set of experiments in well plates with primary microvascular endothelial cells (mVECs) was to determine the cell seeding density which yielded a confluent monolayer the day after cell injection. Various cell densities of mVECs were seeded into a 96 well plate and imaged over four days in culture to observe the change in level of confluence. Seeding cells at an 80% confluency yielded a confluent monolayer on the second day of culture (Figure 41.a).

The MTS assay was used to assess the mVEC viability upon exposure to various media conditions. The assay ran for 2.5 hours to yield a sensitive absorbance range to assess the cellular metabolic activity of the mVECs (Methods sub-section 2.8.2, Table 12, Table 26). The cells were seeded into well plates in ECGM medium in a concentration of 9000 cells/well, and media changed to the various compositions on day 1 after the confirmation of a uniform

monolayer of cells. Cell morphology was observed daily and viability/metabolic activity measured every second day over a period of up to 16 days (Figure 41.b). The cell monolayer looked disrupted in the WAT media while the other media combinations were able to maintain the monolayer with differing reaction times with the MTS reagent, indicating variable metabolic activity (Figure 41.c). The FullW media and 1 to 1 media performed like the ECGM medium in maintaining cell viability. These options were tested on the adipocytes in the WAT-chip.

Table 26: Shortforms of media combinations for the media optimization studies on mVECs and adipocytes

Shortform	Details about the media condition
ECGM	Commercially available endothelial cell media
WAT	Chip culture maintenance media for WAT-chips (Rogal et al., 2020)
1 to 1	A mixture of ECGM and WAT media in the ratio 1:1
Full E	ECGM medium containing all the supplements of the WAT medium
Full W	WAT media containing all the components of the ECGM medium

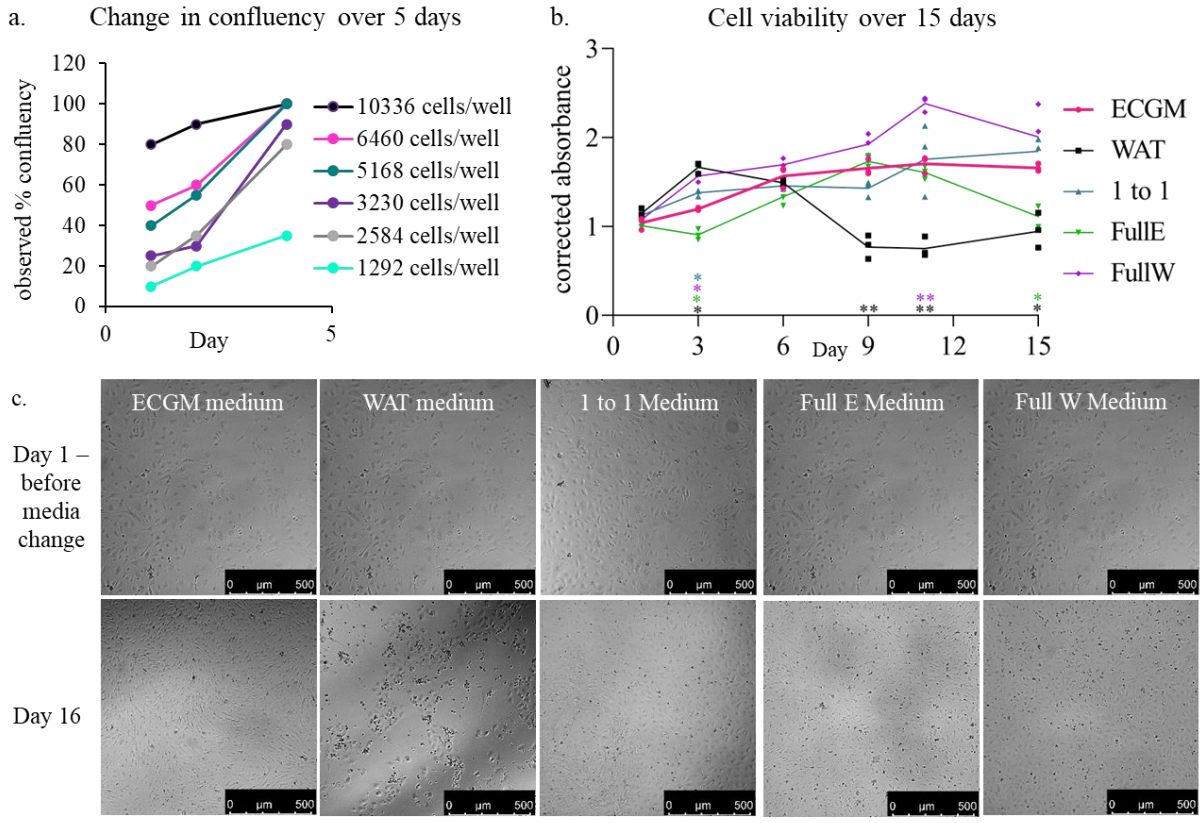

Figure 41: Assessment of cell viability of mVECs in wellplates exposed to various media combinations, (a.) Change in observed confluence of cells over five days based on differing seeding confluency, (b.) Assessment of cell viability over a 15 day period for cells exposed to varying media combinations (n=3 per media condition, per day). The effluents from the well plates were sampled and metabolism by the cells of MTS reagent was assessed for the different media conditions. Background absorbance from the respective media without cells was subtracted from each condition, and individual data points plotted. A 2-Way ANOVA was performed, comparing the cell viability of each media condition with the ECGM baseline media, with p values represented as * = 0.0332, ** = 0.0021. The p values have been color coded to the legend and placed at the bottom of the graph at each data point (c.)

Brightfield images of cell morphology on day 1 compared to day 16 for the mVECs exposed to different media combinations, (9000 cells/well at the start of the experiment). Scalebar: 500 µm.

Given the results above for the endothelial cells in well plates, adipocytes were injected into the WAT-chips and were then exposed to these media combinations over a period of six days under perfusion. The chips were imaged with brightfield imaging and exhibited a morphology of cell death by bursting in the presence of ECGM medium (Figure 42.a). Daily monitoring of LDH release confirmed the morphology disruption observed for ECGM medium. Upon normalizing the data with respect to control chips (chips without cells), the chips exposed to ECGM medium had the highest concentration of LDH in the effluent over a week in culture, followed by the 1 to 1 medium (Figure 42.b).

Cell viability of adipocytes exposed for six days to the different media combinations was assessed by the MTS assay for three different donors. The cells exhibited similar metabolic activity when exposed to FullW medium as they did when exposed to the WAT medium (Figure 42.c). Donor variability was evident in the case of 1to1 and FullW medium where some replicates had a viability close to zero.

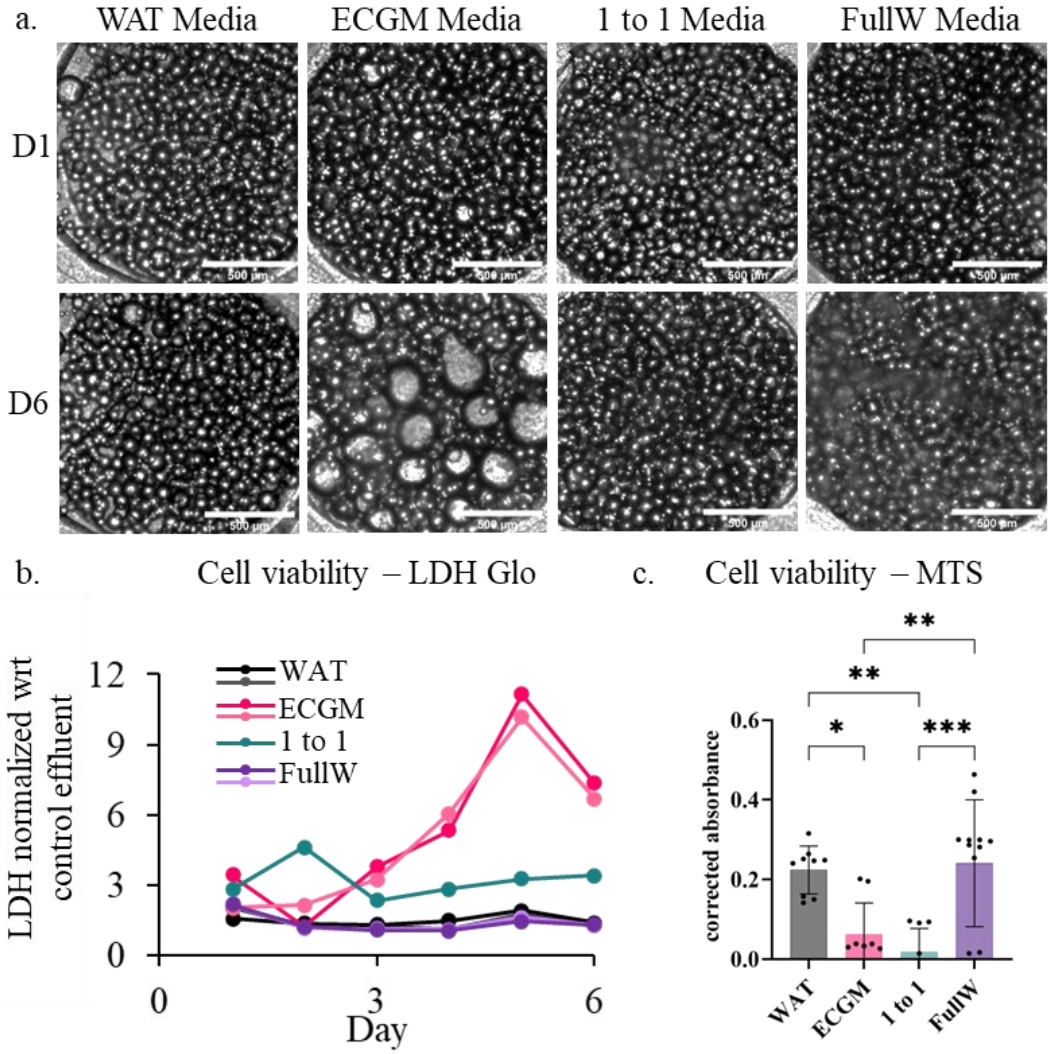

Figure 42: Assessment of cell viability of adipocytes in the WAT-chips exposed to various media combinations. (a.) Brightfield images of one representative chamber in the WAT-chips per media

conditions on day 1 compared to day 6 (Scalebar: 500 μm), (b.) Cell viability assessed by daily LDH released into the chip effluents upon exposure to different media conditions. The effluents from the chips with cells were normalized against effluents of chips without cells as hydrogel blanks (n=2 for all except n=1 for the 1to1 media condition), (c.) Cell viability assessed by the MTS assay of the chip effluents after two weeks of perfusion of cells with the various media components. The assay was performed with MTS reagent mixed into the inlet media and perfused for 4 hr at 20 μL/h. Background effluent and inlet absorbance values were subtracted from the outlet effluent absorbance values. For all data, the values are mean ± SD. One way ANOVA followed by Tukey's t test was performed with p values as *** for p= 0.0002, ** for p< 0.003, *for p< 0.02 (n=3 chips per media condition for WAT, ECGM, 1to1 media and n=4 chips for FullW, with triplicates of absorbance value per chip).

The function of adipocytes in the WAT-chips could be assessed by the uptake and release of a fluorescent short chain fatty acid-analog (4 μM BODIPY™ 500/510 C1, C12) (Figure 43.a). Upon comparing FullW and the WAT media where the function of adipocytes had already been characterized on-chip, the adipocytes exposed to FullW medium seemed to take up and release the SCFA analog at a faster rate (Figure 43.b). Over the course of three days in culture, chips were also exposed to CellTox Green, a fluorescent compound as a measure of cell death due to increased membrane permeability. A region of interest was fit within each tissue chamber of the fluorescent images obtained of the chips mean gray value analyzed for each media composition. The fluorescence intensity of chambers exposed to ECGM and 1to1 medium seemed higher and more scattered than that exposed to FullW and WAT medium, suggesting a tendency towards higher dead cells in the ECGM and 1to1 medium. (Figure 43.c). Glycerol was also quantified in the effluent of the WAT-chip when the adipocytes were exposed to the various media combinations. The results showed that the adipocytes secreted glycerol to a similar extent in the FullW medium as in the WAT medium (Figure 43.f).

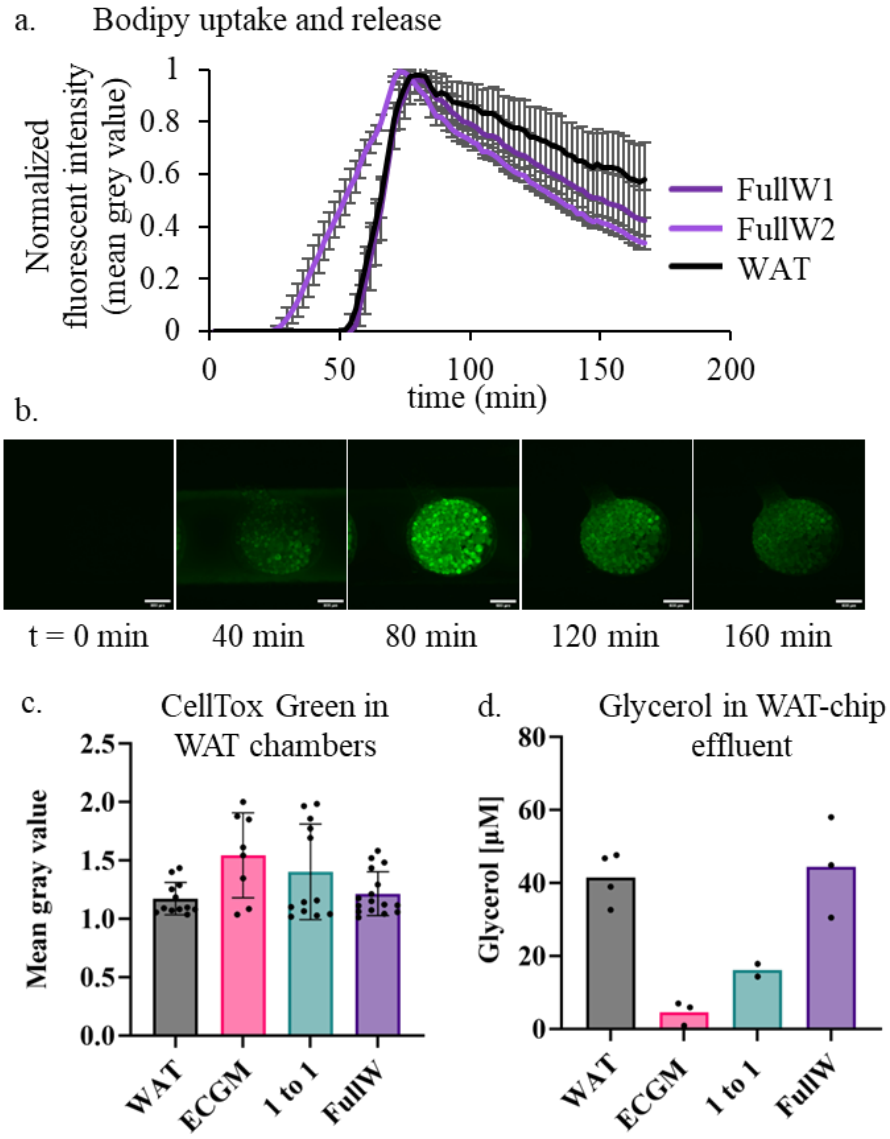

Figure 43: Functional assessment of adipocytes in the WAT-chip exposed to different media conditions (a.) Real-time monitoring of the uptake and release profile of a fluorescent fatty acid analog (4 µM BODIPY ™ 500/510 C1, C12) perfused across chips for 60 minutes at 80 µL/h, followed by perfusion of the respective media up to 160 min (n=4 tissue chambers for WAT condition, n=8 chambers for the FullW condition), followed by evaluation and normalization of mean gray fluorescent intensity (b.) Fluorescent images of a representative tissue chamber in the FullW condition, for various time points (Scalebar: 500 µm), (c.) Quantified mean gray value for a region of interest covering each tissue chamber in the WAT-chip fluorescent images taken on day 3 of perfusion of the chips with different media conditions, represented as mean ± SD (n=8-16 tissue chambers), (d.) Quantification of glycerol secreted by the adipocytes in the effluent of the WAT-chips exposed to various media conditions. Calibration curve fit to the glycerol standard dilutions, blank chip effluent values subtracted from the chip effluent values (n=2-4).

These results revealed that the FullW medium could be used as the optimal medium for coculture of adipocytes with endothelial cells on-chip. The final workflow of creating a coculture for this chip included first injecting the adipocytes into the chip, followed by culturing them static in WAT medium overnight. The next day, endothelial cells were seeded

in the chip at 80% confluency, and they successfully formed a confluent monolayer after just 1 day of static culture overnight. These cell types were co-cultured in FullW medium, and after five days in culture, the adipocytes maintained their unilocular lipid droplets and CD31 positive endothelial cells maintained a mostly confluent monolayer across the length of the media channel (Figure 44.c). The only noticeable region of break in confluency was in the beginning of the media channel as flow proceeded from right to left (Figure 44.b), where the coverage of endothelial cells closer to the inlet appeared disrupted but recovered after the second tissue chamber.

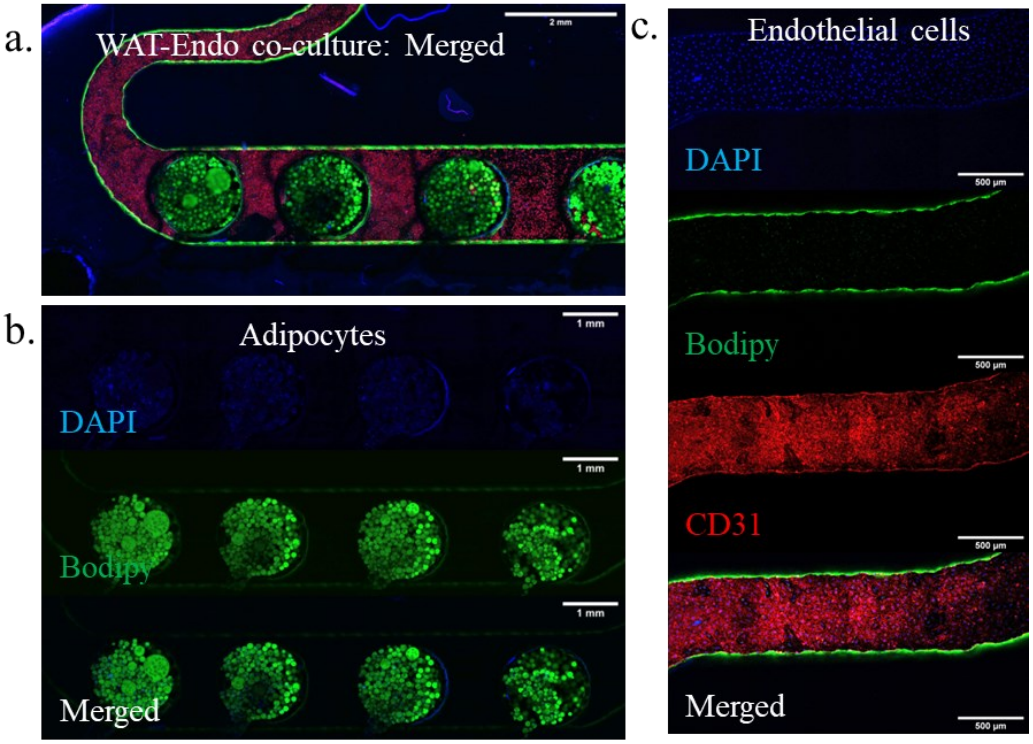

Figure 44: Fluorescent images of adipocytes cocultured with endothelial cells in the WAT-chip, perfused with FullW medium for 5 days at 20 µL/h. (a.) Tile scan of an overview of the chip for an overview of the WAT tissue chambers and endothelial cells (b.) Tile scan of the adipocytes stained for their lipid droplet via a fluorescent fatty acid analog Bodipy™ (green) and nuclei (blue), (c.) Tile scan of the mVECs stained for nuclei (blue), CD31 (red) and lipid droplets (green).

3.4. Liver-chip: fabrication, injection and characterization

This sub-chapter discusses the fabrication iterations, computational models, cell injection strategies and on-chip characterization for the liver-chip. The liver Biochip is currently being developed by Dynamic42 GmbH for commercial purposes, and the liver-chip in this thesis was modified and scaled down to fit the design criteria for the connection system, keeping the hexagonal shape of the liver Biochip. The liver-chip in this thesis consisted of a media channel designed similarly to the WAT-chip, running below a tissue channel, separated by an isoporous membrane. The tissue channel had a hexagonal layout, with a broad chamber region which narrowed out on either side to facilitate reduced shear on the shear-sensitive hepatocytes which would be housed in this chamber. A hepatocyte cell-line was selected to establish the chip and the co-culture model, with HepaRG™ cells being seeded into the tissue channel. Primary

microvascular endothelial cells were seeded into the media channel to facilitate the connection with the WAT-chip (Figure 45.a).

3.4.1. Design iterations of the Liver-chip

The liver-chip underwent some fabrication iterations with the final goal being to enable pilot scale production and with simple world-to-chip connections. In this section, three major versions of the liver-chip have been discussed (Figure 45.b) (older chip versions have been summarized in Appendix section 8.3).

3.4.1.1. Version 1: PMMA chip

The first trials of the chip-seeding protocol were attempted on a chip fabricated entirely out of PMMA. The tissue and media channels were 175 µm high, with a PMMA top with ports for minimal absorption of small molecules. The top part had ports of diameter 1.45 mm to enable connection to perfusion with the cannula with tubing cladding world-to-chip connector. However, this version of the chip was riddled with inconsistencies of membrane wrinkling, and additionally the deterioration of health of hepatocytes over time in the chip. These challenges and the shape of the chip were improved upon in the following versions.

3.4.1.2. Version 2: PDMS reservoir chip

However, with the high oxygen consumption rate of hepatocytes and low oxygen permeability of version 1 of the liver-chip, reservoirs were introduced on top of the version 2 liver-chip to nourish the hepatocytes on the tissue-side in a static culture while the endothelial cells in the media channel would be perfused by the FullW medium. Additionally, the tissue and media channels fabricated out of laser patterned TPE of height 750 µm and 250 µm respectively, with PC top and bottom covers to seal the channels. The height of the channels increased the media to cell ratio from 294 µL/million cells in version 1 to 672 µL/million cells in version 2 of the liver-chip. A 5 µm pore size PET membrane was incorporated between the two channels. A PDMS layer with reservoirs was added to the tissue channel such that the reservoirs held media specific for the HepaRG™ cells in a static culture (Methods sub-section 2.3.2.1). The tissue channel was plugged with 3-D printed plugs during perfusion. This chip could sustain a liver-mVEC coculture for up to a week, with possibilities of media replenishment and sampling on the tissue-channel side in addition to the perfusion effluent from media channel. However, the PDMS top layer with reservoirs was labor intensive to fabricate and this was alleviated in the next version of the chip and made it consistent with the top of the final version of the WAT-chip.

3.4.1.3. Version 3: PMMA-Top chip with step connectors

In this version, the top part of the chip was switched from a PDMS layer to a PMMA top with embedded PDMS connectors to minimize the absorbing components in the system and to ensure simple world-to-chip connections. This provided stability to the thin and flexible chip layers below, while still enabling flexible connections via a cannula. The tissue and media channel dimensions were maintained as per version 2. While fabrication was carried out on an individual chip basis (Methods sub-section 2.3.3), this version exhibits possibilities for scale up to pilot scale fabrication.

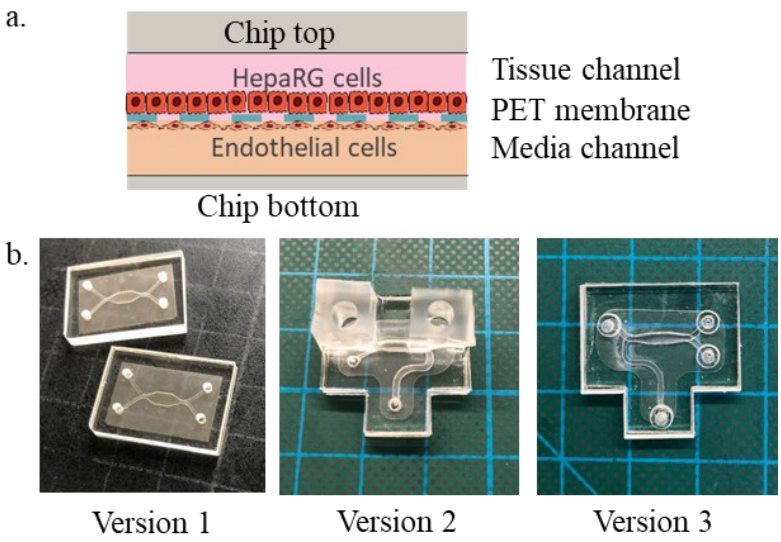

Figure 45: Schematic and pictures of liver-chip versions 1 to 3. (a.) Schematic of the cross-section of the liver-chip with a monolayer of hepatocytes on top of the membrane and endothelial cells lining the media channel (b.) Pictures of the various fabrication versions 1-3 of the liver-chip.

3.4.2. Simulation of flow and transport of species

Perfusion of media at 20 µL/h was studied for the version 2 of liver-chip. The pressure drop across the media channel was 0.25 Pa and velocity in the media channel was close to 3 x 10^{-5} m/s. Both these values are higher than in the WAT-chip, given the narrower channel surface area but still much lower than pressure drop across venules *in vivo* (House & Johnson, 1986). (Figure 46.c,d). The velocity in the tissue channel was zero, given that the membrane shields the tissue channel from direct convective flow, implying that any dissolved small molecule would diffuse across the membrane to be taken up by the hepatocytes. A time-series simulation of the perfusion of an arbitrary small molecule of concentration 1 mM into the media channel at a flowrate of 20 µL/h noted a time of 90 min to completely diffuse into the tissue channel with the molecule given the height of the tissue channel (Figure 46.e).

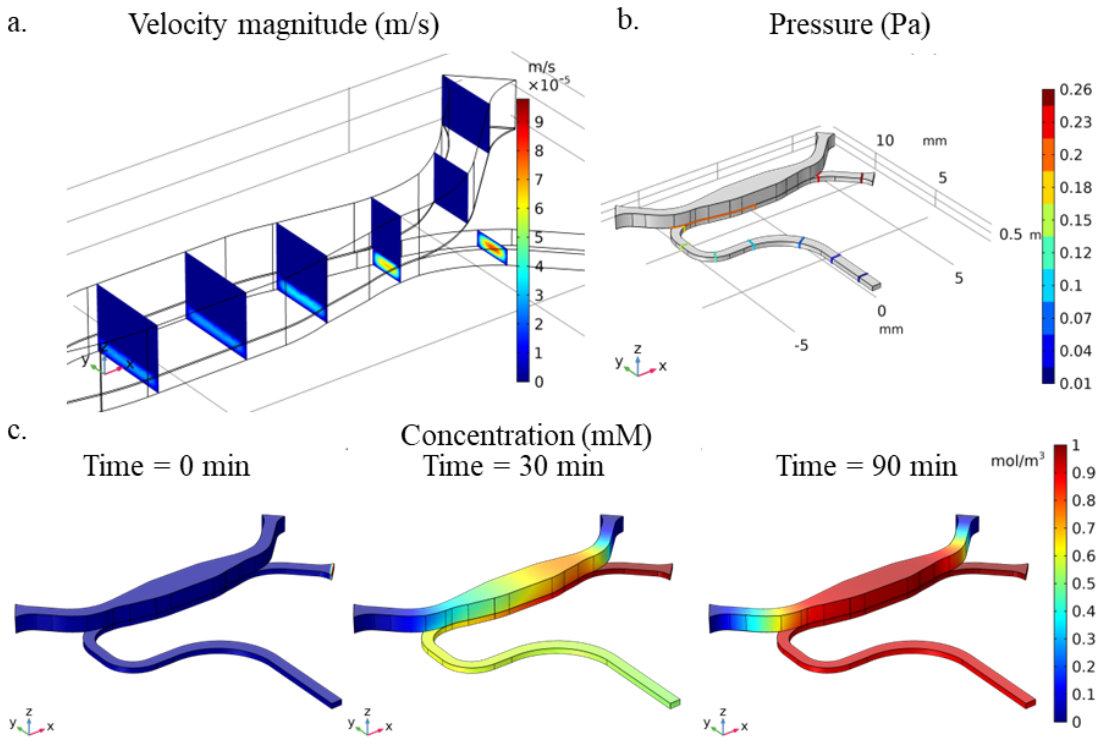

Figure 46: Simulations to characterize the perfusion across the liver-chip (a.) the velocity of media perfused across the liver-chip at a flowrate of 20 µL/h, (b.) Pressure drop across the liver-chip, (c.) Time-series simulation of the transport of species across liver-chip

3.4.3. Cell injection and biological characterization

3.4.3.1. Injection of the HepaRG™ cells

Differentiated HepaRG™ cells were injected into the tissue channel of the pre-coated liver-chips with a concentration of 3 million cells/mL. The HepaRG™ differentiation protocol involved the use of DM with 2% DMSO. This led to loss of cell coverage over time, and a reduction in the percentage of hepatocyte-like cells in the culture. Especially in the case of the thawed hepatocytes, the cells completely detached when thawed with 2% DMSO, and this led to the development of a protocol of thawing the hepatocytes in MM for two days until confluent, followed by a switch to TM (MM with 1% DMSO) for 5 days until injection into the chip (Figure 47).

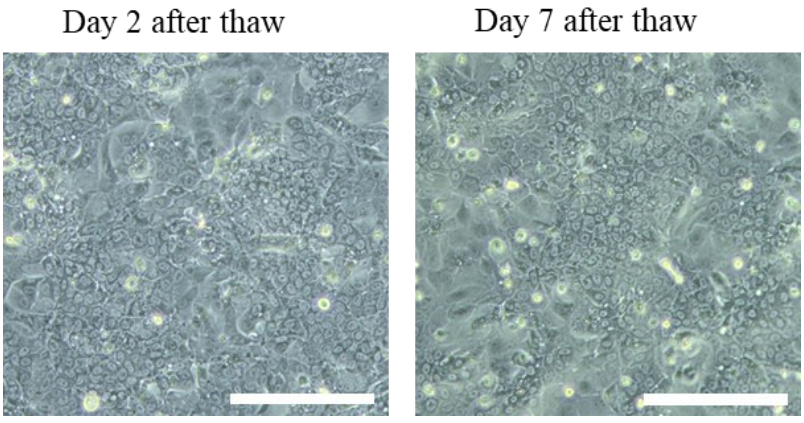

Figure 47: Morphology of HepaRG™ cells in well plates a week after thawing. Scalebar: 100 µm

The 750 µm height of the tissue channel in version 2 compared to version 1 led to a higher media to cell ratio, maintaining the confluence and health of cells in culture. A material test of cells plated on well plates lined with the chip materials revealed that the PET membrane of the liver Biochip exhibited better cell attachment and expression of hepatocyte-specific markers such as apoB, MRP-2, CYP3A4 and ASGPR1, compared to the PC membrane used in version 1 of the liver-chip (Figure 48).

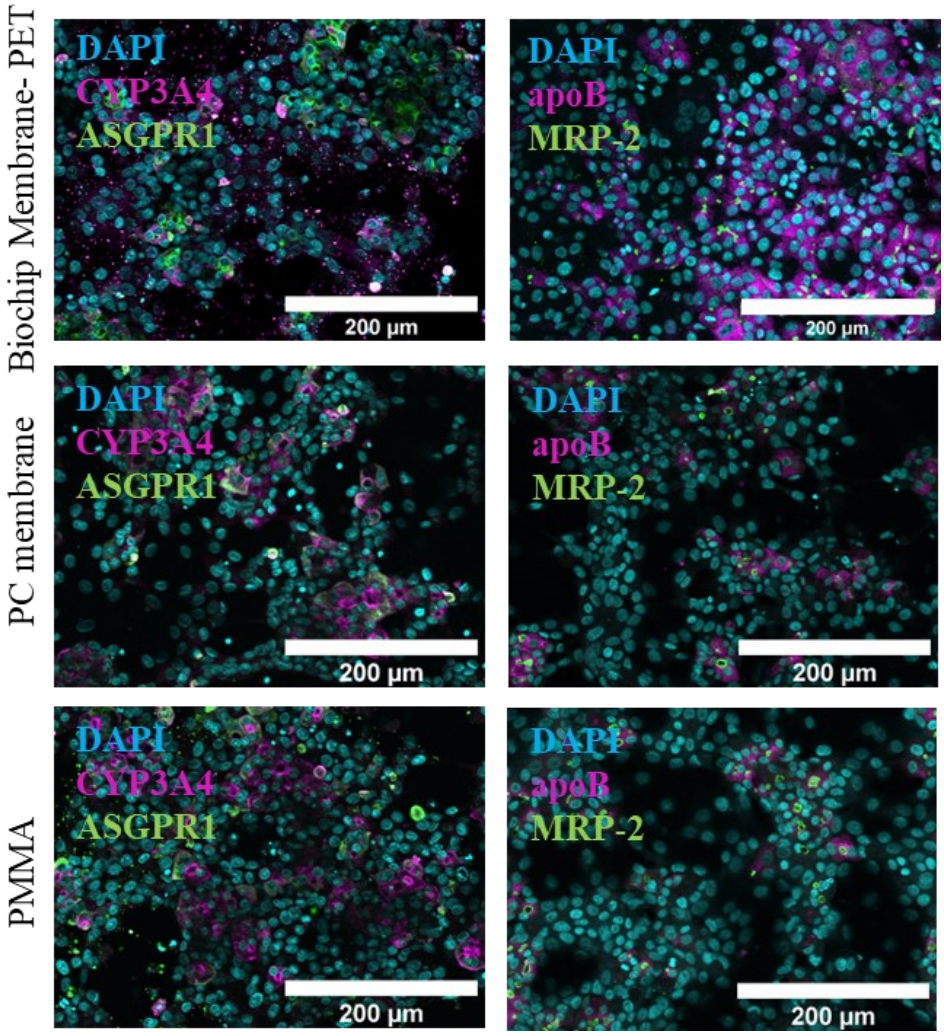

Figure 48: Expression of hepatocyte-specific markers by HepaRG™ cells seeded on the PET membrane, PC membrane and PMMA pieces in well plates. The cells were stained for CYP3A4 and apoB (magenta), ASGPR1 and MRP-2 (green) and nuclei (blue).

Version 2 of the liver-chip contained PDMS reservoirs on top of the liver tissue channel which were plugged with a 3D printed plug such that the tissue channel remained plugged static during perfusion culture (Figure 49.a). The hepatocyte coverage was uniform across the length of the chip, as indicated by live-dead staining after five days in culture (Figure 49.b). In another experiment after three days of perfusion, the HepaRG™ cells stained directly on-chip expressed E-Cadherin, CYP3A4, Albumin (Figure 49.c). It was observed in some cases where hepatocytes were injected into the tissue channels of the chips without endothelial cells, that the cells also seemed to infiltrate into regions in the media channel. This could be attributed to

chip fabrication inconsistencies, but further investigation is required. However, these chips were discarded before connection to perfusion.

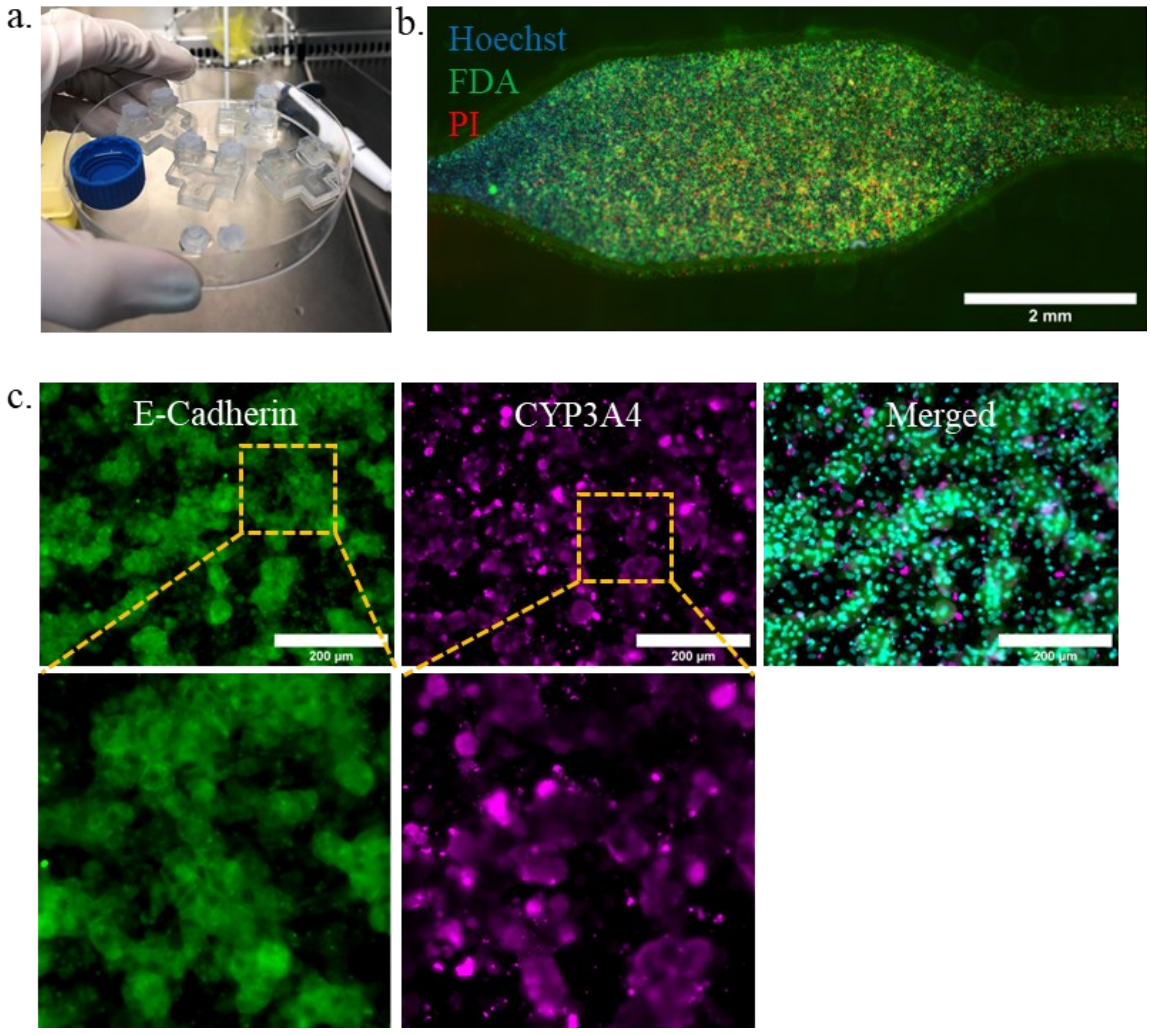

Figure 49: Functional marker expression by HepaRG™ cells cultured in the liver-chip. (a.) Picture of the tissue channel reservoirs plugged after the injection of HepaRG™ cells, (b.) Live-dead imaging to visualize the coverage of cells across the tissue channel, indicated by FDA (Green) and PI (red), with Hoechst (Blue) staining the nuclei, (c.) Expression of markers like E-cadherin (green) and CYP3A4 (magenta) by the hepatocytes after 3 days of perfusion (Scalebar: 200 µm).

3.4.3.2. Hepatocyte-endothelial cell coculture on-chip

The seeding protocol for the endothelial cells cocultured with hepatocytes was established based on the experience from Dynamic42 GmbH, Germany, but with mVECs instead of HUVECs. The mVECs were injected into version 2 of the liver-chip at a concentration of 4 million cells/mL and the chips flipped to allow the cells to adhere to the underside of the membrane (Methods sub-section 2.7.4). The next day, the HepaRG™ cells were injected into the chip. HepaRG™ and primary mVECs were cocultured in the liver-chip for a week with the media channel perfused with FullW medium and the tissue channel in static culture with HepaRG™ chip-culture medium. The cells were fixed and stained on-chip, and expression of various markers was compared for the cells on-chip and for cells seeded in well plates.

Perfusion seemed to have a positive effect on the expression of MRP-2, CYP3A4 and albumin compared to the cells in well plates, indicated by qualitative differences in immunofluorescence staining (Figure 50.a). The endothelial cells showed a different morphology on-chip compared to the well plates, with smaller nuclei and clumping on the underside of the membrane (Figure 50.b). The endothelial cells lining the media channel also showed differences in morpholohy within the channel itself. The endothelial cells formed a lumen in the media channel, with a confluent monolayer of cells forming at the base of the media channel opposite the membrane, while the cells just below the HepaRG™ cells at the membrane seemed to lose their points of contact and developed a clumpy morphology (Figure 50.c). This could be attributed to the presence of HepaRG™ seeding medium across the hepatocyte layer on the liver tissue side, but further investigation is required, given that HepaRG™ chip culture media had been optimized by the Mosig group to support the co-culture of hepatocytes and endothelial cells (Rennert et al., 2015).

Imaging the cells on chip was less clear compared to the well plates, given the cell orientation above and below the membrane. The effluent from the media channel having perfused across the hepatocyte-mVEC coculture, and the static tissue channel media in contact with the coculture was sampled and triglyceride secretion quantified to reveal that the hepatocytes on the liver-tissue side secreted a higher amount of triglycerides compared to the liver-effluent (Figure 50.d).

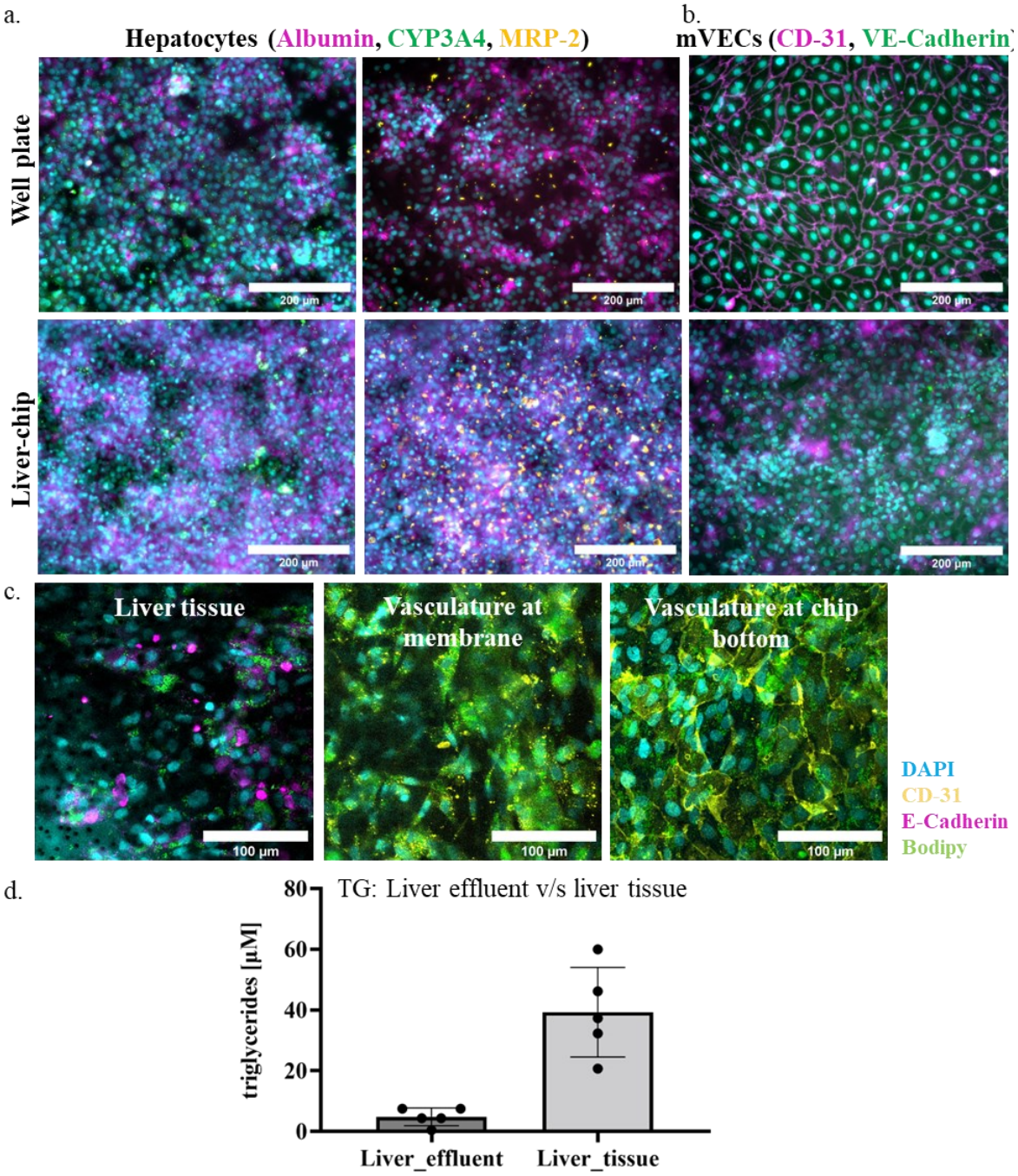

Figure 50: Staining and effluent characterization of HepaRG™-mVEC coculture on-chip (a.) Immunofluorescence imaging of the hepatocytes on-chip and in well plates, stained for nuclei (cyan), albumin (magenta), CYP3A4 (green) and MRP-2 (yellow) expression, (b.) Immunofluorescence imaging of the endothelial cells on-chip and in well plates, stained for nuclei (cyan), CD31 (magenta) and VECadherin (green) expression, (c.) Confocal images of slices of the coculture on the liver-side of the membrane with hepatocytes expressing E-cadherin (magenta) and lipid droplets (green), and the vascular side of the membrane with endothelial cells directly under the membrane compared to the endothelial cells lining the bottom of the media channel on the opposite channel face to the membrane, expressing CD31 (yellow) (d.) Evaluation of triglycerides secretion in the liver-chip media effluent compared to the liver-chip tissue channel during HepaRG™-mVEC coculture, reported as mean ± SD (n=5 chips, with 3 technical replicates per chip).

3.4.4. Simulations of channel height, flowrate, and oxygen consumption

The oxygen consumption rate of a hepatocyte monolayer at the membrane in the liver-chip was investigated using a COMSOL model. The cell coverage was assumed to be the same as the known values of cell coverage of 10 million HepaRG™ cells in a T75 well plate, calculated as 0.133 million cells/cm^2. With a 0.18 cm^2 chip area, the calculated total number of cells in the chip was 23,906. Young and Young reported a protein content of 5.5 µg/well for a HepaRG™ cell seeding density of 15,800 cells/well (Young & Young, 2019). They measured a basal oxygen consumption rate (OCR) of 18.4 pmol/min/µg protein via the Seahorse assay (or 1 x 10^{-7} nmol $s^{-1}cell^{-1}$). Given the cell number in the liver-chip, the basal OCR was calculated to be 2.55 x 10^{-3} nmol/s. With a tissue channel area of 17.93 mm^2 and assuming a cell layer height of 10 µm, the tissue volume was calculated as 0.18 µL, and this yielded an OCR of 1.42 x 10^{-2} mM/s, in standardized units for the COMSOL model. This OCR was set up at the membrane, quantifying the depletion of ambient oxygen in media by the hepatocytes as it passed along the chip with a negligible diffusion of oxygen into the chip from the environment, given the rigid plastic chip body. For a flowrate of 20 µL/h, an oxygen concentration consumption of 50% was observed within 4 min for a media channel height of 250 µm, and within 6 min for a 750 µm channel height. Other flowrates were tested, where the oxygen concentration dropped by 50% in 9 min for perfusion at 60 µL/h and in 12 min for perfusion at 100 µL/h (Figure 51). In the recirculation setup, perfusion proceeded at a rate of 100 µL/h for a channel height of 750 µm, but the assumption of complete oxygen saturation in this setup can be made since the media would interact with gas-permeable tubing before being pumped back into the system. For a linear perfusion model with flowrate of 100 µL/h, over 60 minutes, the oxygen concentration in the medium varied from 0.2 mM in the chamber inlet to 0.1 mM in the chamber outlet.

Thus, increasing channel height and flowrate improved the oxygen concentration in the medium but it is evident that the rate of consumption of oxygen by the hepatocytes is extremely high and must be noted for future chip designs and perfusion cases, given the oxygen impermeable nature of rigid plastics. TPE exhibits a lower level of oxygen permeability than PDMS and this should also be factored into the model in the future (Matsunaga et al., 2005). The oxygen concentration in hepatic vasculature varies as (Vollmar & Menger, 2009).

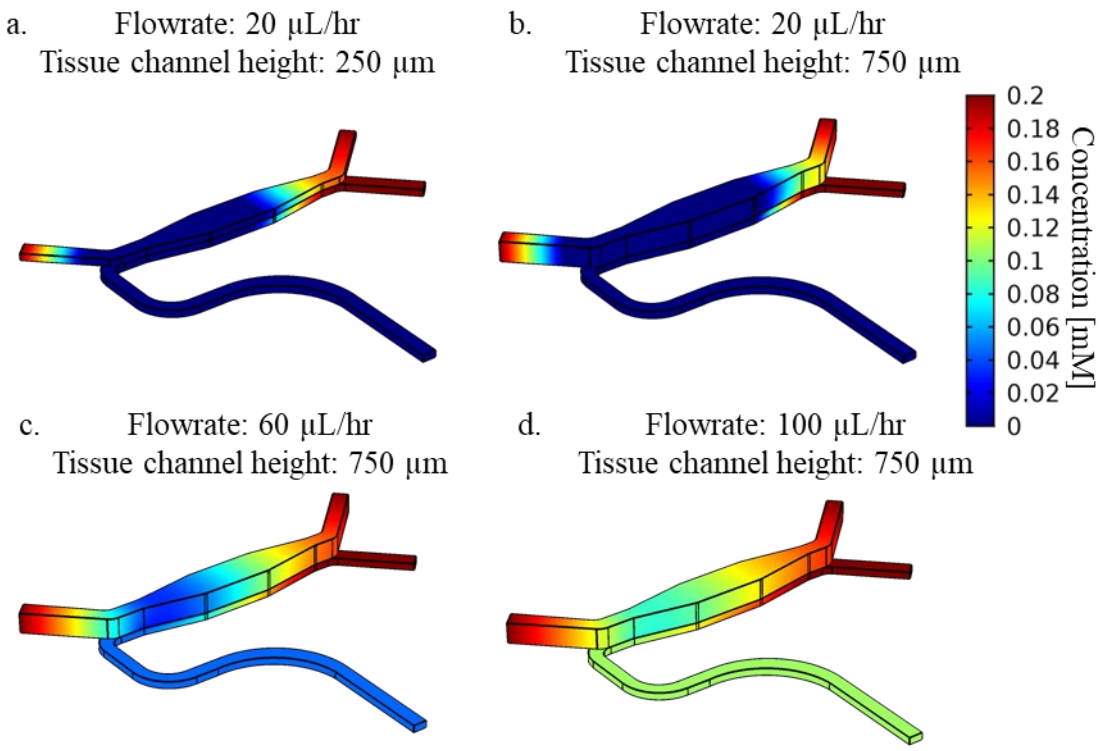

Figure 51: Simulation of oxygen concentrations in the liver-chip at 1 hour of perfusion for variations in channel height and flow rate. (a.) Flowrate of 20 µL/h and a tissue channel height of 250 µm, (b.) Flowrate of 20 µL/h and tissue channel height of 750 µm, (c.) Flowrate of 60 µL/h, (d.) Flowrate of 100µL/h.

3.5. Functional organ-scaling of WAT- and liver-chips

During the chip design phase, organ-scaling calculations were performed to decide the volume of liver relative to adipose tissue-on-chip to obtain a reasonable effect of one organ on the other upon connection. The WAT- and liver tissue channels designed with the inbuilt connection approach considered the nature of the tissues and their interaction, which defined the first iteration of scaling based the publication by Moraes *et al.* (Moraes et al., 2013). The volumetric scaling of the WAT- and liver-chips, using liver as a starting point, was defined based on physiological organ density and cell numbers in healthy adults. The percent body weight of liver is 2.2% and for adipose tissue was taken to be 20% (Chan et al., 2006; Loprinzi et al., 2016; Mubbunu et al., 2018). Based on an average estimate of a 75 kg male, the weight of the liver and fat were obtained to be 1,650 gm and 15,000 gm (Walpole et al., 2012). The density of liver and fat was taken to be 1.05 g/mL and 0.9 g/mL respectively (Loprinzi et al., 2016; Overmoyer et al., 1987). The volumes of the organs were calculated to be 1955.12 mL and 16,666.67 mL for liver and WAT based on the equation:

$$vol_{organ} = mass_{organ}/density_{organ}.$$

The volume ratios of visceral fat and subcutaneous fat were obtained from literature (Jang et al., 2011). The area of total, visceral and subcutaneous fat was obtained from computed tomography (CT) scans, and from this, the physiological volume ratios of fat to the liver were calculated (Table 27).

Table 27: Physiological volume ratios calculated for the different types of adipose tissue to liver based on literature (Jang et al., 2011).

	Physiological volume ratio
Total fat: liver	8.5 : 1
Visceral fat: liver	3.1 : 1
Subcutaneous fat: liver	5.4 : 1

As perfusion experiments proceeded and functional data obtained about the metabolites from the chips, another scaling approach of functional scaling could be employed to ensure that an organ makes a physiological contribution of metabolites within the MOC. For the liver, the functional activity is metabolism, and given the constraints of the system and number of cells, the metabolic activity of the liver could be scaled relative to the adipose tissue given blood circulation parameters. The structure of the liver tissue chamber followed the same hexagonal structure of the liver Biochip, but the channel dimensions varied to match the perfusion rate of blood in the liver. The body holds a volume of 5 L of blood, and flows through the liver at a rate of 1.5 L min^{-1}. Given that the liver has 1.76 x 10^5 million cells, the blood flow per cell number in the human liver is approx. 8.5 x 10^{-6} µL $cell^{-1}min^{-1}$. Given that the liver-chip holds approx. 40,000 cells, the perfusion rate was calculated to be approx. 20 µL/h. The volume ratio of WAT tissue chambers to liver tissue channel was calculated to be 7.88, closer to the ratio of total fat to liver volume, confirming the physiological volume ratio calculation from before. Upon fabrication and characterization of the WAT- and liver-chip systems, some parameters were deduced, and further scaling could be performed with the aid of *in silico* models (Table 28). Here, residence time is defined by the volume of the media channel divided by flowrate, as the time that a particle spent within the media channel. When perfused with media with 7 mM glucose indicating a fed state, the liver and WAT-chips produced 400 and 362 µM of lactate respectively.

Table 28: Parameters from the WAT- and liver-chips to enable *in silico* modeling

	Liver tissue (HepaRG™)	**Liver media (ECs)**	**WAT tissue chamber**	**WAT media (ECs)**
Channel area (mm^2)	17.93	23.53		38
Channel height (mm)	0.75	0.25	0.2	0.25
Channel volume(µL)	13.45	5.88	1.41	9.5
Cell number	0.4 million	0.3 million	2100	0.04 million
Injected cell conc. (million cells/mL)	3	4	NA*	4
Cells/area	2250	1000	NA**	1000
Flow conditions in channels	Static, Liver SM	FullW	Static, FullW	FullW
Media channel volume (µL)	-	5.88	-	9.5
Residence time (min) for flowrate 20 µL/h	-	17.6	-	28.5
Effluent concentrations				
Glucose conc. in media	7 mM	7 mM	7 mM	7 mM
lactate production in effluent	-	400 µM	NA§	362 µM

triglyceride production in chip	40 µM	10 µM	NA§	-
Glycerol production in chip	-	-	NA§	8.36 µM

* cell concentration in adipocytes cannot be counted during injection
** cells/area not calculated for the 3D adipose tissue model
§ effluents not measured for the plugged WAT-tissue channel

3.6. Demonstration of applications of the modular cassette

This section describes two applications of the modular cassettes with respect to chip connection. The first involved the connection and perfusion of WAT- and liver-chips with the PMMA modular slot cassette. The second application involved the integration of glucose and oxygen sensors to measure glucose and oxygen uptake for each chip, with the 3D printed modular insert cassette. Different perfusion regimes were also tests for the applications.

3.6.1. Application 1: Flexible and modular WAT-Hepatic-chip connection

The WAT- and liver-chips were connected within the PMMA modular slot cassette and perfused for a period of six days via vascularized media channels from the WAT to liver-chip. Perfusion proceeded with a one-way linear push regime at a flowrate of 60µL/h with a syringe pump and the optimized FullW media (with 7 mM glucose). Effluent was sampled every day. When the experiment was terminated, the chips were fixed and stained to assess the expression of identity markers and to characterize the endothelial cell monolayer. Both WAT- and liver-chips had an intact monolayer of endothelial cells expressing the endothelial cell-specific marker CD31 (Figure 52.a). VE-Cadherin, a marker determining the endothelial cell contact integrity was also expressed by the cells in the regions of confluent monolayers (Figure 52.b). The CD31 expression appeared patchy even though the nuclei and VE-Cadherin staining indicated an endothelial cell coverage. The unilocular lipid droplet of the mature adipocyte was maintained in each chamber, as evidenced by the Bodipy staining (Figure 52.c). The endothelial cell monolayer across the WAT-chip was slightly irregular at the media inlet of the WAT-chip but recovered along the length of the media channel after the first chamber (Figure 52.d).

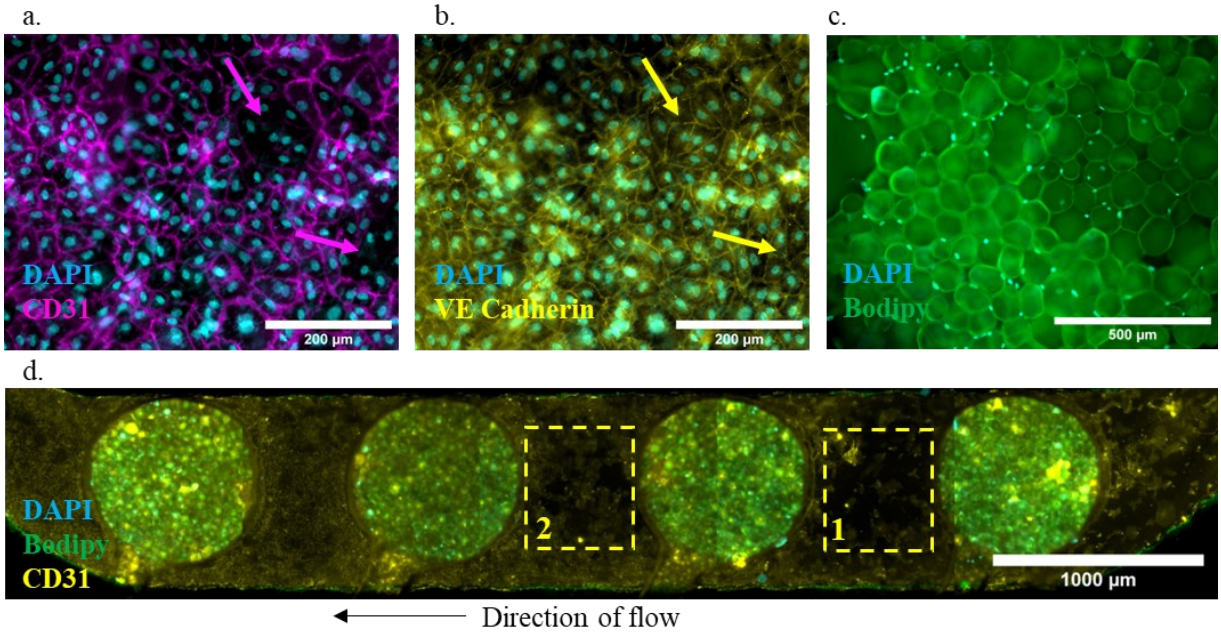

Figure 52: Fluorescence images of adipocytes and endothelial cells co-cultured in the WAT-chip (a.) CD31 (magenta) positive endothelial cells with some patches indicating nuclei (cyan) but CD31 negative cells (magenta arrows) (Scalebar: 200 µm), (b.) Endothelial cells expressing VE-Cadherin (yellow) with a confluent monolayer in the same region corresponding to the CD31-negative patches (yellow arrows) (Scalebar: 200 µm), (c.) Unilocular lipid droplet of mature adipocytes (stained with BODIPY™ dye) and nuclei (cyan) (Scalebar: 500 µm), (d.) Tile scan of the WAT-chip with adipocytes (green) and CD31-positive (yellow) endothelial cell monolayer, with an irregular coverage between the first and second tissue chamber (yellow box region 1) as it recovers along the direction of flow (yellow box region 2).

The liver-chip positioned downstream of the WAT-chip was exposed to the effluent of the WAT-chips over the six days of connection. The tissue channel showed a uniform coverage of HepaRG™ cells expressing E-Cadherin, an epithelial cell-specific marker (Figure 53.a). Lipid droplets were visible, present in the hepatocytes and stained with the fatty acid analog (BODIPY™) (Figure 53.b). It appears the cells in the tissue channel tended to clump on top of each other to form islets, such that the coverage was thicker than a monolayer and the fluorescent signal for hepatocyte-specific markers and accumulation of lipid droplets appeared higher in these regions. The hepatocytes expressed MRP-2, indicating functional bile canaliculi (Figure 53.c). While partly out of focus owing to the 2.5 D nature of the tissue, the MRP-2 staining pointed towards the polarizing tendency of the hepatocytes. The media channel showed a confluent monolayer of endothelial cells expressing CD31 under direct perfusion (Figure 53.d).

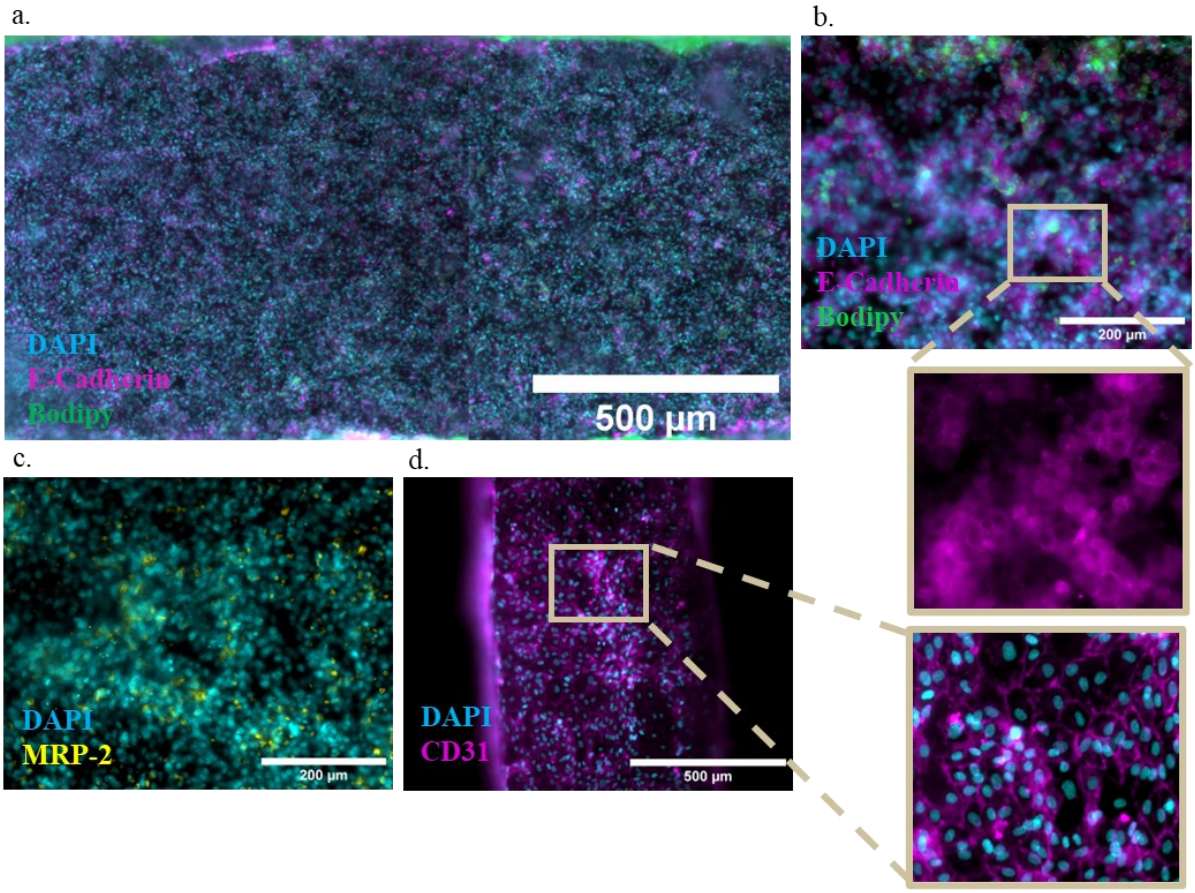

Figure 53: Fluorescent images of the HepaRG™ and mVECs co-cultured in the liver-chip (a.) Coverage of hepatocytes in the liver-chip stained for E-cadherin (magenta) and lipid droplets (BODIPY™), (b.) A zoomed in image showing higher signal of E-cadherin at the islets formed by the hepatocytes, (c.) Hepatocytes stained for MRP-2 (yellow), (d.) Endothelial cell monolayer expressing CD31 (magenta).

The triglycerides and glycerol content of the effluent was analysed on days 1 and 6 to assess the effect of connection on effluent (Figure 54). The effluent showed an overall decrease in the level of triglycerides over the week of culture. The base triglyceride level from the WAT-chip and liver-chip was lower than that of the connected chips. It seemed as if the extent of decrease in triglyceride production was higher in the unconnected liver-chip than the connected liver-chip but further investigation is required to understand whether connection might actually impact triglyceride secretion of the hepatocytes. The glycerol production was higher in the WAT-chip compared to the liver, and this level was comparable with and without connection on days 1 and 6. Adipocytes are known to secrete glycerol and further investigation is required whether the hepatocytes take up the glycerol during connection.

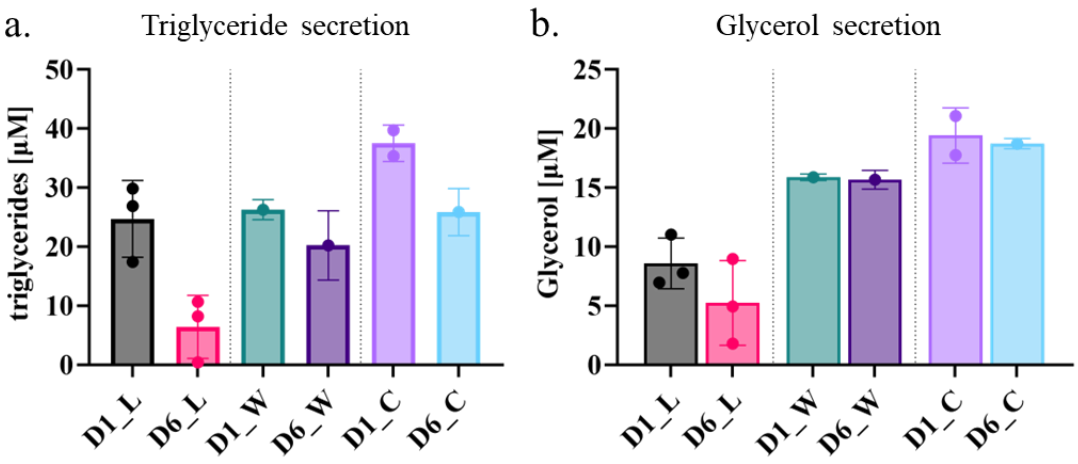

Figure 54: Effluent quantification of the WAT, Liver and connected chips. (a.) Triglyceride quantification of chip effluents. Background effluent of blank chips (chips without cells, also connected to perfusion with the same media) was subtracted from the chips with cells. The error bars indicate 3 technical replicates of the effluent from a chip and the dots indicate the separate chips. (Conditions are marked D1 or D6 depending on the day of effluent collection, and L for liver-only chips, W for WAT-only chips and C for WAT-Liver connected chips) (b.) Glycerol quantification of chip effluents. Background effluent of blank chips (chips without cells, also connected to perfusion with the same media) was subtracted from the chips with cells. The error bars indicate 3 replicates of the effluent from a chip and the dots represent separate chips. Conditions are marked D1 or D6 depending on the day of effluent collection, and L for liver-only chips, W for WAT- only chips and C for WAT-Liver connected chips

The expression of cell markers appeared blurry and non-specific when directly imaged with the fluorescent microscope. Attempts were made to detach the various chip layers and to image the chips directly on a glass slide leading to clearer visualization of the E-Cadherin and MRP-2 staining for the HepaRG™ cells in the liver-chips cocultured with endothelial cells and exposed to connection with WAT-chip and ECGM medium (Figure 55.a). The confluent monolayer of endothelial cells was also visible. However, the liver-chips with hepatocytes cocultured with endothelial cells and exposed to ECGM medium showed a higher expression of E-cadherin and MRP2, while the CD31 staining appeared more scattered (Figure 55.b). An observation of the HepaRG™ cells in the liver-chip connected to the WAT-chip was that these cells accumulated more lipid droplets compared to the chips not connected to WAT-chips. Given that the media contained 7 mM of glucose, this observation pointed towards the interaction with the adipocytes leading to a higher accumulation of lipid droplets (Figure 55.c).

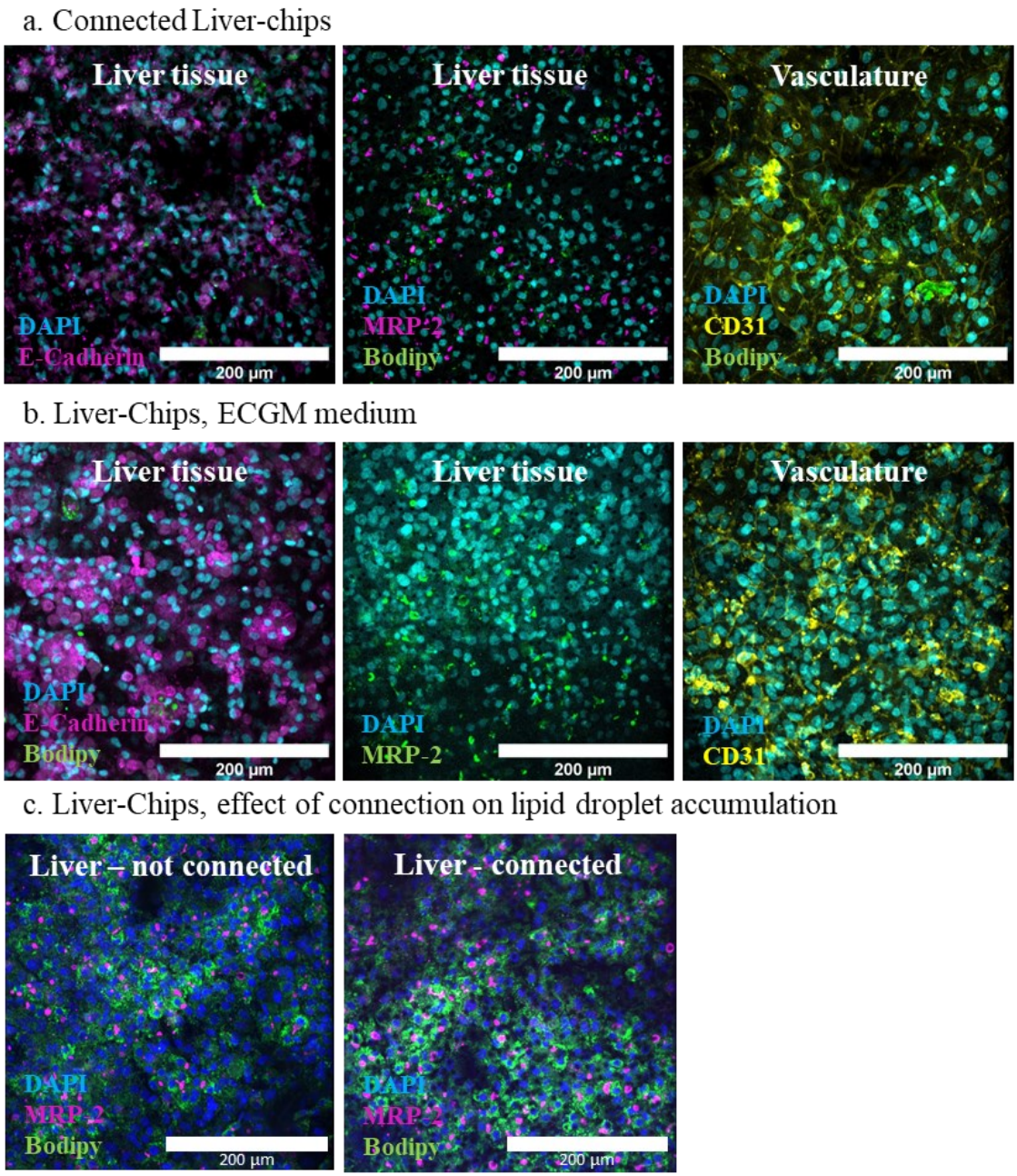

Figure 55: Confocal images of functional marker expression for HepaRG™ cells co-cultured with mVECs. (a.) Images of the liver-chips that were connected downstream of the adipocytes and perfused with FullW medium, for the expression of E-cadherin, MRP-2 (magenta), lipid droplets (green) on the hepatocyte side and CD31 (yellow) on the vasculature side. (b.) The liver-chips perfused with ECGM medium expressing E-Cadherin (magenta) and MRP-2 (green) on the tissue side and CD31 on the vasculature side, (c.) Lipid droplet imaging comparing connected liver-chips to non-connected liver-chips (Scale bars: 200 µm).

3.6.2. Application 2: Flexible and modular sensor integration

It is relevant to study the metabolism of glucose and the influence of insulin, given that WAT and liver are major metabolising organs involved in energy homeostasis and exchange of metabolites. A main feature of OoC technology involves the possibility of sensor integration, to track the uptake and release of dissolved species such as glucose and oxygen in real time. The 3D printed modular insert cassette was modified to fit and fix sensor cables below a

connection channel equipped with sensor spots developed in the group of Dr. Torsten Mayr by Stefanie Fuchs at TU Graz, Austria. This version of the cassette drew from the general design of the PMMA modular cassette version but involved some specific features –

- Completely 3D printed body of the cassette, that could withstand multiple experiments and reuse with the application of pressure from the springs and screws
- Insert style of connection instead of the slot given 3D printing as the new method of cassette fabrication
- Holes in the cassette for the insertion of sensor cables at a fixed spot, to be located directly below the sensor spots fixed in the connection channel, for the real-time monitoring of glucose and oxygen within the chip
- A stylus for the fixation of the connection channel aligned with the sensor cable holes
- Pillars to support the reservoirs directly on top of the media inlet in the chip, to enable recirculation perfusion.
- Viewing window under the tissue chambers of the chip to view the cells in the chips during seeding, connection and to allow for microscopy imaging.

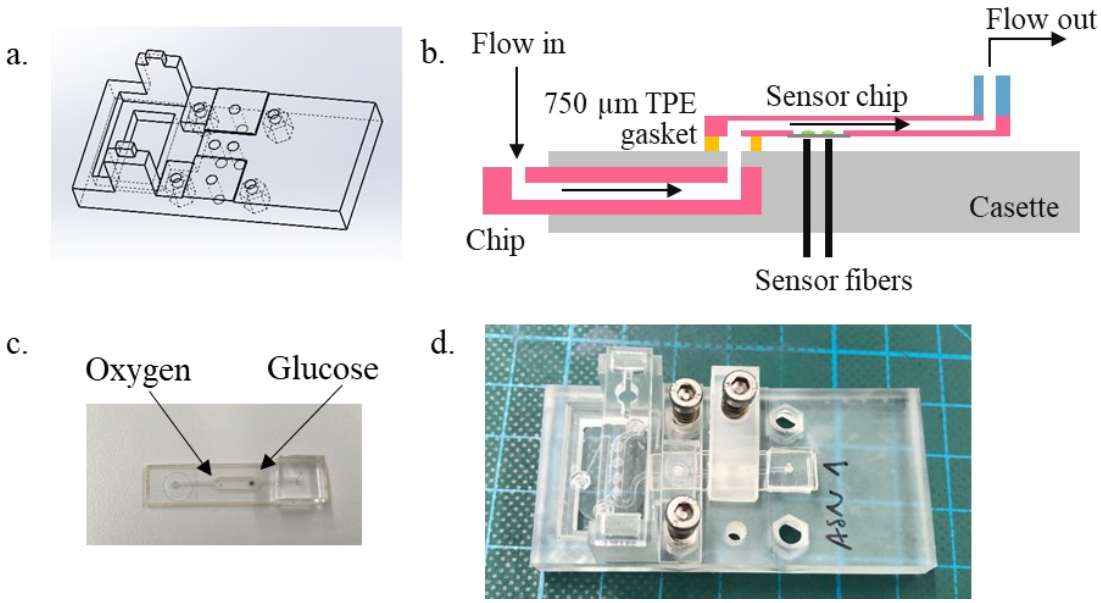

Figure 56: Design of the 3D printed modular insert cassette for sensor integration (a.) Schematic of the 3D printed cassette modified for recirculation perfusion, with columns to support the reservoir, (b.) Schematic of the cross section of the flow across the chip contained in the cassette (gray), through the sensor chip and out of the PDMS connector (blue). TPE is color coded pink and the gasket is yellow, (c.) Picture of the sensor chip with the gasket on the left and PDMS port connection on the right. The oxygen and glucose sensors are housed in the middle (d.) A picture of the setup with the WAT-chip inserted into the 3D printed cassette via the spring-laden screw connector, the sensor chip held in place by the 3D printed pressure stylus, and the reservoir support added onto the pillars of the cassette.

The goal of this system was to assess the glucose consumption rate of adipocytes and hepatocytes on-chip, scaling down literature reported values of glucose uptake and endogenous glucose production in WAT and liver tissue based on tissue weight for WAT and cell number for liver (Honka et al., 2018) (Table 29). Additionally, a study was performed to minimize the dead volumes within the cassette systems, to improve the system response time to changes in glucose concentrations (Table 30).

Table 29: Theoretical calculations of the oxygen consumption rate for the WAT- and liver-chips and endogenous glucose production in liver-chips

WAT		
	Value	**Unit**
Glucose uptake (GU) cut off for insulin sensitivity (IS) to resistance (IR)	11.50	µmol/kg tissue/min
Average GU, IR	9.00	µmol/kg tissue/min
Average GU, IS	18.00	µmol/kg tissue/min
total tissue weight	15.00	kg
total GU in body	172.50	µmol/min
density of adipocytes	0.90	g/mL
weight of adipocytes in chip	1.27×10^{-3}	g
total GU in chip, IR	1.14×10^{-5}	µmol/min
total GU in chip, IS	2.29×10^{-5}	µmol/min
volume perfused for 2 hours at 20 µL/h	40.00	µL
GU for this volume	0.02	mM/hr
Liver		
	Value	**Unit**
Average GU, IR	13.00	µmol/kg tissue/min
Average GU, IS	31.00	µmol/kg tissue/min
no. of hepatocytes per kg of liver	1.16×10^{5}	Million cells
total tissue weight assuming 75 kg male	1.65	kg
total hepatocytes in body	1.91×10^{11}	
Average GU, IR per hepatocyte	1.12×10^{-10}	µmol/heps/min
Average GU, IS per hepatocyte	2.67×10^{-10}	µmol/heps/min
total hepatocytes in liver-chip	40342.50	
Average GU, IR in liver-chip	4.52×10^{-6}	µmol/min
Average GU, IS in liver-chip	1.08×10^{-5}	µmol/min
volume perfused for 2 hours at 20 µL/h	40.00	µL
GU for 40 µL	0.01	mM/hr
volume perfused for 1 hour at 100 µL/h	100.00	µL
GU for 100 µL	2.71×10^{-3}	mM/hr
Endogenous glucose production (EGP) in Liver in body	11.00	µmol/kg body/min
EGP in liver per hepatocyte	4.31×10^{-9}	µmol/heps/min
EGP in liver-chip	1.74×10^{-4}	µmol/min
volume perfused for 2 hours at 20 µL/h	40.00	µL
EGP for 40 µL	0.26	mM/hr
volume perfused for 1 hour at 100 µL/h	100.00	µL
EGP for 100 µL	0.10	mM/hr

Table 30: Calculations of dead volumes in the two versions of the WAT- and liver-chip setups connected in the 3D printed modular insert cassette

	Version 1 of setup	Vol (µL)	Notes	Version 2 of setup	Vol (µL)	Notes
WAT	WAT-chip volume	9.50	rev 1 WAT-chip	WAT-chip volume	9.50	rev 2 WAT-chip
	connector volume	0.88	PDMS top	connector volume	0.66	step connector
	TPE gasket voume	2.36	750 µm high, 2 mm diameter	TPE gasket volume	0.20	250 µm high, 1 mm diameter
	sensor volume up to glucose sensor	15.34	750 µm high sensor channel	sensor volume up to glucose sensor	4.86	250 µm high sensor channel
	total volume up to glucose sensor from media inlet	25.70		total volume up to glucose sensor from media inlet	15.23	
	residence time for 20 µL/h flowrate (min)	77.11		residence time for 20 µL/h flowrate (min)	45.68	
	residence time for 100 µL/h flowrate (min)	15.42		residence time for 100 µL/h flowrate (min)	9.14	
Liver	liver-chip volume	5.88	rev 2 liver-chip	liver-chip volume	5.88	rev 3 liver-chip
	connector volume	0.88	PDMS top	connector volume	0.66	step connector
	TPE gasket volume	2.36	750 µm high, 2 mm diameter	TPE gasket volume	0.20	250 µm high, 1 mm diameter
	sensor volume up to glucose sensor	15.34	750 µm high sensor channel	sensor volume up to glucose sensor	3.84	250 µm high sensor channel
	total volume up to glucose sensor from media inlet	22.08		total volume up to glucose sensor from media inlet	10.58	
	residence time for 20 µL/h flowrate (min)	66.25		residence time for 20 µL/h flowrate (min)	31.75	
	residence time for 100 µL/h flowrate (min)	13.25		residence time for 100 µL/h flowrate (min)	6.35	

Version 1 of the setup comprised a wider cassette with a longer sensor channel, gaskets with inner diameter 2 mm and 750 µm high TPE and a sensor channel of height 750 µm. This was perfused at 20 µL/h with a linear push perfusion regime. Version 2 of the setup moved to a recirculation setup with higher flowrate of 100 µL/h, thinner and shorter sensor channels of height 250 µm and gaskets of height 250 µm and inner diameter 1 mm. The cassette dimensions were also adjusted to ensure the closest possible alignment of the sensor cables to one another. This greatly reduced the lag time, which was demonstrated in experiments to be nearly 60 min for the liver-chip with linear perfusion (Figure 57.a). While the sensors reported the values of low glucose as approximately 4.55 mM and high as approximately 7 mM, no conclusions could

be drawn about the actual consumption of glucose by the hepatocytes. With the introduction of the recirculation regime in Version 2 of the setup, the lag time was not calculated anymore but instead, when a new media condition was added to the reservoir, the system was flushed at a high flowrate (3000 µL/h) to replenish the system with the new medium. Over a period of 40 hours, there was an observed decrease in oxygen concentration in a recirculation system with liver-chips compared to the blank chips (collagen-coated chips without cells, connected in an identical manner to the liver-chips) (Figure 57.b). The reduction in oxygen concentration could be due to the high rate of oxygen consumption by cells, and differences in oxygen consumption rates across chips could be attributed to differences in cell coverage across the chips or the formation of bubbles. The oxygen sensor was used as a reference measurement for oxygen compensation and the slight variation in oxygen concentration or sensor deterioration might have influenced the decline in glucose concentration reported by the sensor in the blank chips as 8.5 mM at t0 compared to 7.5 mM at the end of 40 hours (Figure 57.c). Hence, further investigation is required to conclude a consumption of glucose in the chips.

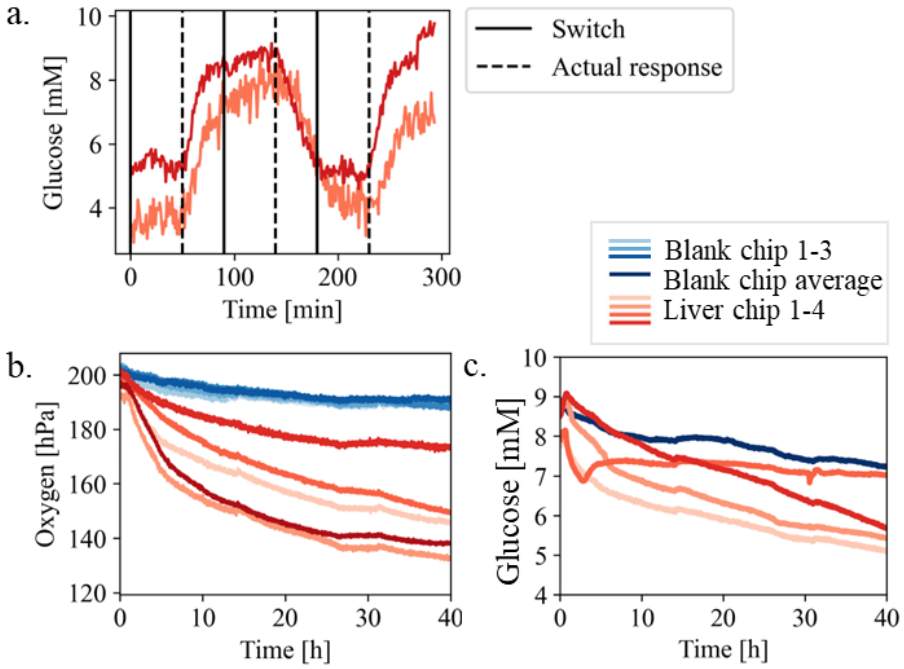

Figure 57: Glucose and oxygen measurements via sensors integrated into the 3D printed modular insert cassette. (a.) Glucose measurements (in mM) as a function of time (min) during a linear perfusion (version 1 of setup) experiment with two liver-chips with cells (red and orange line data). The solid black lines indicate the actual timepoint of switching the medium conditions while the dotted black lines shows the timepoint of response of the system to this switch. At t=0 and 180 min, the media was switched from low glucose (4.55 mM glucose) to high (7 mM glucose) and at t=90 min, the media was switched from high to low glucose. (b.) Oxygen concentrations in the liver-chip (lines in shades of red and orange) compared to blank chips (lines in shades of blue) in a recirculation flow setup (version 2) showing a decrease in the oxygen concentration during circulation in the chip over 40 hours for the chips with cells compared to the blank chips, (c.) Glucose concentration in the chips with hepatocytes (shades of red) compared to the blank chips (blue) as a function of time in a recirculation flow setup (version 2).

The resolution of the sensors was compared to a standard commercially available Quantichrome glucose detection assay (Table 31). Based on the calculations above, it was clear

to use a recirculating perfusion regime to accumulate enough glucose to be within the range of sensitivity and resolution of the sensors. All three sensor characteristics were lower for the glucose sensors compared to the glucose assay, in addition to measurements in real-time as opposed to from the effluent.

Table 31: Comparison of glucose sensor characteristics to that of a commercial glucose assay

	Glucose sensor	Commercial glucose assay
Resolution [mM]	0.086	0.128
LOQ [mM]	0.858	1.28
LOD [mM]	0.257	0.422

The sensor integration experiments demonstrated that with certain design considerations and system modification, it was possible to integrate sensors and track parameters affecting cell culture on-chip in real-time. However, experimental setup considerations were noted from these experiments for the future -

- The choice of syringes used in the syringe pump influenced the glucose readout. With the use of syringes with a plastic plunger (B Braun™ Injekt™ Solo), the data appeared jerky for every timepoint. Peristaltic pumps provided smoother flow profiles as well (Figure 58.a.).
- Maintaining the setup at 37˚C in the ALS box and degassing the media was important due to the shape of the sensor serving as a bubble trap and leading to a failed readout. Flushing out the bubble at a high flowrate of 1000 µL/h recovered the readout and bubble-formation had to be closely monitored when the media was not degassed before perfusion through the system (Figure 58.b).
- The formulation of the sensor cocktail influenced the sensor properties and stability. Further studies are also required to assess the effect of chip sterilization method on the sensors.

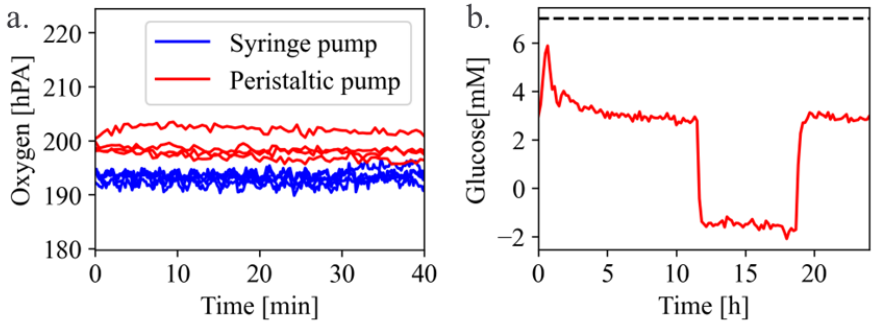

Figure 58: Impact of the experimental setup on sensor readout, (a.) Difference in oxygen readouts obtained when perfused with a syringe pump with syringes with a plastic plunger in linear push perfusion regime compared to a linear recirculating perfusion regime via the peristaltic pump, (b.) Change in glucose readout (red) in the linear perfusion regime with the presence of a bubble and subsequent recovery of readout after flushing out the bubble (the black dotted line indicates the concentration of glucose being perfused in the chip, at 7 mM.

3.7. Design and Fabrication of a Liver-Sinusoid-on-Chip (LSOC)

In the human body, a gradient exists in the environment around the hepatocytes in a sinusoidal unit, such that the hepatocytes exhibit differing functional activity along the length of the sinusoid. Adding this feature to a liver-chip can add physiological significance, going from Zone I (periportal) to Zone III (perivenous). This was attempted by designing a modification in the liver Biochip to create a liver sinusoid-on-chip (LSOC) in collaboration with the company Dynamic42 GmbH, Jena, Germany. Beginning with a simulation study of the possible methodologies to incorporate zonation, design criteria were established and fabrication strategies for the LSOC were explored. Finally, a case study was performed where oxygen zonation was observed in a chip in real-time with integrated sensors. Parallelly, a zonation study was established and performed on HepaRG™ cells in well plates to assess their sensitivity to induced gradients of various species.

3.7.1. Simulation of zonation concepts in the liver Biochip

COMSOL simulations were employed to study the mixing effect of two streams, one containing a dissolved media component being mixed into the media channel of the liver-chip. 2D simulations were set up to study the flow and mixing patterns for an external stream adding a certain component into the main media channel, with the intention of finding the ideal mixing strategy which could be fabricated as an add-on feature onto the liver Biochip. The main simulations have been highlighted below for the media channel dimensions of the liver Biochip, taking a concentration of 1 mM for an arbitrary molecule being mixed into the media stream. The media stream would have a concentration of zero for the molecule at the start.

3.7.1.1. Version 1: Branch channel concept

With the branch channel concept, a side channel connects into the media channel to pour its contents into the media channel such that the two flows mix along the length of the channel. The side stream flows into the media channel at various points along the channel such that mixing occurred at intervals with sequentially increasing concentration of the species. The width of the channels varied to account for the resistance within the channel, to ensure equal flow across the entire branched side channel. Up to a certain flowrate within the media channel, the mixing created a diffusion-driven gradient (Figure 59.a,c) and simulations of higher flowrates show a more abrupt gradient given the convective flow component dominating the flow patterns in the media channel (Figure 59.b,d). Practically, this model would be challenging to fabricate and integrate into the footprint of the liver Biochip given the limited space around the tissue chambers, so the branched shower concept was studied next.

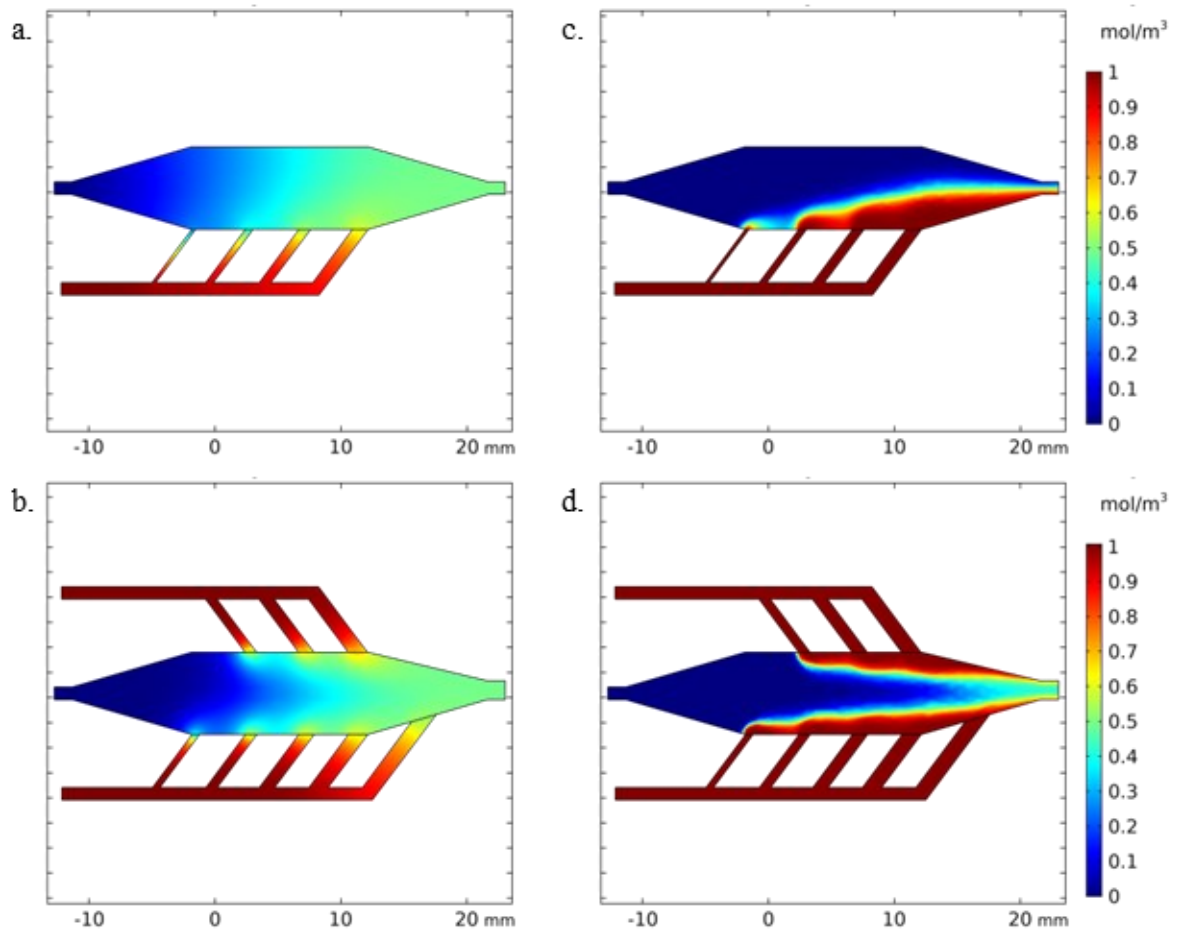

Figure 59: Simulated concentration profile of a 1 mM solution of species A perfused into the branched channel, mixing with the media channel with species A concentration of zero. (a.) Single branch channel with branch flowrate = media flowrate = 50 µL/min, (b.) Double branch channel, with branch flowrate = media flowrate = 50 µL/min, (c.) Single branch channel with branch flowrate = media flowrate = 5 mL/min, (b.) Double branch channel, with branch flowrate = media flowrate = 5 mL/min

3.7.1.2. Version 2.a.: Branched shower concept

This concept of LSOC added parallel channels on top of the media channel, such that the stream with species A could be showered onto the media channel. The first idea for this concept involved a network of channels flowing across the top of the media channel, perpendicular to the direction of media flow and showering contents onto the media channel below through pores of fixed radii in a 75 µm thick rigid plastic film. The pore diameters were calculated based on the criteria of equal flowrate through all pores across the length of the shower branch (methods section 2.9.1). For these simulations, the flowrate of one row of shower pores was chosen to be up to 10% of the media flowrate so as not to add significant shear to the hepatocytes. This concept was tested with a row of 9 pores, with shower flowrate 10% of media flowrate. Taking glucagon as a specific example of a dissolved species which could influence zonation in the LSOC, the shower inlet concentration was fixed to 1 mM, leading to a gradient of 0 to 150 µM of glucagon across base of the media channel (Figure 60.a). This principle was expanded to 4 rows of 11 pores each, and this time a shower flowrate of 1% of media flowrate per branch was explored, to create a uniform distance leading to a gradient across the base of the media channel without significantly changing the shear rate on the cells (Figure 60.b). With

an inlet glucagon concentration of 1 mM, the gradient that the hepatocytes would experience at the base of the media channel is between 0 to 40 nM (40 x 10^{-6} mol.m^{-3}). This implied that a much higher starting concentration of glucagon would be required to achieve the desired final gradient concentration 150 µM at the base of the media channel. Additionally, the wall shear stress plots at the base of the media channel revealed that the shear stress experienced by the hepatocytes at the base of the media channel would be similar for the cases of flowrates of 1% or 10% (Figure 60.c).

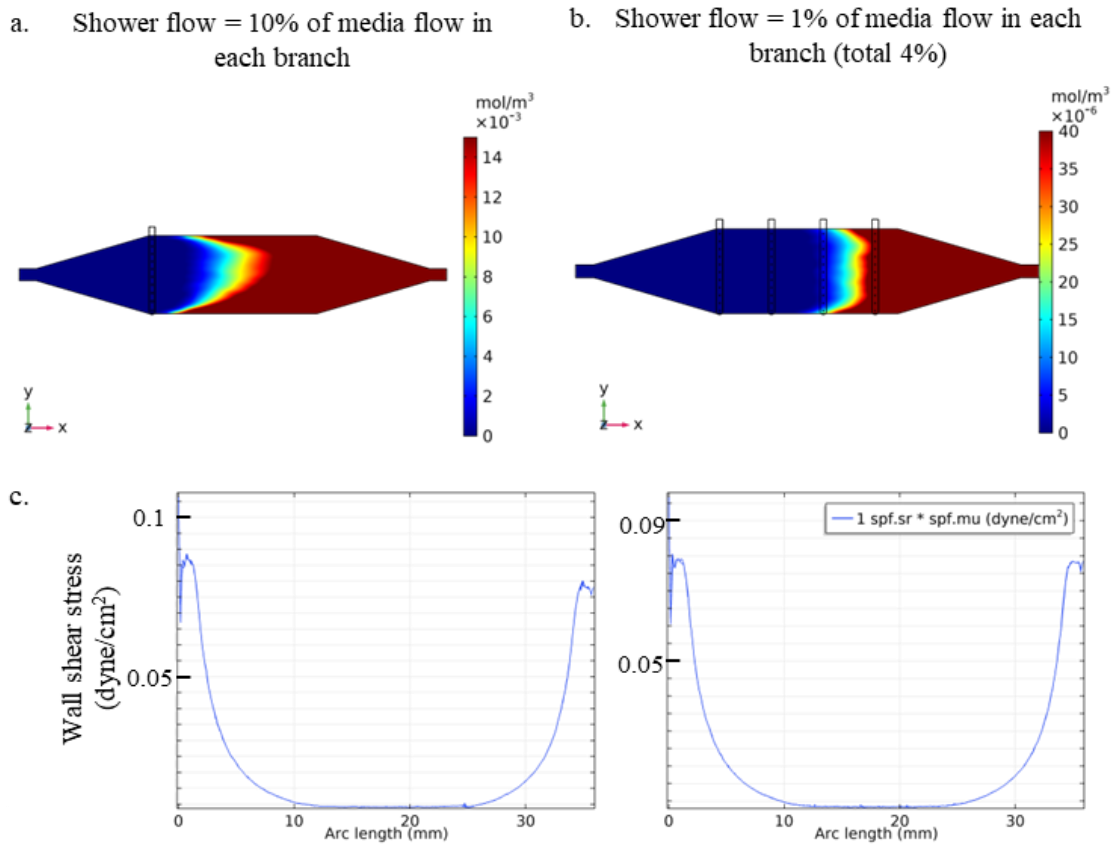

Figure 60: Simulations of the branched shower concept, of flow and concentrations of glucagon at the base of the media channel. (a.) Single branch with branch flowrate = 10% of media flowrate, (b.) Flow through 4 branches where branch flowrate for each branch = 1% of media flowrate, (c.) Wall shear stress calculated across the length of the media channel from inlet to outlet at the base of the media channel.

The concept of the branched shower channels was fabricated out of lasercut PMMA, with the shower inlet bifurcating to the branches leading perpendicularly above the media channel (Figure 61). This branched shower concept would be bonded to the top of the media channel of the liver Biochip.

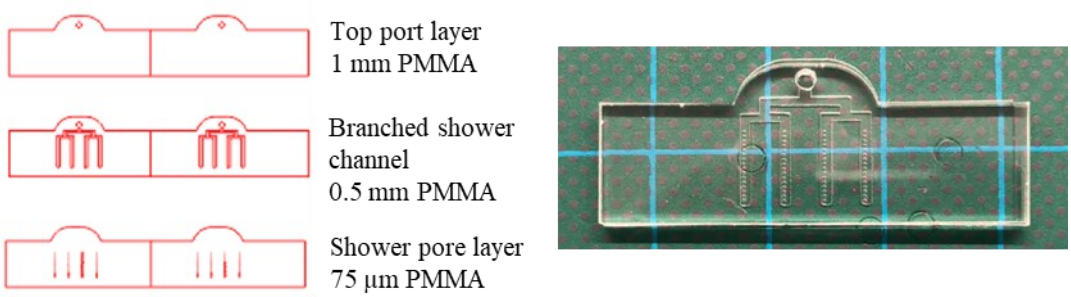

Figure 61: Design of the branched shower top for the liver Biochip with PMMA layers (red) and a picture of the final assembly, bonded via thermal fusion bonding.

The first iteration of fabrication with branched shower had a 75 µm PMMA shower pore layer and parameters were optimized on a lasercutter at Fraunhofer IGB with manual height adjustment of the laser (Universal Laser Systems). The expected dimensions of the smallest and largest pore were 110 µm and 200 µm respectively for a 75 µm thick shower pore layer. Large variations in pore diameter were observed during the lasercutting process and this could influence the flow patterns through the branches upon fabrication. The branch channels themselves had varying dimensions, and the next version of the shower channel mitigated these deviations.

Table 32: Dimensions of pores in the branched shower concept while lasercutting a 75 µm thick PMMA sheet (none: indicates that the material was not cut through).

Trial	Power (%)	Speed (%)	PPI (%)	Smallest pore diameter (µm)	Largest pore diameter (µm)
1	10	10	1000	177, 175	238, 272
2	5	10	1000	none	none
3	5	15	1000	none	None
4	10	5	1000	269, 247	333, 267
5	10	7	1000	207, 230	298. 271
6	7	10	1000	153, 148	230, 212

3.7.1.3. Version 2.b.: Unbranched shower concept

The branched shower concept was further simplified where a parallel shower channel was placed on top of the media channel, separated by a film of rigid plastic with pores ablated into it. This alleviated the fabrication challenges of the branched shower, where even minor misalignments could lead to a change in flow pattern. The unbranched shower concept also eliminated the need to calculate resistance because the front of liquid entering the shower would flow through the rows of ports in a uniform fashion, leading to a smooth mixing gradient across the media channel (Figure 62.b).

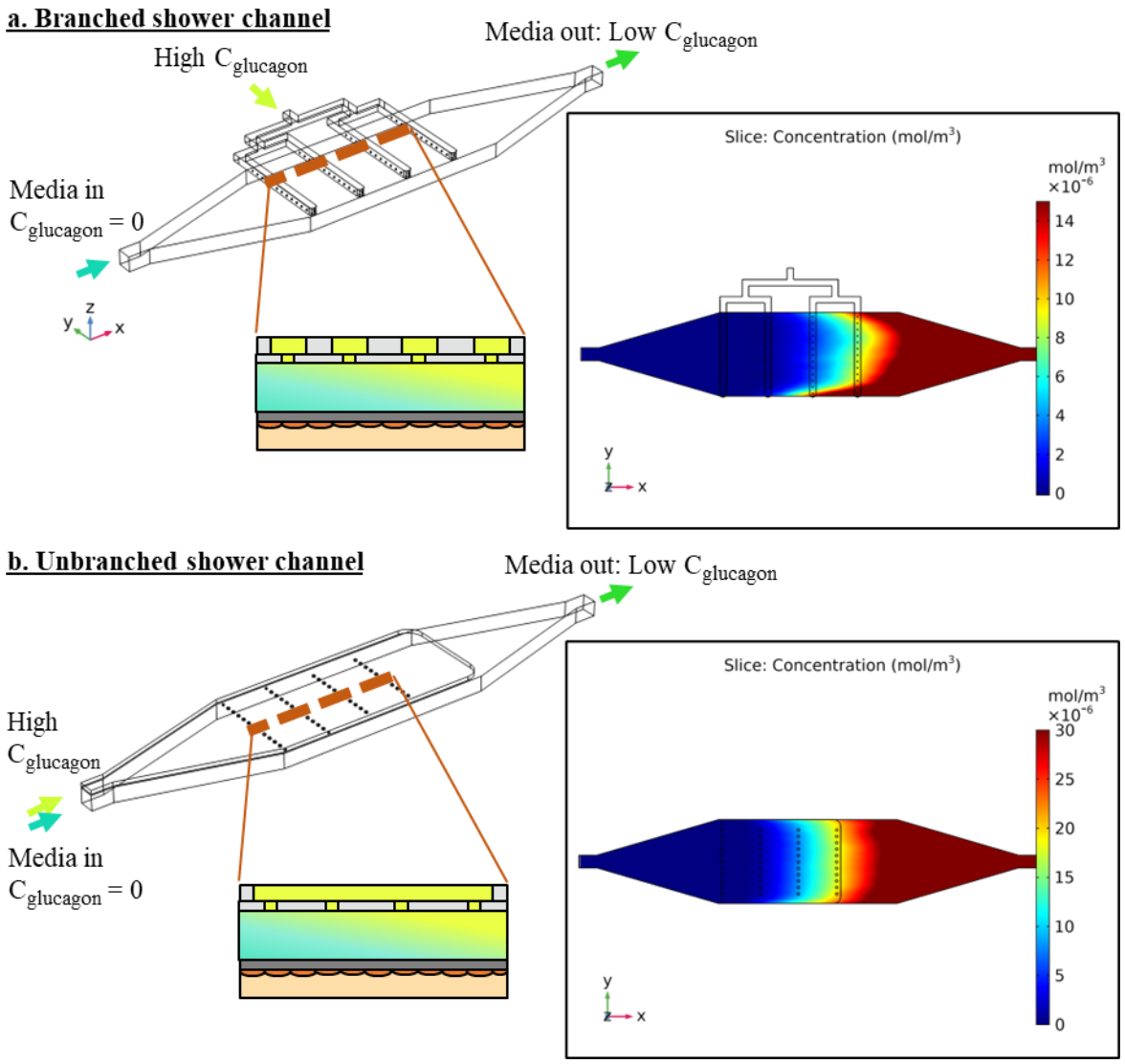

Figure 62: Design schematic and differences in mixing patterns created by the branched v/s unbranched shower layer (a.) Branched shower concept where the shower inlet for a high concentration glucagon stream entering perpendicular to the media flow direction mixes with the media flow via the branched pore layer. Branch flowrate = 10% of media flowrate, and Cglucagon = 1 mol/m^3 (b.) Unbranched shower concept where the shower inlet with a high concentration glucagon stream entering parallel to the media flow direction mixes with the media flow via the pore layer. Shower flowrate = 10% of media flowrate and Cglucagon = 1 mol/m^3.

3.7.1.4. Modeling and characterization of zonation in the liver Biochip version BC005

The liver Biochip underwent a design modification to reduce the tissue channel area, reducing the number of cells required per chip in version BC005 (tissue culture volume of version BC002: 100 µL, tissue culture volume of version BC005: 55 µL,). Fabrication of the ShowerTop on this version of the Biochip allowed for a larger bonding area around the sides of the tissue channel (Figure 63). A model was set up in the liver Biochip to study the gradients formed by four media components as drivers of zonation – insulin, glucagon, glucose, and oxygen. The appropriate physiological concentrations of dissolved species were explored, with the intention of moving fabrication processes to the new version with smaller tissue chamber footprint (Table 33).

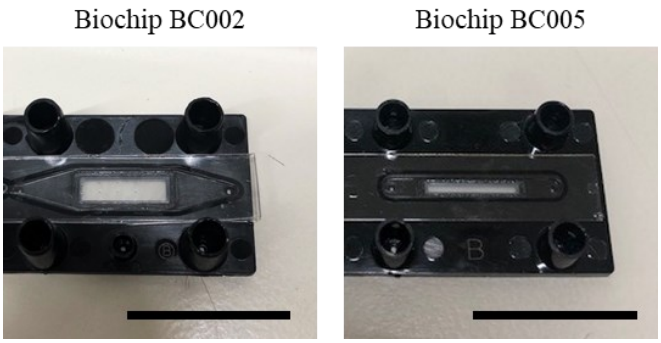

Figure 63: Pictures of Biochip versions BC002 and BC005. Scalebar: 26 mm

Table 33: Simulated concentrations of dissolved species in the shower inlet and media outlet

Species	Shower inlet [µM]	Media outlet [µM]	Diffusion coefficient [m^2/s]	Reference
Glucagon	1.44	0.1	1.5×10^{-10}	(Buladi et al., 1996)
Glucose	55×10^3	8.5×10^3	9.1×10^{-10}	
Insulin	11.1	0.9	1.5×10^{-10}	
Oxygen	200	178	3.15×10^{-9}	(Brischwein et al., 2009)

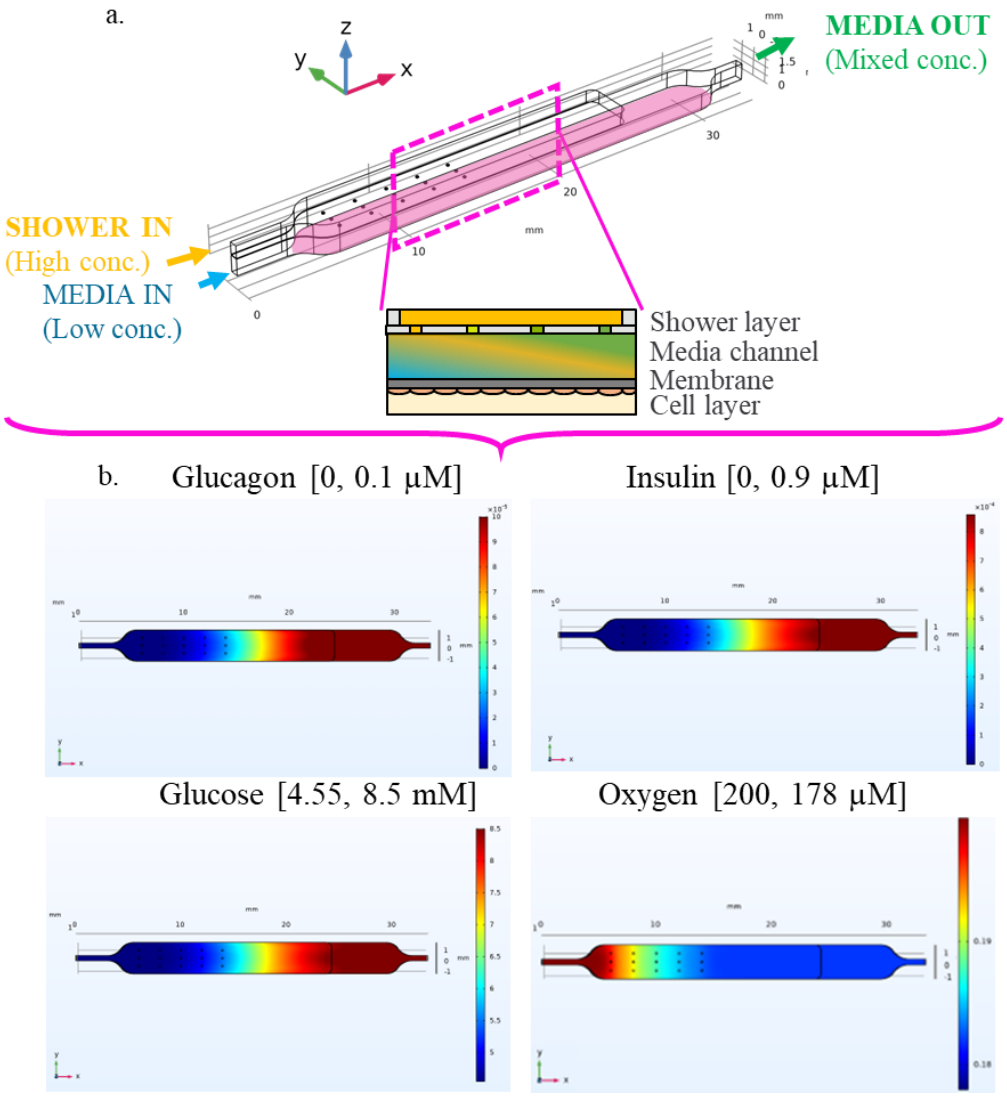

Figure 64: Simulation of concentrations of zonation parameters in the version BC005 of the liver Biochip (a.) Schematic of the Biochip media channel with the shower channel running parallel to media flow such that a molecule of higher concentration (yellow) showered on top of the media channel mixes with the media (blue) leading to a gradient of the molecule along the length of the media channel (green) as experienced by the cells below the membrane. The simulations are presented for a fluid layer near the base of the media channel (pink layer) (b.) Simulations of each zonation parameter with the range of the color legend in box brackets [blue value of legend, red value of legend] for a flowrate of 100 µL/h in the media channel and shower flowrate being 10% of media flowrate.

3.7.2. Design criteria, fabrication strategies and characterization of the ShowerTop of the LSOC

The unbranched shower channel part (ShowerTop) was investigated for fabrication for the LSOC with the following design criteria:

- Fabrication to ensure completely flat shower pore layer, composed of minimally thick rigid plastic for minimal resistance (in this case, the 50 µm PC bonding foil used in the liver Biochip for the chip bottom)
- Material designs compatible with the fabrication strategies such as thermal fusion bonding and laser welding, ensuring minimal change in dimensions during fabrication
- Inlet of the ShowerTop located at a reasonable point to allow imaging, and interfacing with the perfusion setup
- Shower flowrate should be up to 10% of media flowrate to impart minimal additional shear stress on the hepatocytes at the base of the media channel

3.7.2.1. ShowerTop for liver Biochip version BC002 – fabrication

The choice of pore layer material was switched from 75 µm PMMA to PC because PMMA tended to expand during thermal fusion bonding (Table 34). Bonding temperatures in the future were maintained lower than the glass transition temperature of PC and this material also allowed for the attachment of the ShowerTop onto the LSOC via laser welding.

Table 34: Measurements of lasercut pore diameters before and after bonding for 75 µm PMMA (expected pore diameter is 150 µm for the smallest pore and 200 µm for the largest pore)

Before bonding (µm)		After bonding (µm)	
smallest	largest	smallest	largest
113	202	125	228
165	214	168	232
159	191	162	219
139	212	170	247

Two trials were explored for the fabrication of the ShowerTop for the LSOC with Biochip version BC002. The first trial involved thermal fusion bonding the PMMA shower channel to the PC top and shower pore bottom layer, and laser welding the entire setup onto the liver Biochip. Due to the large unsupported area of the shower channel, supporting structures were created in the shower channel to prevent warping of the shower pore layer (Figure 65.a). The thermal fusion bonding temperatures were in the range of 115°C and carried out in the hotpress and hence, a thicker shower pore layer was used to also prevent heat-induced warping of the layers. In the second fabrication trial, the PMMA shower layer was replaced by TPE.

Fabrication could be carried out at lower temperatures (as low as 60°C), and the shower pore layer was now constructed from PC of 50 µm (Figure 65.b). In this case, the shower pore layer was directly laser welded onto the liver Biochip, followed by layering the upper layers and bonding the setup in the oven via a ramping protocol (Methods sub-section 2.3.2.2).

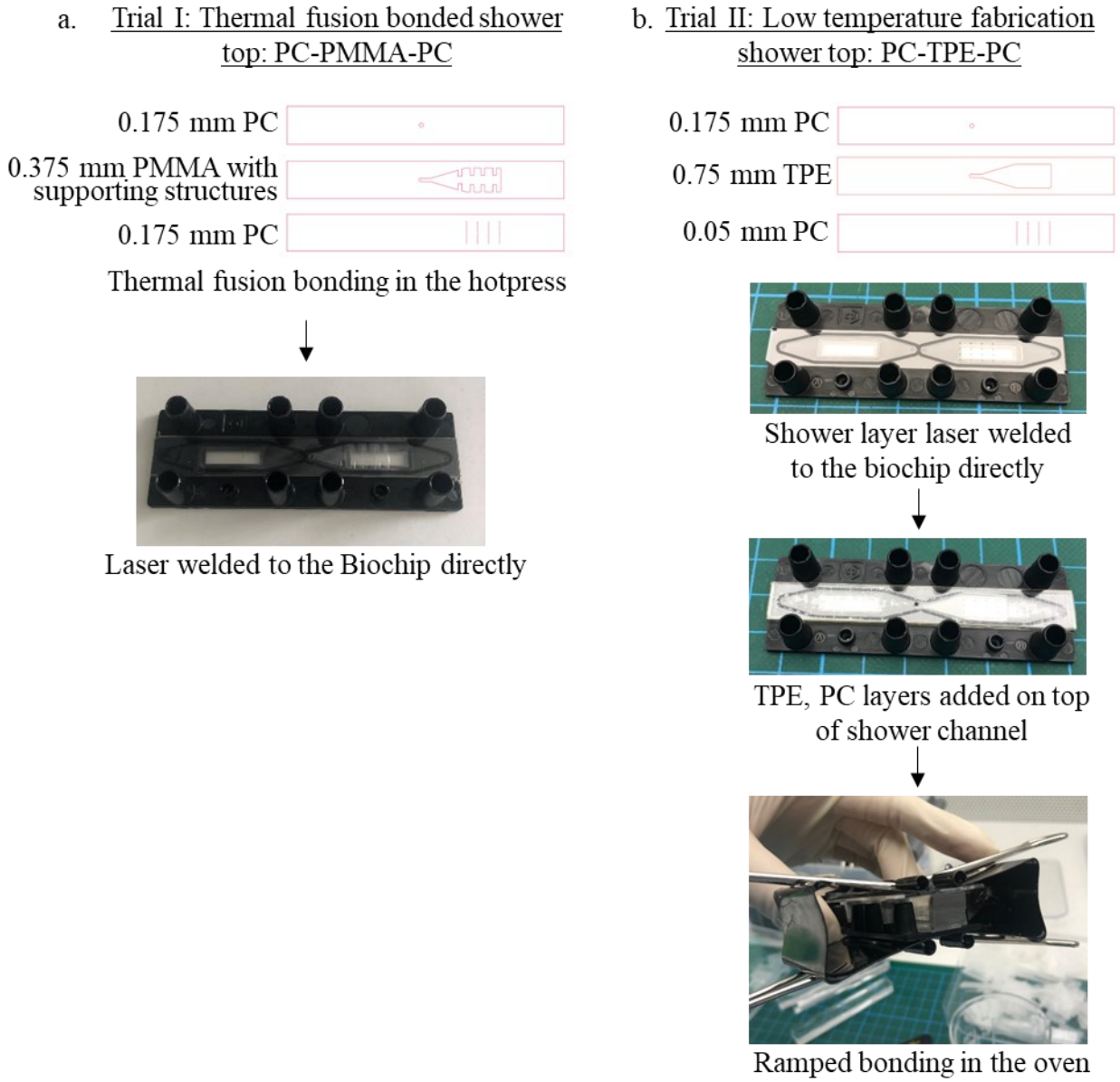

Figure 65: Fabrication trials for the unbranched ShowerTop (a.) Fabrication trial 1 involving PC-PMMA-PC bonding at 115°C in the hotpress. The PMMA had supporting structures and PC foil was thicker to prevent warping during the thermal fusion bonding process. The ShowerTop was then laser welded onto the liver Biochip, (b.) Fabrication trial II involving PC-TPE-PC, starting with laser welding the shower pore layer to the Biochip, and then bonding the two upper layers at 60°C in the oven via a ramping protocol.

3.7.2.2. ShowerTop for liver Biochip version BC002 – Demonstration of gradient formation

Gradient formation in the LSOC was assessed by flowing a solution of FITC-dextran into the shower channel, showered over a PBS solution flowing in the media channel. The flowrate of

the shower channel was 10% of the flowrate of the media channel, set to 50 µL/min. The chip was mounted onto a spinning disc confocal microscope and imaged at four regions over a period of time (Figure 66.a). For four regions in the chip, fluorescent imaging showed an increase in fluorescent intensity of the dye, indicating the formation of a gradient (Figure 66.b).

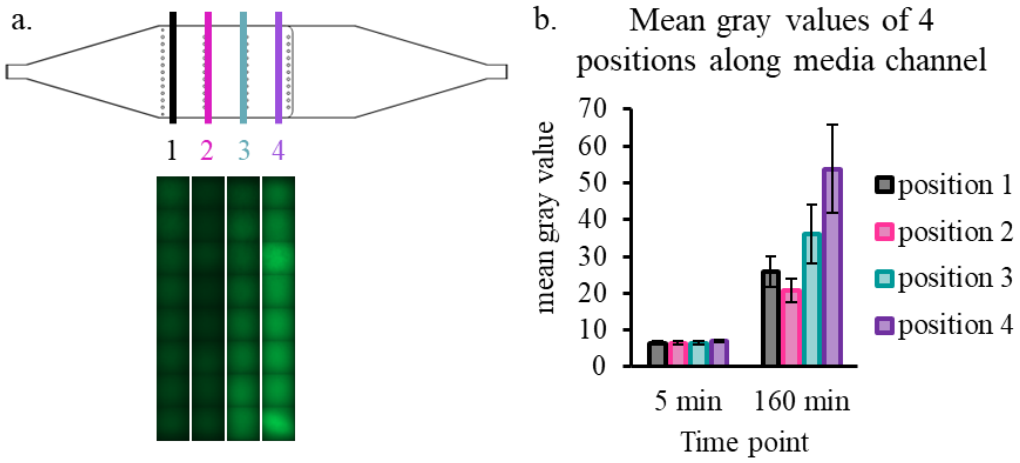

Figure 66: Fluorescence gradient of FITC-dextran across version BC002 of the liver Biochip (a.) Schematic of the 4 regions at which tile scans of fluorescent images were obtained via a spinning disc confocal microscope along with the fluorescent images (each tile measured 400 µm and a total of 8 tiles per column), (b.) Plot of mean gray value of the tile scan at t=5 min and t=160 min for the four positions.

3.7.2.3. ShowerTop for liver Biochip version BC005

These fabrication trials were combined in the final bonding strategy on version BC005 of the Biochip, with smaller tissue channels and increased bonding area around the tissue channel. The final fabrication strategy involved first bonding all the layers PC-TPE-PC in the oven via the ramping protocol, and then laser welding the ShowerTop onto the Biochip (methods section 2.9.2). The lasercutting parameters for the shower channel were optimized to yield consistent pores of 200 µm diameter with every cut in the 50 µm high PC layer, measured via microscopy (Figure 67.a, b). The ShowerTop fabricated with material combinations PC-TPE-PC and PC-PMMA-PC were compared for bond strength via a burst pressure test (Methods sub-section 2.5). Burst test results revealed that the transfer of fabrication protocol to a TPE shower layer had similar bond strength to the PMMA ShowerTop (Figure 67.c).

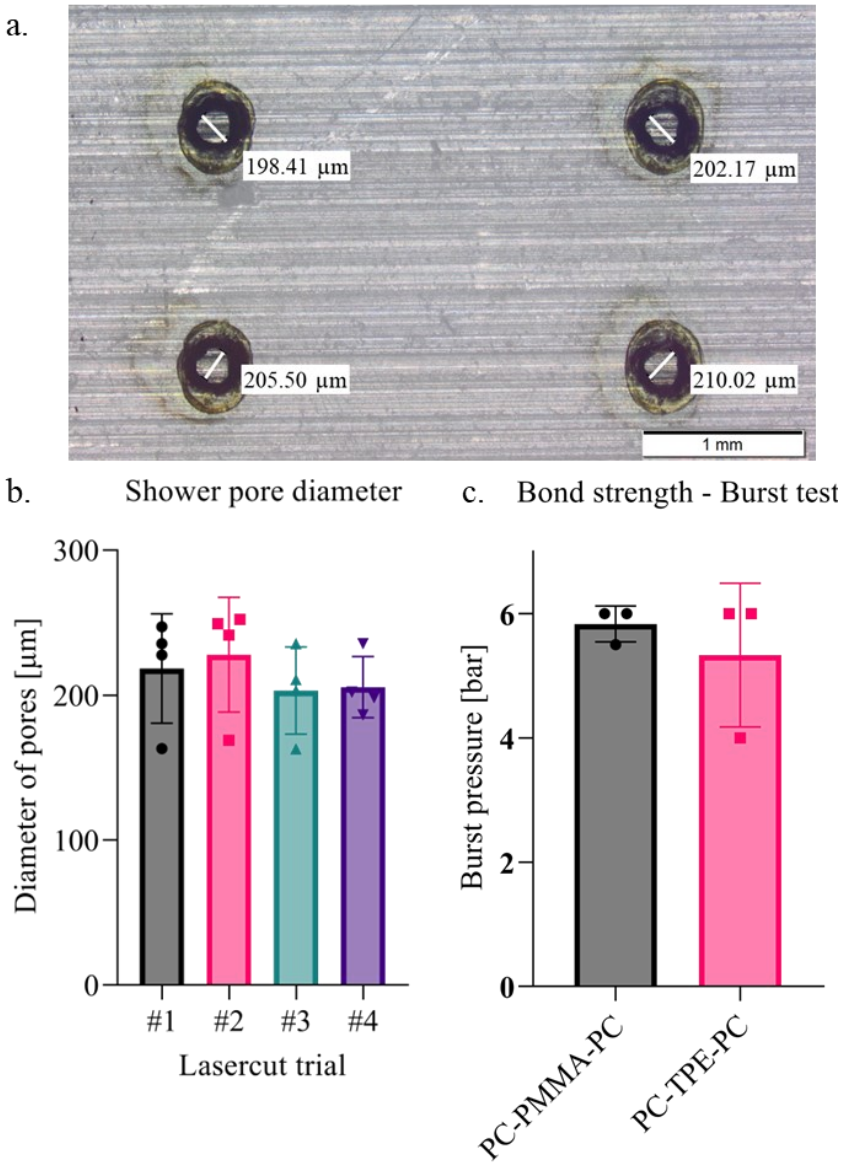

Figure 67: Characterization of fabrication of the ShowerTops in version BC005 of the liver Biochip (a.) Representative microscope image of the PC shower lasercut pores with measured diameters, (b.) Diameter of shower pores measured for n=4 pores for 4 different laser cutting trials with the same parameters on 50 µm PC. Data is presented as mean ± SD and each data point represents a measurement along the diameter of a pore, (c.) Bond strength comparison of ShowerTops fabrication out of PC-PMMA-PC (black) compared to PC-TPE-PC (pink). The data is presented as mean ± SD, for n=3 ShowerTops in each condition.

3.7.2.4. ShowerTop for liver Biochip version BC005 – Demonstration of gradient formation

A demonstration of zonation for liver Biochip version BC005 was set up to evaluate the formation of an oxygen gradient. For this, OxNANO oxygen sensing beads were immobilized in a collagen I hydrogel in the tissue channel of the liver-chip (Figure 68.a). Oxygen saturated PBS was flushed into the media channel at a rate of 50 µL/min and a sodium sulfite solution was flushed through the shower channel at a rate of 0.5 µL/min, gradually mixing and scavenging oxygen from the PBS in the media channel (Figure 68.b). This flowrate showed a clear formation of zonation across the length of the channel, for measured oxygen

concentrations at three points along the length of the channel (Figure 68.c). An equilibrium state was reached over a period of two hours, and a stable gradient maintained for the 6 hour duration of the experiment. While this experiment demonstrated the principle of shower flow-influencing zonation, sodium sulfite is known to be cytotoxic and cannot be used directly in the shower chip unless paired with cobalt nitrate (Kang et al., 2020). Thus, a strategy would need to be devised to indirectly scavenge oxygen from media before the oxygen depleted media is perfused into the shower chip (Tjell *et al.,* in preparation).

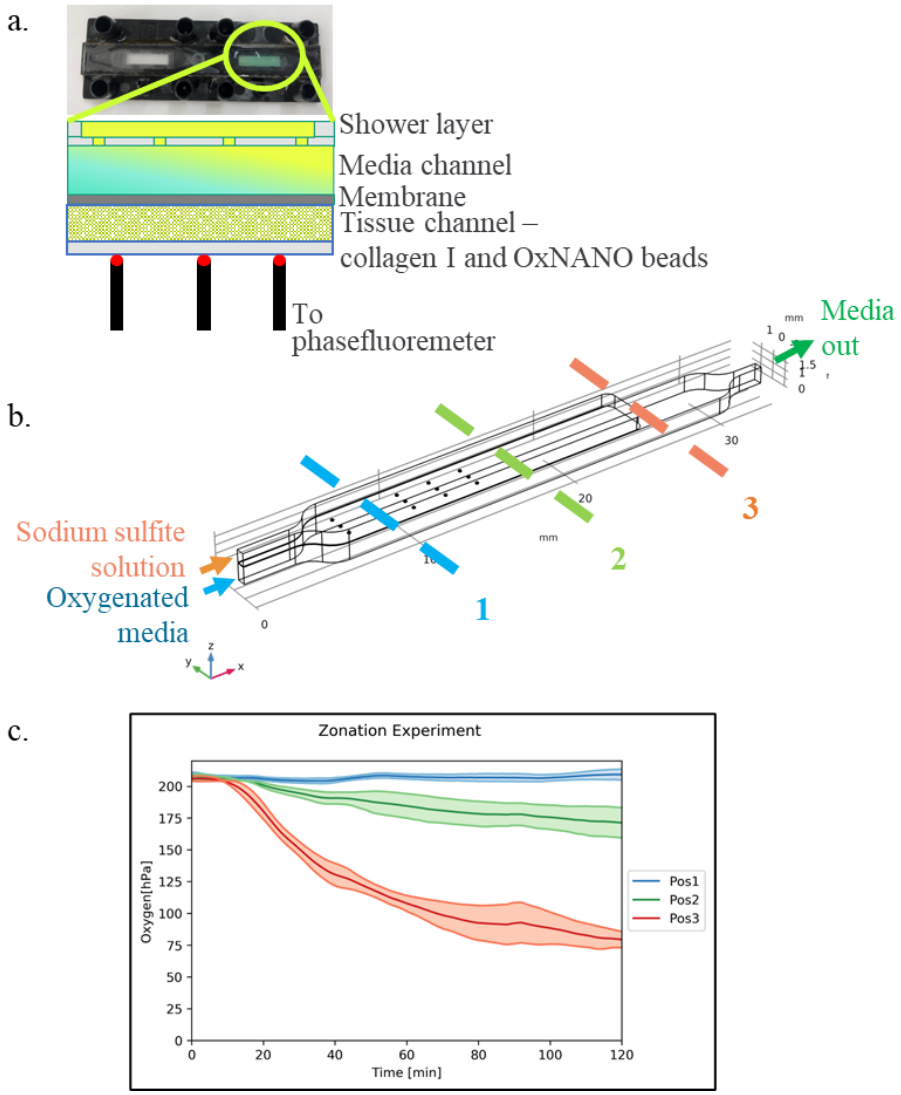

Figure 68: Measurement of the oxygen gradient formation in the liver Biochip version BC005. (a.) Picture of the LSOC with a schematic of the cross section showing the tissue channel with oxygen sensing beads suspended in a hydrogel. The reduction in oxygen levels was measured at the tissue channel where three probes were placed at three points below the tissue channel, connecting to the phasefluorometer, (b.) Schematic of the oxygen gradient setup, and a marking of positions 1 (blue), 2 (green) and 3 (orange) where the oxygen concentration was measured in the tissue channel, (c.) oxygen concentration as a function of time measured by the phasefluorometer for the three positions along the length of the LSOC. Data is presented as mean ± SD for n=3 chips.

The intended use case of this zonation model is to shower a high concentration stream of the zonation parameter (insulin, glucose and glucagon) via the shower channel onto the media

channel, to create a positive gradient going from zero to a defined value (Figure 69.a). Only oxygen would be scavenged across the length of media channel, but the extent of this dilution would be limited. If a high concentration stream of oxygen were perfused across the media channel and showered with a zero-concentration (oxygen depleted) medium, a maximum dilution of 15% can be achieved via the simulations when the flowrate of the shower stream is 10% of the media stream (Figure 69.b).

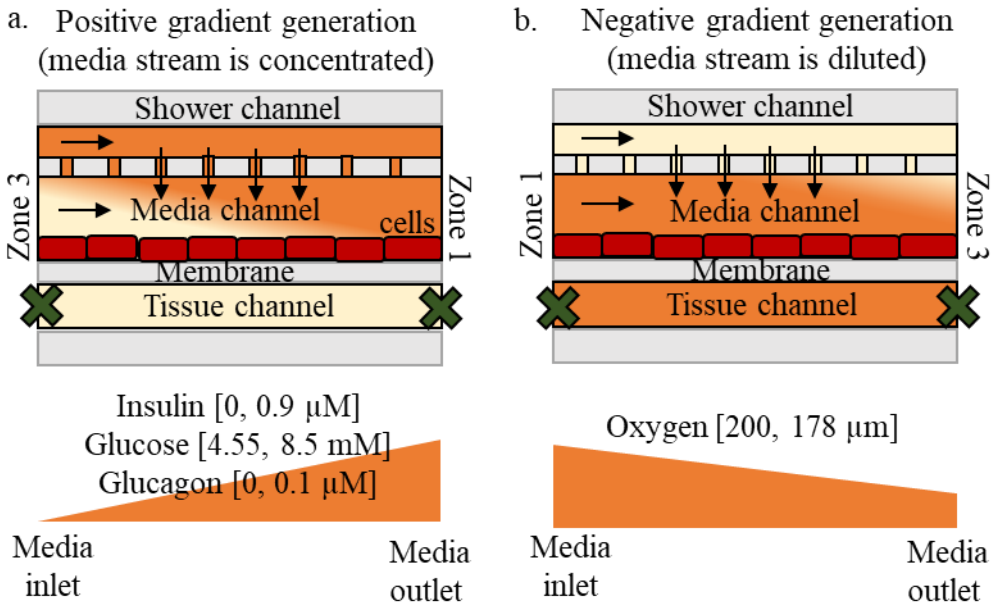

Figure 69: Modes of operation of the LSOC and possible gradients (a.) Positive gradient with the concentration of media stream being showered with high concentrations of zonation parameters, resulting in the appropriate concentrations of insulin, glucose and glucagon. (b.) Negative gradient where the media stream is diluted with the shower stream containing zero concentration of the zonation parameter, resulting in a depletion of oxygen along the length of the media channel. (The concentrations above have been modelled for a flowrate of 100 µL/h, with shower flowrate being 10% of media flowrate).

3.7.3. Study of zonation in HepaRG™ cells

Off-chip experiments were performed on HepaRG™ cells in well plates to evaluate whether the hepatocyte cell line would respond to gradients of glucose, insulin and glucagon. A protocol was developed to starve the hepatocytes with low glucose media, as an important step to create insulin sensitivity (Methods sub-section 2.9.6) (Davidson et al., 2021; Davidson & Khetani, 2020). Four groups of scenarios were studied, and three conditions creating zones 1,2 and 3 per group:

- Physiological concentrations of insulin, glucose and glucagon (Greco et al., 1979).
- The effect of varying concentrations of glucose keeping insulin and glucagon concentrations constant
- Control fed and fasted conditions with HepaRG™ culture-specific concentrations of insulin and glucose and no glucagon
- The effect of activated ammonia cycle for zone 1 conditions of each of the groups above

To quantify response to different combinations of glucose, insulin, glucagon and ammonia, the storage of glycogen, and expression of albumin, CYP3A4, MRP-2, DPPIV, ASS1, GS and presence of lipid droplets within the hepatocytes were studied via staining (Table 35). Qualitative evaluation by microscopy and quantitative measurement using plate reader measurements of plate fluorescence were performed.

Table 35: Expression of markers in hepatocytes based on zone, indicating a higher expression in the periportal (PP) for Zone 1 or perivenous side (PV) for Zone 3

Marker	PP/ PV	References
Argininosuccinate synthetase 1 (ASS-1)	PP	(Cunningham & Porat-Shliom, 2021)
Albumin	PP	(Tonon et al., 2019)
CYP3A4	PV	(Tonon et al., 2019)
dipeptidylpeptidase-4 (DPP-IV)	PV in NAFLD	(Segovia-Miranda et al., 2019)
Glutamine synthetase-1 (GS-1)	PV	(Cunningham & Porat-Shliom, 2021)
Lipid droplets	PV	(Mashek, 2021)
MRP-2	PP, PV	(Čížková et al., 2005)

Periodic acid and Schiff reagent (PAS) and Hoechst staining was performed on fixed cells to assess cell coverage and the glycogen storage by cells across the wells (Figure 70.a). The amylase control, with digested glycogen served as a negative control for the samples and showed lower fluorescence compared to a representative sample. The evaluation of fluorescence of the Hoechst staining revealed uniform cell coverage with all conditions showing similar fluorescence values for nuclei (Figure 70.b). The grouped and normalized PAS staining revealed a significantly higher glycogen storage in the control fed, condition of the HepaRG™ cells compared to the control fasted condition (Figure 70.c). It seemed that changing only the glucose concentrations keeping the insulin and glucagon concentrations constant did not affect the glycogen storage in the HepaRG™ cells. The glycogen storage in zone 1 for the physiological liver condition seemed to be higher than zone 2 or 3 for the same conditions, but the cell coverage for the zone 1 condition also seemed to be irregular.

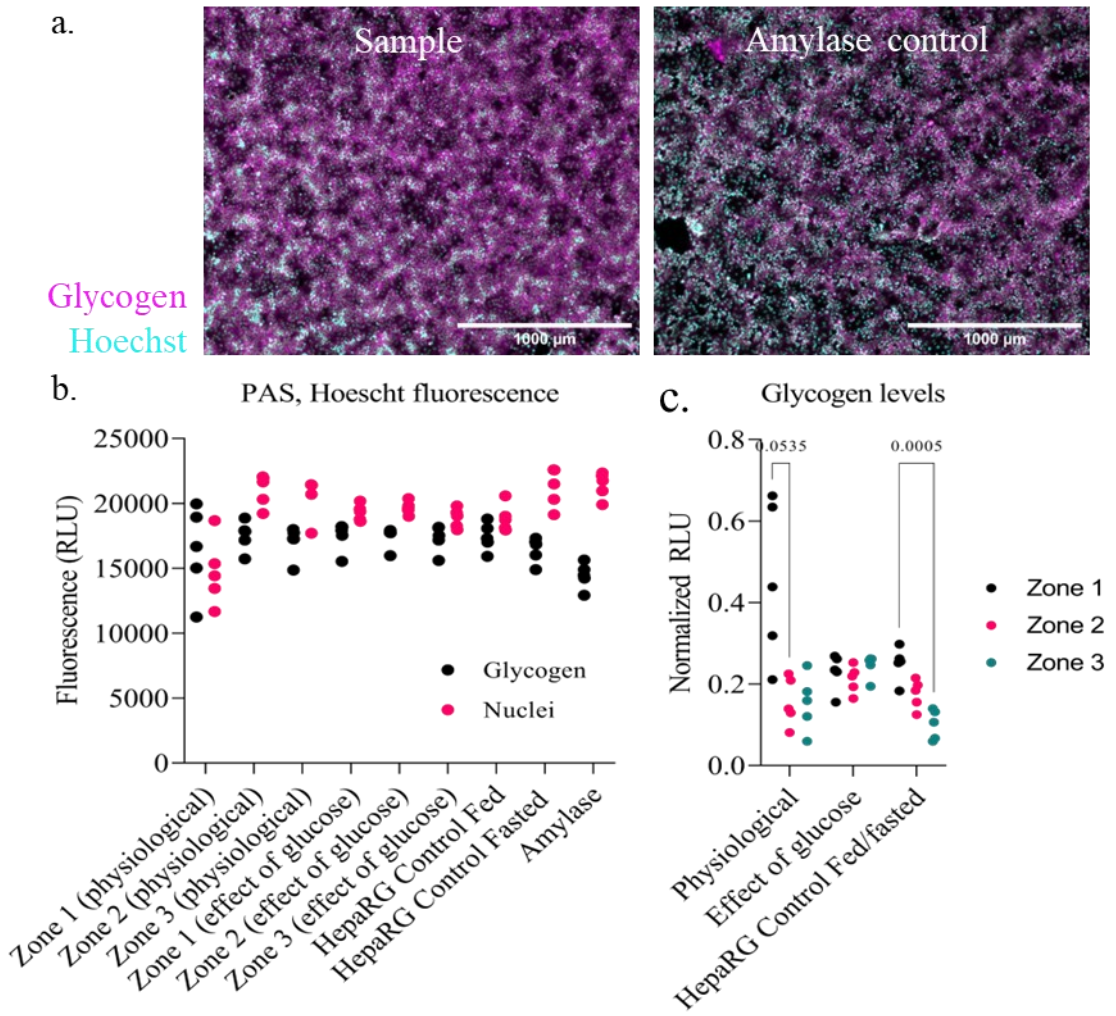

Figure 70: Glycogen storage within HepaRG™ cells for varying media concentrations of glucose, insulin and glucagon. (a.) Representative fluorescent images of a sample stained with PAS compared to an amylase (negative) control where the glycogen is digested. Fluorescence of the glycogen (magenta) and nuclei (cyan) was later quantified via a plate reader (Scalebars: 1000 µm), (b.) Raw values of fluorescence measured on the plate reader for hepatocytes in a 96 well plate for the glycogen (black dots) and Hoechst (pink dots) per well for each condition compared to the amylase (negative) control (n=5 wells of a 96 well plate per condition), (c.) Grouped normalized glycogen fluorescence was calculated by normalizing PAS fluorescence to Hoechst nucleus fluorescence and the amylase control subtracted from each value , to compare each of the conditions for Zone 1 (black dots), Zone 2 (pink dots) and Zone 3 (green dots). 2-way ANOVA conducted on the samples showed insignificant difference between normalized glycogen content in hepatocytes between Zone 1 to 3 in physiological conditions and upon varying glucose concentrations in media, but a significant ($p \leq 0.0005$) for HepaRG™ control fed/fasted conditions (n=5 wells of a 96 well plate per condition).

The hepatocytes were stained and imaged via fluorescence imaging to qualitatively observe the effects of zonation parameters on marker expression. In the physiological concentration scenario, zone 3 seemed to have a higher lipid droplet storage. Higher GS-1 expression was observed in zone 3 for the variable glucose concentration scenario, and higher CYP3A4 expression was observed in control fasted wells with the activation of urea cycle. These images serve to show the cell coverage of hepatocytes and biliary cells and conclusions cannot be drawn without a quantitative evaluation of the entire well for each condition.

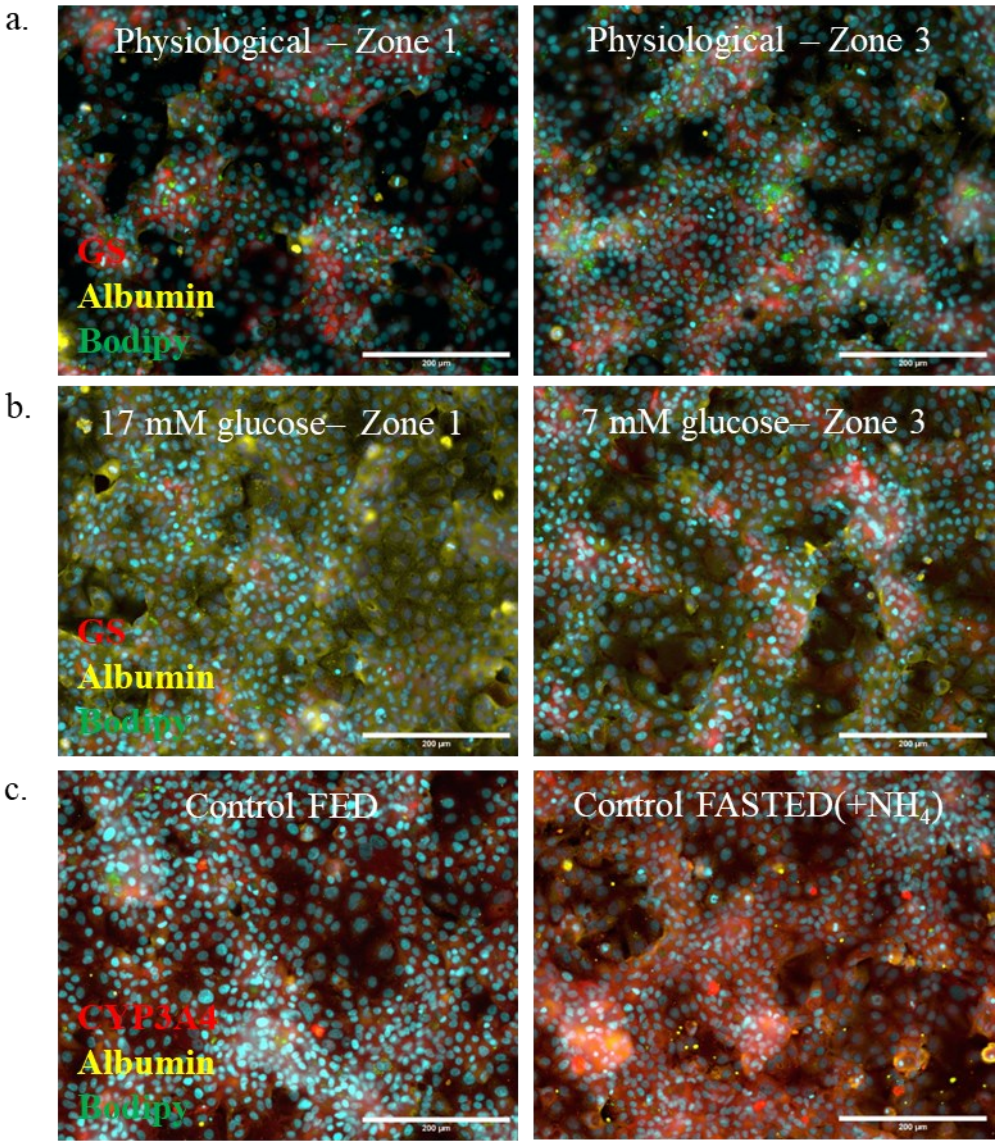

Figure 71: Fuorescent images of zonation parameters influencing HepaRG™ cell functional marker expression (a.) Expression of glutamine synthetase (GS) (red), Albumin (yellow) and lipid droplet storage (green) for zone 1 and 3 with physiological concentration of insulin, glucose and glucagon, (b.) Expression of GS (red), albumin (yellow) and lipid droplet storage (green) for zone 1 and zone 3 for varying glucose concentrations keeping insulin and glucagon constant, (c.) Expression of CYP3A4 (red), Albumin (yellow) and lipid droplet storage (green) between the control fed and control fasted (with activated ammonia cycle). Scalebars: 200 µm

The fluorescence of the stainings was quantified via a plate reader and plotted as a fold change of marker expression from zone 1 to zone 3. The physiological concentrations of glucose, insulin and glucagon led to a higher expression of GS, ASS1 in zone 1 compared to MRP-2, DPPIV in zone 3. The expression of GS is contrary to that observed *in vivo* (Cunningham & Porat-Shliom, 2021). Upon varying the concentrations of glucose only, there seemed to be a higher expression of all markers in zone 3 compared to zone 1. In the comparison of control fed to fasted controls, there was a higher expression of CYP3A4 in zone 3 compared to zone 1 (Figure 72.a).

The ammonia cycle being activated by ammonium chloride showed to induce a zone 3 tendency, as can be seen in the varying glucose conditions and control fed conditions (Figure 72.b). Interestingly the CYP3A4 expression was higher expressed in the zone 1 cases of the control fed and control fasted conditions.

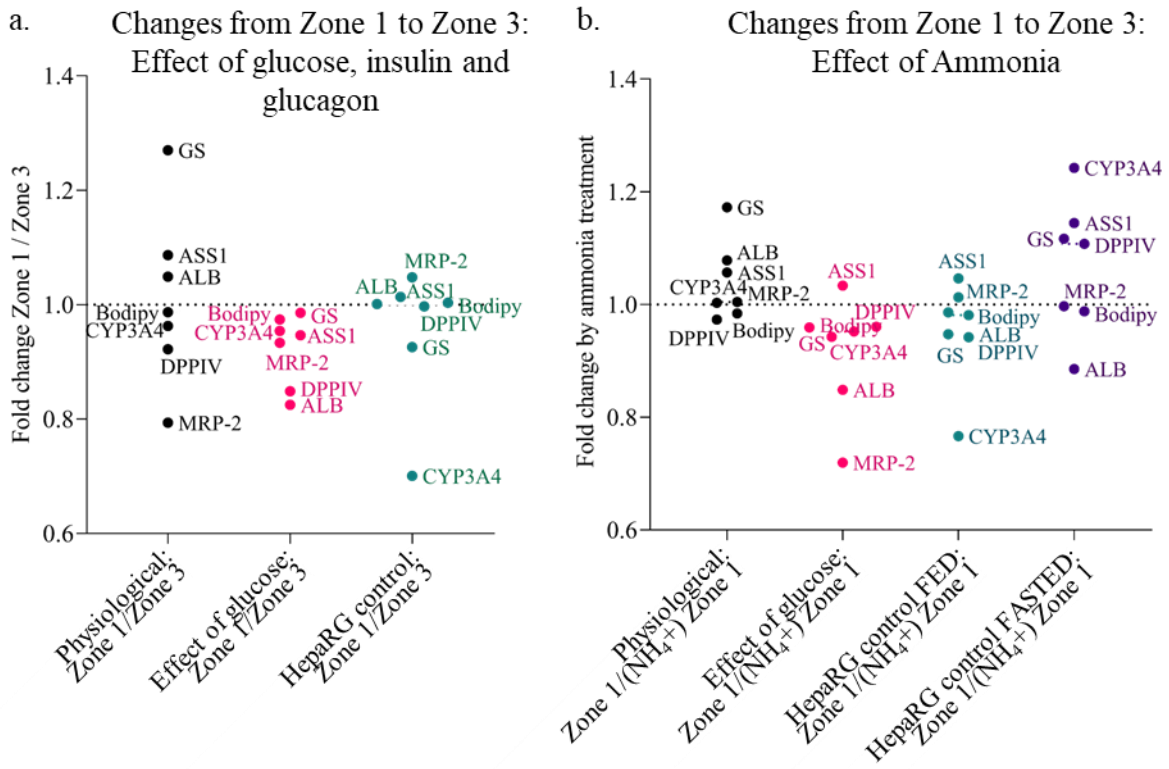

Figure 72: HepaRG™ cell functional marker expression across zone 1 and 3, influenced by zonation parameters. The marker fluorescence was normalized by dividing by Hoechst fluorescence across all wells. (a.) The mean expression of markers for the corresponding fluorescence for zone 1 was divided by zone 3, for the scenarios of physiological concentrations (glucose, insulin, glucagon), variation in glucose concentrations (insulin, glucagon constant), and control fed to fasted for HepaRG™ media (b.) The mean expression of marekrs for corresponding fluorescence for zone 1 was divided by zone 1 with ammonium chloride for the scenarios of physiological concentrations, variation in glucose concentrations, control fed and control fasted for HepaRG™ media. (n=1 well for GS, CYP3A4, ASS1, MRP-2, DPPIV, n=3 wells for Albumin, n=4 wells for Bodipy)

Tests were also performed on HepaRG™ cells in well plates for other zonation stimuli such as CHIR99021 and oxygen. The small molecule CHIR99021 is known to activate Wnt/ β-catenin pathway leading to the induction of zonation (Russell & Monga, 2018), while oxygen concentration differences have characterized the environment of Zone 1 with 84-91 µM and Zone 3 with 42-49 µM oxygen (Jungermann & Kietzmann, 2000). A detailed study would need to be performed to understand all the changes in marker expression upon the introduction of CHIR. Hypoxia tends to lead to an increase in lipid droplet accumulation and the CHIR condition tends to cause a reduction in cell coverage for the maximum intensity project images of HepaRG™ in a well plate (Figure 73.a).

A gradient of sodium sulfite was also studied (Kang et al., 2018) where calculated amounts of sodium sulfite and cobalt nitrate were added to the culture media to study physiological oxygen

concentrations corresponding to 18% and 8% oxygen. The cell morphology and marker expression appeared to show qualitative differences in fluorescent images of these conditions (Figure 73.b). This indicates that oxygen depletion within the chip could drive hepatic zonation in addition to a gradient of glucose, insulin and glucagon.

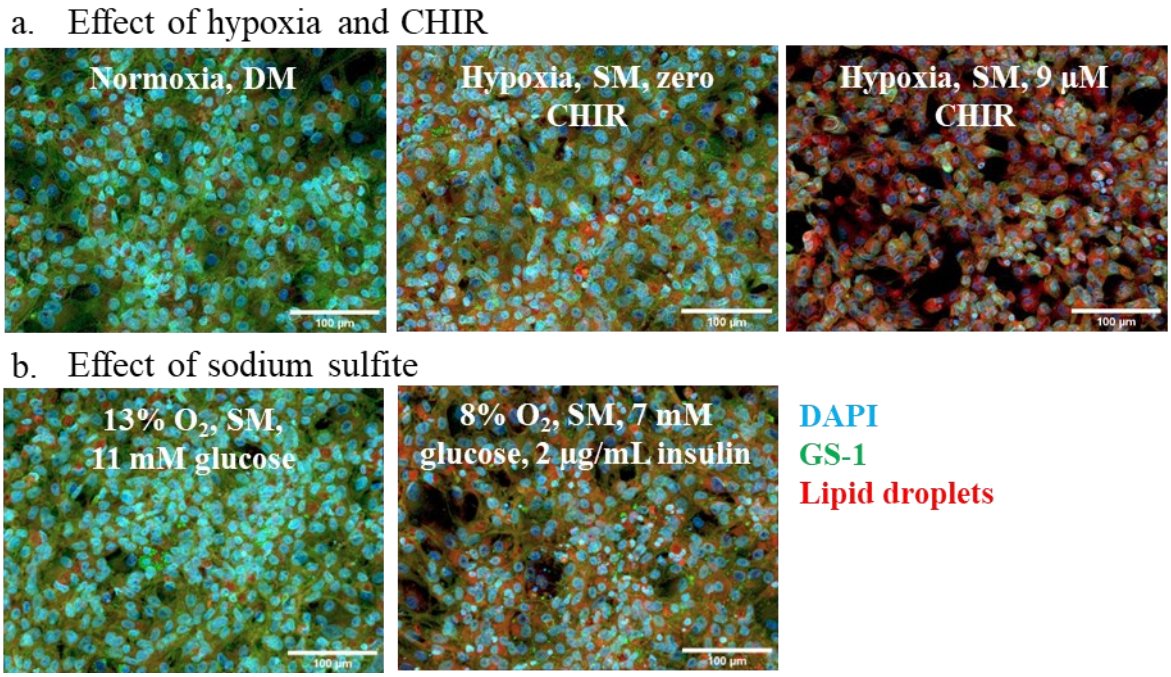

Figure 73: Fluorescent images of other zonation parameters (oxygen and CHIR) on HepaRG™ cells in well plates. Cells stained for GS-1 (green), lipid droplets (red) and nuclei (cyan) (a.) Cells exposed to normoxia and DM (2% DMSO) compared to cells exposed to hypoxia, SM (0.1% DMSO) and zero and 9 µM CHIR (b.) cells in SM exposed to 13% oxygen media and 11 mM glucose, compared to cells exposed to 8% oxygen, 7 mM glucose and 2 µg/mL insulin. (Scalebars: 100 µm).

3.8. Immune cell reservoir

It has been a challenge to integrate circulating immune cells into OoC models for reasons such as their fragile and easily activable nature, tendency to attach to rough surfaces, and tendency to sediment in static to low flow. The immune cell reservoir was developed to be integrated into a generalized MOC platform for the long-term suspension and perfusion of PBMCs (Figure 74). This sub-chapter discusses the concept, construction, and characterization of an immune cell reservoir.

3.8.1. Concept of the immune cell reservoir

The design of the immune cell reservoir accounted for the following considerations:

- Minimizing sharp edges
- Protection of immune cells from direct shear
- Enabling flexible and user-friendly interfacing with MOC platforms
- Elimination of glass as a building material
- Provision of sufficient upward flow to ensure immune cell suspension.

- X-y spatial footprint of 25 by 25 cm on the MOC platform, with an aspect ratio to ensure stable connection onto the platform

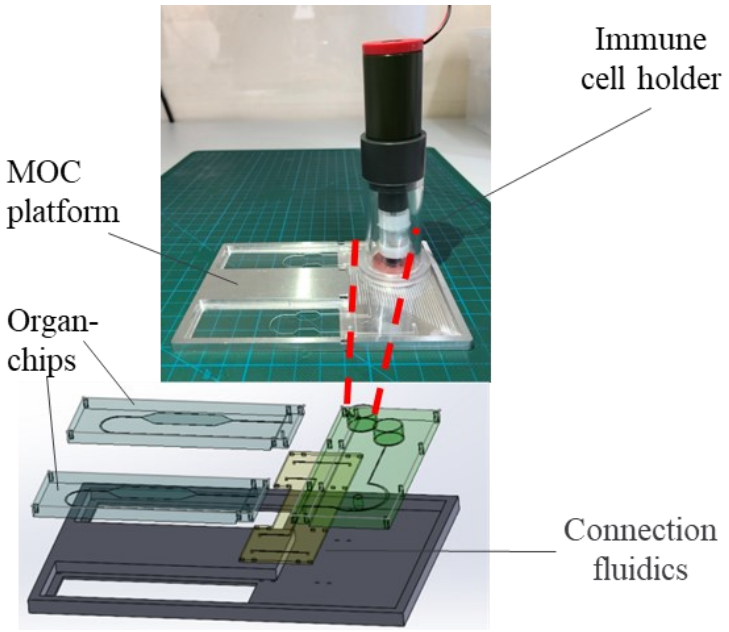

Figure 74: Concept of the immune cell reservoir interfacing with an MOC platform

3.8.2. Simulations of the immune cell reservoir for flow focusing

COMSOL simulations were used to study flow patterns within the immune cell reservoir, to test the effect of mixing on the flow patterns. The original idea of the reservoir design was constructed to include two compartments – a lower mixing chamber and an upper cell chamber, separated by an isoporous membrane. For the simulations, a porous media flow module was set up, with a disc-mixer to model the overall flow pattern of the fluid in the reservoir and to decide on the addition of features to the cell suspension chamber (CSC) (Figure 75.a). The model revealed that a concentric CSC with the mixing chamber focused the flow in the upward direction inside the CSC with fluid velocities higher than 15 µm/s, the approximate settling velocity of a cell (Figure 75.b). Reducing the gap between the CSC and mixing chamber and extending the wall of the CSC into the mixing chamber led to flow focusing outside the CSC (Figure 75.c,d). These simulations served as a basis to build the immune cell reservoir approaches. In the future, further complexity could be introduced into the COMSOL model by accurately defining the interaction between the fluid and the mixer with the incorporation of the COMSOL Mixer Module.

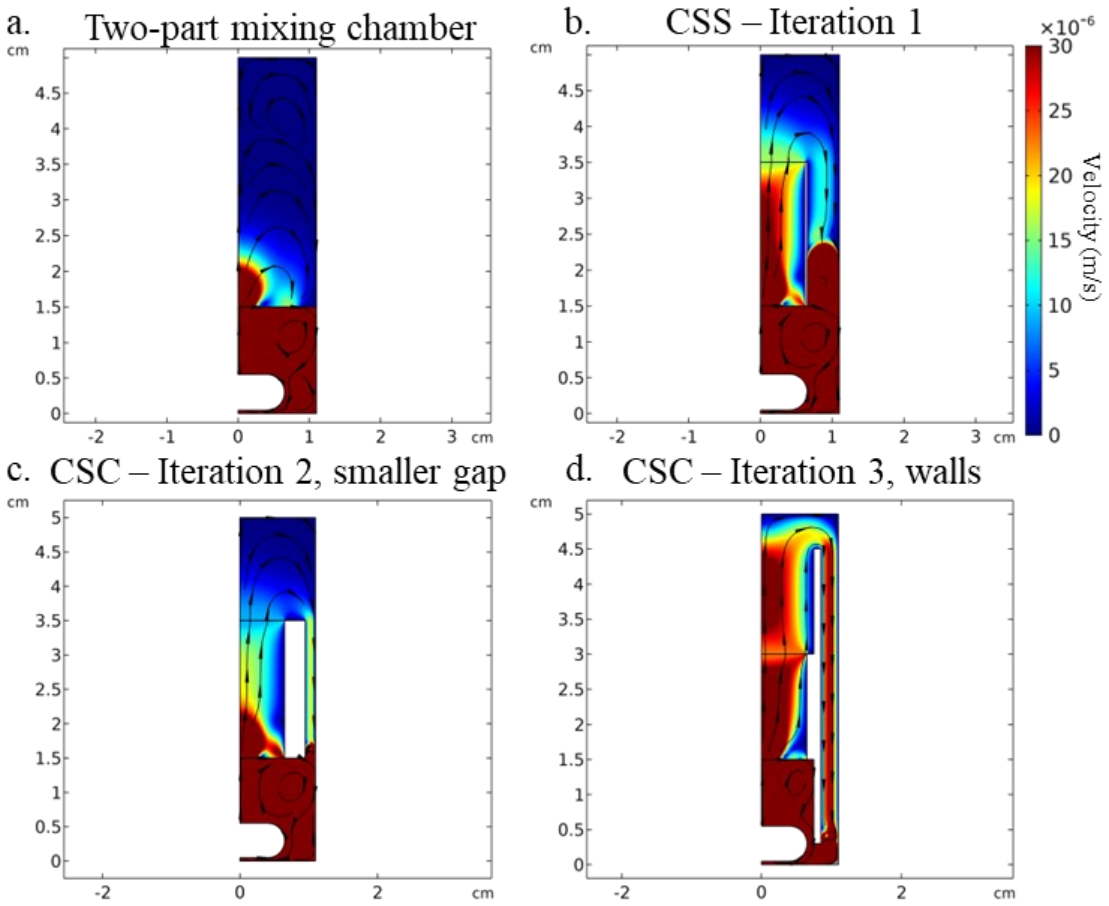

Figure 75: Simulation of flow in varying dimensions of the immune cell reservoir. The porous media flow module of COMSOL was used to set up a simple model for a disc mixer with radial symmetry for a cylindrical immune cell reservoir of total height 5 cm and 2 cm diameter. The target upward fluid velocity within the CSC is greater than 15 μm/s, the approximate settling velocity of a cell. (a.) The two-part mixing chamber model with 500 rpm of the mixer, (b.) a 2 cm high CSC suspended within the mixing chamber, with a gap of 4.5 mm between the CSC and mixing chamber, (c.) CSC wall of 3 mm thickness, with a gap of 1.5 mm between the CSC and mixing chamber, with 500 rpm, (d.) CSC wall of 2 mm thickness, 500 rpm for rotation and the wall extensions measuring 1.2 cm upwards and downwards from the CSC.

3.8.3. Fabrication of the immune cell reservoir

For the fabrication of the immune cell reservoir, a cell suspension chamber (CSC) was created, as a cylindrical chamber with isoporous membranes on either sides, where cells could be confined while in suspension (Figure 76.a). This CSC was confined within an outer mixing chamber housing a mixer to guide media upwards across this CSC at a high enough speed to match the settling velocity of cells. To this end, two mixing approaches were conceptualized (Figure 76.b). The first relied on an outer mixing chamber which housed the CSC, with access ports into and out of the CSC. Flow focusing could be achieved by means of a motorized impeller or magnetic stirrer driving flow upwards through the inner cylinder and back down along the gap between the two cylinders. The second approach employed an external mini-peristaltic pump to pump liquid upwards across the CSC in a flow pattern perpendicular to the flow accessing the cells in the CSS, so as to guide the cells from left to right out of the CSC

(Figure 76.c). The location of access ports for the setup was chosen to be at the base of the CSC to minimise dead volumes while connecting this mixer to the platform.

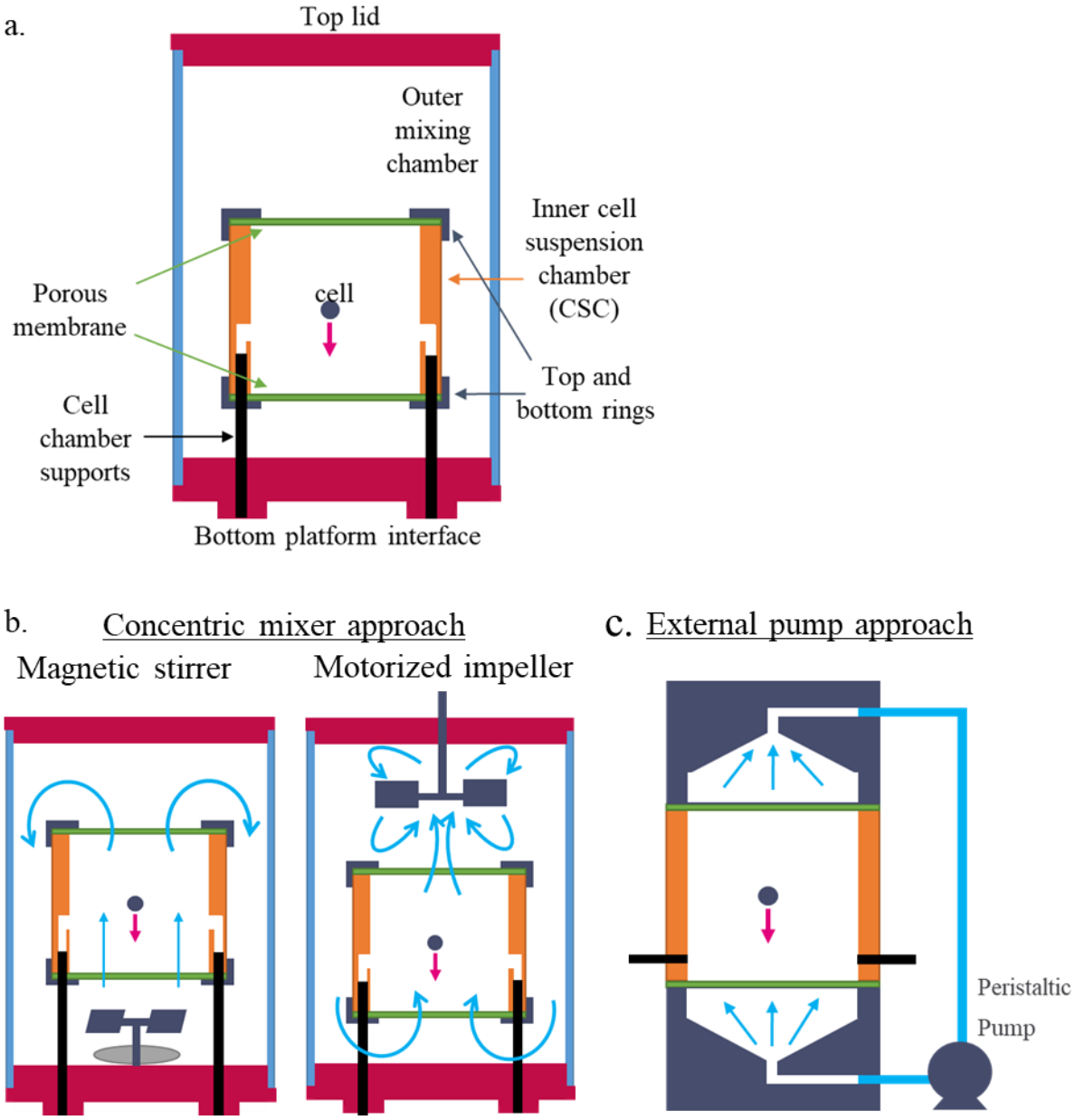

Figure 76: Immune cell reservoir design approaches (a.) Main features of the immune cell reservoir including the inner cell suspension chamber (orange), isoporous membranes (green), cell chamber support cannulas (black), outer mixing chamber (blue), flexible top lid and bottom platform interface (magenta), (b.) Schematic of the concentric mixer approach including the magnetic stirrer and motorized impeller version, (c.) Schematic of the external pump approach

3.8.4. Concentric mixer approach

The first iteration of the concentric mixer approach involved a CSC suspended inside the mixing chamber by means of three supports at the top, like a transwell insert (Figure 77.a). Access ports led through the side of the inner CSC and out of the mixing chamber, with commercial connectors to interface the mixer with the platform. The side access along the curved chambers was prone to leakage and added dead volume into the system due to tubing connections. The second design iteration had CSC access points as cannulas into the top of the

CSC, with the CSC being suspended in the mixing chamber with the help of a step and ring insert (Figure 77.b). However, the top access cannulas led to increased dead volumes given that the tubing would have to loop down to the reservoir base to interface with the MOC platform.

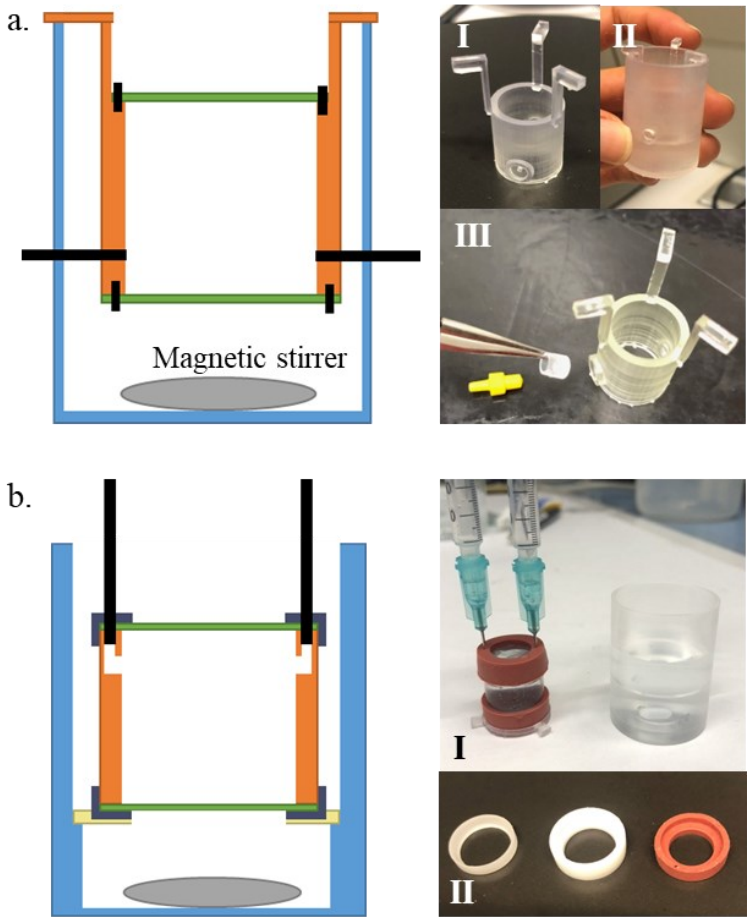

Figure 77: Design schematic of the concentric mixer approach (a.) The transwell insert-shaped CSC (orange, inset figure: I) placed inside the mixing chamber (blue, inset figure: II), with membranes (green) above and below the insert. Commercially available connectors (black, inset figure: III) interfaced with the sides of the insert to connect it to the MOC platform. (b.) Top access points (black) of the CSC (orange), suspended in the mixing chamber (blue) via a support ring (yellow, inset figure: I). The membranes (green) were fixed onto the CSC via fixation hoops (dark blue, inset figure: II).

Iteration 3 of the concentric mixer approach interfaced with the MOC platform from the bottom via 23 G cannulas, the cannulas were placed below the CSC (holding volume 1.5 mL) and were the means of suspension of the CSC in the mixing chamber (holding volume 5 mL) (Figure 78.a). The base of the mixer was composed of silicone rubber and had two protrusions into the platform, for a tight seal to the platform. This minimized dead volume and enabled direct connection to the platform. A magnetic stirrer was first chosen as a method of providing the upward force, to counterbalance the settling velocity of the cells. The size of the magnetic stirrer was limited by the diameter of the CSC since the stirrer had to be placed directly under it. Commercial bar magnetic stirrers of length less than 1 cm tended to be displaced in the wide magnetic field of a commercial magnetic stirring plate. This displacement was alleviated by the addition of an instep in the silicone rubber bottom and by creating a custom magnetic

stirring surface below the MOC platform with a a small block magnet (Q-05-05-03-N52N, Supermagnete) mounted onto a computer fan motor (EB40101S2-000U-999, Sunon), with rotational speed tuned with the voltmeter (PS-303D, Conrad Electronics Germany) (Figure 78.a.II). An upward flow was created using a rotating bar magnet fitted with a clockwise impeller head, rotating directly under the CSC to pull in flow from the sides and force it upwards through the CSC. For this, a specialized attachment was created to stabilize a 3D printed impeller head onto a disc magnet, added to the instep in the silicone base (Figure 78.b.III, IV). The concept was tested with introducing colored water near the base of the impeller and observing the movement of fluid up the CSC in the absence of membranes (Figure 78.c).

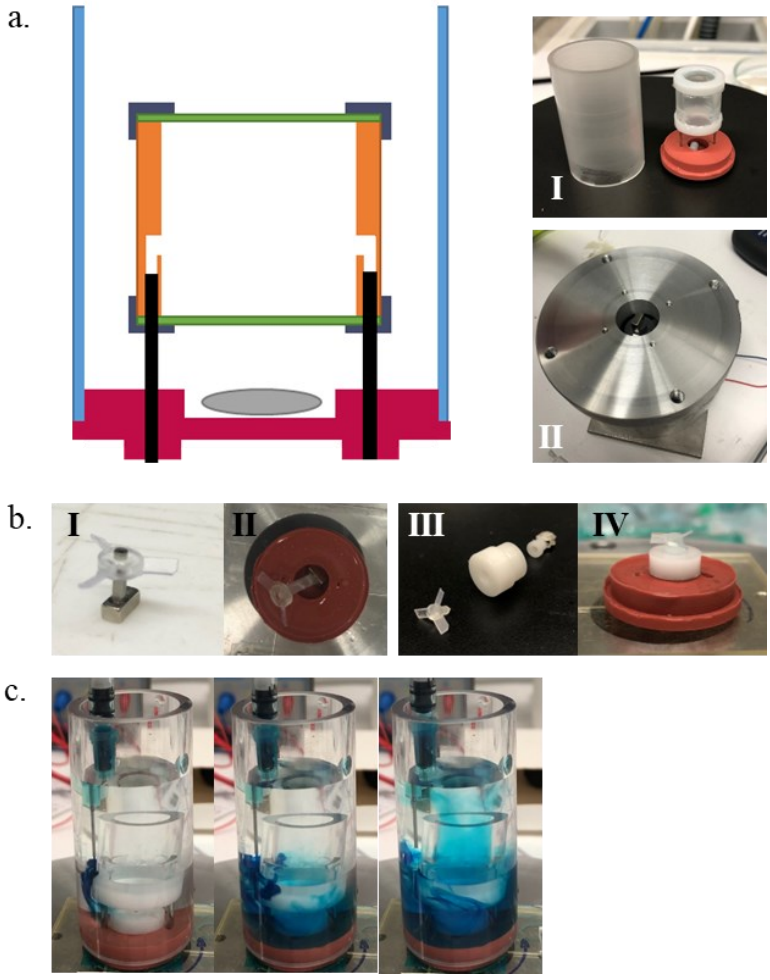

Figure 78: Design schematic of iteration 3 of the concentric mixer approach with magnetic stirrer. (a.) CSC (orange) fully supported via two metal cannulas (black), with enclosing membranes (green), with a silicone base (magenta) interfacing with the MOC platform placed inside the mixing chamber (blue, inset figure: I). The setup is mounted on a custom-made magnetic stirring surface with a magnet mounted on a computer fan (Insert figure II) (b.) First attempt of fixing an upward flow impeller on a magnet and subsequent collapse of this setup (Insert figure: I, II) and the final setup of an impeller mounted onto a fitting with the magnet from the under-side, to fit within the silicone base (Insert figure: III, IV) (c.) Proof of concept pictures of colored water injected near the rotating impeller (voltage setting 8 V on voltmeter), and being pushed upwards through the CSC without membranes.

While the magnetic impeller concept could conveniently provide an upward flow in the absence of membranes on the CSC, it failed to produce a strong enough upward flow when membranes were introduced onto the CSC and hindered the fluid path. A stronger flow could be generated by a motorized impeller at the top of the CSC through the membranes. The top hoop (or fixture, as in the case of percussion instruments) to fix the membrane onto the CSC was designed to have higher walls than the bottom hoop, to fit around the impeller head, attached to the motor holder. The motor holder was mounted onto the top of the mixing chamber and held a motor (Brushless 12V DC motor, Maxon Group) and impeller mounted onto a shaft with a shaft seal (3-10-6, Alexander Engel KG). The rotational speed of the impeller could be controlled with a voltmeter (PS-303D, Conrad Electronics Germany) attached to the motor. For all tests, the voltage was set to 8 V (Figure 79.b).

The flow test platform had a simple alignment of channels leading into and out of a base with holes to interface with the rubber bottom of the immune cell mixer. Syringe pumps were connected to the platform inlet and a collection receptacle to the outlet. With the motor, the height of the immune cell reservoir was approx. 11 cm and diameter 2.6 cm. This high aspect ratio created a toppling instability. To secure the immune cell reservoir onto the fluidic base, a fastening mechanism like a bayonet mount was constructed, with a ring inserted around the mixing chamber, turned into place with the help of an L-slot. This mount added pressure onto the rubber bottom, thus ensuring a tight fit into the fluidic platform (Figure 79.d).

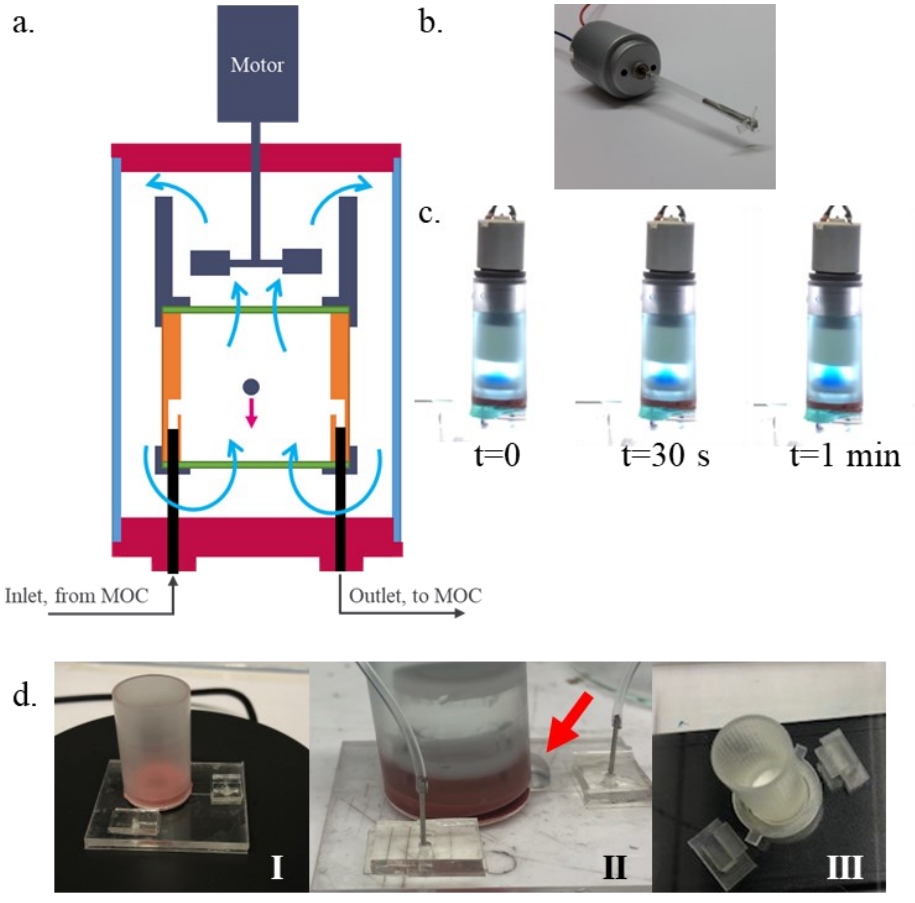

Figure 79: Design schematic of iteration 3 of the concentric mixer approach with motorized impeller. (a.) CSC (orange) fully supported via two metal cannulas (black), with enclosing membranes

(green), with a silicone base (magenta) interfacing with the MOC platform placed inside the mixing chamber (blue). A motorized impeller is mounted on top of the CSC and the top membrane hoop (dark blue) has higher walls to enable flow focusing. (b.) Picture of the 3D printed impeller attached to the motor via a shaft (c.) Pictures of a flow test with colored water injected directly into the CSC via the metal cannulas, being pulled across the CSC and recirculated by the motor, (d.) Picture of the mixing holder and silicone base on a test fluidic platform with an inlet and outlet port (insert figure: I), leakage (red arrows) given the height of the immune cell reservoir to the diameter (Insert figure: II), picture of the bayonet locking mechanism to fix the immune cell reservoir onto the microfluidic platform (Insert figure: III).

3.8.5. External pump approach

Another approach to create upward forces across membranes is with the introduction of a perpendicular stream of medium via an external pump. A miniature peristaltic pump was employed for this purpose, to provide an upward force in the CSC without the need for a concentric external mixing chamber (Figure 80.a). The parts of the upward flow mixer were 3D printed and connected in a way that the cell chamber was secured between two membranes and attached to the top and bottom conical parts. 18G needle tips were used to connect the peristaltic pump (MP-1, Binaca Pumps, USA), reservoir and mixer. The peristaltic pump was controlled by a voltmeter. Introducing a reservoir to the setup allowed for a bubble trap, since the small peristaltic pump created microbubbles which could lead to cell activation (Figure 80.b).

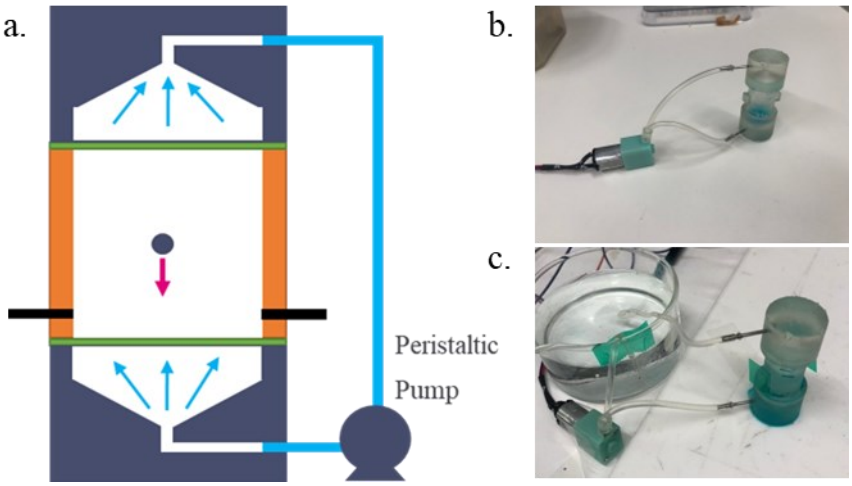

Figure 80: Design concept and schematic of the external pump approach. (a.) CSC (orange) enclosed between membranes (green) and two parts (dark blue) guiding flow across a peristaltic pump in a bottom-up direction. The CSC interfaces with the MOC platform via side access points (black) (b.) Picture of the external pump approach in a closed loop flow circuit without a reservoir (c.) Picture of the external pump approach with a reservoir located downstream of the pump acting as a bubble trap.

3.8.6. System characterization

3.8.6.1. Maximum upward velocity provided by the systems

Videos were made of the rise of coloured water in the CSC to calculate the upward velocity of the fluid in the CSC. These values were compared with the settling velocity of a cell (V_t) in water, calculated as

$$V_t = g * d^2 * \frac{(\rho_c - \rho_m)}{18 * \mu}$$

Where g is the gravitational acceleration, d is the diameter of the cell, ρ_c is the cell density, ρ_m is the medium density, and μ is the medium viscosity. The mini-peristaltic pump provided an upward flow of 2 x 10^{-5} m/s, on the order of magnitude of the settling velocity of cells, while the other mechanisms provided a higher upward velocity when set to the maximum voltage setting, such as 1.2 x 10^{-4} m/s for the motorized impeller with membranes, which confirms tunability to the settings that the immune cells would require.

3.8.6.2. Bead flow test

A baseline comparison was established for the immune cell reservoir being developed to validate its capacity to keep particles in suspension. This was perfomed with a commercially available syringe pump (NeMix™, Cetoni GmbH) mixing pump. A mixture of fluorescent beads was loaded into the syringe pump, which was maintained in suspension while being pumped via tubing into a sampling receptacle. The expectation of a uniform concentration of beads, and hence a uniform fluorescent intensity of the effluent was not met, given that there could be some settling of beads within the NeMix reservoir but longer times of perfusion would need to be investigated (Figure 81.b). This bead suspension protocol could be translated to the immune cell reservoir by injecting a high concentration mixture of beads into the CSC at t0, then flushing PBS across the MOC via a syringe pump and collecting effluent at regular time intervals. If beads remained in suspension and were washed out with the flow, the concentration of beads will decrease as per the dilution rate defined by the flowrate of perfusion.

3.8.6.3. Baseline endotoxin measurement

An important characterisation for the system involved the measurement of endotoxins present in the system before perfusion, to test the cleanliness of the holder and assembly process. The basic cleaning process involved wiping all newly fabricated parts to be assembled with 70% ethanol, followed by drying in the biosafety cabinet. Then the reservoir was assembled and exposed to UV light in the biosafety cabinet for 30 minutes. The reservoir was then filled with PBS, capped with the rubber cap, and connected to pre-filled syringes (Figure 81.c). The setup was perfused at 37°C overnight and effluent collected the next day and stored in the fridge overnight. To run samples in parallel, the system was exposed to an endotoxin removal treatment comprising of exposure to 1M NaOH for 1 hour, followed by two thorough washes with endotoxin free water by replacing the entire fluid in the immune cell reservoir. The system was then refilled with PBS and connected to the syringe pump and perfused again overnight. The next day, effluent was sampled, and the endotoxin levels measured. The endotoxin levels were observed to be at the lower observable limit from the point of assembly so it can be concluded that a thorough cleaning process with 70% ethanol and UV light treatment assures an endotoxin level of 0.17 EU/mL, lower than the suggested baseline endotoxin level of 2.75 EU/mL which could interfere with *in vitro* culture studies (Nomura et al., 2017) (Figure 81.d).

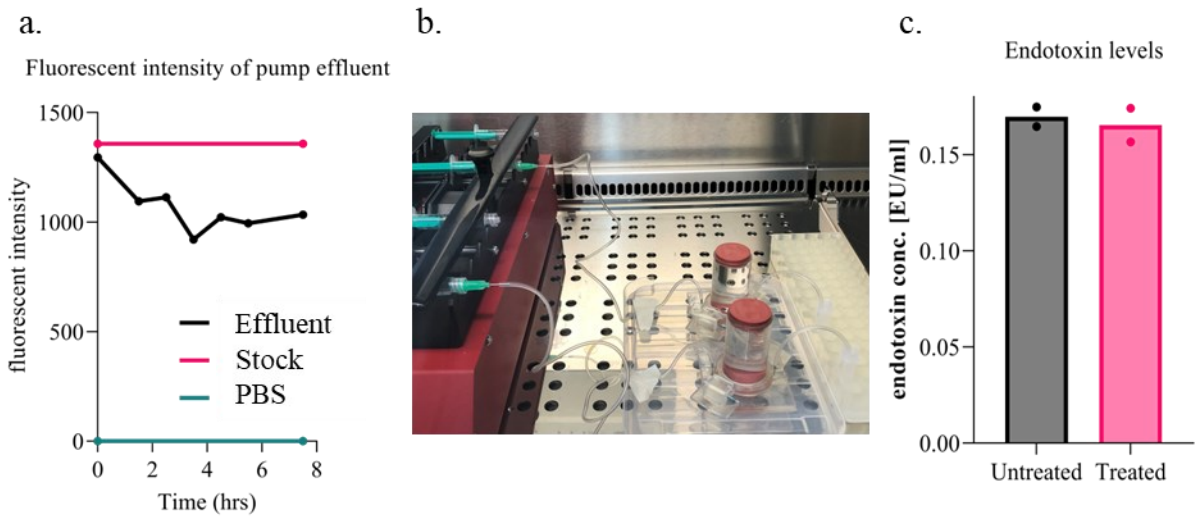

Figure 81: Characterization of the immune cell reservoir (a.) Fluorescent intensity of effluent during the bead flow test of the NeMix mixer, perfused at 100 µL/h compared to the fluorescence of PBS and the stock solution sampled at 1 hour and 8 hours, (b.) Picture of the setup to characterize the baseline endotoxin levels within the system, (c.) Quantification of the endotoxins before and after the treatment with 1M NaOH solution. Data presented as mean for n=2 immune cell reservoir setups.

4. Discussion

MOCs enable the study of a specific mechanism of organ-crosstalk, capturing complex (patho)physiological processes by integrating multiple cell types, organ-specific extracellular matrix, and in some cases, aspects of the immune system in addition to organ-interactions. They build on the complexity of single organ-chips which enable the study of organ-specific pharmacokinetic aspects such as absorption of a compound into the gut, distribution of the compound into the adipose tissue, metabolism in the liver and excretion in the kidney (Huh et al., 2010; Jang et al., 2019; Rennert et al., 2015).

In the case of MOCs, the organ-chips interact with each other to exchange metabolites via microchannels. Connecting OoCs directly via tubing could lead to large dead volumes and lag times within the system, and the inability to integrate sensors into this tubing connection. The MOC model in this thesis aims to alleviate these issues by enabling flexible connection of organ models with similar size footprints and the absence of tubing in the connections.

Taking the specific case of the interactions between white adipose tissue and hepatic tissue, this model aims to study the influence of one organ on the other by connecting a WAT-chip with a liver-chip in a robust and reversible fashion. There is also a possibility for sensor integration directly into the connection channel such that parameters such as glucose and oxygen in the effluents going from one organ-chip to the other can be monitored in real time (Figure 82). The material choice of the chips ensures that the absorption of drugs into the material of the chip is kept to a minimum.

This chapter addresses the challenges faced during MOC design, development, and experimentation, through the lens of the state-of-the-art research, presenting mitigation strategies and an outlook for future developments in this topic.

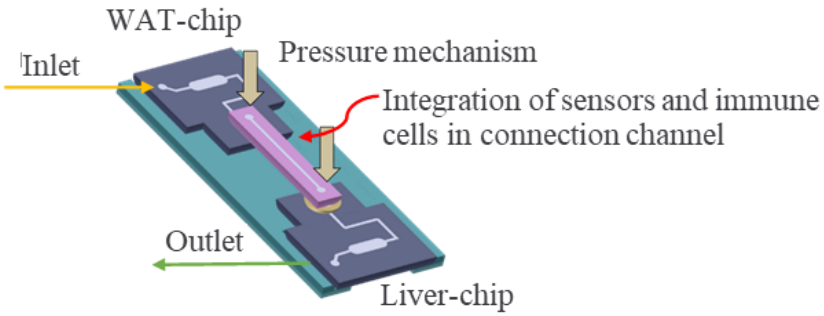

Figure 82: Schematic of the WAT-Liver MOC and with the possibility to integrate sensors and immune cells into the chip connection.

4.1. MOC design – organ-chips and connection approaches

The three approaches for establishing vascular connections were compared through the lens of developing a robust and flexible connection method for two organ-chips with sampling and sensor integration. Given the design considerations, differing organ-chip designs between the WAT- and liver-chips and the difference in cell injection strategies, the inbuilt connection approach appeared as the most inflexible option for establishing a reversible connection between the organ-chips despite the minimal dead volume. Fabrication complications were

anticipated given that chip geometry would vary based on the type of tissue being connected. However, if sampling at the chip connection were not required and if the tissue chambers for the connected organs followed a simple design, this connection approach could be considered. The modular connection approach was interpreted as the case of stacking two chips on top of each other. The dead volume within the system would only be the gasket volume and apart from the chip design changing per organ-chip, the outer chip shapes would be consistent across the corresponding top-chips and bottom-chips irrespective of the cells being injected. Sampling or sensing between the chips would require the addition of a connection chip with sampling features or integrated sensors, stacked in between the two chips, altering the structure of the chips. This alteration can be incorporated into the case of the modular cassette systems. The chips in the systemic connection approach were envisioned to be the most consistent, with only the tissue channel design changing while the ports remained the same and interfaced with the fluidic interface. Reports of systemic connections were seen for insert-based systems where the tissues were cultured on transwell or glass slide inserts and could be transferred into a fluidic interface for common perfusion (Ronaldson-Bouchard et al., 2022; Schimek et al., 2020). This landscape is however changing, as highlighted by the TOP fluidic platform where custom chips can be integrated into a specialized platform adhering to ISO conform regulations (Vollertsen, et al., 2020; Vollertsen, et al., 2021).

Before the research of our group, there were very few documented instances of successful cultivation of adipocytes in an *in vitro* platform (Rogal et al., 2020; Rogal, Roosz, Teufel, et al., 2022). These cells are difficult to culture *in vitro* due to their fragility and tendency to float in media. Reports of static culture, by trapping adipose tissue explants or sandwiching the WAT-tissue between sheets of adipose derived stromal cells have bypassed some of these issues but did not account for the vascularized perfusion of these tissue models (Brooks et al., 2016; Lau et al., 2018). A hyaluronic acid-based hydrogel was selected to suspend the adipocytes, which required a gel with low stiffness (Lin et al., 2016; Ruiz-Ojeda et al., 2019).

The liver-chip followed a 2D monolayer format on the tissue channel, separated from the media channel by a membrane. While this design shielded the hepatocytes from the shear stress caused by perfusion across the media channel, the hepatocytes, being over 400 µm away from the bottom of the chip, were difficult to image clearly. Imaging was limited to the 20x objective on the fluorescent microscope, with blurred features from the E-cadherin and lipid droplet staining in the hepatocytes (Figure 53).

The effluent characterization of the WAT- and liver-chips could support future functional scaling questions. Markers such as albumin, urea, adipokines, free fatty acids, triglycerides, glycerol and cytokines can be directly analysed from the collected effluent. This collected effluent data could be entered into a physiologically based pharmacokinetic (PBPK) model and results scaled up to human-scale, to predict clinical outcomes and predict early onset of NAFLD or therapeutic doses (Arakawa et al., 2020; Shroff et al., 2022; Tsamandouras et al., 2017). DPPIV secretion in the effluent could serve as a functional readout and a basis for relative scaling given that it is a potential mediator between obesity, inflammation, and hepatic/adipose tissue insulin resistance (Deacon, 2019; Zhuge et al., 2016).

4.2. Scalable, robust MOC fabrication

Several manufacturing techniques were employed in this thesis, for different aspects of the MOC construction. The connection mechanisms were prototyped with lasercut PMMA, assembled either by thermal fusion bonding or gluing. However, the gluing process was not consistent when performed by hand and was labour-intensive. The cassette bottom included a 250 µm thin PMMA layer which deformed over multiple times of use, especially with the screw pressure mechanism where the threads also had to be built into each cassette manually. The 3D printed modular insert cassette aimed to automate fabrication and create one solid cassette block which would no longer delaminate and deform with repeated use. Additionally, threads could be directly printed into each cassette. While the threads could still be prone to wear and tear, the spring-laden screw and hex nut connectors mitigated this and allowed for repeated use of the cassette. However, the 3D printed cassette was prone to bending during fabrication. The bending could be a factor of uneven UV crosslinking and increasing the cassette thickness accommodated this to some extent (Dizon et al., 2021; Wu et al., 2019) but hindered imaging with high magnification objectives (higher than 20x). Design modifications such as ribs were suggested to mitigate this effect, in addition to a more sophisticated 3D printer or stronger resin (results sub-section 3.1.4).

An ongoing challenge in the OoC field is the acceptance of a universally preferred chip material. Thermoplastics have the advantage of simple structuring, manufacturing, and control over dissolved gas concentrations in the media (Schneider, Gruner, et al., 2021). However, challenges such as the collapse of fine features during mass production and high temperature thermal fusion bonding were encountered (Shakeri et al., 2022). The thermoset TPE was introduced into chip fabrication in this thesis, due to its ability to be embossed, reducing the bonding temperature to facilitate the thermal fusion bonding of channels with fine features (Schneider, Bubeck, et al., 2021). TPE embossed off SU-8 wafers via the epoxy molding method (methods sub-section 2.2.2.2) offers advantages of smooth channels and convenience of embossing up to heights only limited by the photolithography technique. The WAT-chip tissue fluidic layer comprised a 100 µm channel embossed in a 250 µm TPE sheet, resulting in a 150 µm film of TPE in the path of light of an inverted microscope attempting to image the adipocytes. This could hinder imaging unless methods are developed to emboss through-features into the TPE. Through-features could be lasercut into the TPE, but led to the feature edges melting and becoming jagged, which then scattered light during imaging steps (Figure 49.b, Figure 53.d). The current method of lasercutting TPE sheets involved sandwiching between two 250 µm PMMA sheets to catch debris while lasercutting. TPE layers thinner than 250 µm were prone to wrinkling upon removal of the layer from the backing material and handling. Hence, the lower limit for lasercutting TPE was maintained at a sheet thickness of 250 µm and thinner TPE materials were hot embossed as needed.

The PC-PMMA compatibility was revealed in the stamp method during bonding. Version 1 of the liver-chip had a PC membrane because PET delaminated during bonding attempts with PMMA (Figure 83.a) (Shakeri et al., 2022). However, PET allowed for clear brightfield imaging of hepatocytes in the liver-chip and the PET membrane was introduced into the next versions of the liver-chips via bonding to TPE tissue and media channels. The WAT-chip still

maintained the PC membrane for both versions because the 100 µm PMMA tissue-layer was thermal fusion bonded to the PC membrane in the first fabrication step.

The prototyping-scale bonding method in the oven with steel foldback clamps led to inconsistencies in bonding. Additionally, the design of the WAT-chip was modified to remove the tapered resistance channel at the end of the tissue fluidic channel, since this tapered channel fused shut in the oven method of bonding (Figure 83.b, red arrow on WAT-chip). PMMA layers of thickness 1 mm and above were not deformed during the oven bonding method. However, the laser path created a tapering cross section during laser structuring of the thick PMMA pieces (Figure 83.c).

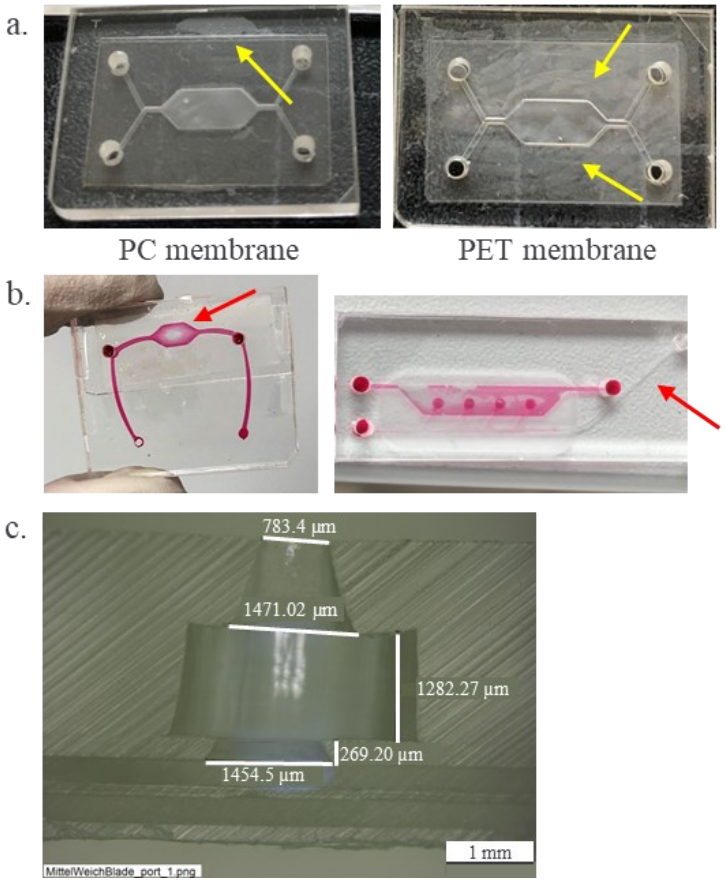

Figure 83: Images of thermal fusion bonding chip layers (a.) Bonding compatibility between PMMA and PC, PET membranes shows unbonded regions spanning across the liver-chip version 1 in the case of the PET membrane compared to the PC membrane (the unbonded region on the PC membrane chip is due to uneven clamping) (b.) Inconsistencies of bonding with the small scale bonding method in the oven, wherein regions of the liver-chip tissue channel and WAT tissue fluidic channel fused and warped during thermal fusion bonding (c.) Microscope image of a cross section of the cone-shape while lasercutting features in PMMA.

The stamp method facilitated embedding the membrane into the PMMA layers, leading to a flat surface onto which the cells could be cultured (Figure 84.a). The edges of the PC membrane, cut with a CO_2 lasercutter were burnt and uneven, and created a bubble trap at the border of the membrane. Thus, the membrane was extended to cover the entire portion of the chip (Figure 84.b).

For the final step fabrication of the liver- and WAT-chips, a ramping protocol was employed (Methods sub-section 2.3.2.2) and given the large region of unsupported membrane, a slow ramping protocol was set, including a slow cool down step to anneal the bonded materials (Sun et al., 2006) (Figure 84.c). The stamp method could be developed into a double stamp, sandwiching the membrane from above and below in the shape of the corresponding channels, thus bonding the entire tissue channel, membrane and media channel in one step, finally requiring only bonding the chip top and bottom to complete the assembly.

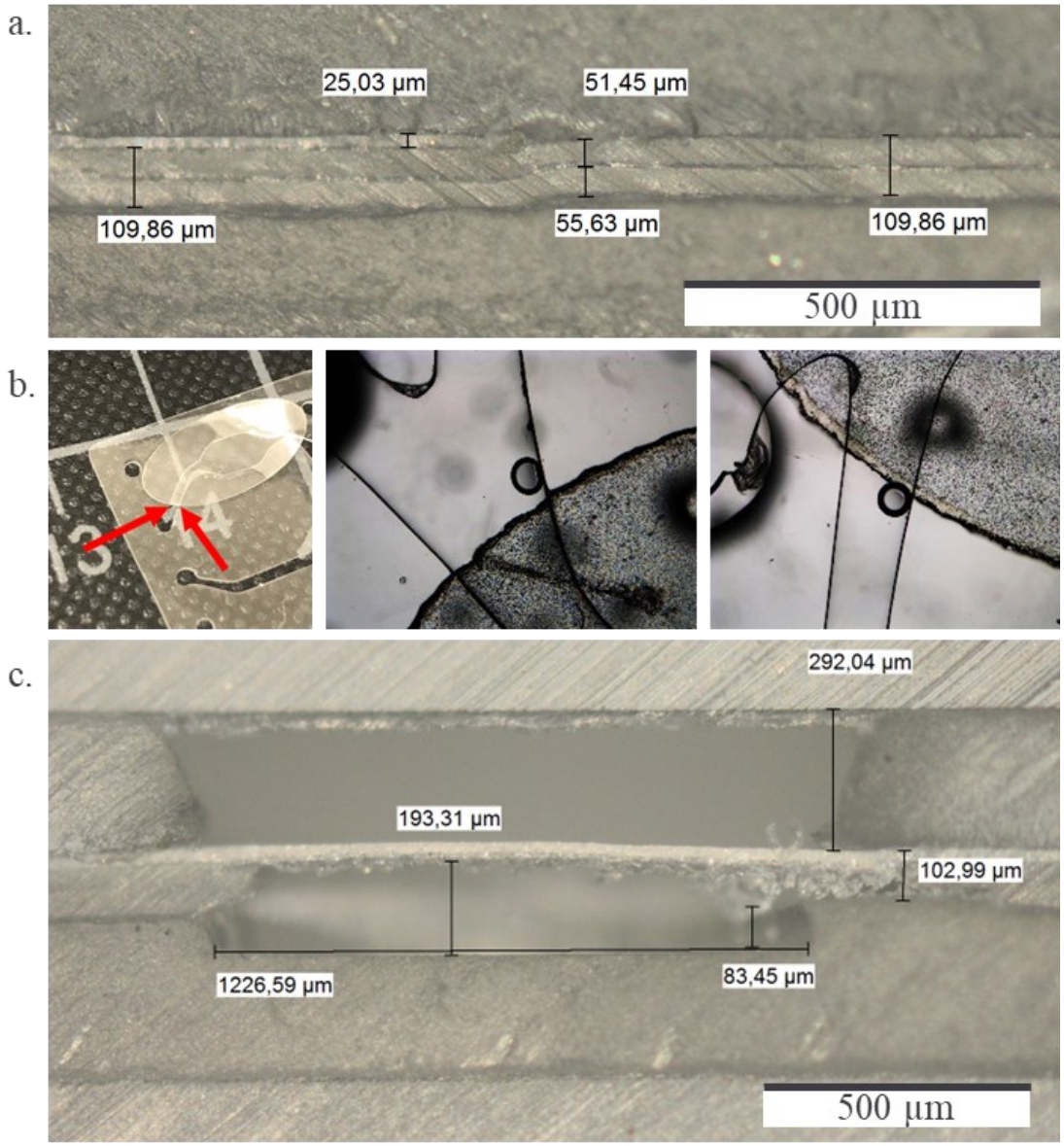

Figure 84: Visualization of the membrane in the thermoplastic chips (a.) a close-up of a cut WAT-chip revealing the membrane (25 µm thick) embedded into the PMMA tissue chamber layers (51.45 and 55.63 µm thick) (b.) Picture of a previous iteration of the liver-chip where the membrane cut across the tissue channel (red arrows), creating a bubble trap during cell culture (c.) a WAT-chip cut at the tissue chamber indicating the 193.31 µm high tissue chamber and flat membrane fabricated with the stamp method.

Some inconsistencies were observed during the fabrication of version 1 of the WAT-chip in the step of APTES-treatment and bonding PMMA to the PDMS top of the chip. The protocol

was modified to flip the top part onto a drop of APTES because submerging the part in the APTES solution caused a failure in the bonding between the PMMA top and PMMA media channel. This could be due to the APTES adhering non-specifically to the underside of the PMMA top part and disrupting future thermal fusion bonding steps. While protocols have reported stable bonding with water as a solvent for APTES (Kim et al., 2010), aprotic solvents have been known to lead to more stable APTES solutions (Miranda et al., 2020). However, ethanol was not a suitable solvent for lasercut PMMA because it led to uneven swelling of the stress-crazed lasercut PMMA and hence cracking of the plastic structure.

To bond TPE to PMMA, an additional step of UV treating the PMMA was introduced (Busek et al., 2021). However, for bonding TPE to PC, this step was not required (Schneider, Brás, et al., 2021). An interesting approach for PMMA-to-PMMA bonding could be via solvent bonding (Tran et al., 2013), assisted by ethanol and UV. However, the application and maintenance of the solvent on the plastic surface proved to be challenging, given the high volatility of solvents like ethanol and isopropanol which are typically used for solvent bonding thermoplastics. Quick bonding times would be required to use ethanol or isopropanol given their ability to crack lasercut PMMA. Chloroform is another typical solvent, but vacuum drying is a crucial step to rid the chip of this before the addition of cells (Faghih & Sharp, 2019). Other reports have used UV and pressure to bond thermoplastics at low temperatures to minimize channel warping during high temperature thermal fusion bonding (Tsao et al., 2007; Uba et al., 2015).

The liver-chip fabrication could also be scaled up to the hotpress and as a next step, it would be beneficial to create an epoxy mold corresponding to version 3 of the liver-chip to directly mold the TPE media channel and bond it to the bottom PC in one step. The tissue channel could be either lasercut or embossed into TPE with through-holes punched to allow alignment with ports.

The design and fabrication of chips required specialized training and user variability impacted chip production yield. The goal of production is to eliminate discrepancies due to variabilities in processes involving unregulated apparatus such as steel foldback clamps, and manual chip alignment, resorting to dowel pins for automated alignment of parts, and use of high throughput and automated production equipment like the hotpress and 3D printer.

The volume of the recirculation setup for the WAT- and liver-chips was of the order of 500 µL, requiring 2 hours of perfusion at 100 µL/h for the glucose levels to build to the detection limits of the sensors. Relative scales of reservoirs and chips should be considered in order to achieve reasonable recirculation volumes without diluting the metabolites from the chips. An example of the scale of chips to reservoirs comes from the liver Biochip, a commercially available system, which when used in recirculation mode for liver culture on-chip requires approx. 1 mL of media per day per chip reservoir. If used in a linear perfusion regime, the media consumption is exponentially higher, discouraging applications such as the integration of a zonation gradient which would only work in a linear perfusion regime.

For the immune cell reservoir to circulate immune cells across an MOC, considerations should be made about the volume of the cell suspension chamber (CSC) so as not to dilute the chip

metabolites during perfusion. The CSC, with a volume of 1.5 mL, requires further scale-down in size for compatibility with microfluidic platforms. This scale down will require different methods of fabrication given the production limits of a factory-scale turning machine. 3D printing and CNC milling could be viable production alternatives for this reservoir. Particle image velocimetry (PIV) could be employed to further characterize the flow patterns in the immune cell reservoir during operation, to correlate impeller rotation with the velocity of fluid produced in the CSC (Li et al., 2018).

4.3. Cell injection and culture on-chip

The presence of bubbles in the system could lead to complete destruction of the cell monolayer by changing the local environment and flow patterns around the cells (Pereiro et al., 2019). The presence of bubbles could be brought about by several factors, some of which have been listed below:

a. Temperature fluctuations of the media: The gas carrying capacity of a liquid corresponds to the temperature by the Henry's law. In the case of PBS, culture medium and all liquids that encountered the channels of the chip, it was essential to ensure that the protocol accounts for the consistency of temperature during operation and handling. Plasma-treatment of the chip ensured an increased wettability at the chip ports and within a channel, to allow quick wetting of the PBS that was first added into the chip at room temperature (Bagiatis et al., 2019). After this, the chip was always submerged and never allowed to dry out. Cold collagen I solution for coating the liver-chips was then washed out with warm media and the chips were handled either one or two at a time in separate petri dishes to prevent the reduction in temperature during operation. Additionally, for long experiments involving the scientist's intervention, the experiments were conducted in the ALS box which maintained the temperature at 37°C and humidity at a maximum system pre-set value of 60%. Additionally, media was equilibrated in the water bath and always maintained at this temperature in one or two conical tubes to ensure the consistency of temperature during operation.
b. Maintenance of a humid environment: When the chips were placed in the incubator, caps filled with PBS were introduced next to the set up within the petri dish to ensure a humid microenvironment and to prevent the chip from drying out
c. Minimization of nucleation sites: Manufacturing operations such as lasercutting sometimes led to jagged edges in the PMMA material and wherever possible, using a lower power laser with multiple runs over the structures, allowed the PMMA time to cool before the next round of cuts. Lasercutting PC membranes with the CO_2 lasercutter led to an imperfect cut with jagged edges and melted material at the site of the cut. These sites were nucleation spots for bubbles and in the case of temperature fluctuations, bubbles began to accumulate at the edges of the membrane if they lay within the channel and immediately compromised media coverage (Figure 84.b). To mitigate this, the membranes were extended across the entire channel.

Chip handling could be a reason for the uneven endothelial monolayer coverage at the media inlet of the WAT-chip for adipose-endothelial cell coculture (Figure 44.c). Another reason could be the wrinkled membrane in some chips due to the variability in chip fabrication

processes. This endothelial coverage issue was also seen in the modular connection system after connection to perfusion (Figure 31). It seems like the coverage in the first chip in a connection tended to be more disrupted. One strategy would be to improve the coating coverage, by adding L-DOPA or glutaraldehyde and covalently bonding the collagen coating to the surface of the PMMA instead of relying on non-specific adhesion of the coating to the surface (Monteiro and Airoldi, 1999; Moulay, 2014). An improvement of culture conditions was seen with the elimination of bubbles but the shear stress of directly connecting the chips to perfusion tubing could be a contributing factor in the disrupted cell monolayer.

In the liver-chip, the coverage of the HepaRG™ cells deteriorated over time in Version 1 of the chip (data not presented in this thesis), which could be attributed to a change in osmolarity of the medium due to the small media volumes and evaporation in the chip. (Alhuthali et al., 2021). Over the next two versions, strict bubble troubleshooting protocols were maintained, in addition to raising the height of the tissue channel to ensure high media to cell ratios (Leung et al., 2022).

Primary mVECs were chosen to facilitate the vascular connection between white adipose and hepatic tissue, from the same donor of the adipose tissue. Regions of the endothelial cell monolayer in the WAT-chip appeared patchy, stained for nuclei and VECadherin but were CD31 negative (Figure 52.a,b). This could be due to the presence of lymphatic endothelial cells in these regions owing to a mixed population during cell isolation (Partanen & Paavonen, 2001). The difference in morphology between endothelial cells at the membrane in contact with adipocytes in the WAT-chip and hepatocytes in the liver-chip was evident. The endothelium in the liver is fenestrated to allow for uninhibited transport of small molecules across the barrier, and there could be a possibility of a media component in the liver-tissue channel causing this morphological shift (Szafranska et al., 2021). According to a report, this difference in morphology could be attributed to sprouting features in the endothelial cells due to the activation of RAF/RAS/MEK/ERK pathway and FAK pathways from the hepatocarcinoma cell line (Chiew et al., 2015). Complexity of cell types could be added to the system at the site of liver-chip, with the introduction of the liver sinusoidal endothelial cells (Poisson et al., 2017) and adipose tissue-specific microvascular cells isolated by cell sorting of CD31 cells from the stromal vascular fraction of adipose tissue (Gogg et al., 2019).

4.4. Outlook

4.4.1. Model relevance: advantages of this MOC model over others

For MOCs to be able to contribute to the 3Rs for animal testing, validation by regulatory authorities is essential (Buchanan, 2021; Paul, 2021). Two *in vitro* validation documents exist, namely GIVIMP and G2611 (OECD, 2018), which elaborate the features and requirements of an *in vitro* model to gain regulatory acceptance. A large part of these documents involves stating the relevance (biological and strategic) of the chosen model over others, in addition to highlighting model limitations and proposing improvements to the model to ensure validation. This sub-chapter makes the case for relevance of this MOC over other models in the design

and biological aspects and provides an outlook for the points to be addressed to adopt this MOC as a relevant preclinical model to study WAT-liver crosstalk.

Non-clinical models to study liver-adipose interactions can be categorized into *in vitro* models and *in vivo*. *In vitro* models include precision-cut tissue slices which are mainly primary tissue (Bale et al., 2016). These models have a short time scale of study and are not representative of the physiological layout of the organs and subsequent interactions. Cell culture models comprise of primary or iPSC-derived cells or cell lines in well plates or transwell cell culture inserts, where interaction could be studied by pipetting from one well to another (Mazzoleni et al., 2009; Parrish et al., 2018). These models lack the perfusion aspect and may or may not include the vascular components, which are crucial for the study of liver- adipose interactions. *In vivo* models are animal models, which provide information on a systemic response in disease progression. While these have provided useful data in the past, the immune cell profiles of animal models differ from humans, and so do critical cell functions. These models might not be able to predict the onset of disease progression, which could occur in humans, especially for chronic metabolism-based diseases (Greek & Menache, 2013; Mestas & Hughes, 2004; Van Der Worp et al., 2018).

OoCs and more specifically, MOCs could alleviate most of the above-mentioned challenges by providing a model to track pathway-specific interactions between hepatocytes and adipocytes, with physiologically relevant vascular perfusion across the systems. It is also possible to integrate immune cells and accurately recapitulate the cellular complexity and spatial orientation of cellular organization with these models (Trapecar et al., 2021). Systemic OoC connection-based platforms have been reported in literature, where various OoCs could be separated, cultured, and integrated into a custom-built connection platform (Shroff et al., 2022). This MOC features a uniform outer chip structure with tuneable tissue channels and chip layouts, to facilitate the same method of connection as long as the chip port locations remain consistent. This is an advantage compared to previously reported systems of insert-based models with limited opportunities to integrate complex tissue types (Ronaldson-Bouchard et al., 2022; Schimek et al., 2020). The MOC in this thesis also allows for real-time sensing and imaging, in addition to vascular integration, compared to a model, which creates a consistent recirculating flow profile with a physically rotating system, inhibiting the ability of live imaging (Busek et al., 2023).

4.4.2. Goals of the model and potential applications

The goals of the project involved engineering a robust minimally absorbing platform to connect two organ-chips in a flexible and reversible manner and to compare the findings of the interaction system with the individual chips, to measure the influence of one chip on another. This model exhibits the following possibilities:

- Staining and imaging of each tissue chip
- Sampling capabilities at inlet, connection, outlet
- Sensor integration at inlet, connection, outlet

The two tissues chosen for this model were the white adipose tissue and hepatic tissue, both cocultured with primary endothelial cells. Their interaction is of relevance for insulin and glucose signaling between two key organs of energy homeostasis (Ye et al., 2017). Adipose

tissue is the reserve for lipids and the liver is a reserve for glucose (Young, B., O'Dowd, G. & Woodford, 2006). With the onset of hepatic insulin resistance, there is a breakdown in the signaling between the adipocytes and hepatocytes which leads to secretion of adipokines and the subsequent accumulation of lipid droplets in the hepatocytes, leading to a condition called NAFLD (Mashek, 2021; Moayedfard et al., 2022; Slaughter et al., 2021).

This model could facilitate the study of the mechanism of this signalling in various conditions such as in a fed state of the system composed of media with high glucose, high insulin concentrations (11 mM Glucose, 60 nM insulin) or in the fasted state of the system composed of media with low glucose, low insulin concentrations (7 mM glucose, 60 pM insulin) (Greco et al., 1979). This model can also be probed with some additional compounds at the inlet to assess the effect on adipocytes and hepatocytes, such as losartan, weight-reducing drugs, insulin sensitizers, and lipid-lowering agents, antioxidants, bile salts, co-factors increasing the mitochondrial transport of fatty acids(Hoofnagle et al., 2013; Kim et al., 2020; Yang & Mottillo, 2020). Effluent markers such as DPPIV can also be analyzed with this model, given the literature about donor characteristics affecting DPPIV expression with increased DPPIV levels in newly diagnosed obese T2DM patients compared to a non-obese control group and higher DPPIV levels in T2DM patients compared to healthy controls.

4.4.3. Model limitations and proposed approaches to increase model robustness

Certain limitations of the model should be addressed to improve model robustness and experiment reproducibility:

1. Chip fabrication protocol variability: Producing a robust supply of chips via defined fabrication protocols has proved to be a challenge to produce. Highly specialized skills are required to produce and transfer manufacturing protocols to pilot-scale operations for a steady chip supply (Moruzzi et al., 2023).
2. Equipment characterization during chip fabrication: Regular calibration and characterization of equipment and individual fabrication steps should be quality-controlled to ensure a high yield of chips.
3. Use of a cell line for the hepatic tissue: The HepaRG™ cell line was chosen as a starting point to create the model because of the similar level of expression of CYP enzymes compared to primary hepatocytes (Berger et al., 2016).
4. A hepatocyte model as opposed to a liver model: the response of hepatocytes in the presence of adipocytes is an important readout but NAFLD and the progression of NASH can only be observed with the addition of stellate cells and Kupffer cells (Carter & Friedman, 2022).
5. Autologous model for NAFLD development: It would be ideal to procure primary hepatocytes, adipocytes, endothelial cells and immune cells from the same patient. Potentially, all three cell types could be differentiated from iPSCs from the same donor and this would facilitate a truly autologous cell culture, leading to the study of a donor-specific response.

Despite these limitations, the model will be able to measure:

- Insulin sensitivity and glucose uptake within the WAT-, liver-chip and connected chips

- Drug concentrations, given the minimally absorbing nature of chip materials
- Quick response times of the model to stimuli due to the efforts of minimizing dead volume and the proximity of a reservoir to the media channel inlet
- Effluent markers like triglycerides, urea, and albumin produced by the hepatocytes
- Effluent markers like glycerol and adipokines produced by the adipocytes
- On-chip staining and imaging capabilities

4.4.4. Definition of performance standards

The following steps can be taken towards ensuring model robustness:

1. The SOP for WAT isolation and injection into the adipose chips has been published and is robust across various users in our group (Rogal, Roosz, & Loskill, 2022)
2. Chip fabrication of the WAT-chip has been transferred to pilot scale production, liver-chip scale-up is underway. The modular connection holder has also been translated into a user-friendly setup, tested by three users in our group.
3. Defined clinically relevant endpoints – lipid droplet analysis via microscopy (Seebacher et al., 2020), effluent analysis to study triglycerides, glycerol and DPPIV.
4. Fetal calf serum (FCS) in the media was replaced by bovine serum albumin to create a more defined serum concentration. The next step is to use a human source of serum.
5. Detailed media optimization was performed (see Results section) with the MTS assay readout to establish the optimal media composition which allows for metabolic viability of the adipocytes and endothelial cells.

The following recommendations will enable the definition of benchmarking standards for biology in the MOC:

1. Inter-user variability: allowing multiple users to build and use the model in different labs to assure protocol robustness
2. Donor variability across adipose tissues: so far, the metabolic assay has been tested with three donors with a certain level of variability. Increased donor numbers are required to test the model further. Sex differences in adipose tissue could vary the FFA uptake and release in chips (Mundi et al., 2014).
3. Baseline characterization of organ-chip function: confirming insulin sensitivity of the adipocytes and hepatocytes before connecting the systems in an experiment. Additional effluent characterization should be performed for the chips (glycerol production for WAT-chip, triglyceride, urea and albumin production for liver-chip)
4. Use of primary hepatocytes instead of the cell line to facilitate an *in vivo*-like response for glucose uptake or endogenous glucose production.
5. A baseline drug characterization should be performed where the drug solution is perfused through the setup without cells to assess the extent of drug absorption and adsorption into the materials of the system.

Once established and characterized, the connection platform will allow plugging in of any two organ-chips to study complex physiological organ interactions. The dimensions and design of organ-chips can be varied based on the tissue-type and mechanism of interaction,

as was demonstrated with the example of vascular interaction between human white adipose and hepatic tissue. The platform could allow for the integration of sensors to track culture parameters like oxygen and glucose in real time. The immune cell reservoir could enable the perfusion of immune cells across the platform during long term culture. This platform will allow the study of disease mechanisms based on multi-organ interactions and contribute to PKPD studies in the pharmaceutical drug development process. The preparation of benchmarking criteria for the model would enable the validation of the MOC by regulatory authorities for the study of therapeutic candidates, environmental toxicants, and other stimuli.

5. Summary and conclusions

OoC technology has made rapid progress over the last decade with advances in microfabrication techniques, cell culture, biomarker analysis techniques and more importantly, considerations about the predictability, scalability, and standardization of the models. In order to achieve the goal of the 3Rs, OoC models need to capture biological complexity in a reproducible fashion. Given the complex and chronic nature of metabolic diseases involving the interactions of multiple organs, MOCs represent a new class of preclinical models aimed at fulfilling the 3Rs (reduction, replacement, refinement) of animal testing for mechanistic toxicity or disease modelling.

The goal of this thesis was the development of novel MOC platform technology to connect two organ-chips with integrated sensors and ancillary features to introduce biological complexity in the model.

A detailed investigation was conducted into creating a modular, flexible connection strategy that led to the development and characterization of the MOC connection platform, comprising of the 3D printed modular insert cassette and chips. The cassette was economically feasible to fabricate on a pilot scale, enabled the integration of sensors, and supported a recirculation perfusion regime. It also contained a viewing window to image the inserted chips. The WAT- and liver-chips were designed and standardized to fit into the cassette, where tissue channels were scaled relative to each other, and tissue structure enabled vascular connection in the cassette. The WAT-chips underwent fabrication iterations to support pilot scale production, with a time improvement of about 20 minutes per chip compared to the small-scale fabrication method. The liver-chip dimensions were modified to account for oxygen consumption by the hepatocytes given the low oxygen permeability of the chip materials. Both chips were fabricated from rigid plastics and TPE considering minimal drug absorption.

The application of this model involved the observation of cells, effluents and media components upon organ-chip connection with perfusion. Glucose and oxygen sensors were integrated into the system in collaboration with Dr. Torsten Mayr's group. The perfusion regime for the sensor integration experiments was chosen considering the glucose uptake and release by the hepatocytes in the liver-chip, to ensure glucose detection given the system specifications. The system could measure glucose and oxygen consumption in the cassette during perfusion relative to blank chips without hepatocytes. When the liver-chip were connected to the WAT-chips, lipid droplets accumulated to a higher extent in the hepatocytes of the connected setup compared to those in unconnected liver-chips.

The development of zonation as a feature of biological complexity in the liver led to the design and construction of LSOC in collaboration with Dynamic42 GmbH. With the consideration of economic pilot-scale fabrication of the ShowerTops, the unbranched shower channel was determined as the final design. Simulations were generated to understand the inlet concentrations to be perfused into the shower channel to obtain physiologically relevant gradients within the LSOC. The flow profiles were characterized on-chip with various methodologies like fluorescent molecules and oxygen-scavenging solutions. In well plates,

strategies were tested to create metabolic zonation in HepaRG™ cells exposed to gradients of insulin, glucose and glucagon.

To support long-term circulation of immune cells across the MOC platform, a prototype of an immune cell reservoir was designed and fabricated to allow for simple integration with the platform. Finally, considerations were made about requirements for the preparation of documentation according to regulatory guidelines keeping the goal of the 3Rs in view. The intention of this thought experiment was to provide an outlook into the requirements for validating the WAT-liver connection platform for preclinical studies in mechanistic toxicology or disease modelling of metabolic diseases involving white adipose tissue and liver tissue.

The topics of this thesis collectively address the long-term culture and interaction of tissues (in this case white adipose tissue and hepatic tissue), with ancillary features, facilitating real-time monitoring of the onset and development of chronic metabolic diseases, and investigations of potential therapies for them.

6. German Summary

Die OoC-Technologie hat in den letzten zehn Jahren mit den Fortschritten in den Bereichen Mikrofabrikationstechniken, Zellkulturen, Biomarker-Analysetechniken und, was noch wichtiger ist, mit den Überlegungen zur Vorhersagbarkeit, Skalierbarkeit und Standardisierung der Modelle rasante Fortschritte gemacht. Um das Ziel der 3R zu erreichen, müssen OoC-Modelle die biologische Komplexität in reproduzierbarer Weise erfassen. Angesichts des komplexen und chronischen Charakters von Stoffwechselkrankheiten, bei denen es zu Interaktionen zwischen mehreren Organen kommt, stellen MOCs eine neue Klasse von präklinischen Modellen dar, die die 3R (Reduktion, Ersatz, Verfeinerung) von Tierversuchen für mechanistische Toxizitäts- oder Krankheitsmodellierung erfüllen sollen.

Das Ziel dieser Arbeit war die Entwicklung einer neuartigen MOC-Plattformtechnologie zur Verbindung von zwei Organchips mit integrierten Sensoren und Zusatzfunktionen, um biologische Komplexität in das Modell einzubringen.

Es wurde eine detaillierte Untersuchung zur Schaffung einer modularen, flexiblen Verbindungsstrategie durchgeführt, die zur Entwicklung und Charakterisierung der MOC-Verbindungsplattform führte, die aus einer 3D-gedruckten modularen Einsatzkassette und Chips besteht. Die Kassette war im Pilotmaßstab wirtschaftlich herstellbar, ermöglichte die Integration von Sensoren und unterstützte ein Rezirkulationsperfusionssystem. Sie enthielt auch ein Sichtfenster, um die eingesetzten Chips abzubilden. Die WAT- und Leberchips wurden so konzipiert und standardisiert, dass sie in die Kassette passten, wobei die Gewebekanäle im Verhältnis zueinander skaliert wurden und die Gewebestruktur eine Gefäßverbindung in der Kassette ermöglichte. Die WAT-Chips wurden iterativ hergestellt, um die Produktion im Pilotmaßstab zu unterstützen, wobei sich der Zeitaufwand pro Chip im Vergleich zur Herstellungsmethode im kleinen Maßstab um etwa 20 Minuten verbesserte. Die Abmessungen der Leberchips wurden geändert, um dem Sauerstoffverbrauch der Hepatozyten Rechnung zu tragen, da die Chips eine geringe Sauerstoffdurchlässigkeit aufweisen. Beide Chips wurden aus Hartplastik und TPE hergestellt, wobei eine minimale Arzneimittelabsorption berücksichtigt wurde.

Die Anwendung dieses Modells umfasste die Beobachtung von Parametern bei Anschluss und Perfusion. In Zusammenarbeit mit der Gruppe von Dr. Torsten Mayr wurden Glukose- und Sauerstoffsensoren in das System integriert, und das Perfusionsregime wurde unter Berücksichtigung der von den Hepatozyten im angeschlossenen Leberchip zu detektierenden Glukosekonzentration unter Berücksichtigung der Systemspezifikationen gewählt. Das System konnte den Glukose- und Sauerstoffverbrauch in der Kassette unter Perfusion im Vergleich zu leeren Chips ohne Hepatozyten messen. Wenn die Leberchips mit den WAT-Chips verbunden waren, sammelten sich in den Hepatozyten des angeschlossenen Systems mehr Lipidtröpfchen an als in den nicht angeschlossenen Leberchips.

Die Entwicklung der Zonierung als Merkmal der biologischen Komplexität in der Leber führte zum Design und zur Konstruktion des LSOC in Zusammenarbeit mit der Dynamic42 GmbH. In Anbetracht der wirtschaftlichen Herstellung der ShowerTops im Pilotmaßstab wurde der unverzweigte Duschkanal als endgültiges Design gewählt, mit Simulationen zum Verständnis

der Einlasskonzentrationen, die in den Duschkanal perfundiert werden müssen, um physiologisch relevante Gradienten innerhalb des LSOC zu erhalten. Die Strömungsprofile wurden auf dem Chip mit verschiedenen Methoden wie fluoreszierenden Molekülen und sauerstoffabfangenden Lösungen charakterisiert. In Well-Platten wurden Strategien getestet, um eine metabolische Zonierung in HepaRG™-Zellen zu erzeugen, die Gradienten von Insulin, Glukose und Glucagon ausgesetzt waren.

Um die langfristige Zirkulation von Immunzellen über die MOC-Plattform zu unterstützen, wurde ein Prototyp eines Immunzellenhalters entworfen und hergestellt, der eine einfache Integration in die Plattform ermöglicht. Mit dem Ziel der 3R wurden Überlegungen zu den Anforderungen an die Erstellung der Dokumentation gemäß den regulatorischen Richtlinien angestellt. Ziel dieses Gedankenexperiments war es, einen Ausblick auf die Anforderungen für die Validierung der WAT-Leber-Verbindungsplattform für präklinische Studien in der mechanistischen Toxikologie oder der Krankheitsmodellierung von Stoffwechselkrankheiten unter Beteiligung von weißem Fett- und Lebergewebe zu geben.

Diese Themen dieser Arbeit befassen sich insgesamt mit der langfristigen Kultur und Interaktion von Geweben (in diesem Fall weißes Fett- und Lebergewebe) mit zusätzlichen Funktionen, die eine Echtzeitüberwachung des Beginns und der Entwicklung chronischer Stoffwechselkrankheiten und die Erforschung potenzieller Therapien für diese Krankheiten ermöglichen.

7. Bibliography

Abaci, H. E., & Shuler, M. L. (2015). Human-on-a-chip design strategies and principles for physiologically based pharmacokinetics/pharmacodynamics modeling. *Integrative Biology*, *7*(4), 383–391. https://doi.org/10.1039/C4IB00292J

Aghila Rani, K., Hamad, M., Zaher, D., Sieburth, S., Madani N. & Al-Tel, T. (2021). Drug development post COVID-19 pandemic: toward a better system to meet current and future global health challenges. *Expert Opinion on Drug Discovery*, 16(4), 365-371. Doi 10.1080/17460441.2021.1854221

Ahluwalia, A. (2017). Allometric scaling in-vitro. *Scientific Reports 2017 7:1*, *7*(1), 1–7. https://doi.org/10.1038/srep42113

Alarcon, P. C., Damen, M. S. M. A., Madan, R., Deepe, G. S., Spearman, P., Way, S. S., & Divanovic, S. (2021). Adipocyte inflammation and pathogenesis of viral pneumonias: an overlooked contribution. *Mucosal Immunology*, *14*(6), 1224–1234. https://doi.org/10.1038/s41385-021-00404-8

Alhuthali, S., Kotidis, P., & Kontoravdi, C. (2021). Osmolality Effects on CHO Cell Growth, Cell Volume, Antibody Productivity and Glycosylation. *International Journal of Molecular Sciences*, *22*(7), 3290. https://doi.org/10.3390/ijms22073290

Amera blog. (2018). How to design parts for SLA 3D printing. https://ameralabs.com/blog/3d-design-parts-sla-3d-printing/

Anstee, Q. M., Lawitz, E. J., Alkhouri, N., Wong, V. W. S., Romero-Gomez, M., Okanoue, T., Trauner, M., Kersey, K., Li, G., Han, L., Jia, C., Wang, L., Chen, G., Subramanian, G. M., Myers, R. P., Djedjos, C. S., Kohli, A., Bzowej, N., Younes, Z., … Younossi, Z. M. (2019). Noninvasive Tests Accurately Identify Advanced Fibrosis due to NASH: Baseline Data From the STELLAR Trials. *Hepatology*, *70*(5), 1521–1530. https://doi.org/10.1002/HEP.30842

Anti-Fibrotic Effects of Losartan In Nash Evaluation Study - Full Text View - ClinicalTrials.gov. (n.d.). Retrieved October 15, 2022, from https://clinicaltrials.gov/ct2/show/NCT01051219

Arakawa, H., Sugiura, S., Kawanishi, T., Shin, K., Toyoda, H., Satoh, T., Sakai, Y., Kanamori, T., & Kato, Y. (2020). Kinetic analysis of sequential metabolism of triazolam and its extrapolation to humans using an entero-hepatic two-organ microphysiological system. *Lab on a Chip*, *20*(3), 537–547. https://doi.org/10.1039/C9LC00884E

Atencia, J., Cooksey, G. A., Jahn, A., Zook, J. M., Vreeland, W. N., & Locascio, L. E. (2009). Magnetic connectors for microfluidic applications. *Lab on a Chip*, *10*(2), 246–249. https://doi.org/10.1039/B913331C

Bagiatis, V., Critchlow, G. W., Price, D., & Wang, S. (2019). The effect of atmospheric pressure plasma treatment (APPT) on the adhesive bonding of poly(methyl methacrylate) (PMMA)-to-glass using a polydimethylsiloxane (PDMS)-based adhesive. *International Journal of Adhesion and Adhesives*, *95*, 102405. https://doi.org/10.1016/j.ijadhadh.2019.102405

Bahmad, H. F., Daouk, R., Azar, J., Sapudom, J., Teo, J. C. M., Abou-Kheir, W., & Al-Sayegh, M. (2020). Modeling Adipogenesis: Current and Future Perspective. *Cells 2020, Vol. 9, Page 2326*, *9*(10), 2326. https://doi.org/10.3390/CELLS9102326

Bale, S. S., Moore, L., Yarmush, M., & Jindal, R. (2016). Emerging in Vitro Liver Technologies for Drug Metabolism and Inter-Organ Interactions. *Tissue Engineering - Part B: Reviews*, *22*(5), 383–394. https://doi.org/10.1089/ten.teb.2016.0031

Barrile, R., van der Meer, A. D., Park, H., Fraser, J. P., Simic, D., Teng, F., Conegliano, D., Nguyen, J., Jain, A., Zhou, M., Karalis, K., Ingber, D. E., Hamilton, G. A., & Otieno, M. A. (2018). Organ-

on-Chip Recapitulates Thrombosis Induced by an anti-CD154 Monoclonal Antibody: Translational Potential of Advanced Microengineered Systems. *Clinical Pharmacology & Therapeutics*, *104*(6), 1240–1248. https://doi.org/10.1002/cpt.1054

Bart van der Worp, H., Howells, D. W., Sena, E. S., Porritt, M. J., Rewell, S., O'Collins, V., & Macleod, M. R. (2010). Can Animal Models of Disease Reliably Inform Human Studies? *PLOS Medicine*, *7*(3), e1000245. https://doi.org/10.1371/JOURNAL.PMED.1000245

Bauer, S., Wennberg Huldt, C., Kanebratt, K. P., Durieux, I., Gunne, D., Andersson, S., Ewart, L., Haynes, W. G., Maschmeyer, I., Winter, A., Ämmälä, C., Marx, U., & Andersson, T. B. (2017). Functional coupling of human pancreatic islets and liver spheroids on-a-chip: Towards a novel human ex vivo type 2 diabetes model. *Scientific Reports*, *7*(1), 14620. https://doi.org/10.1038/s41598-017-14815-w

Bell, C. C., Dankers, A. C. A., Lauschke, V. M., Sison-Young, R., Jenkins, R., Rowe, C., Goldring, C. E., Park, K., Regan, S. L., Walker, T., Schofield, C., Baze, A., Foster, A. J., Williams, D. P., van de Ven, A. W. M., Jacobs, F., Houdt, J. van, Lähteenmäki, T., Snoeys, J., … Ingelman-Sundberg, M. (2018). Comparison of Hepatic 2D Sandwich Cultures and 3D Spheroids for Long-term Toxicity Applications: A Multicenter Study. *Toxicological Sciences*, *162*(2), 655–666. https://doi.org/10.1093/toxsci/kfx289

Berger, B., Donzelli, M., Maseneni, S., Boess, F., Roth, A., Krähenbühl, S., & Haschke, M. (2016). Comparison of Liver Cell Models Using the Basel Phenotyping Cocktail. *Frontiers in Pharmacology*, *7*. https://doi.org/10.3389/fphar.2016.00443

Bhatia, S. N., & Ingber, D. E. (2014). Microfluidic organs-on-chips. In *Nature Biotechnology* (Vol. 32, Issue 8, pp. 760–772). Nature Publishing Group. https://doi.org/10.1038/nbt.2989

Booth, R., & Kim, H. (2012). Characterization of a microfluidic in vitro model of the blood-brain barrier (μBBB). *Lab on a Chip*, *12*(10), 1784. https://doi.org/10.1039/c2lc40094d

Borók, A., Laboda, K., & Bonyár, A. (2021). PDMS Bonding Technologies for Microfluidic Applications: A Review. *Biosensors*, *11*(8), 292. https://doi.org/10.3390/bios11080292

Braian, M., Jönsson, D., Kevci, M., & Wennerberg, A. (2018). Geometrical accuracy of metallic objects produced with additive or subtractive manufacturing: A comparative in vitro study. *Dental Materials*, *34*(7), 978–993. https://doi.org/10.1016/j.dental.2018.03.009

Brischwein, M., Grundl, D., Zhang, X., & Wolf. (2009). *Finite Element Modelling of Microphysiometry on Cellular Specimen* (pp. 30–33). https://doi.org/10.1007/978-3-642-03887-7_9

Brooks, J. C., Ford, K. I., Holder, D. H., Holtan, M. D., & Easley, C. J. (2016). Macro-to-micro interfacing to microfluidic channels using 3D-printed templates: application to time-resolved secretion sampling of endocrine tissue. *Analyst*, *141*(20), 5714–5721. https://doi.org/10.1039/C6AN01055E

Buchanan, V. (2021). *H.R.2565 - 117th Congress (2021-2022): FDA Modernization Act of 2021*. http://www.congress.gov/

Buladi, B. M., Chang, C. C., Belovich, J. M., & Gatica, J. E. (1996). Transport phenomena and kinetics in an extravascular bioartificial pancreas. *AIChE Journal*, *42*(9), 2668–2682. https://doi.org/10.1002/aic.690420928

Busche, M., Rabl, D., Fischer, J., Schmees, C., Mayr, T., Gebhardt, R., & Stelzle, M. (2022). Continous, non-invasive monitoring of oxygen consumption in a parallelized microfluidic in vitro system provides novel insight into the response to nutrients and drugs of primary human hepatocytes. *EXCLI Journal*, *21*, 144–161. https://doi.org/10.17179/excli2021-4351

Busche, M., Tomilova, O., Schütte, J., Werner, S., Beer, M., Groll, N., Hagmeyer, B., Pawlak, M., Jones, P. D., Schmees, C., Becker, H., Schnabel, J., Gall, K., Hemmler, R., Matz-Soja, M., Damm,

G., Beuck, S., Klaassen, T., Moer, J., … Stelzle, M. (2020). HepaChip-MP - a twenty-four chamber microplate for a continuously perfused liver coculture model. *Lab on a Chip*, *20*(16), 2911–2926. https://doi.org/10.1039/D0LC00357C

Busek, M., Aizenshtadt, A., Koch, T., Frank, A., Delon, L., Martinez, M. A., Golovin, A., Dumas, C., Stokowiec, J., Gruenzner, S., Melum, E., & Krauss, S. (2023). Pump-less, recirculating organ-on-a-chip (rOoC) platform. *Lab on a Chip*. https://doi.org/10.1039/D2LC00919F

Busek, M., Nøvik, S., Aizenshtadt, A., Amirola-Martinez, M., Combriat, T., Grünzner, S., & Krauss, S. (2021). Thermoplastic Elastomer (TPE)–Poly(Methyl Methacrylate) (PMMA) Hybrid Devices for Active Pumping PDMS-Free Organ-on-a-Chip Systems. *Biosensors*, *11*(5), 162. https://doi.org/10.3390/bios11050162

Cameron, T. C., Randhawa, A., Grist, S. M., Bennet, T., Hua, J., Alde, L. G., Caffrey, T. M., Wellington, C. L., & Cheung, K. C. (2022). PDMS Organ-On-Chip Design and Fabrication: Strategies for Improving Fluidic Integration and Chip Robustness of Rapidly Prototyped Microfluidic In Vitro Models. *Micromachines*, *13*(10), 1573. https://doi.org/10.3390/mi13101573

Carter, J. K., & Friedman, S. L. (2022). Hepatic Stellate Cell-Immune Interactions in NASH. *Frontiers in Endocrinology*, *13*. https://doi.org/10.3389/FENDO.2022.867940

Casas, B., Vilén, L., Bauer, S., Kanebratt, K. P., Wennberg Huldt, C., Magnusson, L., Marx, U., Andersson, T. B., Gennemark, P., & Cedersund, G. (2022). Integrated experimental-computational analysis of a HepaRG liver-islet microphysiological system for human-centric diabetes research. *PLOS Computational Biology*, *18*(10), e1010587. https://doi.org/10.1371/journal.pcbi.1010587

Chan, S. C., Liu, C. L., Lo, C. M., Lam, B. K., Lee, E. W., Wong, Y., & Fan, S. T. (2006). Estimating liver weight of adults by body weight and gender. *World Journal of Gastroenterology*, *12*(14), 2217–2222. www.wjgnet.comhttp://www.wjgnet.com/1007-9327/12/2217.asp

Chawla, M., Verma, V., Kapoor, M., & Kapoor, S. (2017). A novel application of periodic acid-Schiff (PAS) staining and fluorescence imaging for analysing tapetum and microspore development. *Histochemistry and Cell Biology*, *147*(1), 103–110. https://doi.org/10.1007/S00418-016-1481-0

Chen, A., & Pan, T. (2011). Universal adhesive-free fit-to-flow microfluidic connections. *Proceedings of the IEEE International Conference on Micro Electro Mechanical Systems (MEMS)*, 372–375. https://doi.org/10.1109/MEMSYS.2011.5734439

Chen, C. F., Liu, J., Hromada, L. P., Tsao, C. W., Chang, C. C., & DeVoe, D. L. (2009). High-pressure needle interface for thermoplastic microfluidics. *Lab on a Chip*, *9*(1), 50–55. https://doi.org/10.1039/B812812J

Chiew, G., Fu, A., Perng Low K. & Qian Luo K. (2015). Physical supports for liver cancer cells are essential for differentiation and remodeling of endothelial cells in a HepG2-HUVEC co-culture model. *Scientific Reports,* 10801, 5(1). Doi 10.1038/srep10801

Chuchuy, J., Rogal, J., Ngo, T., Stadelmann, K., Antkowiak, L., Achberger, K., Liebau, S., Schenke-Layland, K., & Loskill, P. (2021). Integration of Electrospun Membranes into Low-Absorption Thermoplastic Organ-on-Chip. *ACS Biomaterials Science & Engineering*, *7*(7), 3006–3017. https://doi.org/10.1021/acsbiomaterials.0c01062

Cipriano, M., Schlünder, K., Probst, C., Linke, K., Weiss, M., Fischer, M. J., Mesch, L., Achberger, K., Liebau, S., Mesquida, M., Nicolini, V., Schneider, A., Giusti, A. M., Kustermann, S., & Loskill, P. (2022). Human immunocompetent choroid-on-chip: a novel tool for studying ocular effects of biological drugs. *Communications Biology*, *5*(1), 52. https://doi.org/10.1038/s42003-021-02977-3

Čížková, D., Mokrý, J., Mičuda, S., Österreicher, J., & Martínková, J. (2005). Expression of MRP2 and MDR1 transporters and other hepatic markers in rat and human liver and in WRL 68 cell line. *Physiological Research*, 419–428. https://doi.org/10.33549/physiolres.930674

Clark, A. M., Sousa, K. M., Jennings, C., MacDougald, O. A., & Kennedy, R. T. (2009). Continuous-flow enzyme assay on a microfluidic chip for monitoring glycerol secretion from cultured adipocytes. *Analytical Chemistry*, *81*(6), 2350–2356. https://doi.org/10.1021/AC8026965

Compera, N., Atwell, S., Wirth, J., von Törne, C., Hauck, S. M., & Meier, M. (2022). Adipose microtissue-on-chip: a 3D cell culture platform for differentiation, stimulation, and proteomic analysis of human adipocytes. *Lab on a Chip*, *22*(17), 3172–3186. https://doi.org/10.1039/D2LC00245K

Cook, S. R., Musgrove, H. B., Throckmorton, A. L., & Pompano, R. R. (2022). Microscale impeller pump for recirculating flow in organs-on-chip and microreactors. *Lab on a Chip*, *22*(3), 605–620. https://doi.org/10.1039/D1LC01081F

Cooksey, G. A., Plant, A. L., & Atencia, J. (2009). A vacuum manifold for rapid world-to-chip connectivity of complex PDMS microdevices. *Lab on a Chip*, *9*(9), 1298–1300. https://doi.org/10.1039/B820683J

Corrêa, L., Heyn, G., Cells, K. M.-, & 2019, undefined. (2019). The impact of the adipose organ plasticity on inflammation and cancer progression. *Mdpi.Com*. https://doi.org/10.3390/cells8070662

Corvera, S. (2021). Cellular Heterogeneity in Adipose Tissues. *Annual Review of Physiology*, *83*, 257–278. https://doi.org/10.1146/ANNUREV-PHYSIOL-031620-095446

Cunningham, R. P., & Porat-Shliom, N. (2021). Liver Zonation – Revisiting Old Questions With New Technologies. *Frontiers in Physiology*, *12*. https://doi.org/10.3389/fphys.2021.732929

Davidson, M. D., & Khetani, S. R. (2020). Intermittent Starvation Extends the Functional Lifetime of Primary Human Hepatocyte Cultures. *Toxicological Sciences*, *174*(2), 266–277. https://doi.org/10.1093/toxsci/kfaa003

Davidson, M. D., Pickrell, J., & Khetani, S. R. (2021). Physiologically inspired culture medium prolongs the lifetime and insulin sensitivity of human hepatocytes in micropatterned co-cultures. *Toxicology*, *449*, 152662. https://doi.org/10.1016/j.tox.2020.152662

Deacon, C. F. (2019). Physiology and Pharmacology of DPP-4 in Glucose Homeostasis and the Treatment of Type 2 Diabetes. *Frontiers in Endocrinology*, *10*. https://doi.org/10.3389/fendo.2019.00080

Dickson, I. (2019). Multispecies liver-on-a-chip for improved drug toxicity testing. *Nature Reviews Gastroenterology & Hepatology 2019 17:1*, *17*(1), 4–4. https://doi.org/10.1038/s41575-019-0244-5

Ding, X., Lin, S. C. S., Kiraly, B., Yue, H., Li, S., Chiang, I. K., Shi, J., Benkovic, S. J., & Huang, T. J. (2012). On-chip manipulation of single microparticles, cells, and organisms using surface acoustic waves. *Proceedings of the National Academy of Sciences of the United States of America*, *109*(28), 11105–11109. https://doi.org/10.1073/PNAS.1209288109/SUPPL_FILE/SM08.AVI

Dizon, J. R. C., Gache, C. C. L., Cascolan, H. M. S., Cancino, L. T., & Advincula, R. C. (2021). Post-Processing of 3D-Printed Polymers. *Technologies*, *9*(3), 61. https://doi.org/10.3390/technologies9030061

Doran, P. M. (1999). Design of Mixing Systems for Plant Cell Suspensions in Stirred Reactors. *Biotechnology Progress*, *15*(3), 319–335. https://doi.org/10.1021/BP990042V

Duivenvoorde, L. P. M., Louisse, J., Pinckaers, N. E. T., Nguyen, T., & van der Zande, M. (2021). Comparison of gene expression and biotransformation activity of HepaRG cells under static and dynamic culture conditions. *Scientific Reports 2021 11:1*, *11*(1), 1–12. https://doi.org/10.1038/s41598-021-89710-6

Eddings, M. A., Johnson, M. A., & Gale, B. K. (2008). Determining the optimal PDMS–PDMS bonding technique for microfluidic devices. *Journal of Micromechanics and Microengineering*, *18*(6), 067001. https://doi.org/10.1088/0960-1317/18/6/067001

Ehrlich, A., Duche, D., Ouedraogo, G., & Nahmias, Y. (2019). Challenges and Opportunities in the Design of Liver-on-Chip Microdevices. *Annual Review of Biomedical Engineering*, *21*, 219. https://doi.org/10.1146/ANNUREV-BIOENG-060418-052305

Eipel, C., Abshagen, K., & Vollmar, B. (2010). Regulation of hepatic blood flow: The hepatic arterial buffer response revisited. *World Journal of Gastroenterology : WJG*, *16*(48), 6046. https://doi.org/10.3748/WJG.V16.I48.6046

Essaouiba, A., Okitsu, T., Kinoshita, R., Jellali, R., Shinohara, M., Danoy, M., Legallais, C., Sakai, Y., & Leclerc, E. (2020). Development of a pancreas-liver organ-on-chip coculture model for organ-to-organ interaction studies. *Biochemical Engineering Journal*, *164*, 107783. https://doi.org/10.1016/J.BEJ.2020.107783

Evander, M., & Tenje, M. (2014). Microfluidic PMMA interfaces for rectangular glass capillaries. *Journal of Micromechanics and Microengineering*, *24*(2), 027003. https://doi.org/10.1088/0960-1317/24/2/027003

Ewart, L., Apostolou, A., Briggs, S. A., Carman, C. v., Chaff, J. T., Heng, A. R., Jadalannagari, S., Janardhanan, J., Jang, K.-J., Joshipura, S. R., Kadam, M. M., Kanellias, M., Kujala, V. J., Kulkarni, G., Le, C. Y., Lucchesi, C., Manatakis, D. v., Maniar, K. K., Quinn, M. E., … Levner, D. (2022). Performance assessment and economic analysis of a human Liver-Chip for predictive toxicology. *Communications Medicine*, *2*(1), 154. https://doi.org/10.1038/s43856-022-00209-1

Faghih, M. M., & Sharp, M. K. (2019). Solvent-based bonding of PMMA–PMMA for microfluidic applications. *Microsystem Technologies*, *25*(9), 3547–3558. https://doi.org/10.1007/s00542-018-4266-7

Fain, J. N., Cheema, P., Madan, A. K., & Tichansky, D. S. (2010). Dexamethasone and the inflammatory response in explants of human omental adipose tissue. *Molecular and Cellular Endocrinology*, *315*(1–2), 292–298. https://doi.org/10.1016/J.MCE.2009.10.004

Fischer-Posovszky, P., Newell, F. S., Wabitsch, M., & Tornqvist, H. E. (2008). Human SGBS Cells – a Unique Tool for Studies of Human Fat Cell Biology. *Obesity Facts*, *1*(4), 184–189. https://doi.org/10.1159/000145784

Franzen, N., van Harten, W. H., Retèl, V. P., Loskill, P., van den Eijnden-van Raaij, J., & IJzerman, M. (2019). Impact of organ-on-a-chip technology on pharmaceutical R&D costs. *Drug Discovery Today*, *24*(9), 1720–1724. https://doi.org/10.1016/j.drudis.2019.06.003

Frayn, K. (2002). Adipose tissue as a buffer for daily lipid flux. *Diabetologia*, *45*(9), 1201–1210. https://doi.org/10.1007/s00125-002-0873-y

Fuchs, S., Johansson, S., Tjell, A. Ø., Werr, G., Mayr, T., & Tenje, M. (2021). In-Line Analysis of Organ-on-Chip Systems with Sensors: Integration, Fabrication, Challenges, and Potential. *ACS Biomaterials Science & Engineering*, 2926–2948. https://doi.org/10.1021/acsbiomaterials.0c01110

Fuchs, S., van Helden, R. W. J., Wiendels, M., de Graaf, M. N. S., Orlova, V. V., Mummery, C. L., van Meer, B. J., & Mayr, T. (2022). On-chip analysis of glycolysis and mitochondrial respiration in

human induced pluripotent stem cells. *Materials Today Bio*, *17*, 100475. https://doi.org/10.1016/j.mtbio.2022.100475

Gage, B. K., Liu, J. C., Innes, B. T., MacParland, S. A., McGilvray, I. D., Bader, G. D., & Keller, G. M. (2020). Generation of Functional Liver Sinusoidal Endothelial Cells from Human Pluripotent Stem-Cell-Derived Venous Angioblasts. *Cell Stem Cell*, *27*(2), 254-269.e9. https://doi.org/10.1016/j.stem.2020.06.007

Gaskell, H., Sharma, P., Colley, H. E., Murdoch, C., Williams, D. P., & Webb, S. D. (2016). Characterization of a functional C3A liver spheroid model. *Toxicology Research*, *5*(4), 1053–1065. https://doi.org/10.1039/C6TX00101G

Glavan, A. C., Martinez, R. v., Maxwell, E. J., Subramaniam, A. B., Nunes, R. M. D., Soh, S., & Whitesides, G. M. (2013). Rapid fabrication of pressure-driven open-channel microfluidic devices in omniphobic RF paper. *Lab on a Chip*, *13*(15), 2922–2930. https://doi.org/10.1039/C3LC50371B

Glieberman, A. L., Pope, B. D., Zimmerman, J. F., Liu, Q., Ferrier, J. P., Kenty, J. H. R., Schrell, A. M., Mukhitov, N., Shores, K. L., Tepole, A. B., Melton, D. A., Roper, M. G., & Parker, K. K. (2019). Synchronized stimulation and continuous insulin sensing in a microfluidic human Islet on a Chip designed for scalable manufacturing. *Lab on a Chip*, *19*(18), 2993–3010. https://doi.org/10.1039/C9LC00253G

Godwin, L. A., Brooks, J. C., Hoepfner, L. D., Wanders, D., Judd, R. L., & Easley, C. J. (2015). A microfluidic interface for the culture and sampling of adiponectin from primary adipocytes. *Analyst*, *140*(4), 1019–1025. https://doi.org/10.1039/C4AN01725K

Gogg, S., Nerstedt, A., Boren, J., & Smith, U. (2019). Human adipose tissue microvascular endothelial cells secrete PPARγ ligands and regulate adipose tissue lipid uptake. *JCI Insight*, *4*(5). https://doi.org/10.1172/jci.insight.125914

Gómez-Lechón, M. J., Tolosa, L., Conde, I., & Donato, M. T. (2014). Competency of different cell models to predict human hepatotoxic drugs. *Expert Opinion on Drug Metabolism and Toxicology*, *10*(11), 1553–1568. https://doi.org/10.1517/17425255.2014.967680

Grant, J., Özkan, A., Oh, C., Mahajan, G., Prantil-Baun, R., & Ingber, D. E. (2021). Simulating drug concentrations in PDMS microfluidic organ chips. *Lab on a Chip*, *21*(18), 3509–3519. https://doi.org/10.1039/D1LC00348H

Greco, A. V, Crucitti, F., Ghirlanda, G., Manna, R., Altomonte, L., Rebuzzi, A. G., & Bertoli, A. (1979). Insulin and Giucagon Concentrations in Portal and Peripheral Veins in Patients with Hepatic Cirrhosis. *Diabetologia*, *17*, 23–28.

Greek, R., & Menache, A. (2013). Systematic Reviews of Animal Models: Methodology versus Epistemology. *International Journal of Medical Sciences*, *10*(3), 206. https://doi.org/10.7150/IJMS.5529

Green, H., & Kehinde, O. (1975). An established preadipose cell line and its differentiation in culture II. Factors affecting the adipose conversion. *Cell*, *5*(1), 19–27. https://doi.org/10.1016/0092-8674(75)90087-2

Hammond, T. G., & Hammond, J. M. (2001). Optimized suspension culture: the rotating-wall vessel. *American Journal of Physiology. Renal Physiology*, *281*(1). https://doi.org/10.1152/AJPRENAL.2001.281.1.F12

Honka, M.-J., Latva-Rasku, A., Bucci, M., Virtanen, K. A., Hannukainen, J. C., Kalliokoski, K. K., & Nuutila, P. (2018). Insulin-stimulated glucose uptake in skeletal muscle, adipose tissue and liver: a positron emission tomography study. *European Journal of Endocrinology*, *178*(5), 523–531. https://doi.org/10.1530/EJE-17-0882

Hoofnagle, J. H., Van Natta, M. L., Kleiner, D. E., Clark, J. M., Kowdley, K. V., Loomba, R., Neuschwander-Tetri, B. A., Sanyal, A. J., & Tonascia, J. (2013). Vitamin e and changes in serum alanine aminotransferase levels in patients with non-alcoholic steatohepatitis. *Alimentary Pharmacology and Therapeutics*, *38*(2), 134–143. https://doi.org/10.1111/APT.12352

Hornung, F., Rogal, J., Loskill, P., Löffler, B., & Deinhardt-Emmer, S. (2021). The Inflammatory Profile of Obesity and the Role on Pulmonary Bacterial and Viral Infections. *Mdpi.Com*. https://doi.org/10.3390/ijms22073456

House, S. D., & Johnson, P. C. (1986). Microvascular pressure in venules of skeletal muscle during arterial pressure reduction. *American Journal of Physiology-Heart and Circulatory Physiology*, *250*(5), H838–H845. https://doi.org/10.1152/ajpheart.1986.250.5.H838

Huh, D., Matthews, B. D., Mammoto, A., Montoya-Zavala, M., Hsin, H. Y., & Ingber, D. E. (2010). Reconstituting Organ-Level Lung Functions on a Chip. *Science*, *328*(5986), 1662–1668. https://doi.org/10.1126/science.1188302

Iori, E., Vinci, B., Murphy, E., Marescotti, M. C., Avogaro, A., & Ahluwalia, A. (2012). Glucose and Fatty Acid Metabolism in a 3 Tissue In-Vitro Model Challenged with Normo- and Hyperglycaemia. *PLoS ONE*, *7*(4). https://doi.org/10.1371/journal.pone.0034704

Irwin M. Arias, Harvey J. Alter, James L. Boyer, David E. Cohen, Nelson Fausto, David A. Shafritz, & Allan W. Wolkoff. (2009). *The Liver* (I. M. Arias, Ed.). John Wiley & Sons, Ltd. https://doi.org/10.1002/9780470747919

Jang, K.-J., Otieno, M. A., Ronxhi, J., Lim, H.-K., Ewart, L., Kodella, K. R., Petropolis, D. B., Kulkarni, G., Rubins, J. E., Conegliano, D., Nawroth, J., Simic, D., Lam, W., Singer, M., Barale, E., Singh, B., Sonee, M., Streeter, A. J., Manthey, C., … Hamilton, G. A. (2019). Reproducing human and cross-species drug toxicities using a Liver-Chip. *Science Translational Medicine*, *11*(517). https://doi.org/10.1126/scitranslmed.aax5516

Jang, S., Lee, C. H., Choi, K. M., Lee, J., Choi, J. W., Kim, K. A., & Park, C. M. (2011). Correlation of fatty liver and abdominal fat distribution using a simple fat computed tomography protocol. *World Journal of Gastroenterology*, *17*(28), 3335–3341. https://doi.org/10.3748/wjg.v17.i28.3335

Jeon, J. S., Chung, S., Kamm, R. D., & Charest, J. L. (2011). Hot embossing for fabrication of a microfluidic 3D cell culture platform. *Biomedical Microdevices*, *13*(2), 325–333. https://doi.org/10.1007/s10544-010-9496-0

Jungermann, K., & Kietzmann, T. (2000). Oxygen: Modulator of metabolic zonation and disease of the liver. *Hepatology*, *31*(2), 255–260. https://doi.org/10.1002/hep.510310201

Kaitin, K. I. (2010). Deconstructing the Drug Development Process: The New Face of Innovation. *Clinical Pharmacology & Therapeutics*, *87*(3), 356–361. https://doi.org/10.1038/CLPT.2009.293

Kang, Y. B., Eo, J., Bulutoglu, B., Yarmush, M. L., & Usta, O. B. (2020). Progressive Hypoxia-on-a-Chip: An In Vitro Oxygen Gradient Model for Capturing the Effects of Hypoxia on Primary Hepatocytes in Health and Disease. *Biotechnology and Bioengineering*, *117*(3), 763. https://doi.org/10.1002/BIT.27225

Kang, Y. B., Eo, J., Mert, S., Yarmush, M. L., & Usta, O. B. (2018). Metabolic Patterning on a Chip: Towards in vitro Liver Zonation of Primary Rat and Human Hepatocytes. *Scientific Reports*, *8*(1), 8951. https://doi.org/10.1038/s41598-018-27179-6

Kim, D. Y., Choi, M. J., Ko, T. K., Lee, N. H., Kim, O. H., & Cheon, H. G. (2020). Angiotensin AT1 receptor antagonism by losartan stimulates adipocyte browning via induction of apelin. *Journal of Biological Chemistry*, *295*(44), 14878–14892. https://doi.org/10.1074/JBC.RA120.013834

Kim, H. J., Huh, D., Hamilton, G., & Ingber, D. E. (2012). Human gut-on-a-chip inhabited by microbial flora that experiences intestinal peristalsis-like motions and flow. *Lab on a Chip*, *12*(12), 2165. https://doi.org/10.1039/c2lc40074j

Kim, K., Park, S. W., & Yang, S. S. (2010). The optimization of PDMS-PMMA bonding process using silane primer. *BioChip Journal*, *4*(2), 148–154. https://doi.org/10.1007/s13206-010-4210-0

Kim, Y.-S., Asif, A., Chethikkattuveli Salih, A. R., Lee, J.-W., Hyun, K.-N., & Choi, K.-H. (2021). Gravity-Based Flow Efficient Perfusion Culture System for Spheroids Mimicking Liver Inflammation. *Biomedicines*, *9*(10), 1369. https://doi.org/10.3390/biomedicines9101369

K&J Magnetics Inc. (n.d.). *K&J online calculator*. Retrieved December 13, 2022, from https://www.kjmagnetics.com/calculator.asp?calcType=block

Ko, J., Park, D., Lee, S., Gumuscu, B., & Jeon, N. (2022). Engineering Organ-on-a-Chip to Accelerate Translational Research. *Micromachines*, *13*(8), 1200. https://doi.org/10.3390/mi13081200

Koui, Y., Kido, T., Ito, T., Oyama, H., Chen, S. W., Katou, Y., Shirahige, K., & Miyajima, A. (2017). An In Vitro Human Liver Model by iPSC-Derived Parenchymal and Non-parenchymal Cells. *Stem Cell Reports*, *9*(2), 490–498. https://doi.org/10.1016/J.STEMCR.2017.06.010

Krishna, M. (2013). Microscopic anatomy of the liver. *Clinical Liver Disease*, *2*(S1), S4–S7. https://doi.org/10.1002/cld.147

Kuri-Harcuch, W., & Green, H. (1978). Adipose conversion of 3T3 cells depends on a serum factor. *Proceedings of the National Academy of Sciences*, *75*(12), 6107–6109. https://doi.org/10.1073/PNAS.75.12.6107

Kuzbari, O., Peterson, C. M., Franklin, M. R., Hathaway, L. B., Johnstone, E. B., Hammoud, A. O., & Lamb, J. G. (2013). Comparative analysis of human CYP3A4 and rat CYP3A1 induction and relevant gene expression by bisphenol A and diethylstilbestrol: Implications for toxicity testing paradigms. *Reproductive Toxicology*, *37*, 24–30. https://doi.org/10.1016/j.reprotox.2013.01.005

Lau, F. H., Vogel, K., Luckett, J. P., Hunt, M., Meyer, A., Rogers, C. L., Tessler, O., Dupin, C. L., St. Hilaire, H., Islam, K. N., Frazier, T., Gimble, J. M., & Scahill, S. (2018). Sandwiched White Adipose Tissue: A Microphysiological System of Primary Human Adipose Tissue. *Tissue Engineering Part C: Methods*, *24*(3), 135–145. https://doi.org/10.1089/ten.tec.2017.0339

Lee, H., Chae, S., Kim, J. Y., Han, W., Kim, J., Choi, Y., & Cho, D. W. (2019). Cell-printed 3D liver-on-a-chip possessing a liver microenvironment and biliary system. *Biofabrication*, *11*(2), 025001. https://doi.org/10.1088/1758-5090/AAF9FA

Lee, S. Y., & Sung, J. H. (2018). Gut–liver on a chip toward an in vitro model of hepatic steatosis. *Biotechnology and Bioengineering*, *115*(11), 2817–2827. https://doi.org/10.1002/bit.26793

Lerche-Langrand, C., & Toutain, H. J. (2000). Precision-cut liver slices: characteristics and use for in vitro pharmaco-toxicology. *Toxicology*, *153*(1–3), 221–253. https://doi.org/10.1016/S0300-483X(00)00316-4

Leung, C. M., de Haan, P., Ronaldson-Bouchard, K., Kim, G.-A., Ko, J., Rho, H. S., Chen, Z., Habibovic, P., Jeon, N. L., Takayama, S., Shuler, M. L., Vunjak-Novakovic, G., Frey, O., Verpoorte, E., & Toh, Y.-C. (2022). A guide to the organ-on-a-chip. *Nature Reviews Methods Primers*, *2*(1), 33. https://doi.org/10.1038/s43586-022-00118-6

Li, G., Li, Z., Gao, Z., Wang, J., Bao, Y., & Derksen, J. J. (2018). Particle image velocimetry experiments and direct numerical simulations of solids suspension in transitional stirred tank flow. *Chemical Engineering Science*, *191*, 288–299. https://doi.org/10.1016/j.ces.2018.06.073

Li, X., Brooks, J. C., Hu, J., Ford, K. I., & Easley, C. J. (2017). 3D-templated, fully automated microfluidic input/output multiplexer for endocrine tissue culture and secretion sampling. *Lab on a Chip*, *17*(2), 341–349. https://doi.org/10.1039/C6LC01201A

Li, X., & Easley, C. J. (2018). Microfluidic systems for studying dynamic function of adipocytes and adipose tissue. *Analytical and Bioanalytical Chemistry*, *410*(3), 791–800. https://doi.org/10.1007/s00216-017-0741-8

Lin, D., Chun, T. H., & Kang, L. (2016). Adipose extracellular matrix remodelling in obesity and insulin resistance. *Biochemical Pharmacology*, *119*, 8–16. https://doi.org/10.1016/J.BCP.2016.05.005

Loprinzi, P. D., Branscum, A., Hanks, J., & Smit, E. (2016). Healthy Lifestyle Characteristics and Their Joint Association With Cardiovascular Disease Biomarkers in US Adults. *Mayo Clinic Proceedings*, *91*(4), 432–442. https://doi.org/10.1016/j.mayocp.2016.01.009

Loskill, P., Marcus, S. G., Mathur, A., Reese, W. M., & Healy, K. E. (2015). µOrgano: A Lego®-Like Plug & Play System for Modular Multi-Organ-Chips. *PLOS ONE*, *10*. https://doi.org/10.1371/journal.pone.0139587

Loskill, P., Sezhian, T., Tharp, K. M., Lee-Montiel, F. T., Jeeawoody, S., Reese, W. M., Zushin, P.-J. H., Stahl, A., & Healy, K. E. (2017). WAT-on-a-chip: a physiologically relevant microfluidic system incorporating white adipose tissue. *Lab on a Chip*, *17*(9), 1645–1654. https://doi.org/10.1039/C6LC01590E

Maass, C., Stokes, C. L., Griffith, L. G., & Cirit, M. (2017). Multi-functional scaling methodology for translational pharmacokinetic and pharmacodynamic applications using integrated microphysiological systems (MPS). *Integrative Biology (United Kingdom)*, *9*(4), 290–302. https://doi.org/10.1039/c6ib00243a

Malarkey, D. E., Johnson, K., Ryan, L., Boorman, G., & Maronpot, R. R. (2016). New Insights into Functional Aspects of Liver Morphology. *Http://Dx.Doi.Org/10.1080/01926230590881826*, *33*(1), 27–34. https://doi.org/10.1080/01926230590881826

Mandrup, S., Loftus, T. M., Macdougald, O. A., Kuhajda, F. P., & Lane, M. D. (1997). Obese gene expression at in vivo levels by fat pads derived from s.c. implanted 3T3-F442A preadipocytes. *Proceedings of the National Academy of Sciences*, *94*(9), 4300–4305. https://doi.org/10.1073/PNAS.94.9.4300

Mashek, D. G. (2021). Hepatic lipid droplets: A balancing act between energy storage and metabolic dysfunction in NAFLD. *Molecular Metabolism*, *50*, 101115. https://doi.org/10.1016/j.molmet.2020.101115

Mastrangeli, M., Millet, S., & van den Eijnden-van Raaij, J. (2019). Organ-on-chip in development: Towards a roadmap for organs-on-chip. *ALTEX*, 650–668. https://doi.org/10.14573/altex.1908271

Materne, E. M., Maschmeyer, I., Lorenz, A. K., Horland, R., Schimek, K. M. S., Busek, M., Sonntag, F., Lauster, R., & Marx, U. (2015). The multi-organ chip - A microfluidic platform for long-term multi-tissue coculture. *Journal of Visualized Experiments*, *98*. https://doi.org/10.3791/52526

Matsunaga, K., Sato, K., Tajima, M., & Yoshida, Y. (2005). Gas Permeability of Thermoplastic Polyurethane Elastomers. *Polymer Journal*, *37*(6), 413–417. https://doi.org/10.1295/polymj.37.413

Mazzoleni, G., Di Lorenzo, D., & Steimberg, N. (2009). Modelling tissues in 3D: the next future of pharmaco-toxicology and food research? *Genes & Nutrition*, *4*(1), 13–22. https://doi.org/10.1007/s12263-008-0107-0

MB Labsamera, https://ameralabs. com/blog/3d-design-parts-sla-3d-printing/. (n.d.). *Designing parts for 3D printing*. Retrieved December 13, 2022, from https://ameralabs.com/blog/3d-design-parts-sla-3d-printing/

McAleer, C. W., Pointon, A., Long, C. J., Brighton, R. L., Wilkin, B. D., Bridges, L. R., Narasimhan Sriram, N., Fabre, K., McDougall, R., Muse, V. P., Mettetal, J. T., Srivastava, A., Williams, D., Schnepper, M. T., Roles, J. L., Shuler, M. L., Hickman, J. J., & Ewart, L. (2019). On the potential of in vitro organ-chip models to define temporal pharmacokinetic-pharmacodynamic relationships. *Scientific Reports*, *9*(1), 9619. https://doi.org/10.1038/s41598-019-45656-4

McCarty, W. J., Usta, O. B., & Yarmush, M. L. (2016). A Microfabricated Platform for Generating Physiologically-Relevant Hepatocyte Zonation. *Scientific Reports 2016 6:1*, *6*(1), 1–10. https://doi.org/10.1038/srep26868

Messelmani, T., Morisseau, L., Sakai, Y., Legallais, C., le Goff, A., Leclerc, E., & Jellali, R. (2022). Liver organ-on-chip models for toxicity studies and risk assessment. *Lab on a Chip*, *22*(13), 2423–2450. https://doi.org/10.1039/D2LC00307D

Mestas, J., & Hughes, C. C. W. (2004). Of Mice and Not Men: Differences between Mouse and Human Immunology. *The Journal of Immunology*, *172*(5), 2731–2738. https://doi.org/10.4049/JIMMUNOL.172.5.2731

Miller, P. G., & Shuler, M. L. (2016). Design and demonstration of a pumpless 14 compartment microphysiological system. *Biotechnology and Bioengineering*, *113*(10), 2213–2227. https://doi.org/10.1002/bit.25989

Miranda, A., Martínez, L., & de Beule, P. A. A. (2020). Facile synthesis of an aminopropylsilane layer on Si/SiO2 substrates using ethanol as APTES solvent. *MethodsX*, *7*, 100931. https://doi.org/10.1016/j.mex.2020.100931

Misun, P. M., Rothe, J., Schmid, Y. R. F., Hierlemann, A., & Frey, O. (2016). Multi-analyte biosensor interface for real-time monitoring of 3D microtissue spheroids in hanging-drop networks. *Microsystems & Nanoengineering*, *2*(1), 16022. https://doi.org/10.1038/micronano.2016.22

Moayedfard, Z., Sani, F., Alizadeh, A., Bagheri Lankarani, K., Zarei, M., & Azarpira, N. (2022). The role of the immune system in the pathogenesis of NAFLD and potential therapeutic impacts of mesenchymal stem cell-derived extracellular vesicles. *Stem Cell Research & Therapy*, *13*(1), 242. https://doi.org/10.1186/s13287-022-02929-6

Monteiro, O. A. C., & Airoldi, C. (1999). Some studies of crosslinking chitosan–glutaraldehyde interaction in a homogeneous system. *International Journal of Biological Macromolecules*, *26*(2–3), 119–128. https://doi.org/10.1016/S0141-8130(99)00068-9

Moradi, E., Jalili-Firoozinezhad, S., & Solati-Hashjin, M. (2020). Microfluidic organ-on-a-chip models of human liver tissue. *Acta Biomaterialia*, *116*, 67–83. https://doi.org/10.1016/J.ACTBIO.2020.08.041

Moraes, C., Labuz, J. M., Leung, B. M., Inoue, M., Chun, T.-H., & Takayama, S. (2013). On being the right size: scaling effects in designing a human-on-a-chip. *Integr Biol (Camb)*, *5*(9), 1149–1161. https://doi.org/10.1039/c3ib40040a

Moruzzi, A., Shroff, T., Keller, S., Loskill, P., & Cipriano, M. (2023). Training the Next Generation of Researchers in the Organ-on-Chip Field. *Education Sciences*, *13*(2), 144. https://doi.org/10.3390/educsci13020144

Moulay, S. (2014). Dopa/Catechol-Tethered Polymers: Bioadhesives and Biomimetic Adhesive Materials. *Polymer Reviews*, *54*(3), 436–513. https://doi.org/10.1080/15583724.2014.881373

Mubbunu, L., Bowa, K., Petrenko, V., & Silitongo, M. (2018). Correlation of Internal Organ Weights with Body Weight and Body Height in Normal Adult Zambians: A Case Study of Ndola Teaching Hospital. *Anatomy Research International*, *2018*, 1–5. https://doi.org/10.1155/2018/4687538

Mueller, D., Krämer, L., Hoffmann, E., Klein, S., & Noor, F. (2014). 3D organotypic HepaRG cultures as in vitro model for acute and repeated dose toxicity studies. *Toxicology in Vitro*, *28*(1), 104–112. https://doi.org/10.1016/J.TIV.2013.06.024

Mundi, M. S., Koutsari, C., & Jensen, M. D. (2014). Effects of Increased Free Fatty Acid Availability on Adipose Tissue Fatty Acid Storage in Men. *The Journal of Clinical Endocrinology & Metabolism*, *99*(12), E2635–E2642. https://doi.org/10.1210/JC.2014-2690

Murphy, E. R., Inoue, T., Sahoo, H. R., Zaborenko, N., & Jensen, K. F. (2007). Solder-based chip-to-tube and chip-to-chip packaging for microfluidic devices. *Lab on a Chip*, *7*(10), 1309–1314. https://doi.org/10.1039/B704804A

Nahak, B. K., Mishra, A., Preetam, S., & Tiwari, A. (2022). Advances in Organ-on-a-Chip Materials and Devices. *ACS Applied Bio Materials*, *5*(8), 3576–3607. https://doi.org/10.1021/acsabm.2c00041

NCT03028740, & clinicaltrials.gov. (2021). *AURORA: A Study for the Efficacy and Safety of Cenicriviroc (CVC) for the Treatment of Liver Fibrosis in Adults With Nonalcoholic Steatohepatitis (NASH)*. https://clinicaltrials.gov/ct2/show/NCT03028740

Newton, J. L., Jones, D. E. J., Henderson, E., Kane, L., Wilton, K., Burt, A. D., & Day, C. P. (2008). Fatigue in non-alcoholic fatty liver disease (NAFLD) is significant and associates with inactivity and excessive daytime sleepiness but not with liver disease severity or insulin resistance. *Gut*, *57*(6), 807–813. https://doi.org/10.1136/GUT.2007.139303

Nomura, Y., Fukui, C., Morishita, Y., & Haishima, Y. (2017). A biological study establishing the endotoxin limit for in vitro proliferation of human mesenchymal stem cells. *Regenerative Therapy*, *7*, 45–51. https://doi.org/10.1016/j.reth.2017.08.004

Novak, R., Didier, M., Calamari, E., Ng, C. F., Choe, Y., Clauson, S. L., Nestor, B. A., Puerta, J., Fleming, R., Firoozinezhad, S. J., & Ingber, D. E. (2018). Scalable Fabrication of Stretchable, Dual Channel, Microfluidic Organ Chips. *Journal of Visualized Experiments*, *140*. https://doi.org/10.3791/58151

Novak, R., Ingram, M., Marquez, S., Das, D., Delahanty, A., Herland, A., Maoz, B. M., Jeanty, S. S. F., Somayaji, M. R., Burt, M., Calamari, E., Chalkiadaki, A., Cho, A., Choe, Y., Chou, D. B., Cronce, M., Dauth, S., Divic, T., Fernandez-Alcon, J., Ingber, D. E. (2020). Robotic fluidic coupling and interrogation of multiple vascularized organ chips. *Nature Biomedical Engineering*, *4*(4), 407–420. https://doi.org/10.1038/s41551-019-0497-x

OECD. (2018). *Guidance Document on Good In Vitro Method Practices (GIVIMP)*. OECD. https://doi.org/10.1787/9789264304796-en

Ong, L. J. Y., Ching, T., Chong, L. H., Arora, S., Li, H., Hashimoto, M., Dasgupta, R., Yuen, P. K., & Toh, Y. C. (2019). Self-aligning Tetris-Like (TILE) modular microfluidic platform for mimicking multi-organ interactions. *Lab on a Chip*, *19*(13), 2178–2191. https://doi.org/10.1039/C9LC00160C

Oomen, P. E., Skolimowski, M. D., & Verpoorte, E. (2016). Implementing oxygen control in chip-based cell and tissue culture systems. *Lab on a Chip*, *16*(18), 3394–3414. https://doi.org/10.1039/C6LC00772D

Overmoyer, B. A., McLaren, C. E., & Brittenham, G. M. (1987). Uniformity of liver density and nonheme (storage) iron distribution. *Archives of Pathology & Laboratory Medicine*, *111*(6), 549–554.

Paoli, R., di Giuseppe, D., Badiola-Mateos, M., Martinelli, E., Lopez-Martinez, M. J., & Samitier, J. (2021). Rapid Manufacturing of Multilayered Microfluidic Devices for Organ on a Chip Applications. *Sensors 2021, Vol. 21, Page 1382*, *21*(4), 1382. https://doi.org/10.3390/S21041382

Parrish, J., Lim, K. S., Baer, K., Hooper, G. J., & Woodfield, T. B. F. (2018). A 96-well microplate bioreactor platform supporting individual dual perfusion and high-throughput assessment of simple or biofabricated 3D tissue models. *Lab on a Chip*, *18*(18), 2757–2775. https://doi.org/10.1039/C8LC00485D

Partanen, T. A., & Paavonen, K. (2001). Lymphatic versus blood vascular endothelial growth factors and receptors in humans. *Microscopy Research and Technique*, *55*(2), 108–121. https://doi.org/10.1002/jemt.1162

Paul, R. (2021). *S.2952 - 117th Congress (2021-2022): FDA Modernization Act of 2021*. http://www.congress.gov/

Paul, S. M., Mytelka, D. S., Dunwiddie, C. T., Persinger, C. C., Munos, B. H., Lindborg, S. R., & Schacht, A. L. (2010). How to improve R&D productivity: the pharmaceutical industry's grand challenge. *Nature Reviews Drug Discovery 2010 9:3*, *9*(3), 203–214. https://doi.org/10.1038/nrd3078

Pereira, T., Kennedy, J. v, & Potgieter, J. (2019). A comparison of traditional manufacturing vs additive manufacturing, the best method for the job. *Procedia Manufacturing*, *30*, 11–18. https://doi.org/10.1016/j.promfg.2019.02.003

Pereiro, I., Fomitcheva Khartchenko, A., Petrini, L., & Kaigala, G. V. (2019). Nip the bubble in the bud: a guide to avoid gas nucleation in microfluidics. *Lab on a Chip*, *19*(14), 2296–2314. https://doi.org/10.1039/C9LC00211A

Poisson, J., Lemoinne, S., Boulanger, C., Durand, F., Moreau, R., Valla, D., & Rautou, P.-E. (2017). Liver sinusoidal endothelial cells: Physiology and role in liver diseases. *Journal of Hepatology*, *66*(1), 212–227. https://doi.org/10.1016/j.jhep.2016.07.009

Pollet, A. M. A. O., & den Toonder, J. M. J. (2020). Recapitulating the Vasculature Using Organ-On-Chip Technology. *Bioengineering*, *7*(1), 17. https://doi.org/10.3390/bioengineering7010017

Raasch, M., Rennert, K., Jahn, T., Peters, S., Henkel, T., Huber, O., Schulz, I., Becker, H., Lorkowski, S., Funke, H., & Mosig, A. (2015). Microfluidically supported biochip design for culture of endothelial cell layers with improved perfusion conditions. *Biofabrication*, *7*(1), 015013. https://doi.org/10.1088/1758-5090/7/1/015013

Ramadori, P., Kam, S., & Heikenwalder, M. (2022). T cells: Friends and foes in NASH pathogenesis and hepatocarcinogenesis. *Hepatology*, *75*(4), 1038–1049. https://doi.org/10.1002/hep.32336

Ramos, M. J., Bandiera, L., Menolascina, F., & Fallowfield, J. A. (2022). In vitro models for non-alcoholic fatty liver disease: Emerging platforms and their applications. *IScience*, *25*(1), 103549. https://doi.org/10.1016/J.ISCI.2021.103549

Rashidi, H., Alhaque, S., Szkolnicka, D., Flint, O., & Hay, D. C. (2016). Fluid shear stress modulation of hepatocyte-like cell function. *Archives of Toxicology*, *90*(7), 1757–1761. https://doi.org/10.1007/S00204-016-1689-8/FIGURES/3

Reitman, M. L. (2018). Of mice and men - environmental temperature, body temperature, and treatment of obesity. *FEBS Letters*, *592*(12), 2098–2107. https://doi.org/10.1002/1873-3468.13070

Rennert, K., Steinborn, S., Gröger, M., Ungerböck, B., Jank, A. M., Ehgartner, J., Nietzsche, S., Dinger, J., Kiehntopf, M., Funke, H., Peters, F. T., Lupp, A., Gärtner, C., Mayr, T., Bauer, M., Huber, O., & Mosig, A. S. (2015). A microfluidically perfused three dimensional human liver model. *Biomaterials*, *71*, 119–131. https://doi.org/10.1016/J.BIOMATERIALS.2015.08.043

Rinella, M. E., Dufour, J. F., Anstee, Q. M., Goodman, Z., Younossi, Z., Harrison, S. A., Loomba, R., Sanyal, A. J., Bonacci, M., Trylesinski, A., Natha, M., Shringarpure, R., Granston, T., Venugopal, A., & Ratziu, V. (2022). Non-invasive evaluation of response to obeticholic acid in patients with

NASH: Results from the REGENERATE study. *Journal of Hepatology*, *76*(3), 536–548. https://doi.org/10.1016/J.JHEP.2021.10.029

Rogal, J., Binder, C., Kromidas, E., Roosz, J., Probst, C., Schneider, S., Schenke-Layland, K., & Loskill, P. (2020). WAT-on-a-chip integrating human mature white adipocytes for mechanistic research and pharmaceutical applications. *Scientific Reports*, *10*(1), 6666. https://doi.org/10.1038/s41598-020-63710-4

Rogal, J., Probst, C., & Loskill, P. (2017). Integration concepts for multi-organ chips: how to maintain flexibility?! *Future Science OA*, *3*(2), FSO180. https://doi.org/10.4155/fsoa-2016-0092

Rogal, J., Roosz, J., & Loskill, P. (2022). Isolation, Integration, and Culture of Human Mature Adipocytes Leveraging Organ-on-Chip Technology. *Methods in Molecular Biology (Clifton, N.J.)*, *2373*, 297–313. https://doi.org/10.1007/978-1-0716-1693-2_18

Rogal, J., Roosz, J., Teufel, C., Cipriano, M., Xu, R., Eisler, W., Weiss, M., Schenke-Layland, K., & Loskill, P. (2022). Autologous Human Immunocompetent White Adipose Tissue-on-Chip. *Advanced Science*, *9*(18), 2104451. https://doi.org/10.1002/advs.202104451

Rogers, J. A., & Nuzzo, R. G. (2005). Recent progress in soft lithography. *Materials Today*, *8*(2), 50–56. https://doi.org/10.1016/S1369-7021(05)00702-9

Ronaldson-Bouchard, K., Teles, D., Yeager, K., Tavakol, D. N., Zhao, Y., Chramiec, A., Tagore, S., Summers, M., Stylianos, S., Tamargo, M., Lee, B. M., Halligan, S. P., Abaci, E. H., Guo, Z., Jacków, J., Pappalardo, A., Shih, J., Soni, R. K., Sonar, S., Vunjak-Novakovic, G. (2022). A multi-organ chip with matured tissue niches linked by vascular flow. In *Nature Biomedical Engineering* (Vol. 6, Issue 4). Springer US. https://doi.org/10.1038/s41551-022-00882-6

Rosen, E. D., & Spiegelman, B. M. (2006). Adipocytes as regulators of energy balance and glucose homeostasis. *Nature*, *444*(7121), 847–853. https://doi.org/10.1038/nature05483

Ruiz-Ojeda, Méndez-Gutiérrez, Aguilera, & Plaza-Díaz. (2019). Extracellular Matrix Remodeling of Adipose Tissue in Obesity and Metabolic Diseases. *International Journal of Molecular Sciences*, *20*(19), 4888. https://doi.org/10.3390/ijms20194888

Russell, J. O., & Monga, S. P. (2018). Wnt/β-Catenin Signaling in Liver Development, Homeostasis, and Pathobiology. *Annual Review of Pathology: Mechanisms of Disease*, *13*(1), 351–378. https://doi.org/10.1146/annurev-pathol-020117-044010

Russell, W. M. S., & Burch, R. L. (1959). *The Principles of Humane Experimental Technique*. Methuen. https://doi.org/10.5694/j.1326-5377.1960.tb73127.x

Schimek, K., Frentzel, S., Luettich, K., Bovard, D., Rütschle, I., Boden, L., Rambo, F., Erfurth, H., Dehne, E.-M., Winter, A., Marx, U., & Hoeng, J. (2020). Human multi-organ chip co-culture of bronchial lung culture and liver spheroids for substance exposure studies. *Scientific Reports*, *10*(1), 7865. https://doi.org/10.1038/s41598-020-64219-6

Schneider, S., Brás, E. J. S., Schneider, O., Schlünder, K., & Loskill, P. (2021). Facile Patterning of Thermoplastic Elastomers and Robust Bonding to Glass and Thermoplastics for Microfluidic Cell Culture and Organ-on-Chip. *Micromachines*, *12*(5), 575. https://doi.org/10.3390/mi12050575

Schneider, S., Bubeck, M., Rogal, J., Weener, H. J., Rojas, C., Weiss, M., Heymann, M., van der Meer, A. D., & Loskill, P. (2021). Peristaltic on-chip pump for tunable media circulation and whole blood perfusion in PDMS-free organ-on-chip and Organ-Disc systems. *Lab on a Chip*, *21*(20), 3963–3978. https://doi.org/10.1039/D1LC00494H

Schneider, S., Erdemann, F., Schneider, O., Hutschalik, T., & Loskill, P. (2020). Organ-on-a-disc: A platform technology for the centrifugal generation and culture of microphysiological 3D cell constructs amenable for automation and parallelization. *APL Bioengineering*, *4*(4), 046101. https://doi.org/10.1063/5.0019766

Schneider, S., Gruner, D., Richter, A., & Loskill, P. (2021). Membrane integration into PDMS-free microfluidic platforms for organ-on-chip and analytical chemistry applications. *Lab on a Chip*, *21*(10), 1866–1885. https://doi.org/10.1039/D1LC00188D

Seebacher, F., Zeigerer, A., Kory, N., & Krahmer, N. (2020). Hepatic lipid droplet homeostasis and fatty liver disease. *Seminars in Cell & Developmental Biology*, *108*, 72–81. https://doi.org/10.1016/j.semcdb.2020.04.011

Segovia-Miranda, F., Morales-Navarrete, H., Kücken, M., Moser, V., Seifert, S., Repnik, U., Rost, F., Brosch, M., Hendricks, A., Hinz, S., Röcken, C., Lütjohann, D., Kalaidzidis, Y., Schafmayer, C., Brusch, L., Hampe, J., & Zerial, M. (2019). Three-dimensional spatially resolved geometrical and functional models of human liver tissue reveal new aspects of NAFLD progression. *Nature Medicine*, *25*(12), 1885–1893. https://doi.org/10.1038/s41591-019-0660-7

Serras, A. S., Rodrigues, J. S., Cipriano, M., Rodrigues, A. v., Oliveira, N. G., & Miranda, J. P. (2021). A Critical Perspective on 3D Liver Models for Drug Metabolism and Toxicology Studies. *Frontiers in Cell and Developmental Biology*, *9*. https://doi.org/10.3389/fcell.2021.626805

Shakeri, A., Khan, S., Jarad, N. A., & Didar, T. F. (2022). The Fabrication and Bonding of Thermoplastic Microfluidics: A Review. *Materials*, *15*(18), 6478. https://doi.org/10.3390/ma15186478

Shroff, T., Aina, K., Maass, C., Cipriano, M., Lambrecht, J., Tacke, F., Mosig, A., & Loskill, P. (2022). Studying metabolism with multi-organ chips: new tools for disease modelling, pharmacokinetics and pharmacodynamics. *Open Biology*, *12*(3). https://doi.org/10.1098/rsob.210333

Sivashankar, S., Agambayev, S., Mashraei, Y., Li, E. Q., Thoroddsen, S. T., & Salama, K. N. (2016). A "twisted" microfluidic mixer suitable for a wide range of flow rate applications. *Biomicrofluidics*, *10*(3), 034120. https://doi.org/10.1063/1.4954812

Slaughter, V. L., Rumsey, J. W., Boone, R., Malik, D., Cai, Y., Sriram, N. N., Long, C. J., McAleer, C. W., Lambert, S., Shuler, M. L., & Hickman, J. J. (2021). Validation of an adipose-liver human-on-a-chip model of NAFLD for preclinical therapeutic efficacy evaluation. *Scientific Reports*, *11*(1). https://doi.org/10.1038/S41598-021-92264-2

Snakenborg, D., Perozziello, G., Geschke, O., & Kutter, J. P. (2007). A fast and reliable way to establish fluidic connections to planar microchips. *INSTITUTE OF PHYSICS PUBLISHING JOURNAL OF MICROMECHANICS AND MICROENGINEERING J. Micromech. Microeng*, *17*, 98–103. https://doi.org/10.1088/0960-1317/17/1/013

Staiger, H., Keuper, M., Berti, L., Hrabě de Angelis, M., & Häring, H.-U. (2017). Fibroblast Growth Factor 21—Metabolic Role in Mice and Men. *Endocrine Reviews*, *38*(5), 468–488. https://doi.org/10.1210/er.2017-00016

Sun, Q., Pei, J., Li, Q., Niu, K., & Wang, X. (2019). Reusable Standardized Universal Interface Module (RSUIM) for Generic Organ-on-a-Chip Applications. *Micromachines 2019, Vol. 10, Page 849*, *10*(12), 849. https://doi.org/10.3390/MI10120849

Sun, Y., Kwok, Y. C., & Nguyen, N.-T. (2006). Low-pressure, high-temperature thermal bonding of polymeric microfluidic devices and their applications for electrophoretic separation. *Journal of Micromechanics and Microengineering*, *16*(8), 1681–1688. https://doi.org/10.1088/0960-1317/16/8/033

Sung, J. H., Kam, C., & Shuler, M. L. (2010). A microfluidic device for a pharmacokinetic–pharmacodynamic (PK–PD) model on a chip. *Lab on a Chip*, *10*(4), 446. https://doi.org/10.1039/b917763a

Szafranska, K., Kruse, L. D., Holte, C. F., McCourt, P., & Zapotoczny, B. (2021). The wHole Story About Fenestrations in LSEC. *Frontiers in Physiology*, *12*. https://doi.org/10.3389/fphys.2021.735573

Tang, T., Sui, Y., Lian, M., Li, Z., & Hua, J. (2013). Pro-inflammatory activated Kupffer cells by lipids induce hepatic NKT cells deficiency through activation-induced cell death. *PLoS ONE*, *8*(12). https://doi.org/10.1371/JOURNAL.PONE.0081949

Temiz, Y., Lovchik, R. D., Kaigala, G. v., & Delamarche, E. (2015). Lab-on-a-chip devices: How to close and plug the lab? *Microelectronic Engineering*, *132*, 156–175. https://doi.org/10.1016/J.MEE.2014.10.013

Tian, X., Wu, L., Gu, D., Yuan, S., Zhao, Y., Li, X., Ouyang, L., Song, B., Gao, T., He, J., Lin, X., Lin, F., Zhu, J., & Li, D. (2022). Roadmap for Additive Manufacturing: Toward Intellectualization and Industrialization. *Chinese Journal of Mechanical Engineering: Additive Manufacturing Frontiers*, *1*(1), 100014. https://doi.org/10.1016/j.cjmeam.2022.100014

Tkachenko, E., Gutierrez, E., Ginsberg, M. H., & Groisman, A. (2009). An easy to assemble microfluidic perfusion device with a magnetic clamp. *Lab on a Chip*, *9*(8), 1085–1095. https://doi.org/10.1039/B812184B

Toh, Y. C., Lim, T. C., Tai, D., Xiao, G., van Noort, D., & Yu, H. (2009). A microfluidic 3D hepatocyte chip for drug toxicity testing. *Lab on a Chip*, *9*(14), 2026–2035. https://doi.org/10.1039/B900912D

Tokashiki, M., & Takamatsu, H. (1993). Perfusion culture apparatus for suspended mammalian cells. *Cytotechnology 1993 13:3*, *13*(3), 149–159. https://doi.org/10.1007/BF00749811

Tonon, F., Giobbe, G. G., Zambon, A., Luni, C., Gagliano, O., Floreani, A., Grassi, G., & Elvassore, N. (2019). In vitro metabolic zonation through oxygen gradient on a chip. *Scientific Reports 2019 9:1*, *9*(1), 1–10. https://doi.org/10.1038/s41598-019-49412-6

Tran, H. H., Wu, W., & Lee, N. Y. (2013). Ethanol and UV-assisted instantaneous bonding of PMMA assemblies and tuning in bonding reversibility. *Sensors and Actuators B: Chemical*, *181*, 955–962. https://doi.org/10.1016/j.snb.2012.11.060

Trapecar, M., Wogram, E., Svoboda, D., Communal, C., Omer, A., Lungjangwa, T., Sphabmixay, P., Velazquez, J., Schneider, K., Wright, C. W., Mildrum, S., Hendricks, A., Levine, S., Muffat, J., Lee, M. J., Lauffenburger, D. A., Trumper, D., Jaenisch, R., & Griffith, L. G. (2021). Human physiomimetic model integrating microphysiological systems of the gut, liver, and brain for studies of neurodegenerative diseases. *Science Advances*, *7*(5). https://doi.org/10.1126/sciadv.abd1707

Tsamandouras, N., Kostrzewski, T., Stokes, C. L., Griffith, L. G., Hughes, D. J., & Cirit, M. (2017). Quantitative Assessment of Population Variability in Hepatic Drug Metabolism Using a Perfused Three-Dimensional Human Liver Microphysiological System. *Journal of Pharmacology and Experimental Therapeutics*, *360*(1), 95–105. https://doi.org/10.1124/jpet.116.237495

Tsao, C. W., Hromada, L., Liu, J., Kumar, P., & DeVoe, D. L. (2007). Low temperature bonding of PMMA and COC microfluidic substrates using UV/ozone surface treatment. *Lab on a Chip*, *7*(4), 499. https://doi.org/10.1039/b618901f

Uba, F. I., Hu, B., Weerakoon-Ratnayake, K., Oliver-Calixte, N., & Soper, S. A. (2015). High process yield rates of thermoplastic nanofluidic devices using a hybrid thermal assembly technique. *Lab on a Chip*, *15*(4), 1038–1049. https://doi.org/10.1039/C4LC01254B

Van Der Worp, H. B., Howells, D. W., Sena, E. S., Porritt, M. J., Rewell, S., O'collins, V., & Macleod, M. R. (2018). Of mice and men – environmental temperature, body temperature, and treatment of obesity. *FEBS Letters*, *592*(12), 2098–2107. https://doi.org/10.1002/1873-3468.13070

Vinci, B., Duret, C., Klieber, S., Gerbal-Chaloin, S., Sa-Cunha, A., Laporte, S., Suc, B., Maurel, P., Ahluwalia, A., & Daujat-Chavanieu, M. (2011). Modular bioreactor for primary human hepatocyte culture: Medium flow stimulates expression and activity of detoxification genes. *Biotechnology Journal*, *6*(5), 554–564. https://doi.org/10.1002/BIOT.201000326

Viravaidya, K., & Shuler, M. L. (2002). Prediction of Naphthalene Bioaccumulation Using an Adipocyte Cell Line Model. *Biotechnology Progress*, *18*(2), 174–181. https://doi.org/10.1021/bp0101684

Viravaidya, K., & Shuler, M. L. (2008). Incorporation of 3T3-L1 Cells To Mimic Bioaccumulation in a Microscale Cell Culture Analog Device for Toxicity Studies. *Biotechnology Progress*, *20*(2), 590–597. https://doi.org/10.1021/bp034238d

Viravaidya, K., Sin, A., & Shuler, M. L. (2008). Development of a Microscale Cell Culture Analog To Probe Naphthalene Toxicity. *Biotechnology Progress*, *20*(1), 316–323. https://doi.org/10.1021/bp0341996

Vivas, A., van den Berg, A., Passier, R., Odijk, M., & van der Meer, A. D. (2022). Fluidic circuit board with modular sensor and valves enables stand-alone, tubeless microfluidic flow control in organs-on-chips. *Lab on a Chip*, *22*(6), 1231–1243. https://doi.org/10.1039/D1LC00999K

Vollertsen, A. R., de Boer, D., Dekker, S., Wesselink, B. A. M., Haverkate, R., Rho, H. S., Boom, R. J., Skolimowski, M., Blom, M., Passier, R., van den Berg, A., van der Meer, A. D., & Odijk, M. (2020). Modular operation of microfluidic chips for highly parallelized cell culture and liquid dosing via a fluidic circuit board. *Microsystems & Nanoengineering 2020 6:1*, *6*(1), 1–16. https://doi.org/10.1038/s41378-020-00216-z

Vollertsen, A. R., Vivas, A., van Meer, B., van den Berg, A., Odijk, M., & van der Meer, A. D. (2021). Facilitating implementation of organs-on-chips by open platform technology. *Biomicrofluidics*, *15*(5), 051301. https://doi.org/10.1063/5.0063428

Vollmar, B., & Menger, M. D. (2009). The Hepatic Microcirculation: Mechanistic Contributions and Therapeutic Targets in Liver Injury and Repair. *Physiological Reviews*, *89*(4), 1269–1339. https://doi.org/10.1152/physrev.00027.2008

Walpole, S. C., Prieto-Merino, D., Edwards, P., Cleland, J., Stevens, G., & Roberts, I. (2012). The weight of nations: an estimation of adult human biomass. *BMC Public Health*, *12*(1), 439. https://doi.org/10.1186/1471-2458-12-439

Wang, J. D., Douville, N. J., Takayama, S., & Elsayed, M. (2012). Quantitative analysis of molecular absorption into PDMS microfluidic channels. *Annals of Biomedical Engineering*, *40*(9), 1862–1873. https://doi.org/10.1007/S10439-012-0562-Z/FIGURES/8

Weisberg, S. P., McCann, D., Desai, M., Rosenbaum, M., Leibel, R. L., & Ferrante, A. W. (2003). Obesity is associated with macrophage accumulation in adipose tissue. *Journal of Clinical Investigation*, *112*(12), 1796–1808. https://doi.org/10.1172/JCI200319246

Wen, X., Takahashi, S., Hatakeyama, K., & Kamei, K. (2021). Evaluation of the Effects of Solvents Used in the Fabrication of Microfluidic Devices on Cell Cultures. *Micromachines*, *12*(5), 550. https://doi.org/10.3390/mi12050550

Wikswo, J. P., Block, F. E., Cliffel, D. E., Goodwin, C. R., Marasco, C. C., Markov, D. A., McLean, D. L., McLean, J. A., McKenzie, J. R., Reiserer, R. S., Samson, P. C., Schaffer, D. K., Seale, K. T., & Sherrod, S. D. (2013). Engineering Challenges for Instrumenting and Controlling Integrated Organ-on-Chip Systems. *IEEE Transactions on Biomedical Engineering*, *60*(3), 682–690. https://doi.org/10.1109/TBME.2013.2244891

Wikswo, J. P., Curtis, E. L., Eagleton, Z. E., Evans, B. C., Kole, A., Hofmeister, L. H., & Matloff, W. J. (2013). Scaling and systems biology for integrating multiple organs-on-a-chip. *Lab on a Chip*, *13*(18), 3496–3511. https://doi.org/10.1039/C3LC50243K

Wilhelm, E., Neumann, C., Duttenhofer, T., Pires, L., & Rapp, B. E. (2013). Connecting microfluidic chips using a chemically inert, reversible, multichannel chip-to-world-interface. *Lab on a Chip*, *13*(22), 4343–4351. https://doi.org/10.1039/C3LC50861G

Wu, D., Zhao, Z., Zhang, Q., Qi, H. J., & Fang, D. (2019). Mechanics of shape distortion of DLP 3D printed structures during UV post-curing. *Soft Matter*, *15*(30), 6151–6159. https://doi.org/10.1039/C9SM00725C

Ya, S., Ding, W., Li, S., Du, K., Zhang, Y., Li, C., Liu, J., Li, F., Li, P., Luo, T., He, L., Xu, A., Gao, D., & Qiu, B. (2021). On-Chip Construction of Liver Lobules with Self-Assembled Perfusable Hepatic Sinusoid Networks. *ACS Applied Materials and Interfaces*, *13*(28), 32640–32652. https://doi.org/10.1021/ACSAMI.1C00794/ASSET/IMAGES/LARGE/AM1C00794_0006.JPEG

Yang, A., & Mottillo, E. P. (2020). Adipocyte lipolysis: from molecular mechanisms of regulation to disease and therapeutics. *Biochemical Journal*, *477*(5), 985–1008. https://doi.org/10.1042/BCJ20190468

Yang, J., Hirai, Y., Iida, K., Ito, S., Trumm, M., Terada, S., Sakai, R., Tsuchiya, T., Tabata, O., & Kamei, K.-I. (2020). Integrated gut–liver-on-a-chip platform as an in vitro human model of non-alcoholic fatty liver disease. *Biorxiv.Org*. https://doi.org/10.1101/2020.06.10.141606

Ye, D. wei, Rong, X. lu, Xu, A. min, & Guo, J. (2017). Liver-adipose tissue crosstalk: A key player in the pathogenesis of glucolipid metabolic disease. *Chinese Journal of Integrative Medicine*, *23*(6), 410–414. https://doi.org/10.1007/s11655-017-2810-4

Young, B., O'Dowd, G. & Woodford, P. (2013.). Wheater's Functional Histology. *Elsevier Health Sciences*. https://books.google.com/books?hl=en&lr=&id=HUlYAQAAQBAJ&oi=fnd&pg=PP1&ots=F8E_10sSBt&sig=RT9iSPx1jyBn5XIHSlx1QUUWUMg

Young, C. K. J., & Young, M. J. (2019). Comparison of HepaRG cells following growth in proliferative and differentiated culture conditions reveals distinct bioenergetic profiles. *Cell Cycle*, *18*(4), 476–499. https://doi.org/10.1080/15384101.2019.1578133

Younossi, Z., Tacke, F., Arrese, M., Chander Sharma, B., Mostafa, I., Bugianesi, E., Wai-Sun Wong, V., Yilmaz, Y., George, J., Fan, J., & Vos, M. B. (2019). Global Perspectives on Nonalcoholic Fatty Liver Disease and Nonalcoholic Steatohepatitis. *Hepatology*, *69*(6), 2672–2682. https://doi.org/10.1002/HEP.30251

Yu, H., Chong, Z. Z., Tor, S. B., Liu, E., & Loh, N. H. (2015). Low temperature and deformation-free bonding of PMMA microfluidic devices with stable hydrophilicity via oxygen plasma treatment and PVA coating. *RSC Advances*, *5*(11), 8377–8388. https://doi.org/10.1039/C4RA12771D

Yuen, P. K. (2008). SmartBuild–A truly plug-n-play modular microfluidic system. *Lab on a Chip*, *8*(8), 1374. https://doi.org/10.1039/b805086d

Yuen, P. K. (2016). A reconfigurable stick-n-play modular microfluidic system using magnetic interconnects. *Lab on a Chip*, *16*(19), 3700–3707. https://doi.org/10.1039/C6LC00741D

Zambon, A., Zoso, A., Gagliano, O., Magrofuoco, E., Fadini, G. P., Avogaro, A., Foletto, M., Quake, S., & Elvassore, N. (2015). High Temporal Resolution Detection of Patient-Specific Glucose Uptake from Human ex Vivo Adipose Tissue On-Chip. *Analytical Chemistry*, *87*(13), 6535–6543. https://doi.org/10.1021/AC504730R/SUPPL_FILE/AC504730R_SI_002.PDF

Zbinden, A., Marzi, J., Schlünder, K., Probst, C., Urbanczyk, M., Black, S., Brauchle, E. M., Layland, S. L., Kraushaar, U., Duffy, G., Schenke-Layland, K., & Loskill, P. (2020). Non-invasive marker-independent high content analysis of a microphysiological human pancreas-on-a-chip model. *Matrix Biology*, *85–86*, 205–220. https://doi.org/10.1016/j.matbio.2019.06.008

Zeigerer, A., Wuttke, A., Marsico, G., Seifert, S., Kalaidzidis, Y., & Zerial, M. (2017). Functional properties of hepatocytes in vitro are correlated with cell polarity maintenance. *Experimental Cell Research*, *350*(1), 242–252. https://doi.org/10.1016/j.yexcr.2016.11.027

Zhang, C., Zhao, Z., Abdul Rahim, N. A., van Noort, D., & Yu, H. (2009). Towards a human-on-chip: Culturing multiple cell types on a chip with compartmentalized microenvironments. *Lab on a Chip*, *9*(22), 3185. https://doi.org/10.1039/b915147h

Zhang, Y. S., Aleman, J., Shin, S. R., Kilic, T., Kim, D., Mousavi Shaegh, S. A., Massa, S., Riahi, R., Chae, S., Hu, N., Avci, H., Zhang, W., Silvestri, A., Sanati Nezhad, A., Manbohi, A., de Ferrari, F., Polini, A., Calzone, G., Shaikh, N., … Khademhosseini, A. (2017). Multisensor-integrated organs-on-chips platform for automated and continual in situ monitoring of organoid behaviors. *Proceedings of the National Academy of Sciences*, *114*(12). https://doi.org/10.1073/pnas.1612906114

Zhuge, F., Ni, Y., Nagashimada, M., Nagata, N., Xu, L., Mukaida, N., Kaneko, S., & Ota, T. (2016). DPP-4 Inhibition by Linagliptin Attenuates Obesity-Related Inflammation and Insulin Resistance by Regulating M1/M2 Macrophage Polarization. *Diabetes*, *65*(10), 2966–2979. https://doi.org/10.2337/db16-0317

8. Appendix

8.1. Previous chip iterations – Inbuilt connection system

The chip for the inbuilt connection system underwent a series of iterations including size reduction, media channel simplification, etc. (Table 36). In general, the media layers and tissue layer thicknesses corresponded to the methods section.

Table 36: Appendix: Chip iterations for the inbuilt connection system chip

Version schematic	Details
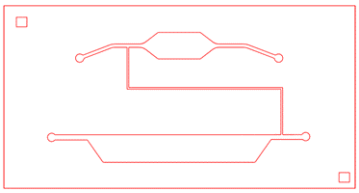	Resistance channel connecting WAT-chip outlet to liver-chip inlet.
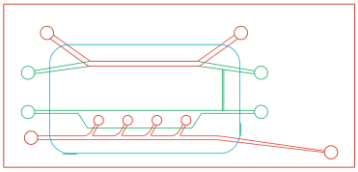	Smaller resistance channel. Tapering tissue fluidic outlet, 1 mm diameter WAT chambers. Straight liver channel.
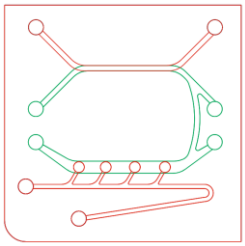	Curved resistance channels. WAT Tissue fluidics have a fixed width.
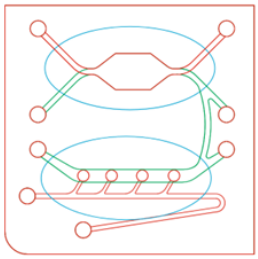	Hexagonal liver-chamber. Membranes split per organ.
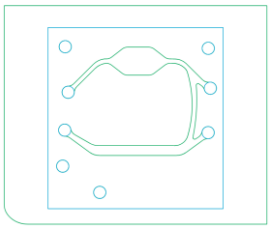	Tissue chambers eliminated, only endothelial cells injected into media channel. Membrane bonded to chip bottom.

8.2. Previous chip iterations – WAT-chip

The initial design of the WAT- chip was prepared by Dr. Julia Rogal in a PDMS chip format. The main features were transferred from the PDMS format to the rigid plastic format, and

certain aspects of the chip were investigated and modified based on manufacturing capabilities (previous iterations of the chips have been summarized below, in Table 37 of the versions of the WAT-chip up to the Versions 1 and 2).

Table 37: Appendix: Chip iterations of the WAT-chip

Version schematic	Details
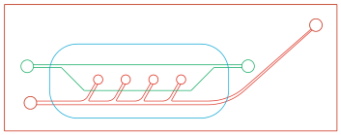	1 mm diameter tissue chambers. Tapering tissue fluidic channel. Membrane intersecting with media channel.
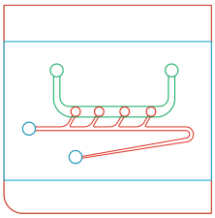	Different orientation of tapering tissue fluidic channel. 22 by 22 mm footprint. Membrane spread across media channel.
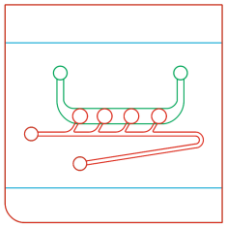	1.5 mm tissue chamber diameter, membrane bonded with stamp method. Tissue fluidic channel of a fixed length. PMMA top port connection.
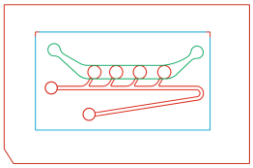	18 by 25 mm footprint. Smaller membrane region. PDMS top port connection.

8.3. Previous chip iterations – liver-chip

The scale and method of fabrication of the liver-chip was modified from the initial design by the Mosig Group (previous iterations of the chips have been summarized below, in Table 38 of the versions of the liver-chip up to the Versions 1, 2 and 3).

Table 38: Appendix: Chip iterations of the liver-chip

Version schematic	Details
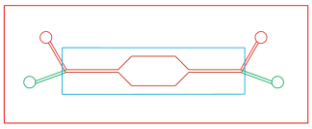	Hexagonal shape of liver-chamber, bonded without stamp method, in the hotpress.

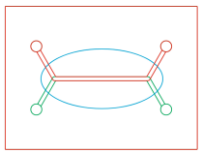	Straight channel liver-chip, channel width of 500 µm.
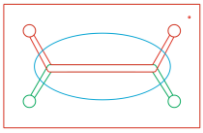	Straight channel liver-chip, channel width of 800 µm.
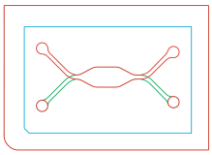	Hexagonal shape of liver-chamber, bonded with stamp method. Membrane extends across entire chip.
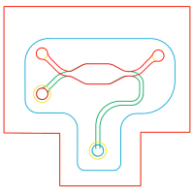	25 by 25 mm footprint Hot embossed tissue and media channels with epoxy molds.

8.4. WAT-chip isolations

All biopsies were conducted at Klinikum Charlottenhaus in Stuttgart (Table 39).

Table 39: Compilation of biopsies that contributed to the adipocytes injected into the WAT-chips

Date of surgery	Donor sex	Donor age	Region	Height [m]	Current weight [kg]	Maximum BMI [kg/m^2]	Present BMI [kg/m^2]	Maximum obesity class	Obesity class
17/09/2019	m	59	abdomen	1.65	74	49.16	27.15	obesity class III	pre-obesity
08/10/2019	f	38	back	1.52	74	57.95	32	obesity class III	obesity class I
11/02/2020	f	33	inner thigh	-	80	-	33	-	obesity class I
03/03/2020	f	50	thigh	1.66	76	42.1	27.58	obesity class III	preobesity
02/03/2021	f	43	butt	1.69	86	50.93	30	obesitiy class III	obesitity class I
16/03/2021	f	48	upper arm	1.57	64	30.47	26	obesity class I	pre-obesity
23/03/2021	f	62	abdomen	1.51	82	49.84	35.85	obesity class III	obesity class II

06/04/2021		50	abdomen	1.64	75	30.49	27.89	obesity class I	pre-obesity
06/07/2021	f	48	abdomen	1.56	80	-	32.81	-	obesity class I
13/07/2021	f	41	thigh	1.7	73	42.56	25.26	obesity class III	overweight
03/08/2021	f	60	abdomen	1.62	81	-	31	-	obesitity class I
28/09/2021	f	44	abdomen	1.65	98.5	52.71	36.18	obesitiy class III	obesity class II
12/04/2022	f	67	abdomen	1.6	88	29.3	-	pre-obesity	-
03/05/2022	f	39	abdomen		88	-	35.6	-	obesity class II
21/06/2022	f	56	side (Flanke)	1.6	83	-	--		-
15/09/2022	f	33	thigh	1.8	96	49.38	-	obesity class III	-
20/09/2022	f	53	abdomen	1.73	71	39.09	-	obesity class II	-

8.5. Previous chip iterations – liver-sinusoid-on-chip

The LSOC underwent iterations depending on the liver Biochip version (BC002, BC005) (Table 40 summarizes the changes until the two shower concepts discussed in the Results section).

Table 40: Appendix: Chip iterations of the LSOC

Version schematic	Details
	Branched shower channel, thermal fusion bonded PMMA. Glued onto the top of the Biochip.
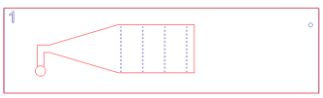	Unbranched PMMA shower.
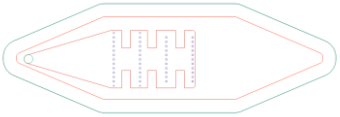	PMMA-PC-PMMA hybrid with supports, thermal fusion bonded in hotpress

	PMMA-PC-PMMA shower, in the width of the Biochip
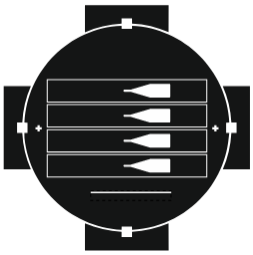	Unbranched shower, hotembossed TPE shower channel with PC top and bottom.
	Unbranched shower, lasercut TPE shower channel extending across the length of the tissue channel for the new version of the Biochip

9. Declaration of contributions to the dissertation

The dissertation work was carried out at Fraunhofer IGB, Stuttgart from 06, 2019 to 05, 2021 and at the Natural and Medical Sciences Institute, Reutlingen from 06, 2021 to 08, 2022, under the supervision of Prof. Dr. Peter Loskill.

The study was designed by me, Tanvi Shroff, with scientific inputs from Prof. Dr. Peter Loskill and Dr. Madalena Cipriano. Additional support was provided by my collaborators, Stefanie Fuchs, Dr. Torsten Mayr, Dr. Martin Raasch and P.D. Alexander Mosig. I supervised Ms. Jillian Gamboa and Ms. Celina Spangenberger for their master thesis and bachelor internship respectively. Their progress was built on and served to guide my thesis towards the achieved results. Specifically, Ms. Jillian Gamboa investigated the design and fabrication of the three connection approaches of the MOC. For this, the two chip designs were simplified to contain the media channels, and connection approaches were fabricated and cultured with human umbilical endothelial cells. Ms. Spangenberger supported the optimization of manufacturing protocols for version 1 of the WAT- and liver-chips. Finally, the immune cell reservoir parts were fabricated in the workshop of the NMI by Mr. Martin Gaier. The concept and dimensions were defined by me with inputs from Prof. Dr. Peter Loskill and Mr. Gaier, who then proceeded to fabricate some parts on the equipment in the workshop, such as the turning machine. All other parts were 3D printed by me.

The following publications occurred during the time of this thesis:

1. **Shroff T,** Aina K, Maass C, Cipriano M, Lambrecht J, Tacke F, Mosig A, Loskill P. Studying metabolism with multi-organ chips: new tools for disease modelling, pharmacokinetics and pharmacodynamics. Open Biology. 2022 Mar 2;12(3):210333.
2. Moruzzi A, **Shroff T,** Keller S, Loskill P, Cipriano M. Training the next generation of researchers in the Organ-on-Chip field. Education Sciences. 2023 Jan 30;13(2):144.

I made a major contribution to the review (1), with collaboration and assistance of the co-authors with the highest contribution from Aina Kehinde. I contributed as a second author for publication (2), supporting Alessia Moruzzi with data collection, analysis and writing the manuscript.

I hereby declare that the doctoral dissertation submitted with the title: “WAT-Liver-Chip with Integrated Sensors to Study Human White Adipose and Hepatic Tissue Crosstalk” was written independently using only the stated sources and aids and that quotes and excerpts, literal or otherwise, are marked correspondingly. I declare on oath that these statements are true and that I have concealed nothing. I am aware that false declarations or affirmations in lieu of an oath can be punished with a jail sentence of up to three years or with a fine.

Tanvi Shroff

08.12.2023, Tübingen

10. Acknowledgments

This research work would not have been possible without the mentorship of Prof. Dr. Peter Loskill. His µOrgano Lab, much like the OoC field, is a unique blend of biology and engineering – two different perspectives, working towards a common goal. Maintaining such a group is a mammoth task and I am grateful for his guidance, which shaped my approach to research. I would also like to thank Prof. Dr. Alexander Weber and PD Dr. Alexander Mosig for their support and for examining this thesis. Prof. Dr. Katja Schenke-Layland and Dr. Markus Wolperdinger, leaders of the NMI and Fraunhofer IGB respectively, fostered productive work environments which meant I could devote my full attention to research.

The members of the µOrgano Lab made research enjoyable and helped me find a silver lining even on the darkest days. My deepest gratitude goes to Dr. Madalena Cipriano for her guidance and for being a role model; in her, I found a mentor for life. I would like to thank Alessia Moruzzi, Dr. Eduardo Brás, Fulya Ersoy, Matthijs van der Moolen, Hannah Graf, Johanna Chuchuy, Dr. Stefan Schneider, Dr. Silke Keller, Cristhian Rojas, Dr. Julia Rogal, Julia Roosz, Dr. Oliver Schneider, Elena Kromidas, Ibrahim Maulana Tengkyu, Dr. Claudia Teufel, Lena Scheying, Franziska Kern and many other lab members for their support, tips, and collaboration, becoming friends in addition to great colleagues. It was a pleasure working with and learning from Mr. Martin Gaier at the NMI, and also supervising Jillian Gamboa and Celina Spangenberger during their research with our group. Katharina Schlünder took many forms during this phase of my life – friend, colleague, flatmate, confidante.

Within the EUROoCS ITN, I was fortunate enough to find excellent collaborators and fellow adventurers. I extend my gratitude to Joanna Nowacka, Stefanie Fuchs, Anders Tjell Orts, Mara Luchetti, Merve Bulut, Kehinde Aina, and the rest of my research contemporaries. Being a part of this ITN gave me the privilege of learning from leaders in the field such as Dr. Andries van der Meer, Dr. Stefan Kauschke, Dr. Susanne Brendler-Schwaab, Dr. Torsten Mayr, Dr. Maria Tenje and countless others as advisors. A specific thank you to our project collaborators PD Dr. Alexander Mosig, the AG INSPIRE group and Dynamic42 GmbH, for hosting me at Universitätsklinikum Jena and teaching me the nuances of working with hepatic cells. Support from Dr. Martin Raasch, Dr. Knut Rennert, and many others enabled a large part of my work and contributed entensively to my learning and experience. The support and guidance of members of the Experimental Medicine program at the University of Tübingen, mainly Dr. Inka Montero, Dr. Lina Maria Cajamara and my classmates (Alex, Agnes, Chao and Linyang) enabled smooth navigation through the program over the years. Other beloved friends and family – Philipp, Peter, Uta, Moritz, Ashley, Rolf, Maike, Paul and Kathleen – made sure I was never alone during the challenging times of the pandemic, and that I was having my share of fun outside of work.

I have been fortunate in learning from and being guided by intelligent, driven and positive people throughout my life in India (my childhood and the Institute of Chemical Technology), the USA (Johns Hopkins University and work at Emulate Inc.) and in Germany. But my biggest source of strength has been my family - Prajakti, Vineet, Mitali, Vedant, Anil, and Nalini Shroff, who shaped my curiosity, self-awareness, and determination with their unfaltering love and support.